

# POLITECNICO MILANO 1863



PHD COURSE IN ARCHITECTURE, BUILT ENVIRONMENT AND  
CONSTRUCTION ENGINEERING

Head of PhD: Prof. Marco Scaioni  
XXXIII Cycle

## **Doctoral Thesis**

# **Bending and fatigue behaviour of externally bonded inorganic-matrix composites**

Supervisor:

Prof. Pierluigi Colombi

Ph.D candidate:

Ing. Angelo Savio Calabrese

Co-Supervisors:

Prof. Tommaso D'Antino

Prof. Carlo Poggi

**March 2021**







*To the Reader.*



## ACKNOWLEDGEMENTS

I would like to acknowledge the supervisors of this thesis work, prof. Pierluigi Colombi, prof. Tommaso D'Antino and prof. Carlo Poggi, for their constant scientific advisement, guidance and support throughout the PhD studies. I also want to thank them for giving me the opportunity to work on this topic, for their confidence in me and for having believed in my ideas and proposals.

My acknowledgements also goes to the researchers and technicians form the Laboratorio Prove Materiali of Politecnico di Milano, with whom I have cooperated in the experimental work, over those years.

The partners from the industry are also thanked for providing me with their expert advices and for having supplied the composite materials adopted in the experimental. They are Ruredil Spa., KERAKOLL Spa, Sika Italia Spa and TCS Srl.

## ABSTRACT

The thesis work reports on the results, procedures, methods and analyses of more than 200 experimental tests performed by the author in the three-year period 2018-2020, at the Materials Testing Laboratory of the Politecnico di Milano. The experimental investigation concerned the mechanical characterization of the adhesion-to-substrate mechanism of inorganic-matrix fiber reinforced composite materials. These materials, typically known as Fabric Reinforced Cementitious Matrix composites (FRCM), are now universally established as innovative externally bonded structural strengthening for reinforced concrete and masonry structures. Due to their low invasiveness, high structural efficiency, high strength-to-weight ratio and partial reversibility after application, they are particularly suitable for the reinforcement of masonry structures. Their execution is simple and quick, it requires adequate preparation of the substrate, on which the FRCM layer is subsequently applied, according to a continuous or discontinuous configuration (wrapping), for a thickness between 10 and 25 mm.

Although the application of these composites has proven to guarantee significant increases to the bearing capacity of the reinforced element, their structural efficiency is closely linked to the quality of their bond with the substrate: the premature triggering of a debonding mechanism from the support would, in fact, cause a sudden reduction of the bearing capacity of the reinforced element, and, sometimes, a fragile type failure of the structure. Therefore, over the years, various test set-ups have been developed for the laboratory study of the adhesion properties of FRCM materials, aimed at analysing the effect of different parameters on their adherence capacity and the consequent debonding mode. In particular, this thesis work focused on the experimental and analytical investigation of the influence of out-of-plane bending and high-cycle fatigue load, on the bond behaviour of FRCM composites. A new test set-up was specifically designed to recreate laboratory conditions similar to those of a real inflected element. The experimental evidence was accompanied by analytical interpretations of the results, based on fracture mechanics approaches, aimed at identifying predictive models of the bond behaviour of specific types of FRCM composites.

Results showed that strengthening applications subjected to bending may exhibit a higher bond capacity, in reason of the development of normal stresses to the composite plane. The increment in bond capacity can be analytically modelled through the introduction of a snubbing friction effect, localized at the fiber exit point, which can be calibrated on the basis of experimental results. In contrast, this extra friction applied on the textile may determine damaging and rupture of fiber filaments under the effect of prolonged cyclic actions or in case of pronounced deflections, particularly for fragile textiles.



## SOMMARIO

Il presente lavoro di tesi riporta risultati, procedure, metodi e analisi di più di 200 prove sperimentali eseguite dall'autore nel triennio 2018-2020, presso il Laboratorio Prove Materiali del Politecnico di Milano. Le indagini sperimentali hanno riguardato la caratterizzazione meccanica dell'aderenza al substrato di materiali compositi fibrorinforzati a matrice inorganica. Tali materiali, tipicamente noti come Fabric Reinforced Cementitious Matrix composites (FRCM), sono ormai universalmente affermati come rinforzi strutturali innovativi per strutture in cemento armato e muratura. In ragione della loro scarsa invasività, alta efficienza strutturale, alto rapporto resistenza/peso specifico e parziale reversibilità dopo l'applicazione, si rendono particolarmente adeguati per il rinforzo di strutture in muratura. La loro messa in opera è semplice e rapida, necessita di un'adeguata preparazione del substrato, sul quale viene successivamente applicato lo strato di FRCM, secondo una configurazione continua o discontinua (fasciatura), per uno spessore compreso tra i 10 ed i 25 mm.

Sebbene l'applicazione di tali compositi provatamente garantisca significativi aumenti di capacità portante nell'elemento rinforzato, la loro efficienza strutturale è strettamente legata alla qualità dell'aderenza al substrato: il prematuro innesco di un meccanismo di distacco dal supporto determinerebbe, infatti, una brusca riduzione della capacità portante dell'elemento rinforzato, e, talvolta, un cedimento di tipo fragile della struttura. Pertanto, sono stati sviluppati, negli anni, diversi set-up di prova per lo studio in laboratorio delle proprietà di aderenza di materiali FRCM, volti ad analizzare l'effetto di diversi parametri sulla loro capacità aderente e sulla conseguente modalità di distacco. In particolare, il presente lavoro di tesi si focalizza sull'indagine sperimentale ed analitica dell'influenza di flessione fuori piano e sollecitazione ciclica ad alta frequenza, sulla capacità aderente dei compositi FRCM. Un set-up di prova è stato appositamente progettato per ricreare delle condizioni di laboratorio simili a quelle di un elemento reale inflesso. L'evidenza sperimentale è stata affiancata ad interpretazioni analitiche dei risultati, basate su approcci di meccanica della frattura, finalizzati ad individuare modelli predittivi del comportamento aderente di specifiche tipologie di compositi FRCM.

I risultati hanno mostrato che applicazioni soggette a flessione esibiscono una maggiore capacità aderente, in ragione dello sviluppo di sforzi normali al piano del composito. Tale incremento di capacità portante è analiticamente riproducibile tramite introduzione del fenomeno localizzato di snubbing friction, calibrato sui risultati sperimentali. Di contro, l'attrito esercitato sul tessuto può determinarne il danneggiamento in caso di inflessioni elevate o di azioni cicliche prolungate, in particolar modo per i tessuti fragili.



## RESEARCH OUTPUT

On the date of publication of this thesis and based on the research work therein presented, the following scientific production was issued.

- [i] Calabrese, A.S., Colombi, P., D'Antino, T. A bending test set-up for the investigation of the bond properties of FRCC strengthenings applied to masonry substrates. *Key Engineering Materials*, 2019. <https://doi.org/10.4028/www.scientific.net/KEM.817.149>
- [ii] Calabrese, A.S., Colombi, P., D'Antino, T. Analytical solution of the bond behavior of FRCC composites using a rigid-softening cohesive material law. *Composites Part B: Engineering*, 2019. <https://doi.org/10.1016/j.compositesb.2019.107051>
- [iii] D'Antino, T., Calabrese, A.S., Poggi, C., Colombi, P., Fava, G., Bocciarelli, M. Strengthening of different types of slabs with composite-reinforced mortars (CRM). Springer - Research for Development, 2020. [https://doi.org/10.1007/978-3-030-33687-5\\_26](https://doi.org/10.1007/978-3-030-33687-5_26)
- [iv] Calabrese, A.S., D'Antino, T., Poggi, C., Colombi, P., Fava, G., Pisani, M.A. Application of externally bonded inorganic-matrix composites to existing masonry structures. Springer - Research for Development, 2020. [https://doi.org/10.1007/978-3-030-33687-5\\_25](https://doi.org/10.1007/978-3-030-33687-5_25)
- [v] Calabrese, A.S., D'Antino, T., Colombi, P., Poggi, C. Study of the bond behavior of FRCC-masonry joints using a modified beam test. *Lecture Notes in Mechanical Engineering*, 2020. [https://doi.org/10.1007/978-3-030-41057-5\\_38](https://doi.org/10.1007/978-3-030-41057-5_38)
- [vi] Calabrese, A.S., D'Antino, T., Colombi, P., Carloni, C., Poggi, C. Fatigue behavior of PBO FRCC composite applied to concrete substrate. *Materials*, 2020. <https://doi.org/10.3390/ma13102368>
- [vii] D'Antino, T., Calabrese, A.S., Poggi, C. Experimental procedures for the mechanical characterization of composite reinforced mortar (CRM) systems for retrofitting of masonry structures. *Materials and Structures/Materiaux et Constructions*, 2020. <https://doi.org/10.1617/s11527-020-01529-1>
- [viii] Calabrese, A.S., D'Antino, T., Colombi, P., Poggi, C. Study of the influence of interface normal stresses on the bond behavior of FRCC composites using direct shear and modified beam tests. *Construction and Building Materials*, 2020. <https://doi.org/10.1016/j.conbuildmat.2020.120029>
- [ix] Calabrese, A.S., D'Antino, T., Colombi, P. Experimental and analytical investigation of PBO FRCC-concrete bond behaviour using direct and indirect shear test set-ups. *Submitted to Composite Structures*, 2021.
- [x] Calabrese, A.S., D'Antino, T., Colombi, P., Poggi, C., Carloni, C. Influence of the test set-up on the bond behavior of FRCC composites. *In press on ACI SP*, 2021.
- [xi] Calabrese, A.S., D'Antino, T., Colombi, P., Carloni, C., Poggi, C. Fatigue behavior of FRCC strengthened RC beams: state of the art and future developments. *Submitted to CICE 2021*
- [xii] D'Antino, T., Calabrese, A.S., Colombi, P., Poggi, C. Numerical study of the effective lap-splice length of FRCC composites. *Submitted to CICE 2021*

# CONTENTS

<b>1 FOREWORD: ON THE VULNERABILITY OF THE BUILT HERITAGE .....</b>	<b>1</b>
1.1 THE VULNERABILITY OF MASONRY STRUCTURES .....	2
1.2 THE INFLUENCE OF FATIGUE ON THE SERVICEABILITY OF STRUCTURES .....	3
1.3 INNOVATIVE SOLUTIONS FOR THE STRENGTHENING OF EXISTING STRUCTURES .....	4
1.4 ORGANIZATION OF THE THESIS WORK .....	5
<b>2 INTRODUCTION: COMPOSITE MATERIALS FOR STRUCTURAL APPLICATIONS AND THEIR MECHANICAL PROPERTIES .....</b>	<b>8</b>
2.1 FIBER REINFORCED POLYMERS (FRP).....	9
2.1.1 <i>Mechanics of FRP composites</i> .....	11
2.2 FABRIC REINFORCED CEMENTITIOUS MATRIX COMPOSITES (FRCM).....	13
2.2.1 <i>Mechanical properties of FRCM composites and their components</i> .....	15
2.3 COMPOSITE REINFORCED MORTARS (CRM) .....	22
2.3.1 <i>Mechanical properties of CRM and their components</i> .....	24
2.4 STEEL REINFORCED GROUT (SRG) .....	27
2.4.1 <i>Mechanical properties of SRG</i> .....	28
2.5 REGULATORY FRAMEWORK .....	28
<b>3 BOND IN FRCM APPLICATIONS .....</b>	<b>32</b>
3.1 EXPERIMENTAL SET-UPS EMPLOYED FOR BOND INVESTIGATION.....	34
3.1.1 <i>Direct set-ups</i> .....	35
3.1.2 <i>Beam test set-ups</i> .....	41
3.2 RELEVANCE OF FRCM BOND CAPACITY ACCORDING TO ITALIAN REGULATION STANDARDS.....	43
3.3 EXPERIMENTAL STUDY OF THE EFFECT OF LOADING RATE ON THE BOND BEHAVIOUR OF FRCM AND SRG COMPOSITES APPLIED TO CONCRETE SUBSTRATE.....	45
3.3.1 <i>Materials</i> .....	46
3.3.2 <i>Experimental set-up and procedures</i> .....	47
3.3.3 <i>Results</i> .....	49

3.3.4 Discussion .....	55
3.4 CONCLUSIONS AND CONSIDERATIONS FOR FUTURE GUIDELINES.....	59
<b>4 BOND BEHAVIOUR OF FRCM-MASONRY JOINTS UNDER BENDING CONDITIONS.....</b>	<b>62</b>
4.1 MATERIAL PROPERTIES .....	63
4.2 MODIFIED BEAM TEST SET-UP.....	64
4.3 SINGLE-LAP DIRECT-SHEAR TEST SET-UP.....	68
4.4 TEST RESULTS AND DISCUSSION .....	69
4.4.1 Discussion of the MB tests results.....	71
4.4.2 Comparison between MB and DS tests results .....	77
4.5 ANALYSIS OF THE BOND BEHAVIOR .....	78
4.6 CONCLUSIONS AND CONSIDERATIONS FOR FUTURE GUIDELINES.....	81
<b>5 STUDY OF THE EFFECT OF FLEXURAL DEFLECTION ON THE BOND BEHAVIOUR OF FRCM-CONCRETE JOINTS .....</b>	<b>84</b>
5.1 MATERIALS .....	87
5.2 EXPERIMENTAL SET-UPS.....	88
5.2.1 Modified beam tests .....	88
5.2.2 Direct shear test.....	90
5.3 TEST RESULTS .....	90
5.3.1 Modified beam test - Bare-fiber layout .....	92
5.3.2 Modified beam test - Bond-gap layout.....	94
5.3.3 Direct shear test.....	96
5.4 DISCUSSION.....	97
5.5 CONCLUSIONS AND CONSIDERATIONS FOR FUTURE GUIDELINES.....	100
<b>6 ANALYTICAL ASSESSMENT OF THE BOND BEHAVIOUR OF FRCM APPLICATIONS USING DS AND MB TESTS.....</b>	<b>102</b>
6.1 RIGID-SOFTENING SIMPLIFIED MODEL FOR THE CML IN FRCM COMPOSITES.....	107
6.1.1 Description of the debonding process.....	109
6.1.2 Snap-back phenomenon .....	118
6.1.3 Estimation of the cohesive material law parameters .....	120
6.1.4 Comparison between analytical provisions and experimental results of pull- out and direct-shear test. ....	122
6.2 ALTERNATIVE ENERGETIC APPROACH TO EVALUATE THE INTERFACE CAPACITY ..	129
6.3 INFLUENCE OF SNUBBING FRICTION ON THE BOND BEHAVIOUR OF MODIFIED BEAM TEST ON FRCM-CONCRETE JOINTS.....	132

6.3.1 Analytical investigation of the debonding process in modified beam test...	133
6.3.2 Analytical solution of the bond differential equation accounting for the snubbing-friction effect .....	136
6.3.3 Analytical model of MB tests .....	136
6.4 CONCLUSIONS AND CONSIDERATIONS FOR FUTURE GUIDELINES.....	140
<b>7 FATIGUE AND POST-FATIGUE BEHAVIOUR OF FRCM COMPOSITES</b>	<b>142</b>
7.1 FATIGUE STRENGTHENING OF RC BEAM WITH FRCM COMPOSITES: STATE OF THE ART .....	144
7.1.1 Database of existing results .....	145
7.1.2 Discussion of existing results.....	149
7.2 EXPERIMENTAL PROGRAM.....	152
7.2.1 Specimen geometry and materials .....	153
7.2.2 Quasi-static monotonic tests .....	155
7.3 FATIGUE TEST.....	156
7.3.1 Bare-fiber layout specimens.....	158
7.3.2 Bond-gap layout specimens .....	161
7.4 POST-FATIGUE TEST .....	164
7.5 CONCLUSIONS AND CONSIDERATIONS FOR FUTURE GUIDELINES.....	168
<b>8 GENERAL CONCLUSIONS AND FUTURE WORKS .....</b>	<b>170</b>
<b>9 REFERENCES.....</b>	<b>172</b>



## LIST OF TABLES

TABLE 2.1: TENSILE PROPERTIES OF INORGANIC BINDERS EMPLOYED IN FRCM TECHNOLOGY [13,24–28].....	16
TABLE 2.2: TENSILE PROPERTIES OF BARE FIBERS EMPLOYED IN FRCM APPLICATIONS [13,24].....	18
TABLE 2.3: AVERAGE TENSILE PROPERTIES OF FRCM COMPOSITES [13,24].....	22
TABLE 3.1: FRCM AND SRG MATERIALS PROPERTIES.....	47
TABLE 3.2: RESULTS OF FRCM STRENGTHENED SPECIMENS. ....	54
TABLE 3.3: RESULTS OF SRG STRENGTHENED SPECIMENS.....	55
TABLE 4.1: FRCM MATERIALS PROPERTIES.....	64
TABLE 4.2: EXPERIMENTAL TEST RESULTS.....	71
TABLE 5.1: MODIFIED BEAM EXPERIMENTAL TEST RESULTS. ....	91
TABLE 5.2: DIRECT SHEAR EXPERIMENTAL TEST RESULTS. ....	91
TABLE 6.1: PARAMETERS OBTAINED FROM THE EXPERIMENTAL PULL-OUT LOAD RESPONSES. ....	125
TABLE 6.2: PARAMETERS OF THE ESTIMATED CMLs. ....	125
TABLE 6.3: FIBER STRESS $\sigma_0$ AND CORRESPONDING GLOBAL SLIP G FOR EACH STAGE OF THE DEBONDING PROCESS. ....	137
TABLE 7.1: MAIN GEOMETRICAL CHARACTERISTICS OF THE EXPERIMENTAL TESTS COLLECTED. ....	146
TABLE 7.2: MAIN MECHANICAL PROPERTIES OF THE MATERIALS AND PARAMETERS AND RESULTS OF THE EXPERIMENTAL TESTS COLLECTED.....	148
TABLE 7.3: MODIFIED BEAM EXPERIMENTAL TEST RESULTS. ....	155
TABLE 7.4: RESULTS OF FATIGUE MODIFIED BEAM TESTS. ....	157
TABLE 7.5: RESULTS OF POST-FATIGUE TESTED MODIFIED BEAM SPECIMENS – BOND GAP LAYOUT.....	166



# LIST OF FIGURES

FIGURE 1.1: OUT-OF-PLANE COLLAPSE MECHANISMS OF MASONRY STRUCTURES [1] .....	3
FIGURE 1.2: FATIGUE FAILURE OF STEEL REBAR IN RC BEAM [2].....	4
FIGURE 2.1: GENERAL ADVANTAGES OF COMPOSITE MATERIALS FOR STRUCTURAL APPLICATIONS .....	9
FIGURE 2.2: CARBON FIBER TEXTILES FOR FRP STRUCTURAL APPLICATIONS (SCALED 1:1): A) UNIDIRECTIONAL, B) BIDIRECTIONAL, C) MULTIDIRECTIONAL.....	10
FIGURE 2.3: A) STRESS-STRAIN BEHAVIOUR OF BARE FIBERS EMPLOYED IN FIBER REINFORCED COMPOSITES; B) STRESS-STRAIN BEHAVIOUR OF FRP COMPOSITE [10]. .....	12
FIGURE 2.4: FRCM COMPOSITES ADVANTAGES COMPARED TO FRPs DRAWBACKS .....	13
FIGURE 2.5: OPEN-MESH FIBER TEXTILES FOR FRCM APPLICATIONS (SCALED 1:1): A) PBO, UNIDIRECTIONAL; B) COATED GLASS, BIDIRECTIONAL BALANCED; C) CARBON, BIDIRECTIONAL BALANCED; D) PBO, BIDIRECTIONAL UNBALANCED; E) HYBRID PBO + GLASS, BIDIRECTIONAL UNBALANCED; F) CARBON, QUADRI-AXIAL UNBALANCED. ....	15
FIGURE 2.6: FRCM TENSILE TEST SET-UPS: A) CLAMPING GRIP; B) CLEVIS-GRIP SET-UP. .	20
FIGURE 2.7: AXIAL STRESS – AXIAL STRAIN RESPONSES OF TENSILE TEST ON FRCM COUPONS. ....	21
FIGURE 2.8: GLASS COMPOSITE GRID FOR CRM APPLICATIONS (SCALED 1:1; DIMENSIONS IN MM): A) TYPE A, PULTRUDED WEFT AND LAMINATED TWISTED WARP; B) TYPE B, LAMINATED WEFT AND LAMINATED TWISTED WARP.....	23
FIGURE 2.9: SHEAR TEST ON GRID JOINTS: A) TEST SET-UP (PULLING WEFT); B) FAILURE OF SPECIMEN (PULLING WARP). ....	25
FIGURE 2.10: FAILURE OF CRM SPECIMENS SUBJECT TO CLAMPING-, A), AND CLEVIS-, B), GRIP TENSILE TEST. ....	26
FIGURE 2.11: UNIDIRECTIONAL UHTSS TEXTILES TYPICALLY EMPLOYED IN SRG SYSTEMS: A) 300 G/M <sup>2</sup> MASS DENSITY [42]; B) 600 G/M <sup>2</sup> MASS DENSITY. ....	27
FIGURE 2.12: REGULATORY FRAMEWORK.....	30

FIGURE 3.1: DEBONDING FAILURE MODES. A) DEBONDING AT MATRIX-FIBER INTERFACE WITH SUBSTANTIAL TEXTILE-MATRIX RELATIVE SLIPPAGE; B) DELAMINATION AT MATRIX-FIBER INTERFACE; C) FRCM-SUBSTRATE DEBONDING; D) DEBONDING WITHIN THE SUBSTRATE. [52].....	33
FIGURE 3.2: TELESCOPIC FAILURE OF FRCM COMPOSITES .....	34
FIGURE 3.3: A(I) PUSH-PULL SINGLE- AND A(II) DOUBLE-LAP DIRECT SHEAR TEST SET-UPS. A(III) PULL-OUT TEST SET-UP. B) SINGLE-LAP DIRECT SHEAR TEST ON FRCM-MASONRY JOINT. ....	35
FIGURE 3.4: DIRECT SHEAR TEST IDEALIZED STRESS RESPONSES. ....	37
FIGURE 3.5: EXPLODED VIEW AND PHOTO OF THE PULL-OUT TEST SET-UP. ....	40
FIGURE 3.6: INDIRECT TEST SET-UPS: A) MODIFIED OR HINGED BEAM TEST; B) NOTCHED BEAM TEST. ....	41
FIGURE 3.7: CONVENTIONAL LIMIT STRESS OF FRCM COMPOSITES [35]. A) TENSILE STRESS - STRAIN CURVE; B) TENSILE STRESS - GLOBAL SLIP CURVE.....	44
FIGURE 3.8: TEXTILE GRIDS GEOMETRY: A) PBO, B) CARBON, C) STEEL.....	46
FIGURE 3.9: A) SPECIMEN GEOMETRY (DIMENSIONS IN MM);B) TEST SET-UP. ....	48
FIGURE 3.10: TYPICAL AXIAL STRESS - GLOBAL SLIP CURVES: A) PBO- AND C-FRCM; B) SRG.....	49
FIGURE 3.11: AXIAL STRESS, $\sigma$ - GLOBAL SLIP, $G$ , CURVES FOR PBO FRCM - A) $v_s=V1$ ; B) $v_s=V5$ ; C) $v_s=V10$ ; AND C FRCM - D) $v_s=V1$ ; E) $v_s=V5$ ; F) $v_s=V10$ - SPECIMENS..	51
FIGURE 3.12: FAILURE MODES OF C-FRCM- AND SRG-STRENGTHENED SPECIMENS: A) TEXTILE FAILURE; B) INTERNAL-EXTERNAL MATRIX LAYER INTERFACE DELAMINATION COMBINED WITH DEBONDING FROM SUBSTRATE; C) STRANDS RUPTURE OUTSIDE THE BONDED LENGTH. ....	52
FIGURE 3.13: AXIAL STRESS, $\sigma$ - GLOBAL SLIP, $G$ , CURVES OF SRG SPECIMENS: A) $v_s=V1$ ; B) $v_s=V5$ ; C) $v_s=V10$ .....	53
FIGURE 3.14: RATE EFFECT ON THE STRESS FIELD, FOR SPECIMENS STRENGTHENED WITH: A) PBO FRCN; B) CARBON FRCM. ....	56
FIGURE 3.15: RATE EFFECT ON THE (A) STRESS AND (B) DISPLACEMENT FIELD, FOR SPECIMENS STRENGTHENED WITH SRG.....	58

FIGURE 3.16: COMPARISON BETWEEN GLOBAL SLIP RATE AND MACHINE STROKE RATE. . .	59
FIGURE 4.1: OUT-OF-PLANE DISPLACEMENT OF MASONRY WALLS, UNDER THE EFFECT OF HORIZONTAL ACTIONS. ....	63
FIGURE 4.2: THREE-BRICK MODIFIED BEAM TEST SET-UPS GEOMETRIES AND DIMENSIONS (MM). ....	65
FIGURE 4.3: ONE-BRICKS MODIFIED BEAM TEST SET-UPS GEOMETRIES AND DIMENSIONS (MM). ....	65
FIGURE 4.4: MODIFIED BEAM TEST SET-UP WITH BARE FIBERS AT THE GAP: A) SIDE VIEW AND B) BOTTOM VIEW (DIMENSIONS IN MM). ....	66
FIGURE 4.5: FREE BODY DIAGRAM OF ONE BLOCK OF THE MB TEST. ....	67
FIGURE 4.6: A) PHOTO OF THE SINGLE-LAP DIRECT-SHEAR TEST SET-UP. B) DETAIL OF THE CRACK AT THE MATRIX-FIBER INTERFACE. ....	69
FIGURE 4.7: AXIAL STRESS $\sigma$ – GLOBAL SLIP $G$ RESPONSE OF SPECIMEN A) MB_3_210_60_B_4 AND B) MB_C_3_210_60_B_5. ....	71
FIGURE 4.8: A) OPENING OF THE MATRIX CRACK AT THE FIBER-MATRIX INTERFACE OF SPECIMEN MB_3_210_60_B_1. B) SPECIMEN MB_C_1_210_60_2 AT COMPLETION OF THE TEST. ....	72
FIGURE 4.9: AXIAL STRESS $\sigma$ – GLOBAL SLIP $G$ RESPONSE OF SPECIMENS IN SERIES A) MB_3_210_60_B, B) MB_1_210_60_B, C) MB_C_3_210_60_B, AND D) MB_C_1_210_60_B. ....	74
FIGURE 4.10: COMPARISON BETWEEN MB TESTS WITH BARE AND EMBEDDED FIBERS IN THE GAP WITH A) PBO AND B) CARBON FIBERS. ....	75
FIGURE 4.11: A) ENVELOPE OF APPLIED FORCE $P$ – MIDSPAN DEFLECTION $\delta$ CURVES OBTAINED BY MODIFIED BEAM TESTS. B) COMPARISON BETWEEN AXIAL STRESS $\sigma$ AND NORMAL STRESS $\sigma_I$ FOR SPECIMENS MB_3_210_60_B_5 AND MB_1_210_60_B_1. ....	76
FIGURE 4.12: COMPARISON BETWEEN MB AND DS TESTS WITH A) PBO FIBERS AND B) CARBON FIBERS. ....	78

FIGURE 4.13: COMPARISON BETWEEN KEY AVERAGE VALUES OF AXIAL STRESS AND CORRESPONDING GLOBAL SLIP FOR SPECIMENS WITH A) PBO AND B) CARBON FIBERS. ....	80
FIGURE 5.1: SKETCH OF A FRCM STRENGTHENED RC BEAM UNDERGOING EXCESSIVE DEFLECTION. ....	86
FIGURE 5.2: A) MODIFIED BEAM TEST GEOMETRY AND SET-UP: B) BARE-FIBER, C) BOND-GAP SPECIMEN MIDSPAN, AND D) DETAIL OF THE FREE END. E) DIRECT SHEAR TEST GEOMETRY AND SET-UP (DIMENSIONS IN MM). ....	89
FIGURE 5.3: LOAD RESPONSES OF BARE-FIBER MB TESTS: A) SPECIMEN MB_300_60_B_3 (G MEASURED AT THE PDS AND FDS) AND B) SPECIMENS MB_300_60_B_1-3 (G MEASURED AT THE FDS). ....	92
FIGURE 5.4: A) FREE BODY DIAGRAM OF THE MB TEST; B) MODIFIED BEAM TEST: MIDSPAN OPENING DISPLACEMENT $G_E$ . ....	93
FIGURE 5.5: MB TEST: A) SIDE VIEW AND DETAIL OF THE MIDSPAN FOR THE B) BOND-GAP AND C) BARE-FIBER LAYOUTS. ....	93
FIGURE 5.6: LOAD RESPONSES OF BOND-GAP MB TESTS: A) SPECIMEN MB_300_60_G_2 AND B) SPECIMENS MB_300_60_G_1-3 [G WAS COMPUTED WITH EQ.(5.2)]. ....	95
FIGURE 5.7: A) LOAD RESPONSES OF DS TESTS. B) DIRECT SHEAR TEST SET-UP. ....	97
FIGURE 5.8: ENVELOPES OF A) $\sigma_0 - G$ AND $\sigma - G$ CURVES OF MB AND DS TESTS, RESPECTIVELY, AND B) $\sigma_0 - \delta$ CURVES OF MB TESTS. ....	99
FIGURE 6.1: DIRECT SHEAR TEST ON PBO-FRCM SPECIMEN. A. APPLIED LOAD P - GLOBAL DISPLACEMENT G CURVE. B. INTERFACE AXIAL STRAIN $\epsilon_{yy}$ PROFILES ALONG THE BONDED LENGTH [105]. ....	104
FIGURE 6.2: A) FITTING CURVE OF $\epsilon_{xx}$ STRAIN PROFILE ALONG THE BONDED LENGTH L; B) PROPAGATION OF THE DEBONDING PROCESS. ....	105
FIGURE 6.3: DEBONDING AT MATRIX-FIBER INTERFACE. ....	106
FIGURE 6.4: SHEAR STRESS $\tau - S$ RELATION EXPERIMENTALLY OBTAINED FROM SPECIMENS EQUIPPED WITH STRAIN GAUGES. ....	107
FIGURE 6.5: SIMPLIFIED CMLS. A) TRI-LINEAR [105]. B) RIGID-SOFTENING ....	108
FIGURE 6.6: SHEAR STRESS DISTRIBUTION IN THE RIGID-SOFTENING STAGE ( $L > L_{EFF}$ ). ....	109

FIGURE 6.7: SHEAR STRESS DISTRIBUTION ALONG THE INTERFACE A) AT THE END OF THE RIGID-SOFTENING STAGE AND B) DURING THE RIGID-SOFTENING-DEBONDING STAGE ( $L > L_{EFF}$ ).....	110
FIGURE 6.8: SHEAR STRESS DISTRIBUTION ALONG THE INTERFACE A) AT THE END OF THE RIGID-SOFTENING-DEBONDING STAGE AND B) DURING THE SOFTENING-DEBONDING STAGE ( $L > L_{EFF}$ ).....	110
FIGURE 6.9: SHEAR STRESS DISTRIBUTION ALONG THE INTERFACE A) AT THE END OF THE RIGID-SOFTENING STAGE AND B) DURING THE SOFTENING STAGE ( $L < L_{EFF}$ ).....	111
FIGURE 6.10: APPLIED LOAD-GLOBAL SLIP RESPONSE FOR A BONDED LENGTH A) HIGHER AND B) LOWER THAN THE COMPOSITE EFFECTIVE BOND LENGTH, $L_{EFF}$ . ....	111
FIGURE 6.11: PLOT OF THE FUNCTIONS $F(L)=\tan(\omega L)$ AND $F(L)=1/\omega(L-L)$ IN THE CASE: A) $L < \pi/2\omega$ AND B) $L > \pi/2\omega$ .....	120
FIGURE 6.12. A) EXPLODED VIEW AND OF THE PULL-OUT TEST SET-UP AND B) PHOTO OF SPECIMEN PO_330_60_5. ....	123
FIGURE 6.13. APPLIED LOAD P-GLOBAL SLIP G RESPONSE OF PBO FRCM COMPOSITES SUBJECTED TO PULL-OUT TESTS. ....	124
FIGURE 6.14. COHESIVE MATERIAL LAWS ESTIMATED. ....	125
FIGURE 6.15. COMPARISON BETWEEN ANALYTICAL AND EXPERIMENTAL LOAD RESPONSES. ....	127
FIGURE 6.16. COMPARISON BETWEEN ANALYTICAL AND EXPERIMENTAL $\sigma - G$ RESPONSES OF DS TESTS.....	128
FIGURE 6.17: ENERGY RATES PROVIDED BY BOND ( $G_C$ ) AND FRICTION.....	131
FIGURE 6.18: A) FIBER PULL-OUT AT AN ANGLE $\alpha$ ; B) MODIFIED BEAM TEST: MIDSPAN OPENING DISPLACEMENT $G_E$ . ....	133
FIGURE 6.19. ANALYTICAL $\sigma$ - AND $\sigma_0$ -G RESPONSES AND FUNCTION $\rho(G)$ FOR GIVEN $\mu$ . ....	135
FIGURE 6.20. A) EXPERIMENTAL AND FITTED $\rho$ CURVES. B) COMPARISON BETWEEN ANALYTICAL AND EXPERIMENTAL $\sigma_0 - G$ RESPONSES OF MB TESTS. ....	139
FIGURE 7.1: TEST SET-UP AND CROSS-SECTION ACTIONS UNDER PURE BENDING CONDITION. ....	145

FIGURE 7.2: STATE OF THE ART ANALYSIS: A) RELATION BETWEEN NORMALIZED MAXIMUM APPLIED FATIGUE LOAD AND FATIGUE LIFE, B) RELATION BETWEEN NORMALIZED FATIGUE LIFE AND REINFORCEMENT RATIO, C) RELATION BETWEEN FRCM (FIBER) STRAIN EXPLOITATION RATIO AND FATIGUE LIFE. .... 150

FIGURE 7.3: GEOMETRY OF BARE-FIBER AND BOND-GAP LAYOUT MODIFIED BEAM TESTS (DIMENSIONS IN MM). .... 153

FIGURE 7.4: PHOTO OF SPECIMEN MB\_300\_60\_B\_F\_3 BEFORE THE BEGINNING OF THE TEST. .... 157

FIGURE 7.5: LOAD RESPONSES OF SPECIMEN; A) MB\_300\_60\_B\_F\_1, B) MB\_300\_60\_B\_F\_2, C) MB\_300\_60\_B\_F\_3, AND D) MB\_300\_60\_B\_F\_4. E) FAILURE OF PBO FIBERS AND F) GLOBAL SLIP VS. NUMBER OF CYCLES FOR SPECIMEN MB\_300\_60\_B\_F\_3. .... 159

FIGURE 7.6: FDS GLOBAL SLIP VS. A) NUMBER OF CYCLES AND B) NORMALIZED NUMBER OF CYCLES FOR SPECIMEN SUBJECTED TO FATIGUE TEST. .... 161

FIGURE 7.7: LOAD RESPONSES OF SPECIMEN; A) MB\_300\_60\_G\_F\_1, B) MB\_300\_60\_G\_F\_2, C) MB\_300\_60\_G\_F\_3, AND D) MB\_300\_60\_G\_F\_4. MIDSPAN DISPLACEMENT VS. A) NUMBER OF CYCLES AND B) NORMALIZED NUMBER OF CYCLES. .... 163

FIGURE 7.8: LOAD RESPONSES OF SPECIMEN; A) MB\_300\_60\_G\_PF\_1, B) MB\_300\_60\_G\_PF\_2 AND C) MB\_300\_60\_G\_PF\_3. .... 165

FIGURE 7.9: CYCLIC STAGE OF SPECIMENS MB\_300\_60\_G\_PF\_1-3, A) MIDSPAN VERTICAL DEFLECTION  $V_G$ , NUMBER OF CYCLES  $N$  CURVES ; B) REPRESENTATIVE 10-CYCLES BLOCK SELECTED AT  $N=1000, 3800, 5600$  AND  $8300$  ..... 167

## LIST OF ABBREVIATIONS AND ACRONYMS

- AR - Alkali resistant
- CRM - Composite reinforced mortar
- CoV – Coefficient of variation
- DIC - Digital image correlation
- EB - Externally bonded
- FDZ - Fully debonded zone
- FDS - Fully debonded side
- FM – Failure mode
- FRCM - Fabric reinforced cementitious matrix
- FRP - Fabric reinforced polymer
- LVDT - Linear variable displacement transducer
- PBO - Polyparaphenylene benzo bisoxazole
- PDS - Partially debonded side
- PSZ - Peak strength zone
- RC - Reinforced concrete
- SFZ - Stress free zone
- STZ - Stress transfer zone
- TRC - Textile reinforced concrete
- TRM - Textile reinforced mortar
- UHTSS - Ultra-high tensile strength steel

## LIST OF SYMBOLS

- $A$  – Surface area.
- $A_c$  – Cross-sectional area of compression rebar.
- $A_f$  – Cross-sectional area of a single yarn/bundle.
- $A_m$  – Cross-sectional area of matrix.
- $A_s$  – Cross-sectional area of steel rebar.
- $A_t$  – Cross-sectional area of tension rebar.
- $a_{II}$  – Amplitude of cracked stage of SRG debonding test.
- $b_1$  – Width of the composite strip.
- $b_f$  – Width of a single yarn/bundle.
- $E_1$  – Elastic modulus of a composite in fiber (strong) direction.
- $E_2$  – Elastic modulus of a composite in transversal (weak) direction.
- $E_{FRP}$  – Elastic modulus of FRP.
- $E_{FRCM}$  – Elastic modulus of FRCM.
- $E_m$  – Elastic modulus of plain matrix.
- $E_f$  – Elastic modulus of bare fiber.
- $F$  – Force on a single yarn.
- $f$  – Cycle frequency.
- $F_{deb}$  – Debonding force on a single yarn.
- $F^*$  – Peak force on a single yarn.
- $F_f$  – Residual/friction force on a single yarn.
- $f_c$  – Compressive strength of concrete.
- $f_f$  – Tensile strength of bare fiber.
- $f_{mt}$  – Tensile strength of matrix.
- $f_{mu}$  – Compressive strength of matrix.
- $g$  – Global slip.



- $G_{12}$  – Shear modulus.
- $G_c$  – Critical energy release rate.
- $G_f$  – Fracture energy.
- $g^*$  – Global slip at peak.
- $\bar{g}^*$  – Global slip at softening limit point.
- $g_A$  – Global slip at the end of load response linear branch.
- $g_{cr}$  – Global slip at the end of the un-cracked stage of SRG debonding test.
- $g_{deb}$  – Global slip at debonding.
- $g_e$  – Midspan displacement.
- $g_{e,A}$  – Midspan displacement at the end of the elastic stage.
- $g_e^*$  – Midspan displacement at peak.
- $g_e^*_{PF}$  – Global slip corresponding to post-fatigue peak capacity.
- $g_f$  – Global slip associate with residual friction stress  $\sigma_f$ .
- $g_{II}$  – Global slip at failure of SRG debonding test.
- $k_1; k_2$  – Slopes of multi-linear bond-slip law.
- $k_1; k_2$  – Coefficients that define the concrete compressive force value and position.
- $l; l_b; l_w$  – Geometrical distances.
- $l_g$  – Bond-gap length.
- $l_{eff}$  – Effective bond length.
- $l_{sb}$  – Snap-back length.
- $l_k$  – Bond-gap length.
- $M_{max}$  – Bending moment at beam mid-span associated with  $S_{max}$ .
- $M_{serv}$  – Bending moment at beam mid-span due to service load.
- $M_u$  – Bending moment at beam mid-span associated with  $P_u$ .
- $N$  – Number of cycles.
- $n$  – Number of textile yarns.

- $\bar{N}$  – Normalized fatigue life.
- $N(x)$  – Axial force along  $x$  direction.
- $N_F$  – Fatigue life.
- $N_{PF}$  – Number of fatigue cycles in post-fatigue test.
- $N_n$  – Normalized number of cycles.
- $P$  – Total load recorded by the machine load cell.
- $p$  – Perimeter.
- $P^*$  – Peak total load.
- $P_{deb}$  – Debonding total load.
- $P_f$  – Total load corresponding with residual friction.
- $P_i$  – Long-term sustained load.
- $P_u$  – Ultimate total load.
- $R$  – Fatigue stress ratio.
- $R_{c28}$  – Compressive strength of a mortar at 28 days.
- $S_{min} S_{max}$  – Minimum and maximum values of the cyclic load.
- $s_f$  – In a bond-slip law, slip corresponding with friction tangential stress  $\tau_f$ .
- $s_F$  – Free-end slip.
- $s_{max}$  – In a bond-slip law, slip corresponding with maximum tangential stress  $\tau_{max}$ .
- $T$  – Force at the composite loaded end.
- $T_I$  – Force at the composite loaded end: orthogonal component to fiber direction.
- $T_{II}$  – Force at the composite loaded end: parallel component to fiber direction.
- $t_f$  – Equivalent thickness of a textile.
- $U_{el}$  – Strain energy.
- $U_f$  – Energy dissipated by friction.
- $v_g$  – Vertical deflection.
- $\alpha$  – Deflection angle.
- $\beta^f$  – Reinforcement ratio.

- $\Gamma$  – Fracture energy.
- $\delta$  – Midspan deflection.
- $\varepsilon$  – Axial strain.
- $\varepsilon_0, \alpha, \beta, x_0$  – Nonlinear regression parameters.
- $\varepsilon_{deb}$  – Debonding axial strain.
- $\varepsilon_f$  – Residual friction axial strain.
- $\varepsilon_{f,max}$  – FRCM (textile) strain associated with  $S_{max}$ .
- $\varepsilon_{f,u}$  – FRCM (textile) strain associated with with  $P_u$ .
- $\varepsilon_{lim,conv}$  – Conventional limit strain.
- $\varepsilon_{T1}$  – Axial strain at the end of uncracked stage.
- $\varepsilon_{T2}$  – Axial strain at the end of stage 2.
- $\varepsilon_u$  – Ultimate axial strain.
- $\varepsilon_{xx}$  – Axial strain in direction  $x$ .
- $\eta$  – FRCM strain exploitation ratio.
- $\mu$  – Snubbing friction coefficient.
- $\nu_f$  – Fiber volume fraction.
- $\nu_\varepsilon$  – Axial elongation rate.
- $\nu_g$  – Global slip rate.
- $\nu_m$  – Matrix volume fraction.
- $\nu_s$  – Machine stroke displacement rate.
- $\rho$  – MB and DS stress ratio, for a given global slip value.
- $\sigma$  – Axial stress.
- $\sigma'_f$  – First derivative of the axial stress with respect to the global slip,  $d\sigma/dg$ .
- $\sigma^*; \sigma_0^*$  – Peak axial/fiber stress.
- $\sigma_0$  – Fiber stress.
- $\sigma_{0,max}$  – Maximum fiber applied stress in a fatigue cycle.

- $\sigma_{0,min}$  – Minimum fiber applied stress in a fatigue cycle.
- $\sigma_{0}^{*PF}$  – Post-fatigue bond capacity.
- $\sigma_A$  – Axial stress at the end of load response linear branch of debonding test.
- $\sigma_{cr}$  – Stress at the end of the un-cracked stage of SRG debonding test.
- $\sigma_{deb}$  – Debonding stress.
- $\sigma_f, \sigma_{0,f}$  – Residual friction stress.
- $\sigma_{fu}$  – Ultimate tensile stress of fiber.
- $\sigma_I$  – Stress at the composite loaded end: orthogonal component to fiber direction.
- $\sigma_{II}$  – Stress at the composite loaded end: parallel component to fiber dir (a.k.a.  $\sigma$ ).
- $\sigma_{lim,conv}$  – Conventional limit stress.
- $\sigma_{MAX}$  – Peak bond stress in SRG debonding test.
- $\sigma_{m.A}$  – Matrix stress.
- $\tau$  – Interfacial shear stress.
- $\tau-s$  – Bond-slip law.
- $\tau_f$  – Friction shear stress.
- $\tau_{max}$  – Maximum interfacial shear stress.





# 1 FOREWORD: ON THE VULNERABILITY OF THE BUILT HERITAGE

In the last decades, the advancing ageing of existing constructions alongside with a general awareness about seismic hazard, oriented local legislators toward more and more stringent standards on structural safety and seismic design. Especially existing buildings required new solutions for their service life extension, seismic retrofitting and bearing capacity enhancement when changes in their intended use are involved. After years of under regulated interventions, recently, a new sensibility started developing, oriented toward the preservation of the identity of existing constructions in both their architectural image and structural concept. Accordingly, designers and operators are called to gain a deep knowledge of the target building and to correct interpret its construction history and materials nature, in a way to guarantee the preservation of the original static system, and, if needed, to provide suitable and compatible retrofitting interventions.

This new approach needs a strong support from the scientific research field, which contribute to proper understand the constructive rules of existing buildings and the chemical compatibility between existing materials and possible strengthening applications, allowing technicians to maintain, strengthen and, when needed, rebuild existing structural and non-structural parts. This is the case of fiber-reinforced composite materials, which have been deeply researched by the scientific community in the last decades, in order to understand their structural behaviour and adapt them to fulfill the specific requirements of several construction-engineering applications. Those materials attracted a great deal of attention in the second half of the 20<sup>th</sup> century in reason of their high strength-to-weight ratio, which allowed to significantly reduce the self-weight of artifacts from aerospace and automotive engineering. At the end of the century, some researchers started conceiving the possibility to adopt fiber-reinforced composites as structural strengthening for the repair and performance enhancement of existing buildings. This solution appeared immediately promising because of the low invasiveness of composite materials strengthenings (low weight and volume) and their speed and easiness of application. Much research has been performed since then, and a wide catalogue of fiber-reinforced composites is nowadays available, to meet the requirements of different building typologies and structural parts applications.

Many questions have already been answered in this research field, others are still open and the present thesis works aims at filling some voids that are present in the concerning scientific literature, with particular attention to the recently developed technology of inorganic matrix composites. Those materials were designed to adapt with greater compatibility to masonry substrates, however, their application to reinforced concrete structures is also promising. The following sections provide a review of the principal collapse mechanisms of reinforced concrete and masonry structures with particular attention paid to out of plane action induced by seismic events and fatigue deterioration, which inorganic matrix composites are typically called to address.

## **1.1 The vulnerability of masonry structures**

Masonry constructions represent a large part of the entire existing built heritage. Those building typologies are largely characterized by the use of unreinforced masonry elements: bearing parts like masonry piers, pillars and arches, flooring systems such as masonry vaults and mixed concrete and hollow bricks slabs, non-structural elements such as moveable partitions and infill walls, etc. The recent seismic events that have



struck the Italian territory emphasized the great vulnerability of those elements, mainly because unreinforced masonry structures are typically designed only for vertical loads, and their out of plane strength is mainly governed by the bond between brick and mortar and by the mortar mechanical properties. Despite masonry has an extraordinary propensity to adequate to local collapses, accounting for new redistribution of stress, the main hazard is related to the fall or overturning of rubble and debris following seismic strikes.

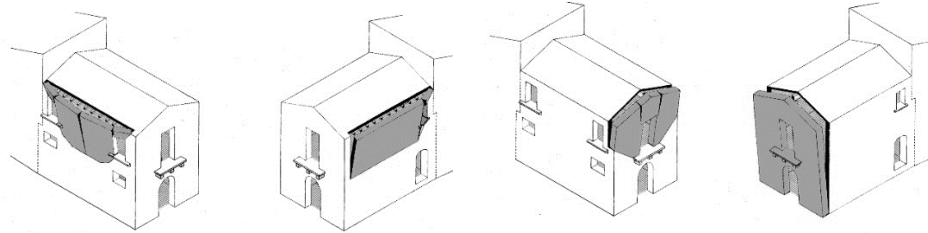


*Figure 1.1: Out-of-plane collapse mechanisms of masonry structures [1].*

Under the effect of lateral actions, the overturning and out-of-plane collapse of masonry panels depends mainly on the wall connection with the surrounding structure and can be triggered or amplified by many factors, such as pre-existing cracks or openings in the facade. Horizontal overturning may also be determined by pushing roof or slabs, and in multi-leaf masonry, collapse may involve only one of the outer faces. Partial/total overturning of infill walls determines one of the major safety hazard for building residents, because of the poor connection between masonry hollow bricks and RC superstructures.

Traditional interventions to mitigate the out-of-plane collapse of masonry structures involves the use of external reinforcement with steel plates or tubes directly attached to the wall leafs, aimed at counteracting horizontal displacement, or surface treatments with steel-net reinforced plaster to prevent rubble and debris fall.

## **1.2 The influence of fatigue on the serviceability of structures**

A large part of the existing bridge structures in western countries is made of reinforced and pre-stressed concrete. The recently developed trade liberalization policies have led to a significant growth of the traffic volume, which is likely to further increase in the next decade. Especially heavy-goods traffic induces repeated oscillatory loads in bridge structural elements, which prolong over the years throughout the whole service life. The combination between cyclic solicitation and steel reinforcement corrosion often results

in crack initiation in the rebar, at the location where stresses concentrate due to material flaws or geometrical discontinuities. The prolonged exposition to those circumstances induces the progressive propagation of the crack within the rebar cross section, which initially propagates at a constant rate with the number of load cycles. The propagation of the fatigue crack determines a growing reduction of the rebar resisting area, which will eventually abruptly fail in a fast fracture once the resisting area is no longer enough to carry the acting load. This phenomenon, known as fatigue failure of steel rebars in RC elements, is one of the major causes of accelerated deterioration of highway and railroad bridges and viaducts, and requires instantaneous intervention, being the damage progression hidden within the structural part.

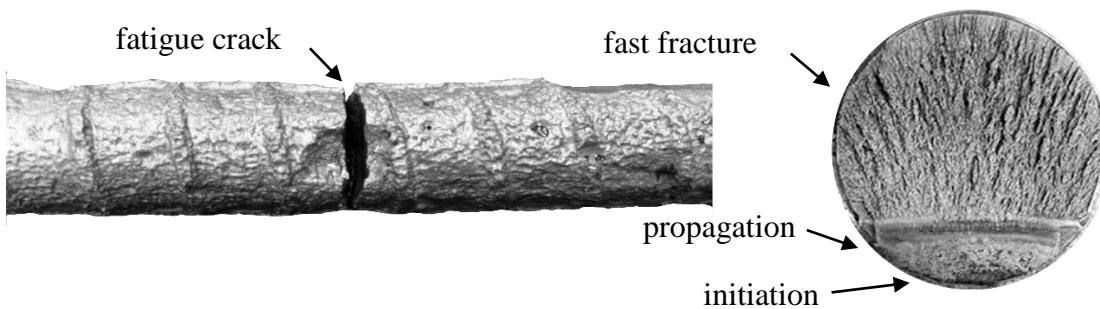


*Figure 1.2: Fatigue failure of steel rebar in RC beam [2]*

Several traditional strengthening measures have been applied to extend the service life of bridge structures and prevent traffic obstruction; most of them aiming at relieving the stress level acting on the fatigue-cracked rebars by the introduction of additional resisting parts such as post-tensioning longitudinal trusses or near surface mounted steel bars.

### **1.3 Innovative solutions for the strengthening of existing structures**

In the last decades, composite materials have established themselves as an excellent solution for strengthening and retrofitting existing structures to the standards of modern structural design, in reason of the high strength to weight ratio, low invasiveness and cost-effectiveness. The application of specific types of composite materials to the external surface of existing building parts, provide a threefold advantage: (i) increase the capacity of structural elements, such as bearing masonry piers or pillars, RC beams (bending capacity) and RC columns (axial capacity). In the case of a change in a building intended-use, involving an increase of imposed loads, composite materials,

externally bonded (EB) to slab joists intrados, may provide an extra load-bearing capacity to the slab and reduce its vertical deflection. (ii) EB composite increase the displacement capacity of strengthened elements, such as beam-column connections in RC structures, determining a significant gain in structure ductility that assumes a fundamental role in seismic engineering, in reason of the energy dissipation that this determines under seismic events. (iii) Continuous composites, like those typically applied to masonry panels, in addition to increase the load carrying and displacement capacity, determine an important containment action against the falling of debris and collapse ruins, which result in an important safety gain of building inhabitants.

In the last years, several typologies of composite systems for structural applications have been developed, among them, fiber reinforced polymers (FRP) have attracted growing attention in reason of their high performances and relatively low price. EB FRP composites are comprised of high strength fiber textiles directly applied to the element surface by means of thermosetting organic matrices, usually epoxy resin. The fiber component represents the proper structural element, carrying the applied tensile action, whereas matrix is responsible for the stress transfer from the substrate to the fiber phase. Other fiber reinforced composite systems, such as fiber reinforced cementitious matrix composites (FRCM), in which epoxy resin is replaced with inorganic matrix, have been later introduced to meet compatibility requirements, especially with masonry substrates. Much research has been performed to date on FRCM systems, however some aspects are still under investigation and further research need to be performed.

## **1.4 Organization of the thesis work**

The text is organized in six main chapters (Chapters 2 to 7). Following this introductory section is Chapter 2, which constitutes a descriptive, theoretical and regulatory framework on composite materials for structural rehabilitation and their applications.

Chapter 3 introduces the central item of this study, namely the bond between inorganic composites and substrate, analysed here from an experimental point of view. The relevance of bond in the reinforcement design procedure, the experimental tests that can be performed to evaluate the adhesion properties of these materials and the corresponding idealized response, are here presented and discussed. Finally, an experimental investigation is described, on the influence of some bond test parameters, such as the loading rate, on the bond response obtained, for different types of inorganic matrix composites.

Chapters 4 and 5 constitute two important experimental nuclei of this thesis, here the influence of the bending action on FRCC composites, applied to masonry (Chapter 4) and concrete (Chapter 5), are evaluated. The bending effect was introduced through a specially designed test set-up, referred to as modified beam test, which, by isolating the flexural contribution offered by the composite material, allowed to evaluate the effect of different parameters on its bond features.

In chapter 6, the analytical approach to the problem of adhesion is explored. After a theoretical and literary framework of the topic, a simplified fracture mechanics analytical model is presented. The model allows predicting the response of direct-shear bond test of FRCC specimens, guaranteeing a simple solution in closed form. A second analytical model is then introduced, which allows processing the response of modified beam tests, through the introduction of a snubbing-friction effect. Both models were validated on experimental tests available in the literature or presented in the previous chapters.

Chapter 7 addresses the issue of fatigue on FRCC application subjected to bending. The problem is initially introduced and an in-depth review of the concerning available literature is presented. Then, the experimental procedures and results of fatigue and post fatigue test performed on FRCC strengthened modified-beam specimens, are presented and discussed.

The end of each chapter includes the main conclusions drawn from that section, and possible ideas and observations for future guidelines.



# 2 INTRODUCTION: COMPOSITE MATERIALS FOR STRUCTURAL APPLICATIONS AND THEIR MECHANICAL PROPERTIES

Fiber reinforced composite materials combine together characteristics of two distinct components, or phases, with different peculiarities, into a high performance material in which advantages and disadvantages of single phases are enhanced and compensated, respectively. High strength fibers of different nature, such as carbon, glass, basalt and PBO (polyparaphenylene benzo bisoxazole), woven in textile form with specific textures, represent the main structural components, which is responsible for carrying the applied tensile action. They are characterized by high uniaxial tensile strength (i.e. in the fiber direction) and elastic modulus, along with relatively low density. Textile plies are embedded within a continuous phase, usually named matrix, which is characterized by low elastic modulus and adequate adhesion properties to bond with the substrate. The matrix allows the stress transfer between substrate and textile and provides for a homogenous stress distribution among different fibers. Matrix prevents the direct exposure of fiber filaments to aggressive environment and is responsible for the composite fire-resistance and high temperature performance. Furthermore, being

externally bonded composite directly applied to the structural element surface, matrix also accounts for the chemical compatibility with the substrate and for its vapour permeability.



Figure 2.1: General advantages of composite materials for structural applications

Fiber reinforced composite materials was introduced at the beginning of 20<sup>th</sup> century, with the development of polymeric resin industry and the patenting of glass fiber production technique. Initially their field of application was limited to the aviation and aerospace industry, but with time it expanded to the automotive sector and finally, since the 80's, to the field of construction engineering.

Nowadays, fiber reinforced composites are fairly affirmed in the construction industry and many different solutions have been developed to account for a wide catalogue of applications. Within this category of materials, those comprising high strength textiles, embedded within a cement-based matrix, typically referred to as fiber (or fabric) reinforced cementitious matrix composites (FRCM), represent one of the relatively recent innovations by virtue of their low vulnerability to high temperatures and their good compatibility with masonry structures. Because of this last feature, as well as the partial reversibility of these applications, the use of FRCM reinforcements may be considered a good alternative to better-established fabric reinforced polymers (FRP), in strengthening and retrofitting of existing structures.

## 2.1 Fiber reinforced polymers (FRP)

Fabric Reinforced Polymers represent a wide category of composite materials, comprising a polymeric organic matrix within which one or more layers of high strength

fiber are embedded. They are nowadays the most commonly employed materials for the structural strengthening and seismic retrofitting of existing buildings and their application is regulated by national standards in most of the developed countries. Typical structural applications of FRPs involve the shear and flexural strengthening of RC beams, columns and slabs, realised through externally bonded application of the composite to the tension face of the member (in the case of flexural strengthening) or to its web side, with U- or closed-wrappings (shear strengthening). Recently, shear strengthening of RC beam-column joints with FRP has been investigated with promising results [3–9].

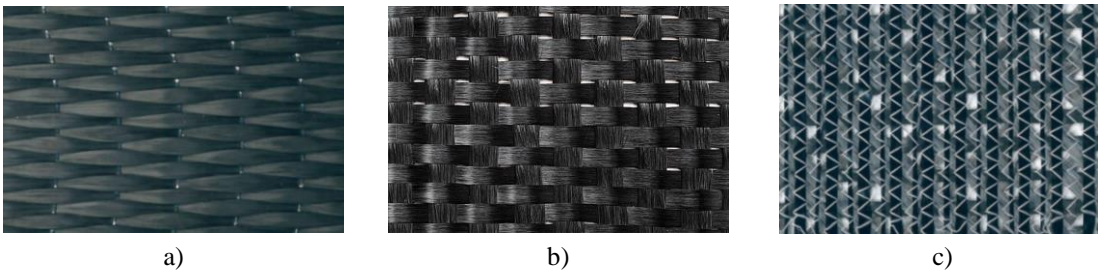


*Figure 2.2: carbon fiber textiles for FRP structural applications (scaled 1:1): a) unidirectional, b) bidirectional, c) multidirectional.*

The polymeric matrix employed in FRPs is ordinarily a thermosetting resin, epoxy or polyester, whereas commonly employed high strength fibers are carbon, glass, aramid or polyparaphenylene benzo bisoxazole (PBO). Fibers can be woven into uni- or multi-directional textiles to realize different geometrical configurations, which allow the composite to have different performances on specific directions. Figure 2.2 shows different layouts for carbon fiber textile, corresponding to different composite behaviour:

- Unidirectional textile (see Figure 2.2a) made up of fiber yarns aligned with one main direction and bound together by a pattern of nylon or polyester filaments. FRP composites comprising unidirectional textiles are characterized by a strongly orthotropic behaviour, with one single strong direction (i.e. fibers direction) characterized by high tensile strength and stiffness. They are commonly employed for flexural strengthening of RC beams, in which the composite contribution is needed just on one direction. Unidirectional composites are also realized by industrial pultrusion.



- Bidirectional textile (see Figure 2.2b) obtained by weaving fiber yarns along two orthogonal directions. This provides high strength to the composite in two orthogonal directions.
- Multidirectional textiles (see Figure 2.2c), characterized by four or more different fiber orientations (e.g. 0/90/+45/-45). Those textiles are characterized by a quasi-isotropic mechanical behaviour and are widely employed for continuous applications, such as out-of-plane strengthening of RC plates or masonry walls.

Externally bonded FRP application methods in construction engineering field include *hand lay-up* and *plate bonding* techniques. The manual or hand lay-up is currently the mostly adopted technique; it consists in the on-site impregnation of bare textiles directly on the element surface, using epoxy resin. The resin serves both functions of matrix and adhesive with the substrate. The plate bonding technique is adopted in the case pre-cured composites (e.g. pultruded strips) which are directly bonded to the element surface, using special adhesives.

### 2.1.1 Mechanics of FRP composites

Like most of the composite materials, a unidirectional lamina of FRP is characterized by a heterogeneous and transversally isotropic mechanical behaviour, with a linear elastic constitutive behaviour until failure. The mechanics of FRP composites comprising a stacking of angle-laminas (layers) is governed by the *Classical Lamination Theory* and their stress-strain relationship is defined by four elastic constants for each composite layer. Namely, the elastic modulus in the lamina fiber direction,  $E_1$ , the elastic modulus in the orthogonal direction,  $E_2$ , the Poisson's ratio,  $\nu_{12}$ , and the shear modulus,  $G_{12}$ . Those four properties of each lamina comprising the FRP laminate depends on both fiber and matrix properties and can be computed, with good approximation, according to the rule of mixtures, given the volume fractions of fiber and matrix, through to the following equation:

$$E_{FRP} = E_m \cdot v_m + E_f \cdot v_f \quad (2.1)$$

in which  $E_{FRP}$  is the composite elastic modulus,  $E_m$  and  $E_f$  are the elastic moduli of matrix and fiber, respectively, and  $v_m$  and  $v_f$  are volume fractions of matrix and fiber, respectively, expressed as the ratio between the volume of each single component and the total composite volume, in a representative unit segment of FRP. According to Eq.

(2.1) the composite elastic modulus is dependent from both matrix and fiber properties, proportionately to their quantity in the composite. Figure 2.3a shows the stress-strain relationship for different bare fibers employed in FRP composite technology, carbon and PBO fibers are characterized by high elastic modulus and tensile strength, whereas glass, having lower tensile properties, is employed in applications requiring lower stiffness (e.g. strengthening of structural walls). Epoxy resin is characterized by very low Young's modulus, for this reason, according to the rule of mixture, the composite overall tensile properties will be reduced as a function of the matrix volume fraction (see Figure 2.3b).

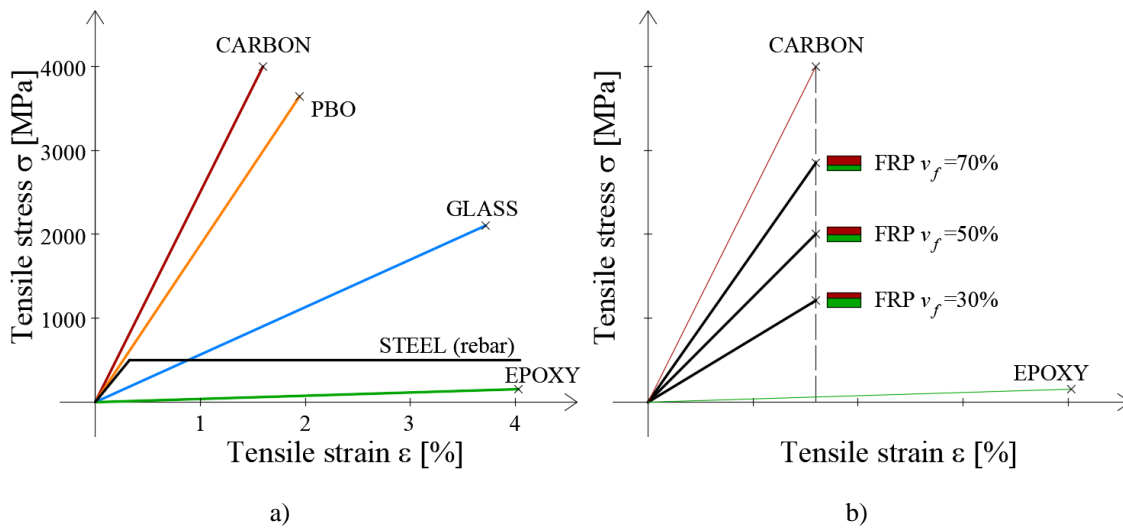
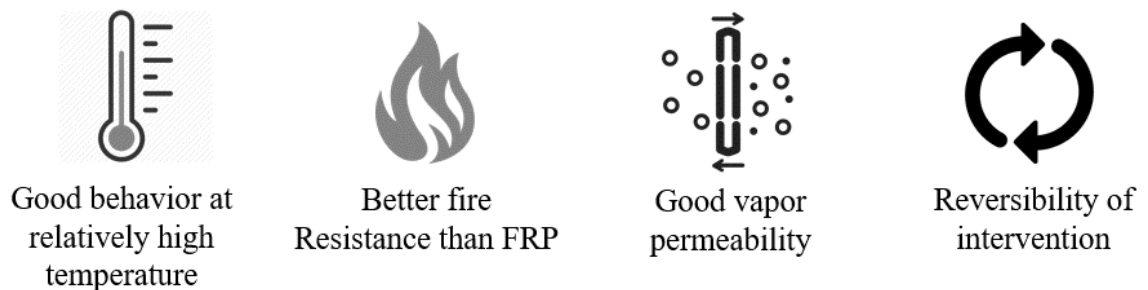


Figure 2.3: a) stress-strain behaviour of bare fibers employed in fiber reinforced composites; b) stress-strain behaviour of FRP composite [10].

Nowadays, several test methods for the mechanical characterization of FRP composites have been developed and published by the ASTM International organization (formerly known as American Society for Testing and Materials). Among them, the ASTM D 3039 describes the procedures for the evaluation of the tensile properties of a rectangular-section thin flat strip of FRP material. Namely, the ultimate tensile strength and corresponding strain, elastic modulus and Poisson's ratio can be determined by monotonically loading in tension the FRP sample while recording the strain field using proper transducers or extensometers. Similarly, the ASTM D 3518 provides the standard test method for the evaluation of the in-plane shear response of FRP materials, namely, the shear stress versus shear strain response, the in-plane shear modulus, the maximum shear stress and strain at  $\pm 45^\circ$ . The test for the evaluation of the in-plane shear properties consists of a uniaxial tension test of a  $\pm 45^\circ$  laminate with loading direction at  $0^\circ$  (i.e.  $45^\circ$  inclined with fiber directions).

## 2.2 Fabric reinforced cementitious matrix composites (FRCM)

Fabric reinforced cementitious matrix composites are innovative strengthening systems comprising open-mesh fiber textiles, embedded within a high performance inorganic matrix. They are also referred to as TRC (textile reinforced concrete), TRM (textile reinforced mortars) or most generically, inorganic matrix composites. Those materials are specifically indicated for the strengthening and retrofitting of masonry structures, due to a better compatibility with the substrate than that of FRPs [11][12][13]. However, they are also used for reinforced concrete element strengthening [14,15][16,17][18,19].



*Figure 2.4: FRCM composites advantages compared to FRPs drawbacks*

The novelty of FRCM composites lies in the inorganic nature of their matrix. Differently from thermosetting resins, the use of inorganic binder allows significant advantages such as a better behaviour at relatively high temperature (considering that the glass transition temperature of most epoxy resin is around 60-70°[12]) and a higher fire resistance, in reason of the higher thickness of the inorganic matrix layers. Furthermore, unlike thermosetting resins, the inorganic matrix guarantees a good vapour permeability with substrate, which allows rising damp and humidity to get outside from the masonry panel [11]. Otherwise, the condensation of capillary humidity at the substrate-composite interface would make the application ineffective, inducing a premature debonding. FRCM also has the advantage to allow a partial reversibility of application, which assumes a fundamental relevance for applications on historical substrates [13]. Indeed, the organic resin employed in FRPs penetrates porous substrates and alters their chemical nature with irreversible damage of the element, whereas inorganic binder employed in FRCM composites, having a better chemical compatibility with the substrate, can be removed with minor damage of the underneath element.

Fabric reinforced cementitious matrix is an extremely versatile technology, which offers a wide catalogue of inorganic binders to pair with different fiber textiles, defining the best fitting solution for each typology of substrate. The inorganic matrix is typically a high-performance cement- or lime-based mortar resulting from sophisticated control of the mix rheology and microstructure. Mortars are characterized by a minor presence of organic aggregates (less than 5%) to ensure proper workability, setting time and mechanical properties. The matrix mix design is usually enriched with short fibers to increase the mixture tensile strength. The water content typically ranges between 20 and 30 %. Non-hydraulic mortars, such as lime-based mortars, may be used for masonry strengthening, particularly in the case of historical structures.

The microscopic structure of inorganic mortars and their water-based nature determines a poor capability of the binder to penetrate and impregnate the fiber filaments in the textile net. This leads to a matrix-textile bond mechanism different from that shown by FRP composites, which requires specific geometries for the textile layer to prevent premature loss of adhesion due to inadequate connection between matrix and textile and between subsequent matrix layers in the stacking sequence. For this reason, fiber textiles adopted in FRCM composites are characterized by an open mesh geometry with free space between yarns not smaller than 5 mm, to allow for a continuity between two subsequent matrix layers interspersed by the textile layer (see Figure 2.5). Commonly employed fibers include polyparaphenylene benzo bisoxazole (PBO), basalt, alkali-resistant (AR) glass and carbon. It is a common practice for FRCM producers to manufacture a specific inorganic matrix designed to pair with a single textile to guarantee the higher mechanical and chemical compatibility between the two components. PBO and carbon fibers are typically combined with cement-based mortars, whereas glass fiber textile may be applied with lime-based mortar due to durability issues depending on the exposition to alkali environment (i.e. within a cement-based matrix), or combined with cement (or geopolymeric) mortar if textile yarns are individually coated with plastic materials (see Figure 2.5b). Hybrid textiles are also manufactured for specific applications (see Figure 2.5e).

Strengthening of masonry structures with FRCM composites include continuous applications on masonry panels to increase their out-of- and in-plane load and displacement capacity, extrados and intrados strengthening of arches and vaults with discontinuous strips, against 3- or 4-hinges cinematic mechanisms induced by horizontal or non-symmetric actions, confinement of columns with closed wrappings

and many others specifically designed applications [20] [21,22] [23]. To ensure a proper stability in the composite in the case of masonry irregular displacement (e.g. sliding along the mortar joint) the textile geometry for the mentioned applications is typically bi- or multi-directional (see Figure 2.5b, c, d, e, and f). Conversely, unidirectional applications such as bending or shear strengthening of reinforced concrete elements, can be realized with unidirectional textiles (see Figure 2.5a). Bidirectional grids having the same number and the same type of yarns along the weft and warp directions, with the same equivalent fibre thickness along those two directions are said balanced.

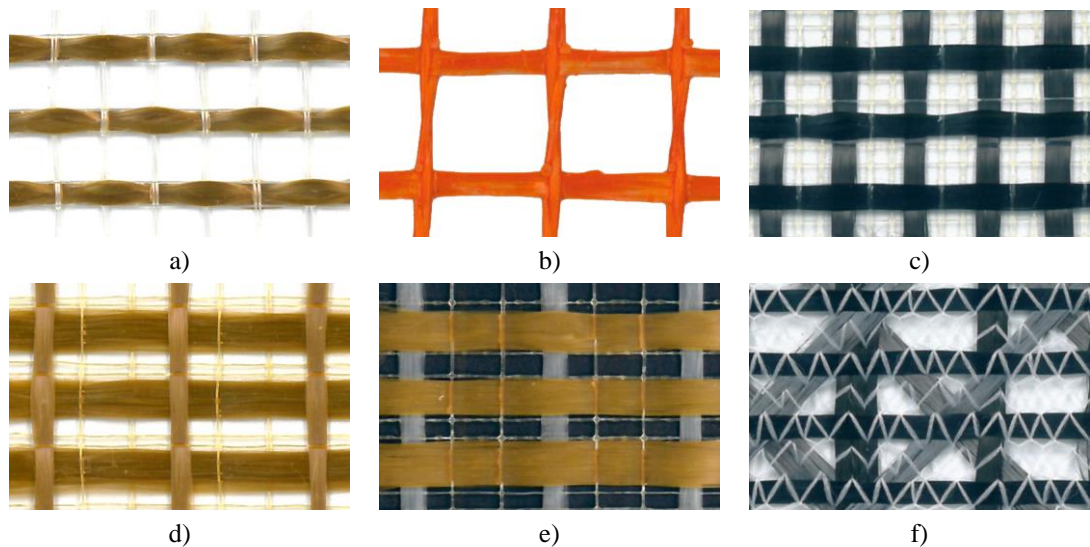


*Figure 2.5: Open-mesh fiber textiles for FRCC applications (scaled 1:1): a) PBO, unidirectional; b) coated glass, bidirectional balanced; c) carbon, bidirectional balanced; d) PBO, bidirectional unbalanced; e) hybrid PBO + glass, bidirectional unbalanced; f) carbon, quadri-axial unbalanced.*

### 2.2.1 Mechanical properties of FRCC composites and their components

The mechanical behaviour of FRCC composites is influenced by several parameters, such as the mechanical properties of its components, the cracking state of the composite (uncracked stage, crack propagation stage and fully cracked stage) and also by the test set-up and procedure, as it will be reported in the following. The results of a wide round robin table (RRT) experimental campaign [13], focused on the tensile and bond characterization of inorganic matrix composites, and involving 5 different FRCC materials (including aramid, basalt, carbon, glass and PBO fiber, paired with different mortars), are used in this section to shed light on the mechanical properties of FRCC and their constituents.

In FRCM composites, the tensile stiffness and the volume fraction of matrix are notably higher than those of the fiber textile, whereas the tensile strength of textile is remarkably higher than that of matrix. This implies that, if the rule mixture is considered (see Eq.(2.1)), being  $v_f$  very small (typically in the range 0.5 - 1%), in the FRCM uncracked stage the composite elastic modulus is essentially consisting with that of matrix. In other words, the main part of tensile stress will be carried by the inorganic matrix until its tensile strength is reached and the major role played by the fibers occurs in the post-cracking stage, in which the fibres bridge across the cracked matrix and the elastic modulus of matrix gets almost null as a consequence of the cracking pattern development.

$$E_{FRCM} = E_m \cdot v_m + E_f \cdot v_f \quad (2.1)$$

Equation (2.1) expresses the composite material elastic modulus in the uncracked stage ( $E_{FRCM}$ ) as a function of that of matrix and fiber,  $E_m$  and  $E_f$  respectively, and of the corresponding volume fraction ( $v_m$  for matrix and  $v_f$  for fibers). It is noteworthy to point out that the elastic stiffness of the mortar reduces depending on the cracking formation and propagation in the composite.

Matrix employed in	Type	Tensile strength [MPa]	Compressive strength [MPa]	Flexural strength [MPa]	Elastic modulus [GPa]
PBO FRCM	Cement	4.27	20-40	2-4	6-12.5
Glass FRCM	Lime	-	6.5-26	8.38	8
Aramid FRCM	Lime	-	10	-	-
Basalt FRCM	Lime	-	15	-	-
	Cement	-	15.5	-	-
Carbon FRCM	Lime	-	6.5-10.3	-	-
	Cement	-	16.4-40	3-4	7-8.5

*Table 2.1: Tensile properties of inorganic binders employed in FRCM technology [13,24–28].*

Table 2.1 reports the tensile properties of some inorganic mortars among the most commonly employed in FRCM applications, collected from research works available in the literature or from producer's datasheets [13,24–28]. The tensile strength of mortar can be experimentally evaluated according to EN 12390-6, whereas the procedures to evaluate its tensile elastic modulus are described in EN 14580. The average flexural strength of the mortar can be obtained by three-point bending tests of 40×40×160 mm mortar prisms according to EN 1015-11. The two portions of the prism obtained after

the three-point bending test are commonly tested in compression to obtain the mortar average compressive strength, EN 196-1:2016. Table 2.1 shows that mainly cement- or lime-based mortar are adopted [13], sometimes enriched with geopolymers or with short fibers. Stronger and stiffer textiles are generally combined with a cementitious matrix, whereas more deformable textiles, such as glass and basalt, are associate to lime mortar.

The tensile properties of different bare fibers employed in FRCM composites are reported in Table 2.2, including polyparaphenylene benzo-bisoxazole (PBO), high-modulus (HM) carbon, high strength (HS) carbon, alkali-resistant grass (E-glass), high-strength glass (S-glass), aramid and basalt. However, it must be noted that the tensile properties of woven textiles (comprising the same fibers in Table 2.2) are typically lower than those of the bare fiber, mainly because the tensile behaviour of the grid is affected by uneven stress distribution between the textile yarns. Indeed, when a single fiber in a non-impregnated bundle of fibers undergoes tensile failure, the load acting on the bundle will be equally distributed among the remaining fibers and the broken fibre will no longer carry any load. This is commonly referred to as equal load sharing process [29]. However, if the bundle is impregnated with organic matrix (e.g. in the case of FRP), the load re-distribution process following the single-fiber rupture is limited by the presence of matrix. In this case, stress is redirected back into the broken fiber by plain shear interaction with the matrix at the interface. The matrix localizes and redistributes the load and this overload is then carried by the fibers nearest to the broken fiber; this phenomenon is known as local load sharing [30]. The local load sharing mechanism may not be activated in FRCM composites due to the low deformability of matrix and due to its poor impregnation capability, determining uneven distribution of stresses within the textile layer. Furthermore, the relatively wide spacing between fiber yarns in open-mesh textiles may further exacerbate this non-uniform stress transfer mechanism.

High-strength textiles employed in FRCM technology are collected in yarns and arranged in stable grids with open-mesh geometry (see Figure 2.5). The thickness of a single yarn is generally in the tenth of a millimetre, however, due to the open-mesh geometry of those textiles and due to the continuous nature of their applications, their tensile properties are typically provided assuming a textile equivalent thickness,  $t_f$ . The equivalent fibre thickness of a textile grid along one direction (either weft or warp), is defined as the ratio between the density of the yarns/strands only in the considered direction and the specific weight of the fibres arranged along that direction. The

equivalent thickness of a textile depends both on the yarn dimension and on the geometry of the grid (i.e. spacing between yarns). Some  $t_f$  values for textiles employed in FRCM systems are provided in [13] and will be reported for the sake of clarity: Aramid (0.033 mm<sup>2</sup>/mm), Basalt (0.033 – 0.058 mm<sup>2</sup>/mm), Carbon (0.047 – 0.063 mm<sup>2</sup>/mm), Glass (0.031 – 0.072 mm<sup>2</sup>/mm), PBO (0.014 mm<sup>2</sup>/mm).

Material	Tensile strength [GPa]	Elastic modulus [GPa]
PBO	5.7-5.8	180-270
Carbon (HM)	2.4	370-390
Carbon (HS)	4.4-4.8	225-260
E-glass	1.9-2	72-85
S-glass	3.2-3.5	85-90
Aramid	2.5-3.8	125-135
Basalt	3.2-4.2	90

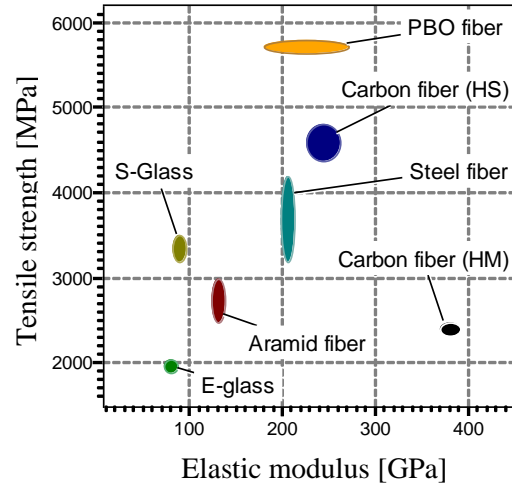


Table 2.2: Tensile properties of bare fibers employed in FRCM applications [13,24].

To study the FRCM composite tensile behaviour different test set-ups were proposed in the literature [24,31–34] and some of them were adopted by current acceptance criteria and design guidelines for externally bonded FRCM composites. Figure 2.6 reports a sketch of the clamping- and clevis-grip test set-ups, employed for the tensile characterization of inorganic composites in the Italian and American acceptance criteria, respectively. An extensive description of the two test set-ups follows:

- Clamping-grip test set-up** (Figure 2.6a): According to the Italian acceptance criteria [35], the tensile properties of the inorganic-matrix composite shall be obtained using the clamping-grip tensile test. In this case test, the ends of a rectangular inorganic-matrix composite coupon are clamped by the machine wedges and pulled until the tensile rupture of the embedded textile occurs [36]. The specimens are equipped with GFRP tabs bonded to the coupon ends to promote an even distribution of the clamping pressure and avoid mortar failure within the wedges. The specimen ends are then directly clamped by hydraulic wedges and the test is carried out by monotonically increasing the end-displacement at a constant rate (0.0034 mm/s according to [35]). An extensometer with appropriate gauge length is applied to the central part of the



specimen to measure the specimen axial strain (Figure 2.7). The extensometer gauge length is determined to capture the majority of the possible matrix cracks. Nevertheless, some cracks may occur close to the wedges, due to stress concentration induced by the clamping pressure and could not be captured. The occurrence of cracks outside the instrument gauge length is well-known in clamping-grip tensile testing of inorganic-matrix composites and may affect the specimen deformability measured [36].

- Clevis-grip test set-up (See Figure 2.6b): The U.S. acceptance criteria [37] indicate the use of clevis-grip tests (See Figure 2.6b) to obtain the tensile acceptance parameters of FRCM and steel reinforced grout (SRG) composites. In the clevis-grip test, metallic plates are bonded to the inorganic-matrix composite coupon ends and are used to transfer the load from the specimen to the machine through clevis-type joints [24]. The steel plates are bonded to the specimens using an epoxy resin and are connected to the testing machine with a through-pin and a clevis-type joint (Figure 2.6b). The tests are conducted by monotonically increasing the machine displacement at a constant rate and the specimen axial strain is measured using an extensometer with an appropriate gauge length, mounted to the central part of the specimen or to the steel plate end portions.

Clamping- and clevis-grip test set-ups generally provide significantly different results in reason of the different boundary conditions to which the specimen is subjected. The clamping-grip tensile test provides an exhaustive mechanical characterization of the FRCM system and of its component materials, whereas the clevis-grip set-ups allow the investigation of the FRCM strengthening application maximum load bearing capacity.

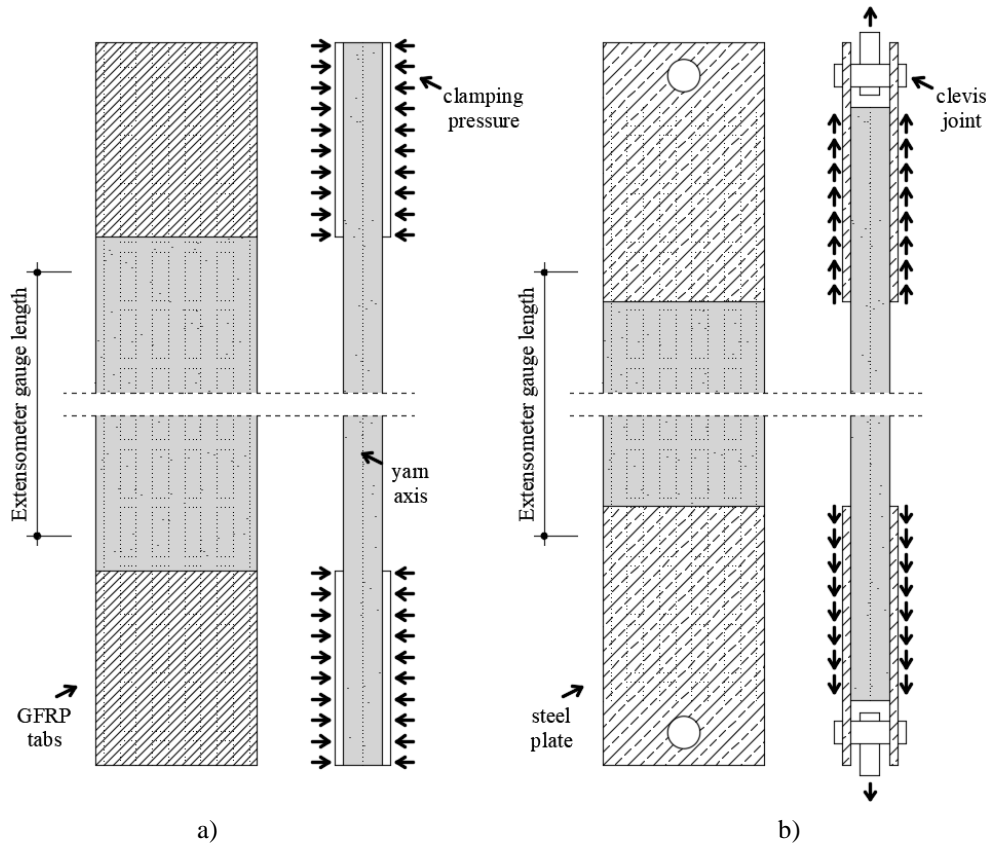


Figure 2.6: FRCM tensile test set-ups: a) clamping grip; b) clevis-grip set-up.

When an FRCM coupon is subject to clamping-grip tensile test (See Figure 2.6a), its axial stress  $\sigma$  - axial strain  $\varepsilon$  response is ideally tri-linear, as shown in Figure 2.7. In Figure 2.7 the tensile axial stress is conventionally referred to the cross-sectional area of the dry textile, regardless of the presence of the matrix. The first linear branch (Stage I in Figure 2.7) is representative of the specimen's uncracked stage and in reason of the higher elastic modulus and volume fraction of the matrix with respect to fibers, its slope,  $E_1$ , is approximately close to that of matrix  $E_m$  ( $E_1 \approx E_m$ ). Stage I ends when the tensile strength of matrix,  $\sigma_{T1}$ , is reached, corresponding with a strain value  $\varepsilon_{T1}$ . Further increasing the imposed displacement beyond the cracking limit will result in redistribution of the tensile stress from the matrix to the bridging fibers, in the cracked zone. This redistribution mechanism characterizes the Stage II of the composite response, in which the constant pulling action of the testing machine induces the formation of new cracks and the gradual transfer of stress from matrix to the fiber layer. The formation of a new crack during Stage II determines a sudden drop in the stress response that is followed by an ascending loading branch along a less-stiff path (see dotted lines in Figure 2.7), which prolong until the matrix tensile strength is reached again at a different position in the specimen. This multiple cracking process occurs at an

approximately constant stress level, for this reason the Stage II of the stress-strain curve is almost horizontal or slightly ascending with slope  $E_2$ . When Stage II ends, the matrix is divided by parallel cracks and any additional tensile action will cause stretching or pull-out of the fibers. At this stage, the rigidity of the textile layer in the composite, determines a new linear ascending branch in the stress response, whose slope is approximately close to that of bare textile ( $E_3 \approx E_f$ ). The specimen failure occurs once the tensile strength of fibers,  $\sigma_{fu}$ , is reached, or even at a lower stress level in the case of uneven distribution of stresses in the textile layer.

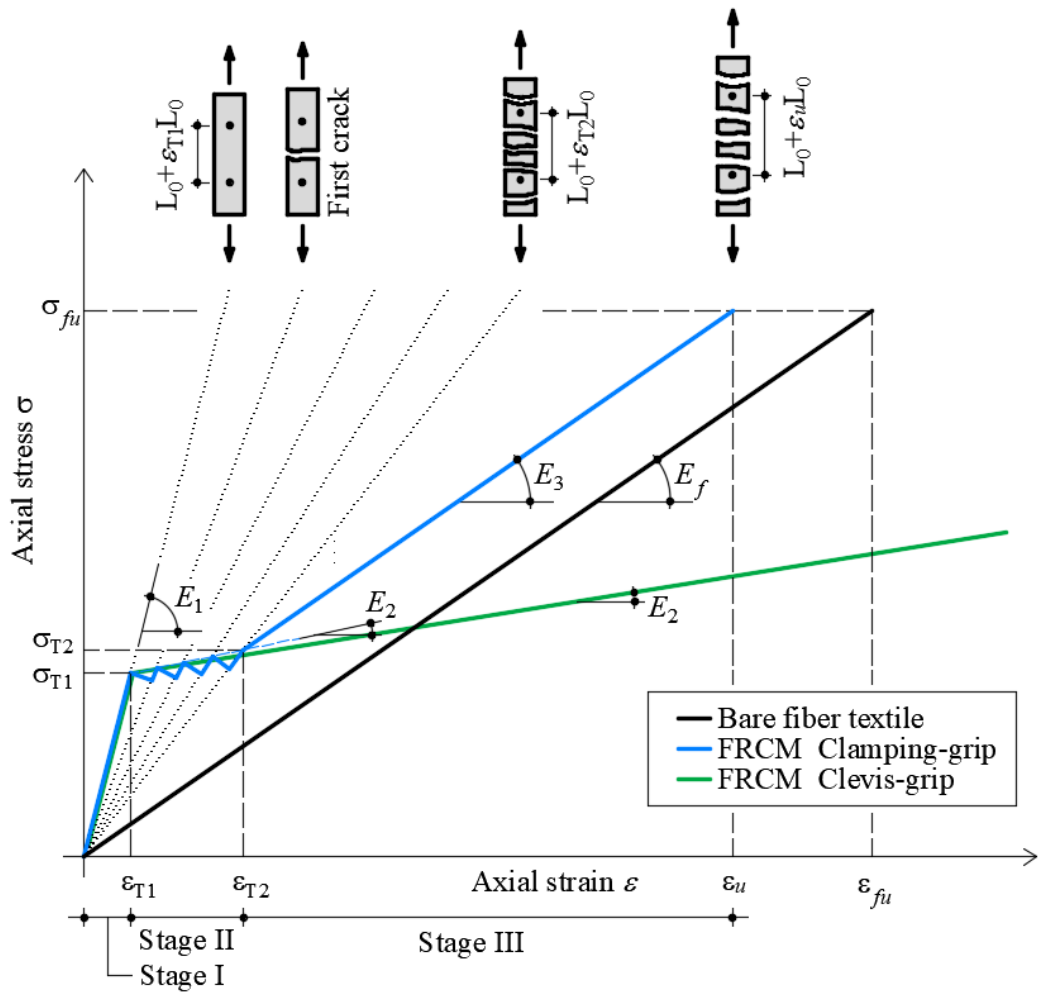


Figure 2.7: Axial stress – axial strain responses of tensile test on FRCM coupons.

The use of clevis-grip set-up for the tensile characterization of FRCM composited determines an idealized bilinear response, with a prolonged Stage II and in which the third phase is not captured. Stage I of clevis-grip tensile test is analogous to that of clamping-grip testing method, mainly governed by the tensile behaviour of matrix, which ends once the tensile strength of matrix is reached. Differently from clamping-grip test response, the Stage II of clevis-grip-tested specimens is characterized by the

cracking of matrix and by high slippage phenomena, because of the lack of clamping pressure on the specimen's ends. Besides, due to the weak impregnation capability of the inorganic matrix, the second Stage of clevis-grip-tested specimens is more extended with respect to that of clamping grip tensile test (higher strains are reached). At this stage a gradual telescopic failure mechanism onset in the fiber yarns, in which only the outermost filaments are impregnated by the surrounding matrix, whereas the core fibers are relatively free to slip. The telescopic failure mechanism of FRCM composites characterizes their bond behaviour in EB application and will be covered in detail in the following chapters. The slope of Stage II of the clevis-grip response,  $E_2$ , is similar to that observed in Stage II of clamping-grip test. The failure occurs due to debonding of fiber from matrix along the clevis grip length, generally at lower stress values than the tensile strength of textile. Rupture of sleeve textile filaments within fiber yarns may occur, or matrix splitting at the fiber-matrix interface.

FRCM Material	$\sigma_{T1}$ [MPa]	$\varepsilon_{T1}$ [%]	$\sigma_{T2}$ [MPa]	$\varepsilon_{T2}$ [%]	$\sigma_{fu}$ [MPa]	$\varepsilon_u$ [%]	$E_3$ [GPa]
PBO	900	0.08	1100	0.5	3300-3468	1.7	210
Glass	500	0.06	700	0.45	800-1294	1.8	50-66
Aramid	-	-	-	-	1089-1354	-	52-61
Basalt	-	-	-	-	1233-1985	-	48-74
Carbon	480	0.06	620	0.24	1043-2832	0.74	154-245

Table 2.3: Average tensile properties of FRCM composites [13,24].

Table 2.3 reports the average tensile properties obtained through clamping-grip testing of several FRCM systems, presented in [36]. In Table 2.3  $\sigma_{T1}$  and  $\varepsilon_{T1}$  are the tensile stress at the end of Stage I (see Figure 2.7) and corresponding strain, respectively,  $\sigma_{T2}$  and  $\varepsilon_{T2}$  are the tensile stress at the end of Stage II (see Figure 2.7) and corresponding strain, respectively, whereas  $\sigma_{fu}$ ,  $\varepsilon_u$  and  $E_3$  are the failure stress and corresponding strain and elastic modulus of Stage III, respectively.

## 2.3 Composite reinforced mortars (CRM)

Fiber-reinforced polymer (FRP) composites can be arranged in form of bi-dimensional grids and employed as internal reinforcement for mortar plasters to realize composite reinforced mortar (CRM) systems. The main difference between CRM systems and FRCMs is that, in the former, a textile grid with net dimensions wider than 30 mm is impregnated with epoxy resin to form an FRP stable grid, which then is embedded

within inorganic mortar, in the latter, one (or more) bare textile layers with smaller net dimensions ( $<30$  mm), is embedded within inorganic mortars layers. The system is applied by fixing the composite grid to the masonry surface through anchors and then spraying the inorganic mortar over it. Accordingly, the main anchoring function is devolved to local anchors (typically 4 or 5 per square meter), whereas mortar has the important role to distribute applied stresses among the grid. The rapidity of this procedure, which does not require the careful alignment of the fiber textile as in the case of FRCM composites, makes CRM an attractive and cost-effective solution for strengthening masonry structures.

In general, the composite grid used in CRM is made by glass fibers impregnated with epoxy resin to form a bi-dimensional rigid grid. The warp and weft yarns have a clear spacing equal to or higher than 30 mm, whereas the matrix thickness can go up to 50 mm. The yarns of the grid employed in CRM applications are made by pultruded (Figure 2.8a) or laminated (Figure 2.8b) yarns in weft (x) direction and laminated yarns in warp (y) direction weaved together using the leno weave technique (Figure 2.8). Accordingly, each warp yarn was comprised of two sub-yarns twisted together and around the weft yarns, which contributed to provide a relatively high stiffness to the grid. The relatively rigid connections (joints) between weft and warp yarns, resulting from the resin impregnation and the leno weave technique adopted, provide the grid geometric stability during transportation and installation.

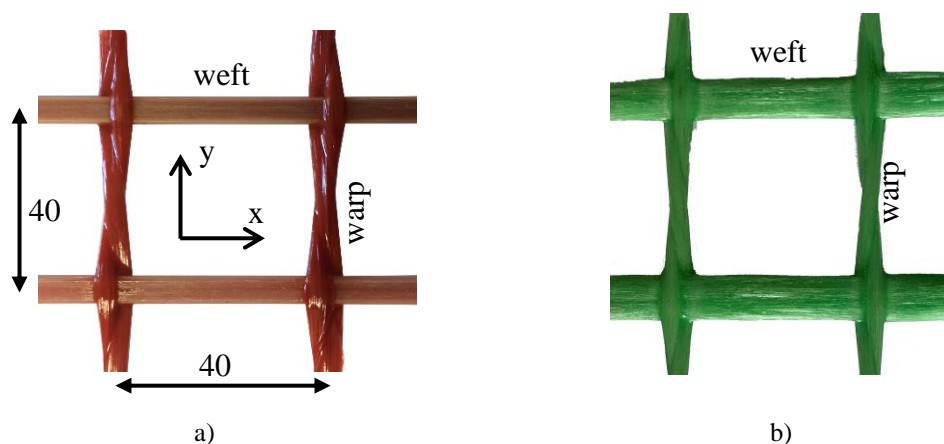


*Figure 2.8: Glass composite grid for CRM applications (scaled 1:1; dimensions in mm): a) type A, pultruded weft and laminated twisted warp; b) type B, laminated weft and laminated twisted warp.*

CRM systems have proved to be effective if applied as externally bonded reinforcement (EBR) of existing masonry members showing promising improvements of load-carrying and deformation capacities. The use of composite-reinforced mortars systems represents a fast and easy solution against the slab intrados crumbling hazard, which is a common deterioration resulting from thermal dilatation and corrosion of the slab reinforcing bars. Slab deterioration and crumbling hazard is emphasized in the case of seismic events, with serious consequences for the building occupants. The application of CRM to the slab intrados represents a fast and effective solution to limit the crumbling hazard and its effectiveness is amplified using punctual grid anchors to slab joists. When anchors are employed a shear failure of a grid bundle close to one anchor may occur, however this bundle failure did not determine the reinforcement collapse, since the stress redistribution in the grid allows for maintaining the applied load.

### 2.3.1 Mechanical properties of CRM and their components

The mortar employed in the CRM system usually includes natural hydraulic lime NHL 5 and metakaolin without the addition of cement. The average flexural strength of the mortar can be obtained by three-point bending tests of 40×40×160 mm mortar prisms according to EN 1015-11 [38]. The two portions of the prism obtained after the three-point bending test are commonly tested in compression to obtain the mortar average compressive strength [38].

The mechanical properties of the grid can be investigated by tensile testing of single weft and warp yarns. In leno weaved grids, the tensile properties of yarns in the two direction typically shows slightly different values due to the misalignment with the load direction of fibers in twisted yarns. These results in a lower elastic modulus and tensile strength of the grid in warp direction (see Figure 2.8).

In reason of the rigid connection between weft and warp yarns in the grid, when a load is applied to the CRM along one of the grid directions, many yarns orthogonal to the applied load direction provide their contribution to the system load-carrying capacity. For this reason, the shear strength of the joints is of fundamental importance when the glass grid is fixed to the support using only anchorages, without being embedded within the mortar, as in the case of applications to prevent intrados crumbling hazards [39].

To verify the stability of the grid joints and measure the maximum force that can be borne by a single joint, grid cruciform specimens, without the presence of the mortar, can be shear-tested following the indications reported in EN ISO 15630-2 [40], even if

this procedure is indicated for steel welded fabrics. This provides information on the behaviour of the grid joint and not on the CRM system. The testing procedure consists in pulling the end of a single yarn (either a weft or a warp yarn), by clamping it with the testing machine wedges. The yarn perpendicular to the clamped one, i.e. the crossing yarn, is inserted within a rigid holder, connected to the machine, and firmly tightened using jaws (see Figure 2.9a). The tests are conducted by monotonically increasing the displacement  $\delta$  of the machine actuator at a constant rate, while the corresponding applied load  $P$  is registered by a load cell. The shear failure of the single crossing yarn is shown in Figure 2.9b.

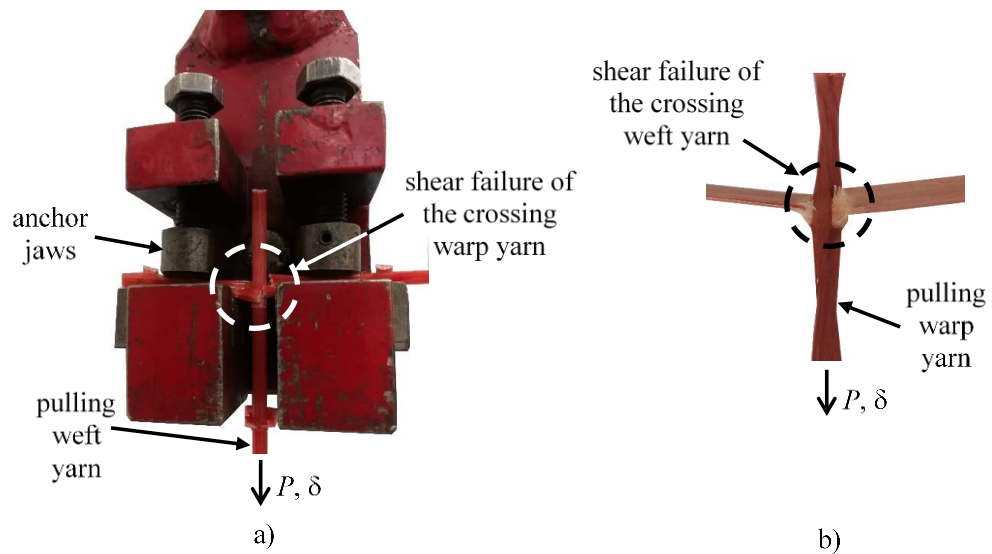


Figure 2.9: Shear test on grid joints: a) test set-up (pulling weft); b) Failure of specimen (pulling warp).

The tensile properties of CRM systems can be investigated using either clamping- or clevis-grip tensile test set-up, to obtain an insight on the interaction between the grid and the matrix when subjected to tensile stress. In both cases, rectangular CRM coupons including 2 longitudinal yarns and having a width that is a multiple of the reinforcing mesh space can be fabricated following the indications of the Italian acceptance criteria for inorganic-matrix composites [35]. The specimen length varies depending on the adopted set-up. Since the two test set-ups provide different  $\sigma - \epsilon$  responses (i.e. axial stress on yarn – axial strain), the peculiarities of each one have been listed below:

- Clamping-grip tensile test: for CRM systems involving a weak matrix (e.g. lime-based mortar), the tested specimen does not show the tri-linear behaviour usually observed in FRCM composites. Indeed, the use of a relatively weak matrix and stiff grid determines the absence of the first and second stages. After

the initial matrix cracking, the specimen shows an approximately linear stress-strain behaviour with a slope that can be associated with the bare grid longitudinal yarn elastic modulus. This indicates that the grid is mainly responsible for the CRM  $\sigma$ - $\varepsilon$  curve slope during the third stage, although the matrix and the transversal yarns slightly contributed to the applied load.

- Clevis-grip tensile test: Clevis-grip tensile tests provide a tensile strength and a slope of the applied stress-axial strain curves  $E_2$  of fully-cracked specimens lower than those observed in clamping-grip tests. These differences are due to the different stress-transfer mechanism that led to a sudden matrix interlaminar failure in clevis-grip tests.

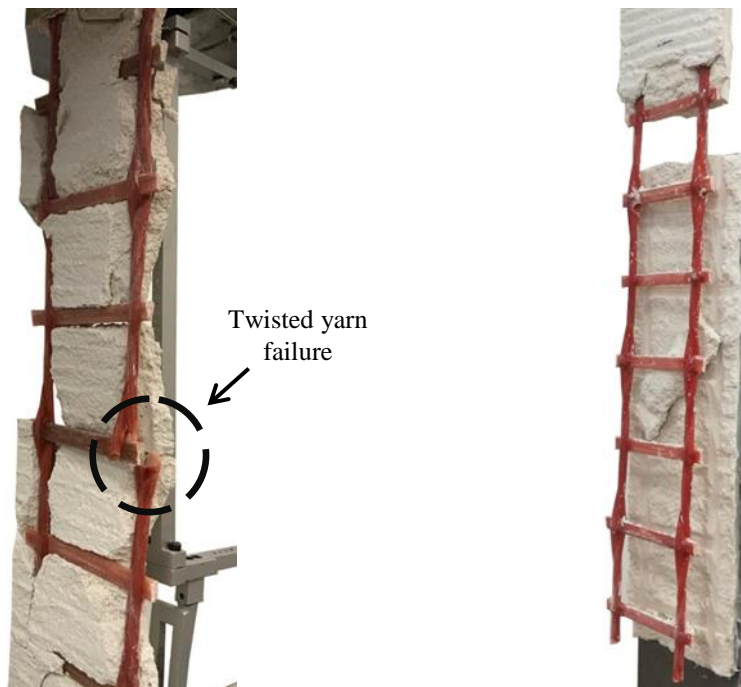


Figure 2.10: Failure of CRM specimens subject to clamping-, a), and clevis-, b), grip tensile test.

A picture of the specimen's failure under the two test set-ups is provided in Figure 2.10. Both specimens exhibit matrix cracks orthogonal to the applied load direction before failure. Cracks were located at the transversal yarn positions. A specimen tested under clamping-grip condition will typically fail due to rupture of one of the two longitudinal grid yarns (see Figure 2.10a), whereas a specimen tested under clevis condition commonly fail due to a sudden matrix interlaminar failure (i.e. splitting along the grid plane [41]), between the bonded steel plates, without rupture of the longitudinal or transversal yarns (see Figure 2.10b). Therefore, in the case of clamping-grip test, the



tensile capacity of the grid could not be fully exploited, which entails for average tensile strength values significantly lower than those obtained by tensile testing of grid bare yarns. Furthermore, the extensive cracking of the matrix led to a large scatter in the results.

## 2.4 Steel reinforced grout (SRG)

Steel reinforced grout composites (SRG) are newly introduced and innovative inorganic composite materials, which are gaining a growing popularity in reason of their outstanding mechanical performances and relatively low cost. SRG composites are comprised of ultra-high tensile strength steel (UHTSS) textiles, embedded within high-performance inorganic, hydraulic and non-hydraulic, mortars.

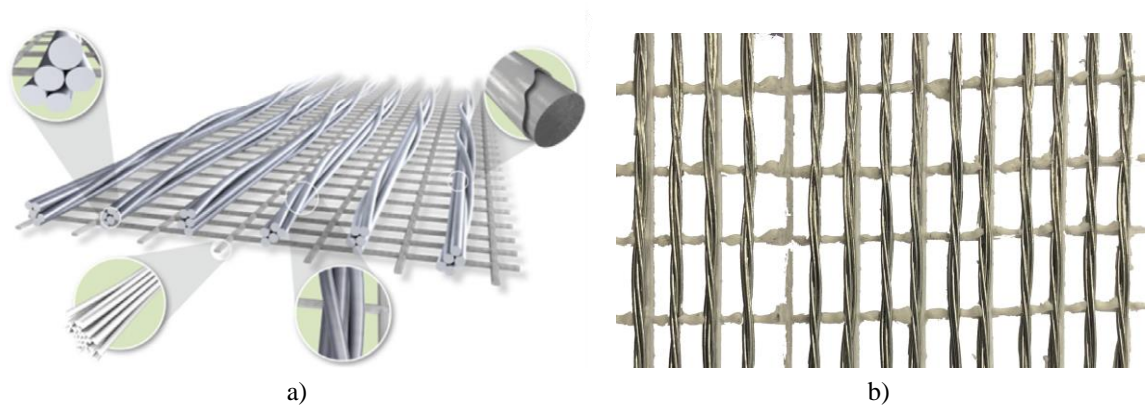


Figure 2.11: Unidirectional UHTSS textiles typically employed in SRG systems: a) 300 g/m<sup>2</sup> mass density [42]; b) 600 g/m<sup>2</sup> mass density.

Unidirectional UHTSS textiles typically employed in SRG systems (see Figure 2.11) are composed of adjacent cords made out of some rectilinear micro wires around which other wires are twisted at a short lay length, in a way to enhance interlocking with mortar. The tensile strength of steel cords is in the range 2800–3200 N/mm<sup>2</sup> and Young's modulus of 180–210 kN/mm<sup>2</sup>. The single wire cross-sectional area is in the order of tenth of mm<sup>2</sup>, resulting in a typical overall cord area and thickness of roughly 0.5 mm<sup>2</sup> and 0.25 mm, respectively. Wires are zinc-coated (galvanized) against rust corrosion and installed on a supporting glass or plastic grid, which provide stability to the textile. The textile surface mass density may range from 600 g/m<sup>2</sup> to 3300 g/m<sup>2</sup> depending on the spacing between the cords, corresponding to maximum loads per unit width varying from 230 kN/m to 1300 kN/m. Cords in the textile are typically spaced apart, in a way to promote mortar penetration and an effective cord-to-mortar interlocking.

Steel reinforced inorganic composites evolved from the field of automotive tyres production and only recently were introduced to construction engineering applications. Typical applications of SRG for structural purposes includes strengthening of reinforced concrete [43] and masonry [44] elements and seismic retrofitting of masonry walls and vaults [45,46].

#### 2.4.1 Mechanical properties of SRG

Despite the multiple similarities with FRCMs, steel reinforced grout systems represent an independent class of composites, mainly due to a different adhesion mechanism between the steel wires textile and the embedding matrix. In fact, due to the strong cord-to-mortar interlocking, no slippage between steel strands and matrix occurs and, thus, no telescopic failure develops in the cracked stage of the composite.

The tensile behaviour of SRG composites, tested under clamping-grip condition (see Figure 2.6a), is ideally characterized by the trilinear response displayed by FRCM materials and represented in Figure 2.7. However, in the case a weak matrix and a high-density steel fiber textile are employed, the first and second stages of the trilinear curve are very limited and the stress-strain curve is comparable with that of unembedded textile. The use of a lower density textile together with a stiff mortar reduces the prevalence of Stage III in the composite stress-strain curve. Consequently, this reflects also in the SRG failure mode, which consists in the rupture of some cords, preceded by a loss of linearity in the response due to steel ductility. The elastic strain recovery following the lateral cord rupture may cause the expulsion of some parts of the matrix layers.

## **2.5 Regulatory framework**

The great popularity that inorganic composites has recently attracted due to their relevant effectiveness as non-invasive strengthening interventions, led the scientific community toward the development of national standards for the definition of acceptance criteria and design rules to govern their use. In this section, the currently available Italian and American Codes and Guidelines for the characterization and design of inorganic composites are reported and described. Besides, in Figure 2.12 a chronicle of the FRCM legislation is presented in parallel with that of FRPs. The first documents to be introduced upon the use of FRCM composite were produced by the U.S. government regulatory body ICC- Evaluation Service (ICC-ES) in 2013, namely AC

434 and ACI 549. The two documents regulate the acceptance and design criteria for the strengthening of RC and masonry structures using FRCM. In particular, AC 434-2013 defines the experimental test methods for the characterization of FRCM materials properties and structural performances, including tensile, bond-to-substrate and durability tests. The structural effectiveness of FRCM application is evaluated through laboratory testing of strengthened elements such as masonry panels, concrete beams and columns. The (ACI 549, 2013) includes general design consideration for the reinforcement of concrete and masonry elements. In particular, shear and flexural strength are analysed with analytical models and design formula.

Until 2018, no codes and guidelines were present in Europe. In the biennium 2018-2019 the Italian government regulatory body (Consiglio Superiore dei Lavori Pubblici - CSLP) published the Guidelines for the qualification and acceptance criteria for FRCM composites [35] (DPCSLP 1/1/2019, “Linee Guida per l’identificazione, la qualificazione ed il controllo di compositi fibrorinforzati a matrice inorganica, denominati FRCM (Fiber Reinforced Cementitious Matrix), impiegati per il consolidamento strutturale”). The Italian Guidelines defines the material properties and test needed for their mechanical characterizations, including tensile test, debonding tests from substrate, lap tensile tests on specimens with spliced length (overlap of the textile layers) and durability tests. In the same period, the National Research Council (CNR) published the guide for the design of FRCM strengthenings [47] (CNR-DT 215/2018, “Guide for the design and construction of externally bonded fibre reinforced inorganic matrix systems for strengthening existing structures”), which defines the FRCM strengthenings design rules, including in- and out-of-plane strengthening of masonry structures, such as piers, arches and vaults, flexural and shear strengthening of RC beams and columns and confinement of columns.

In 2019 the Italian government regulatory body (CSLLPP) published the Guide Lines for the acceptance and qualification of CRM systems (see Section 2.3) “Linea Guida per la identificazione, la qualificazione ed il controllo di accettazione dei sistemi a rete preformata in materiali compositi fibrorinforzati a matrice polimerica da utilizzarsi per il consolidamento strutturale di costruzioni esistenti con la tecnica dell’intonaco armato CRM (Composite Reinforced Mortar)”, which defines acceptance rules and test methods for the characterization of CRM composites and their components.

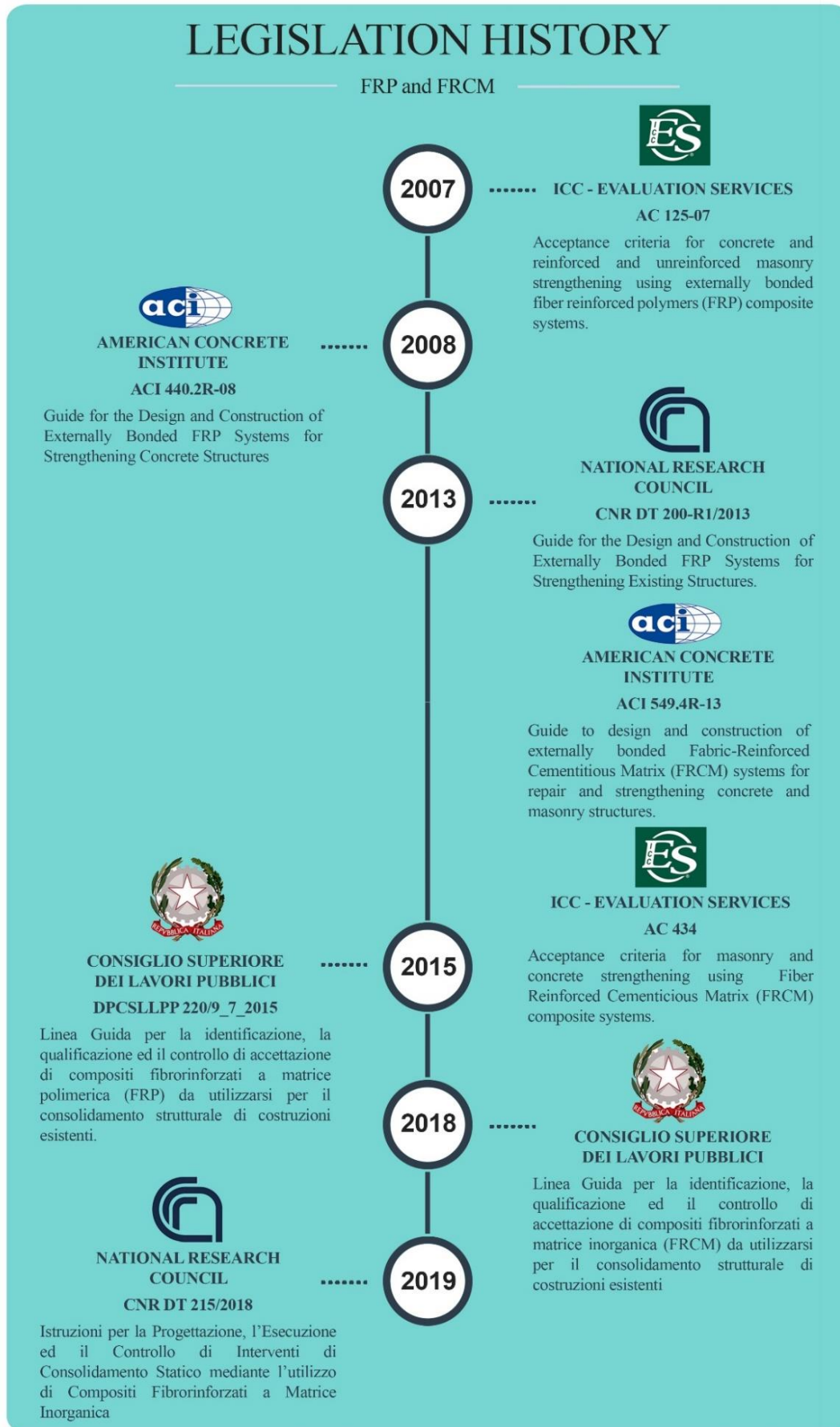


Figure 2.12: Regulatory framework



# 3 BOND IN FRCCM APPLICATIONS

In reason of the high mechanical properties observed in FRCCM composites (see Table 2.3), they are extremely effective if externally bonded to the tension side of existing elements, to increase their flexural and displacement capacity. However, in most of the cases their performances are not fully exploited due to a premature loss of adhesion of the composite from the substrate, which induces a sudden failure in the strengthened element. The composite debonding represents a key issue in structural design, in reason of the brittle failure it causes in the strengthened element. For this reason, the bond strength of FRCCM (as well as of FRP) application assumes a crucial role in the design process of EB strengthening. Accordingly, in addition to tensile tests of the inorganic-matrix composite and of its components [31,34,48,49], bond tests should be performed to investigate the bond behaviour of the composite, with respect to the specific substrate considered [47,49–51]. Several analytical models have been developed to predict the bending and shear capacity of structural elements strengthened with FRCCM composites, which assume the FRCCM-substrate bond capacity as one of the main design parameter and are employed in national standards available nowadays.

FRCCM debonding failure, which is typically associated with a stress level significantly lower than the tensile strength of corresponding FRCCM coupons [36], may occur at one of the interfaces present in the strengthened member, depending on the substrate and composite layout and properties [16][52]. Figure 3.1 shows the various interfaces at which debonding may take place within the strengthened element and the corresponding

failure modes: i) at the matrix-fiber interface with high relative slippage between fiber and matrix (Figure 3.1a); ii) at the matrix-fiber interface with interlaminar failure (i.e. delamination) of the composite and detachment of the external matrix layer (Figure 3.1b); iii) at the composite-substrate interface with loss of adhesion of the inner matrix layer from the substrate (Figure 3.1c); iv) within the substrate, with removal of a thin layer of substrate that remains attached to the composite strip (Figure 3.1d). FRCC composite strips comprising one or two layers of textile generally fail due to debonding at the matrix-fiber interface with relative fiber slippage from the surrounding matrix (Figure 3.1a), whereas FRCC strengthening employing more than one textile layer and SRG composites typically undergoes interlaminar failure (Figure 3.1b) that also may be mixed with local debonding from substrate (Figure 3.1c). The detachment from the substrate may also be associated with inappropriate substrate preparation before the composite application, as in the case of unwashed or not properly roughened substrate, or with poor chemical compatibility between the FRCC matrix and the substrate.

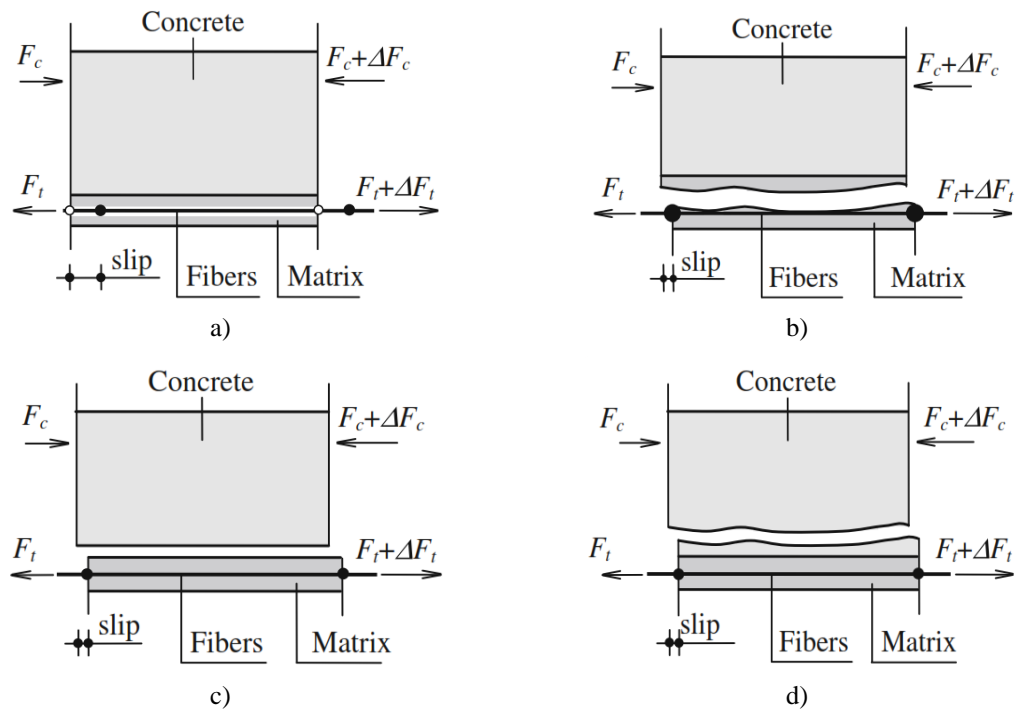


*Figure 3.1: Debonding failure modes. a) debonding at matrix-fiber interface with substantial textile-matrix relative slippage; b) delamination at matrix-fiber interface; c) FRCC-substrate debonding; d) debonding within the substrate. [52]*

The telescopic failure mode (Figure 3.1a) assumes a great relevance especially for fiber reinforced inorganic composites due to the poor impregnation capability of the inorganic matrix they are comprised of. Indeed, due to the dimensions of their

components, inorganic binders can hardly impregnate all fiber filaments of bare (i.e. not impregnated) textiles. This leads to premature debonding at the matrix-fiber interface, typically associated with the telescopic slippage of core filaments with respect to sleeve filaments and surrounding matrix, under the effect of the applied force  $F$  (see Figure 3.2) [53].

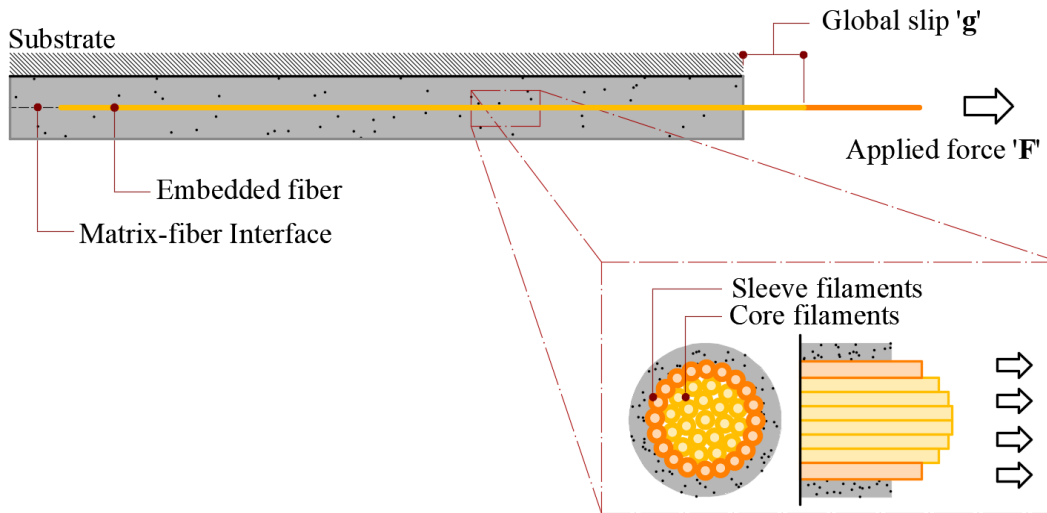


Figure 3.2: Telescopic failure of FRCM composites

In this chapter, the experimental procedures to compute the bond capacity of FRCM are analysed and discussed, then some considerations about the relevance of debonding in the design process suggested by Italian and American guidelines are carried on, to provide an exhaustive insight of the bond behaviour of inorganic composites, which will be discussed in the following chapters.

### 3.1 Experimental set-ups employed for bond investigation

Several parameters affect the bond behaviour of FRCM composites, such as the spacing of the textile, properties of the inorganic matrix, substrate preparation, and level of impregnation of the fibers. In addition, the test set-up may influence the results. Different set-ups are employed to study the debonding process of FRCM composites, which can be generally classified in two macro-classes: direct test set-ups and indirect test set-ups. In the former category, a tensile force is directly applied to the composite, whereas in the latter, a pulling action is indirectly induced in the composite as the effect of the presence of a bending moment. Due to the peculiarity of each set-up category, different results are provided by tests. Indeed, some direct test set-ups were shown to provide a lower bound estimation of the load-carrying capacity [54], whereas results of indirect bond tests provide measures of the composite load-carrying capacity, that could



be directly employed to estimate the capacity of specific FRCM applications, such as the strengthening of masonry arches and RC beams [55]. In this section, peculiarities, drawbacks and advantages of each set-up are analysed and discussed. Then, an experimental study on the effect of testing rate on the response of direct shear test is presented.

### 3.1.1 Direct set-ups

Direct bond test set-ups are the most popular and commonly employed test set-ups for the evaluation of the bond properties of FRCM composites, applied to existing substrates. Among them, the single- (Figure 3.3a(i)) and double-lap (Figure 3.3a(ii)) direct shear test set-ups, which were proposed by [56–58], are those adopted in the most important national standards, although alternative pull-out test set-ups were recently proposed (Figure 3.3a(iii))[59].

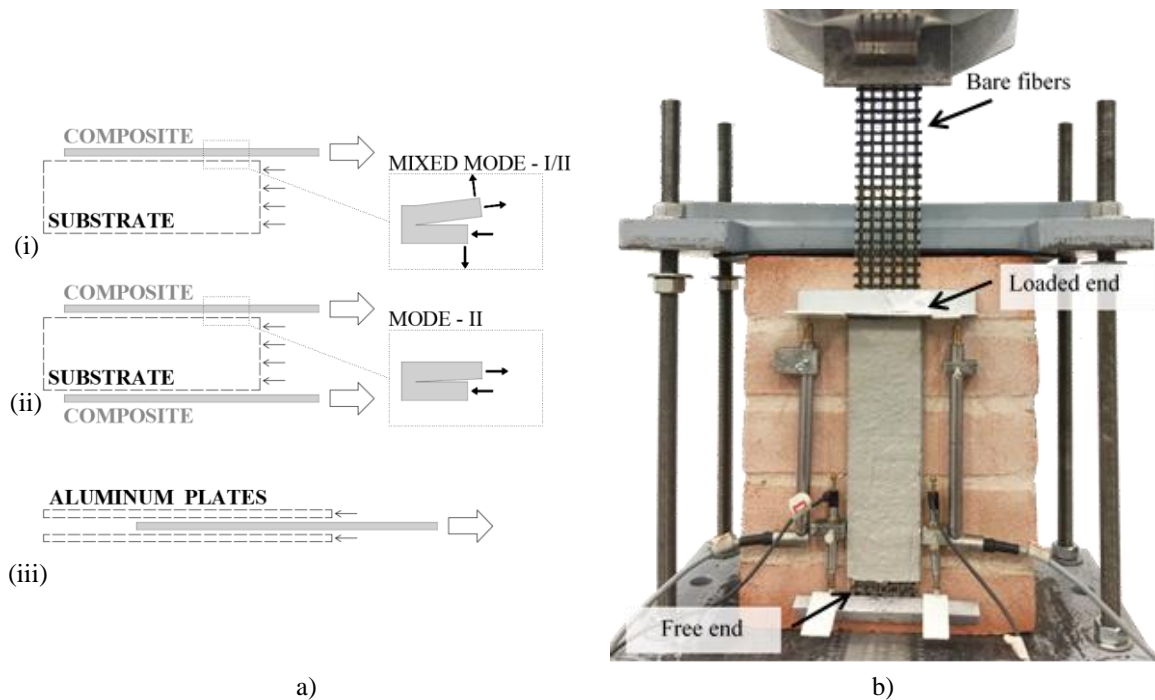


Figure 3.3: a(i) Push-pull single- and a(ii) double-lap direct shear test set-ups. a(iii) Pull-out test set-up. b) Single-lap direct shear test on FRCM-masonry joint.

In a single-lap direct shear test (Figure 3.3b) a composite strip is applied by means of formworks to a regular prismatic block having the same property of the specific substrate object of the investigation. In the case of masonry substrates, small wall samples can be specifically realized, made by the same bricks and mortar in the masonry, or they can be extracted from the original wall using a disk saw. In particular cases, such as for intervention on heritage buildings, direct shear test can be performed

on the construction site, by applying a composite sample directly on a portion of the existing structure.

The composite strip has a width typically proportional to the spacing between longitudinal textile yarns (i.e. yarns aligned with the applied load direction), whereas the strip bonded length and thickness may vary depending on the material typology and number of textile layers. The composite strip bonded length typically start 30 mm apart from the support edge to comply with the indications of the Italian acceptance criteria for FRCM composites [35]. This gap is recommended to avoid support wedge in the substrate joints. Part of the textile layer is not impregnated with matrix and left bare outside from the bonded area, at the loaded-end of the strip (see Figure 3.3b). This bare textile portion is fundamental to the test execution: it is clamped by the testing machine and pulled throughout the test, to eventually induce debonding in the specimen (steel plates, epoxy-bonded to the loose end of the bare textile strip, can be adopted to promote uniform machine grip clamping). An L-shaped aluminum plate is bonded to the bare textile portion, just outside the loaded-end, to allow the measurement of the relative slippage between fiber and substrate at this point. Two LVDTs, bonded to the support on the two lateral sides of the strip, reacting off of the L-shaped aluminum plate, provide the textile global slip  $g$ . In a similar way, other two LVDTs can be applied to an L-shaped aluminum plate at the free-end of the strip and used to measure the possible textile free-end slippage (see Figure 3.3b).

The test is carried out using a servo hydraulic or electric testing machine, equipped with a load cell with adequate capacity, by monotonically increasing the machine piston displacement at a constant rate (a 0.2 mm/min displacement rate for the testing machine stroke is suggested by the Italian acceptance criteria for FRCM composites [35]). If a pull-push configuration is adopted, the substrate block is restrained to the testing machine (e.g. using a rigid steel frame as shown in Figure 3.3b), which is thus subjected to compression, while the reinforcing textile is pulled by the machine piston at a given rate [60]. The machine pull, directly applied to the textile layer, induces shear stresses at the composite-substrate interface, which is generally assumed to be subjected to a pure in-plane shear stress, i.e. to a pure Mode-II fracture mechanics loading condition (Figure 3.3a(ii)) [61].

The stress (or load) response of a direct shear test of FRCM strengthened sample depends on many parameters, such as the FRCM material properties, the compatibility between fiber and matrix in the FRCM and between composite and substrate, the

number of textile layers, the grid spacing dimensions and others. Figure 3.4 reports three possible idealized stress responses of FRCM-concrete joints, corresponding to three different FRCM configurations, namely (i) single-ply E-Glass FRCM (eG FRCM), (ii) 4-ply PBO FRCM (C FRCM) and (iii) single-ply PBO FRCM.

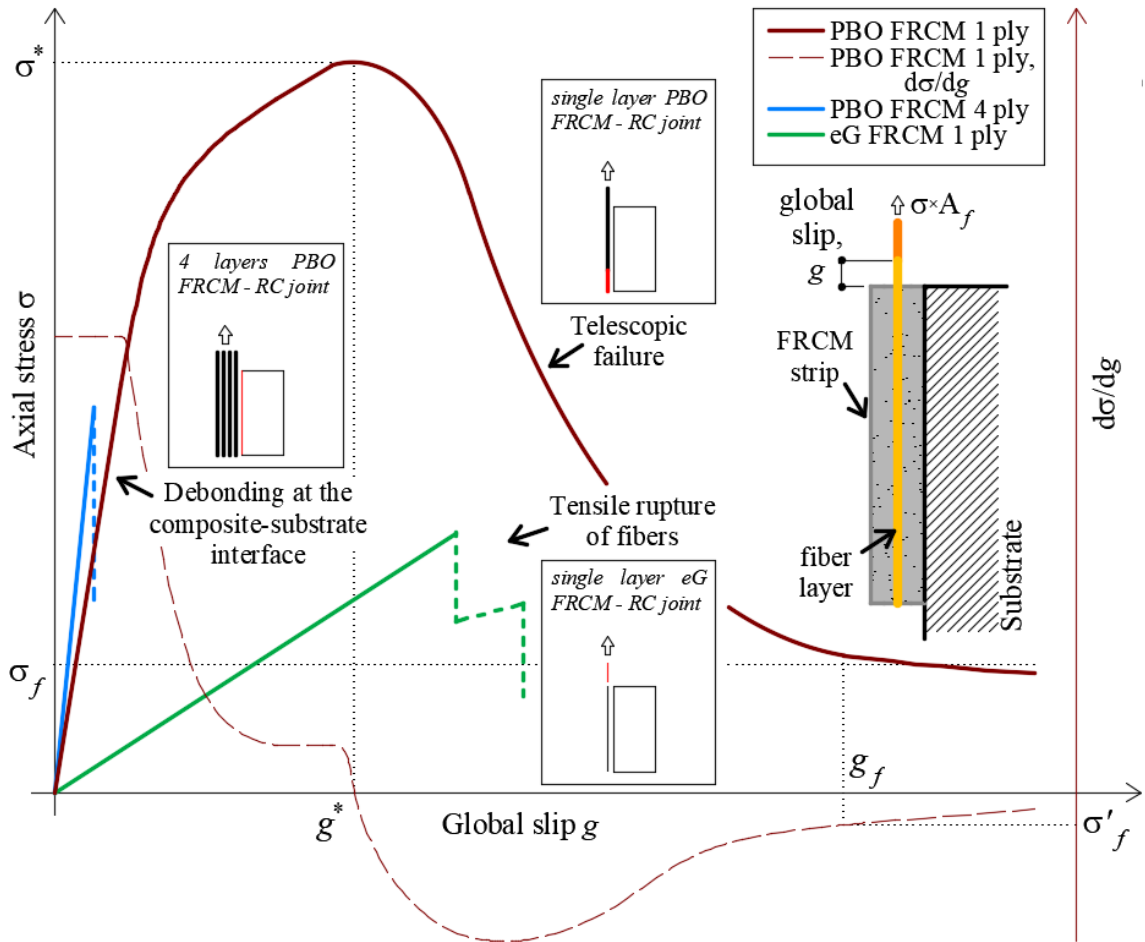


Figure 3.4: direct shear test idealized stress responses.

The idealized stress response of the eG FRCM strengthened specimen (green curve in Figure 3.4) is mainly governed by the E-Glass textile tensile behaviour. This is due to the relatively low tensile strength of the glass fiber, which does not allow a full bond-stress transfer between fiber and matrix. Since the bond strength of the composite is higher than the tensile strength of the textile, the idealized response will be linear-elastic until a sudden failure, due to tensile rupture of the bare fiber yarns outside from the composite. The actual response (i.e. not idealized) may not be perfectly linear due to uneven distribution of the tensile action on the textile layer, which determines the premature rupture of those filaments on which stress concentrate, with a gradual reduction of the curve's slope before failure.

When more than one textile layer is employed in the FRCM strip, debonding at the composite-substrate interface can be observed [62–65]. The  $\sigma$ - $g$  response of a 4-ply PBO FRCM composite, which fails due to debonding at the composite-substrate interface (see Figure 3.1c), is depicted with blue in Figure 3.4. The response may be either linear or partially non-linear, depending on whether the composite entered or not in its cracked stage, before the occurrence of debonding. Debonding at the composite substrate interface is extremely brittle and is more likely to occur in the case of non-pure Mode-II loading conditions, such as in the case of RC beams subjected to bending moment.

Debonding of PBO FRCM specimens comprising one single layer of textile reportedly occurs at the matrix-fiber interface, with significant slippage of the fiber with respect to the embedding matrix (see Figure 3.1a and Figure 3.2)[62]. This debonding mode is accountable to the poor capability of inorganic matrix to impregnate PBO filaments within each bundle, which eventually determines a telescopic slippage between core and sleeve filaments and with the matrix itself. The single-layered PBO FRCM strengthened specimen response (dark-red curve in Figure 3.4) shows an initial linear branch, associate to the composite uncracked stage. This initial stage of the  $\sigma$ - $g$  curve is governed mainly by the matrix tensile behaviour and it ends once the matrix tensile strength is reached. At this point some cracks start appearing in the matrix and the applied stresses gradually transfers from matrix to fibers. The propagation of the crack pattern determines a growing reduction of the curve's slope, until a cohesive crack (i.e. tangential to the fiber yarns lateral surface) opens at the matrix-fiber interface, close to the loaded end of the strip. The progressive interfacial debonding in the composite strip is associated with the propagation of the interfacial crack, from the loaded-end toward the free-end. After the onset of debonding at the specimen's loaded end, the load carrying capacity of the composites may further increase, provided a sufficient bonded length, due to the contribution of friction and interlocking between fiber and matrix, along the debonded portion of the strip. For relatively high values of bonded length, this determines a linear increase in the idealized  $\sigma$ - $g$  curve, until the specimen's bond capacity  $\sigma^*$  is reached (see Figure 3.4). After the peak stress  $\sigma^*$  is attained, the applied stress decreased with increasing global slip  $g$ , as a consequence of the weakening of matrix and progressive debonding of the fibers from the embedding matrix. The  $\sigma$ - $g$  curve eventually stabilizes at an almost constant stress value, indicate with  $\sigma_f$  in Figure 3.4. This residual stress is caused by the presence of friction/interlocking at the matrix-

fiber interface, after the onset of debonding along the whole strip length. The residual constant stress provided by friction  $\sigma_f$ , can be identified analyzing the derivative of the axial stress with respect to the global slip,  $d\sigma/dg$  (dashed dark-red curve in Figure 3.4). In Figure 3.4, the friction residual stress has been evaluated averaging the axial stress values associated with a derivative  $d\sigma/dg$  comprised within the range  $\sigma'_f$  and 0 MPa/mm. The specific value of  $\sigma'_f$  can be determined through critical analysis on the  $\sigma$ - $g$  response of bond test. The value of  $g_f$  is defined as the first global slip value for which the inequality  $\sigma'_f \leq d\sigma/dg \leq 0$  MPa/mm holds.

In single lap direct shear tests, the interface is generally assumed to be subjected to a pure fracture mechanics Mode-II loading condition. However, due to the eccentricity between the applied load and the restraining force, a minor peeling component, i.e. a Mode-I fracture mechanics loading condition, is always present in single-lap direct shear tests and entails for a non-pure Mode-II condition at the composite-substrate interface (Figure 3.3a(i)), which may affect the test response [66]. The presence of interface normal stress components that tend to open the interface crack, was observed at the ends of FRP-strengthened RC beams and was postulated to be responsible of the plate end debonding failure [67]. To balance the eccentricity between the forces applied to the bonded strips and substrate [68], double-lap direct shear test set-up were introduced (Figure 3.3a(ii)). This test set-up entails for a symmetric strengthening with two equal composite strips on opposite sides of the same substrate block. The loose ends of the bare textile portion, fighting out of the two composite strip loaded ends, are clamped by the testing machine and pulled simultaneously. Specific clamping devices are used to keep the bare portion of textile aligned with the matrix-fiber interface plane, throughout the test. In double-lap shear tests, the symmetric pull of the two composite strip limits the out-of-plane action on the composite, but the randomly distributed properties of materials and interfaces lead to a non-uniform stress redistribution among the two composite strips and, accordingly, debonding does not occur and propagate symmetrically in the specimen [62]. Therefore, results of double-lap direct shear tests are expected to provide a lower bound measure of the composite bond capacity and global slip [54]. However, it was observed that, on FRCM-substrate joints, due to the beneficial confining effect of the matrix layer that covers the fiber textile, the Mode I loading condition of single lap direct shear test have a limited influence [69].

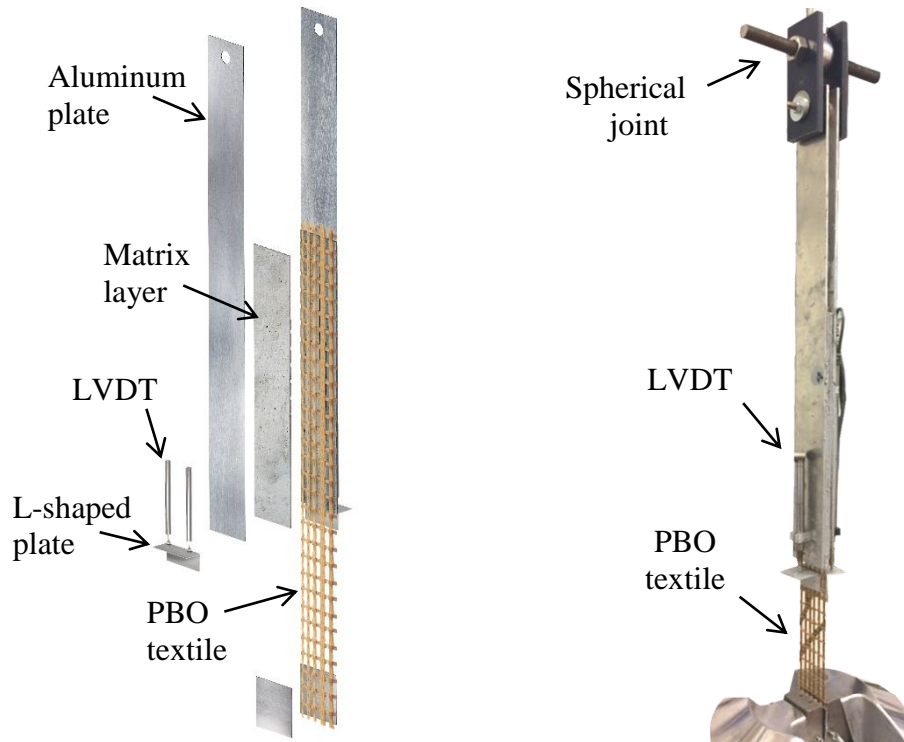


Figure 3.5: Exploded view and photo of the pull-out test set-up.

Direct shear test of FRP-masonry substrates exhibited a  $\sigma$ - $g$  response which was affected by the presence of mortar joints between the bricks in the substrate block [70]. Indeed, failure of FRP-masonry joints usually occurs within a thin layer of the substrate and the difference between the properties of brick and mortar affects the composite bond behaviour [71]. Since debonding of FRCM specimens comprising one layer of textile reportedly occurs at the matrix-fiber interface with high relative slippage between fiber and embedding matrix (see Figure 3.1a and Figure 3.2)[62], the presence of the mortar joints does not affect the composite bond behaviour, provided that failure does not involve the substrate. Accordingly, alternative simple pull-out test set-ups were recently proposed (Figure 3.5)[59] which allows to get rid of the substrate part of the specimen. Since failure is expected to not involve the substrate, the block is replaced by two aluminum plates, attached on the opposite faces of a composite strip using epoxy resin (see Figure 3.3a(iii) and Figure 3.5). The aluminum plates were connected to the testing machine through a spherical joint while the bare textile end was gripped by the machine wedges and pulled to induce debonding in the specimen. The pull-out test set-up allows for investigating the effect of the bonded length limiting the presence of fracture mechanics Mode-I loading conditions.

### 3.1.2 Beam test set-ups

In direct test set-ups, the FRCM-substrate interface is mainly subjected to a fracture mechanics Mode-II loading condition (see Figure 3.3). However, when the composite material is applied to curved substrates, such as arches or vaults, the member geometry entails for a combined presence of shear and normal stresses at the composite-substrate interface [55]. The effect of the non-pure Mode-II loading condition on the bond behavior of externally bonded composites was investigated using direct shear tests of FRP- and FRCM-masonry joints with curved substrates [72,73]. Similarly, in FRCM-strengthened RC members subjected to bending, the member cross-section curvature determines the presence of a stress component orthogonal to the FRCM textile plane, which may result in a bond behaviour different from that observed in direct shear tests. The interface capacity decreases when the normal stresses induce a Mode-I loading condition, whereas it may increase when the normal stresses are directed toward the support [66].

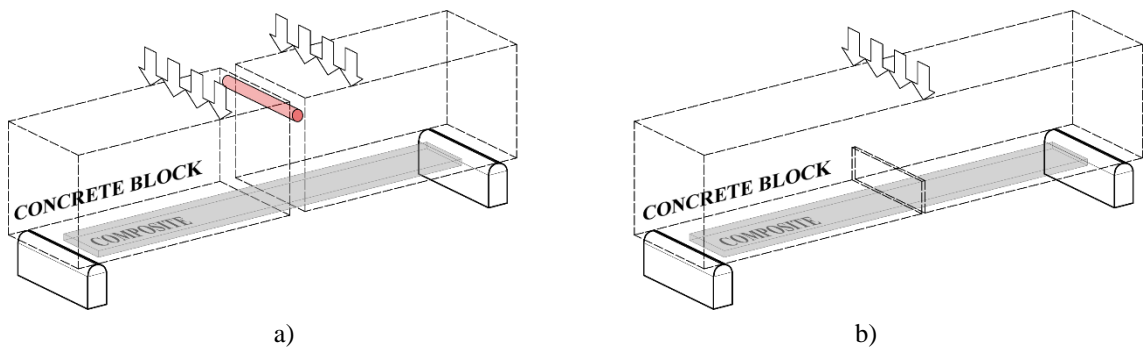


Figure 3.6: indirect test set-ups: a) modified or hinged beam test; b) notched beam test.

To investigate the effect on the FRCM bond behaviour of bending moment, flexural deflection and orthogonal stress to the composite plane, small-scale beam tests can be adopted (Figure 3.6), in which the tensile action is indirectly applied to the composite through a flexural scheme. Besides, differently from direct set-ups, in which the axial force at each position of the composite strip is only function of the applied load and of the bond properties of the substrate-matrix-fiber pairing, in modified beam test of FRCM applications it is also affected by the bending moment and shear force, which varies along the beam as a function of the applied loads. Furthermore, in the push-pull direct shear test configuration (the most widely adopted) the substrate block is subjected to a uniform compression, as a result of the block restraining (push), while the composite is subjected to tension through the testing machine action (pull). Differently,

in beam test set-ups, the substrate member is partially compressed and tensed, depending on the neutral axis position, resulting in the presence of tensile stresses at the interface with the FRCM strip (applied on the beam tension side).

Among the various beam test set-ups, two principal models have been reported in the literature: i) in the modified beam test (see Figure 3.6a), two prisms made of concrete or masonry (depending on the substrate of interest) are connected by a steel element that functions as a cylindrical hinge. The FRCM composite strip is applied to the face of the two prisms opposite to the steel hinge and the assembly is then tested in a three- or four-point bending test set-up. However, quite limited results are available regarding beam tests aimed at studying the FRCM-concrete behaviour, whereas more contribution can be found on the behaviour of the FRCM-masonry interface due to the significant normal stress component that may arise where cracks in masonry members occur [74]. ii) In the notched beam test (Figure 3.6b), a single substrate prism is tested in a three-point bending test set-up [75]. The prism is notched similarly to a fracture mechanics test specimen. The FRCM composite strip is then applied to the face of the prism where the notch mouth is located, i.e. perpendicular to the faces of the notch.

In both modified and notched beam set-ups, the specimen midspan deflection induces the development of normal stresses to the composite plane, throughout the test. This determines the establishment of a non-pure Mode-II loading condition, which has been shown to affect the specimen's response, with substantial increase in its bond strength (see chapters 5, 4 and 6). Although attempts were made to relate the results obtained by direct shear tests with those of corresponding masonry panels and RC beams, strengthened with inorganic composites and subjected to flexural tests [21,76], the relationship between direct shear tests and modified and notched beam tests still needs to be investigated.



### 3.2 Relevance of FRCC bond capacity according to Italian regulation standards

The tensile behaviour of inorganic matrix composites discussed in section 2.2.1, may not be enough to fully characterize the mechanical behaviour of externally bonded FRCC applications. Indeed, several failure mechanisms involve the loss of adhesion of the composite from the substrate, at different interfaces (see Figure 3.1).

For this reason, the Italian acceptance criteria for FRCC composites [35] included the evaluation of the composite-substrate bond properties within the mechanical characterization procedure. Accordingly, a standardized direct-shear bond test procedure was defined with the threefold objective of: (i) identifying the debonding failure mode of the specific FRCC-substrate joint; (ii) evaluating the maximum bond strength of the FRCC application; (iii) determining adequate stress and strain values to adopt for the design procedure, which involve the system bond properties. On this purpose, a specific stress level, referred to as conventional limit stress ( $\sigma_{\text{lim,conv}}$ ), was defined, which represented the characteristic bond strength of the FRCC-substrate joint, evaluated through bond tests (i.e. the average peak stress minus two times the standard deviation). The conventional limit stress is not a property of the FRCC material, but it depends on the specific substrate typology. It is obtained by dividing the characteristic value of the peak load, obtained through direct-shear testing (see Figure 3.7b), by the area of fiber.

The conventional limit strain,  $\varepsilon_{\text{lim,conv}}$  is obtained comparing the response of direct-shear test with that of corresponding tensile test on bare textile (Figure 3.7), and is computed according to Eq. (3.1), where  $E_f$  is the elastic modulus of bare textile.

$$\varepsilon_{\text{lim,conv}} = \frac{\sigma_{\text{lim,conv}}}{E_f} \quad (3.1)$$

In [13], the results of a wide round robin table (RRT) experimental campaign, focused on the tensile and bond characterization of inorganic matrix composites, are presented. The comparison between tensile test results with that of corresponding bond test, allowed shedding light on the tensile strength exploitation at bond failure. Results showed that the exploitation ratio may range from 27% to 96% for a same FRCC material, as a function of the interaction between textile and matrix and between composite and substrate, and so of the debonding mode. The highest value is typically associate with tensile rupture of fibers during bond test (e.g. glass or basalt). FRCC

system including carbon and PBO, whose failure mode included telescopic failure, showed exploitation ratios in the range 47-53% and 46%, respectively.

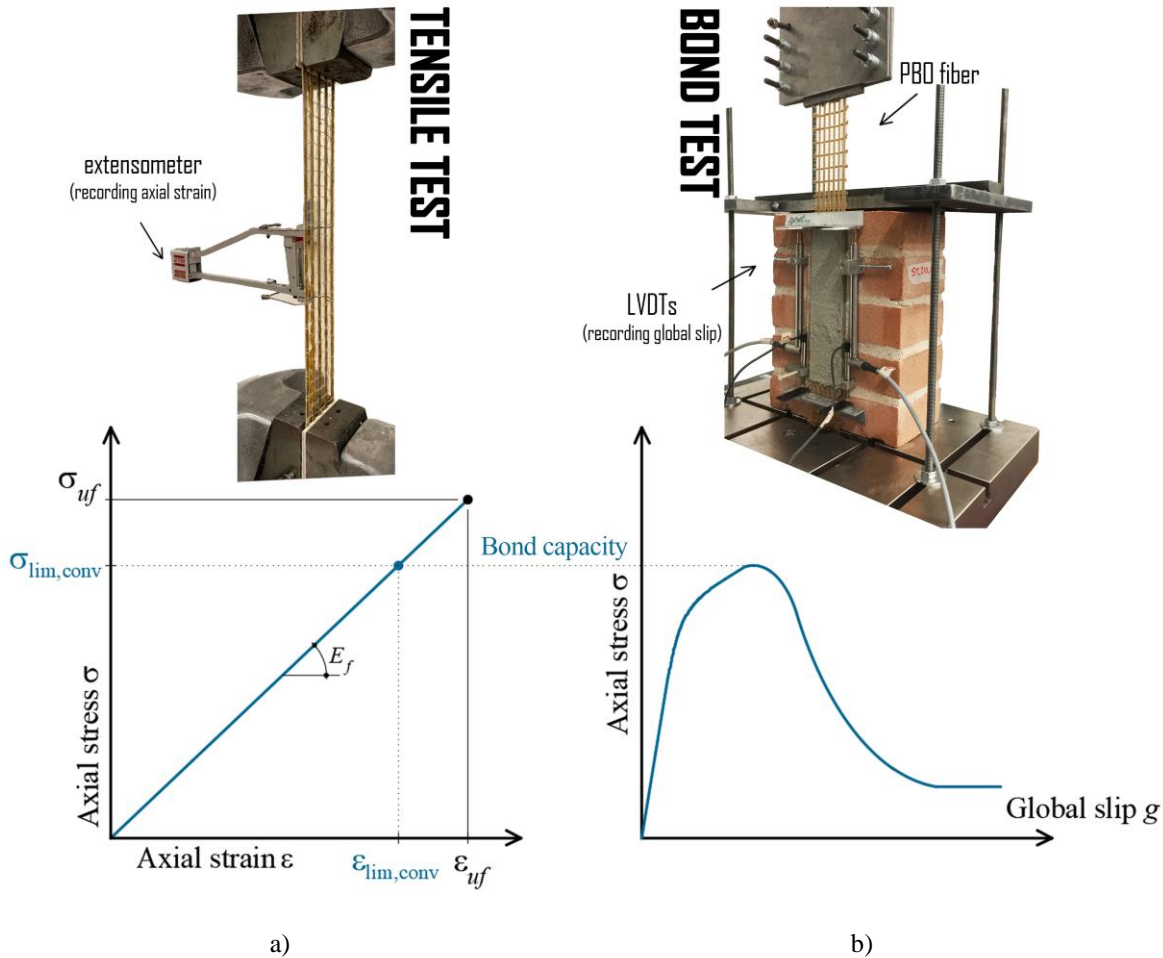


Figure 3.7: Conventional limit stress of FRCC composites [35]. a) Tensile stress - strain curve; b) tensile stress - global slip curve.

The use of the conventional limit stress, and corresponding strain, allow to design strengthening intervention which prevent the element from failing by composite debonding for all the cases in which, due to the weak impregnation capability of the cementitious embedding matrix, the telescopic or composite-substrate debonding is allowed. Partial safety factors and conversion factors, shall be applied to these values [35]. In the situations governed by the tensile strength of the textile rather than by the debonding of the FRCC system or by the slippage of the textile within the matrix, the values of the parameters to be adopted in design problems are the ultimate strain of the dry textile and the corresponding ultimate stress.

### **3.3 Experimental study of the effect of loading rate on the bond behaviour of FRCM and SRG composites applied to concrete substrate**

The great popularity achieved by FRCM composite in recent years, oriented national legislators and public research institutions toward the production of guidelines and technical documents to regulate the design and the acceptance criteria for the use of those materials to strengthen and retrofit masonry and RC structures. Since it has been established that bond is a crucial parameter to determine the effectiveness of FRCM applications (see Section 3.1), bond tests are often required by regulatory standards to evaluate the FRCM-substrate bond capacity, for each specific application [35]. For this purpose, the push-pull single-lap direct-shear test configuration is commonly adopted due to the simplicity in specimen preparations and the easiness (eventually also on-site) of test execution.

One of the principal parameters in the execution of displacement-controlled direct-shear tests is the displacement rate at which the test is performed. Different control types may be adopted to govern a single-lap direct-shear test, such as the machine stroke rate control, the global slip rate control and strain rate control. The stroke rate control consists in the definition of a constant speed of the machine stroke during the test. The global slip rate control requires instead the use of linear variable displacement transducers (LVDT) to record the global slip during the test. The strain rate control requires a measure of the composite elongation during the test. In all cases, the implemented control system will adapt the applied displacement to produce a monotonic stroke, global slip or strain increase at a constant rate. It should be noted that, in general, a constant stroke rate might not imply a constant strain or global slip rate.

In the Italian acceptance criteria for FRCM composites [35] a 0.2 mm/min stroke rate is suggested, whereas the US acceptance criteria for FRCM composites [77] does not provide for the execution of bond test, however a standard stroke rate of 0.2 mm/min is recommended for the execution of tensile tests on FRCM coupons.

The rate at which direct-shear test is performed may influence the test response of composite reinforced specimens. Studies conducted by [78,79] indicate that the strain rate has an influence on bond capacity, maximum interfacial stress and interfacial fracture energy of BFRP-concrete joints. In [75] the influence of testing rate on the

response of a PBO FRCM composite applied to a concrete substrate was investigated. Results showed that certain rates of global slip influence both the initial stiffness and the bond capacity.

In this section, the influence of the machine stroke rate on three inorganic composites, namely a PBO FRCM, a Carbon FRCM and a SRG composite, was experimentally investigated. Different parameters of the specimen responses were compared to capture the effect of testing rate, such as the bond capacity (i.e. maximum load) and the corresponding slip, the residual stress, the amplitude of the post peak stage and the global slip at failure.

### 3.3.1 Materials

Two FRCM and one SRG systems were investigated in this study. The two FRCM systems employed a bidirectional PBO and Carbon fiber textile, respectively, embedded with two different cement-based mortars, whereas the SRG composite was comprised of a unidirectional galvanized high-strength steel fiber textile combined with a geopolymer mortar.

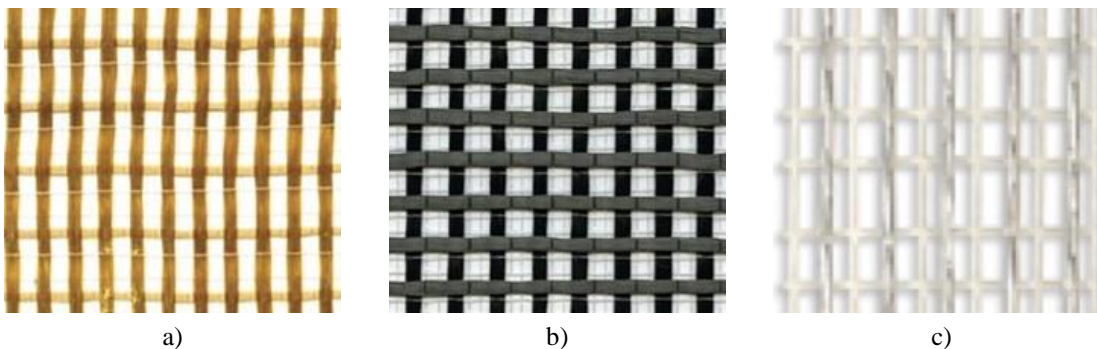


*Figure 3.8: textile grids geometry: a) PBO, b) carbon, c) steel.*

The bidirectional PBO textile (Figure 3.8a) employed in the PBO-FRCM composite was unbalanced, with longitudinal yarns (i.e. in the load direction) spaced at 10 mm on centre and transversal yarns (i.e. 90° inclined with load direction) spaced at approximately 17,5 mm on centre [80]. Besides, a bidirectional balanced textile was employed in the C-FRCM composite (Figure 3.8b), with both longitudinal and transversal yarns spaced 10 mm on centre [81]. Finally, unidirectional galvanized steel textile (Figure 3.8c) was used, with strands spaced at 7.5mm [82]. Table 3.1 reports the width ( $b_f$ ), thickness ( $t_f$ ), area ( $A_f$ ) and number ( $n$ ) of single yarns of the three textiles, along with the tensile strength  $f_f$ , ultimate strain  $\varepsilon_f$ , and elastic modulus  $E_f$  of the corresponding bare textile, obtained by tensile tests, for PBO and carbon [49,54], or

provided by the producer in the case of steel fibers. Different cement-based matrix were employed for PBO and carbon FRCM composite and their compressive strength ( $R_{c28}$ ) is reported in Table 3.1, along with that of the geopolymer mortar employed in SRG, as provided by the producers [25,26,83].

Composite	$b_f$ [mm]	$t_f$ [mm]	$A_f$ [mm <sup>2</sup> ]	$n$ [-]	$f_f$ [MPa]	$\varepsilon_f$ [-]	$E_f$ [GPa]	$R_{c28}$ [MPa]
PBO-FRCM	5	0.092	0.46	6	3014	0.0145	206	40
C- FRCM	5	0.084	0.42	6	1944	0.0095	203	40
SRG	-	-	0.538	9	3000	-	190	50

*Table 3.1: FRCM and SRG materials properties.*

The composite materials were comprised of a single layer of textile embedded within two 5 mm thick layers of matrix, which entail for an overall composite thickness of 10 mm. The composite strips were bonded to the lateral surface of a concrete prism with dimensions 150×150 mm (cross-section) ×500 mm (length). The average compressive strength of the concrete blocks was determined by testing six 150 mm -edge cubes and was 37.9 MPa (coefficient of variation, CoV, equal to 6.02%). The average concrete tensile strength, obtained from splitting tests of 5 100 mm × 200 mm cylinders, was 2.50 MPa (CoV=18.40%). Prior to applying the composite strip, the substrate was roughened using a grinder and then thoroughly cleaned from dust with compressed air. Additionally, the substrate was wet using water few minutes before the application. A first matrix layer was applied directly to the block surface using rectangular formworks, which allows maintaining a constant 5 mm thickness for the layer. The textile net was then embedded on the matrix layer, and pushed against it to guarantee good impregnation. Finally, the second matrix layer was applied and the strip was left for a 28 days curing time in a 90% controlled humidity environment.

### 3.3.2 Experimental set-up and procedures

Twenty-seven specimens were tested using a single-lap direct-shear test set-up, 9 strengthened with PBO-FRCM, 9 with C-FRCM and 9 with SRG. Specimens consisted of a 450 x 60 mm composite strip, 10 mm thick, which includes  $n = 6$ , 6 and 9 bundles (see Table 3.1), for the PBO, carbon and steel textile, respectively. A portion of textile was left bare beyond the bonded area at the loaded end, for a length  $l_b=250$  mm (Figure 3.9a). A 50 mm bare textile length was also considered at the free-end of the composite strip. L-shaped aluminum plates were attached to the bare textile just outside the bonded

area at both the loaded- and free-end to allow a direct measurement of the fiber-matrix relative displacement throughout the test. The strip loaded end (Figure 3.9a) was located 30 mm apart from the prism edge to prevent the support edge rupture throughout the test.

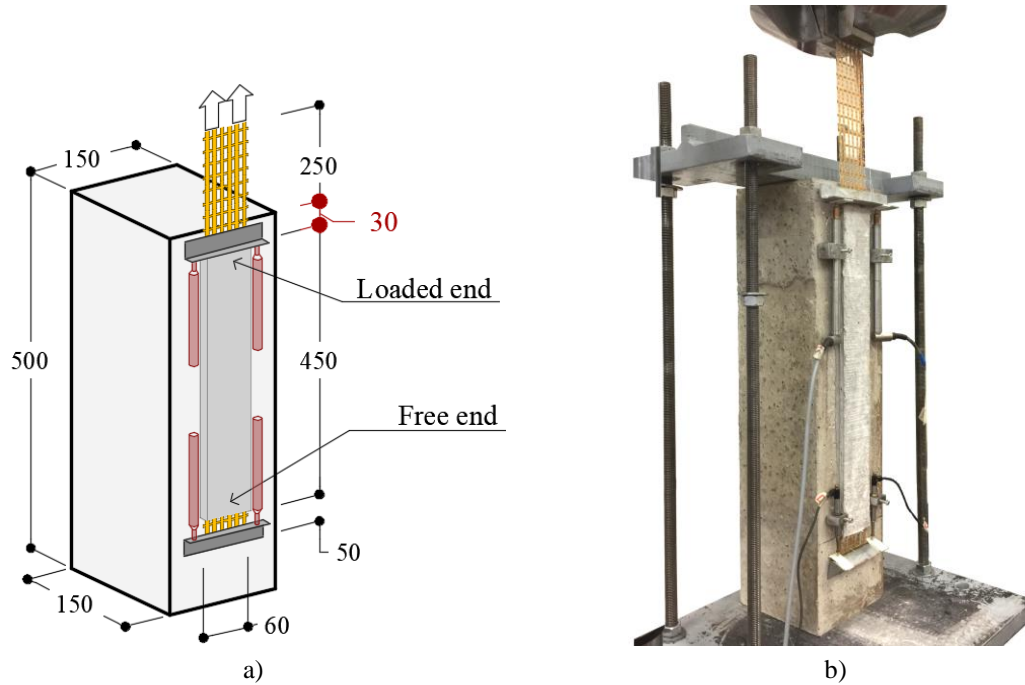


Figure 3.9: a) specimen geometry (dimensions in mm); b) test set-up.

The block was restrained to the testing machine using a rigid steel frame (see Figure 3.9), whereas the pulling action was directly applied to the bare fibers outside the specimen's loaded end through a displacement-controlled input, which entails for a constant motion of the machine piston at a given rate. Simultaneously, the applied load was recorded by a 250 kN load cell, of which the machine piston was equipped. Thin steel plates were attached to the bare textile end using epoxy resin, to promote an effective and uniform machine gripping. The displacements of the L-shaped plates with respect to the concrete prisms were measured by 4 LVDTs attached to the concrete substrate on the side of the composite strip, one pair at the loaded end and one pair at the free end (Figure 3.9a).

To investigate the effect of loading rate on the debonding process of the tested specimens, three rates were used to control the machine stroke displacement:

- $v_s = v1 = 0.04 \text{ mm/min}$  (0.00067 mm/s);
- $v_s = v5 = 0.20 \text{ mm/min}$  (0.00333 mm/s);
- $v_s = v10 = 0.40 \text{ mm/min}$  (0.00667 mm/s);

respectively corresponding to 1/5, 1 and 2 times the loading rate suggested by the Italian guidelines for the displacement (stroke) control [35].

### 3.3.3 Results

Specimens were named according to the notation DS\_*t*\_X\_Y\_νN\_*n*, where DS stands for the adopted test set-up (direct shear), *t* indicates the material (C=carbon FRCM, P=PBO FRCM, S=SRG), X and Y are the bonded length and width, respectively, (in mm), νN indicates the test rate (N=1, 5 or 10) and *n* is the specimen serial number.

Figure 3.10a and b show the typical axial stress  $\sigma$  - global slip  $g$  response for the FRCM and SRG composites, respectively, where  $g$  is the average of the two LVDT readings at the loaded-end and  $\sigma$  is computed according to the equation:

$$\sigma = \frac{P}{n \cdot A_f} \quad (3.2)$$

where  $P$  is the force applied by the testing machine,  $n$  and  $A_f$  are the number of fiber yarns and the corresponding transversal area, respectively (see Table 3.1). Figure 3.10a also reports  $s_F$ , which is the average of the two LVDT reading at the composite free-end.

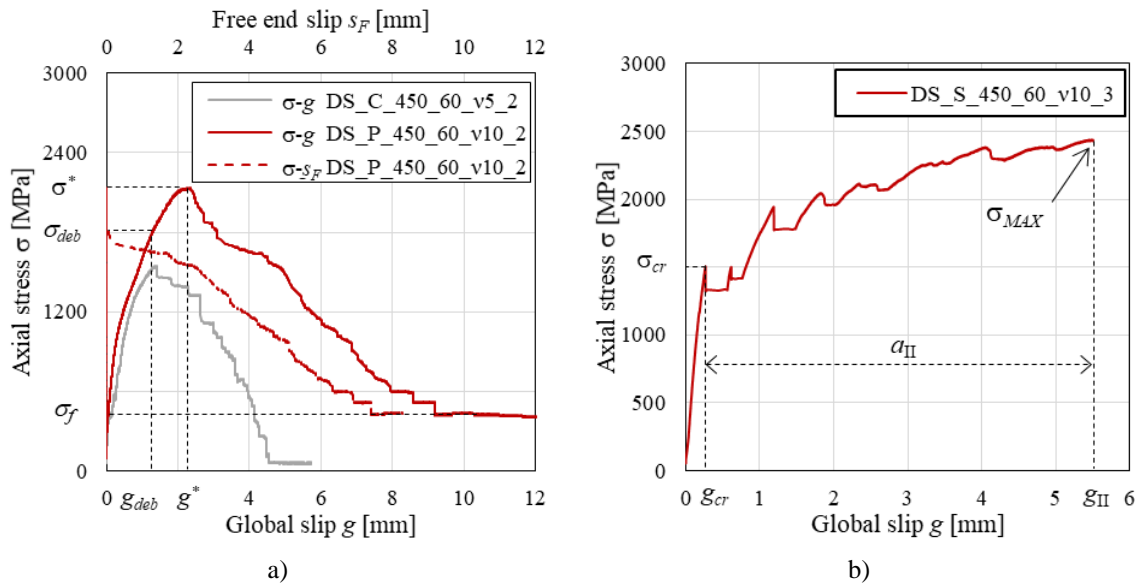


Figure 3.10: Typical axial stress - global slip curves: a) PBO- and C-FRCM; b) SRG.

Failure of all PBO- and C-FRCM specimens was due to debonding at the matrix-fiber interface, with high slippage between fiber and the surrounding matrix. Only in two cases, C-FRCM specimens DS\_C\_450\_60\_ν1\_1 and DS\_C\_450\_60\_ν10\_3 failed due to textile rupture at the specimen's loaded-end (see Figure 3.12a). The stress responses

of specimens strengthened with the two FRCM materials (either CFRCM or PBO FRCM), which exhibited matrix-fiber interfacial debonding, were qualitatively similar, with an initial linear branch associated with the interface elastic behaviour, which ended once the matrix-fiber interface start developing softening in the portion closer to the strip loaded end, and a change in the curve's slope was recorded at this point. With increasing the applied displacement, the curve's slope reduction becomes more evident due to the propagation of softening and micro-cracking at the matrix-fiber interface, until the interfacial stress transfer mechanism between fiber and matrix was fully established, and the debonding stress  $\sigma_{deb}$  was approached, in correspondence with a global slip  $g_{deb}$ . At this point debonding established at the specimen's loaded end, corresponding with the formation of one interfacial crack at the fiber-matrix interface. Some specimens exhibited the formation of localized transversal cracks along the strip length (i.e. normal to the load direction) during this stage. Beyond  $\sigma_{deb}$ , an almost linear increase in the response was recorded, due to friction and interlocking between fiber and matrix along the debonded length. The extent of this branch of the response is related with the length of the bonded area ( $L=450\text{mm}$ ). At the end of this stage, the specimen's bond capacity,  $\sigma^*$ , was reached, corresponding with the attainment of the global slip  $g^*$ . From this point, the propagation of debonding in the matrix-fiber interface determined a reduction in the specimen's bond stress, which eventually plateaued at a constant stress value,  $\sigma_f$ , associated with pure friction between fibers and matrix. According to what discussed in section 3.1 (see Figure 3.4), the residual stress  $\sigma_f$  was computed as the average applied stress at the end of the test for which the derivative  $d\sigma/dg$  was comprised within the range  $-150$  and  $0$  MPa/mm. In correspondence with the attainment of  $\sigma^*$ , LVDT reading at the composite strip free end  $s_F$  was recorded. It must be noted that, in some cases, a delay in the  $s_F$  reading with respect to the peak stress attainment was registered. This is attributed to a non-uniform free-end slippage of the different yarns, which led to a discordant reading of the two LVDTs reacting off of the L shaped plate bonded outside the free-end. The  $\sigma - s_F$  curve of specimen DS\_P\_450\_60\_v10\_2 is shown in Figure 3.10a.

Figure 3.11 reports the axial stress,  $\sigma$  - global slip,  $g$ , responses for FRCM strengthened specimens (see also Table 3.2). Test DS\_P\_450\_60\_v1\_3 was prematurely interrupted due to a breakdown of the testing machine, whereas the results of test DS\_C\_300\_60\_v5\_1 were disregarded from this analysis due to incoherent testing machine settings.



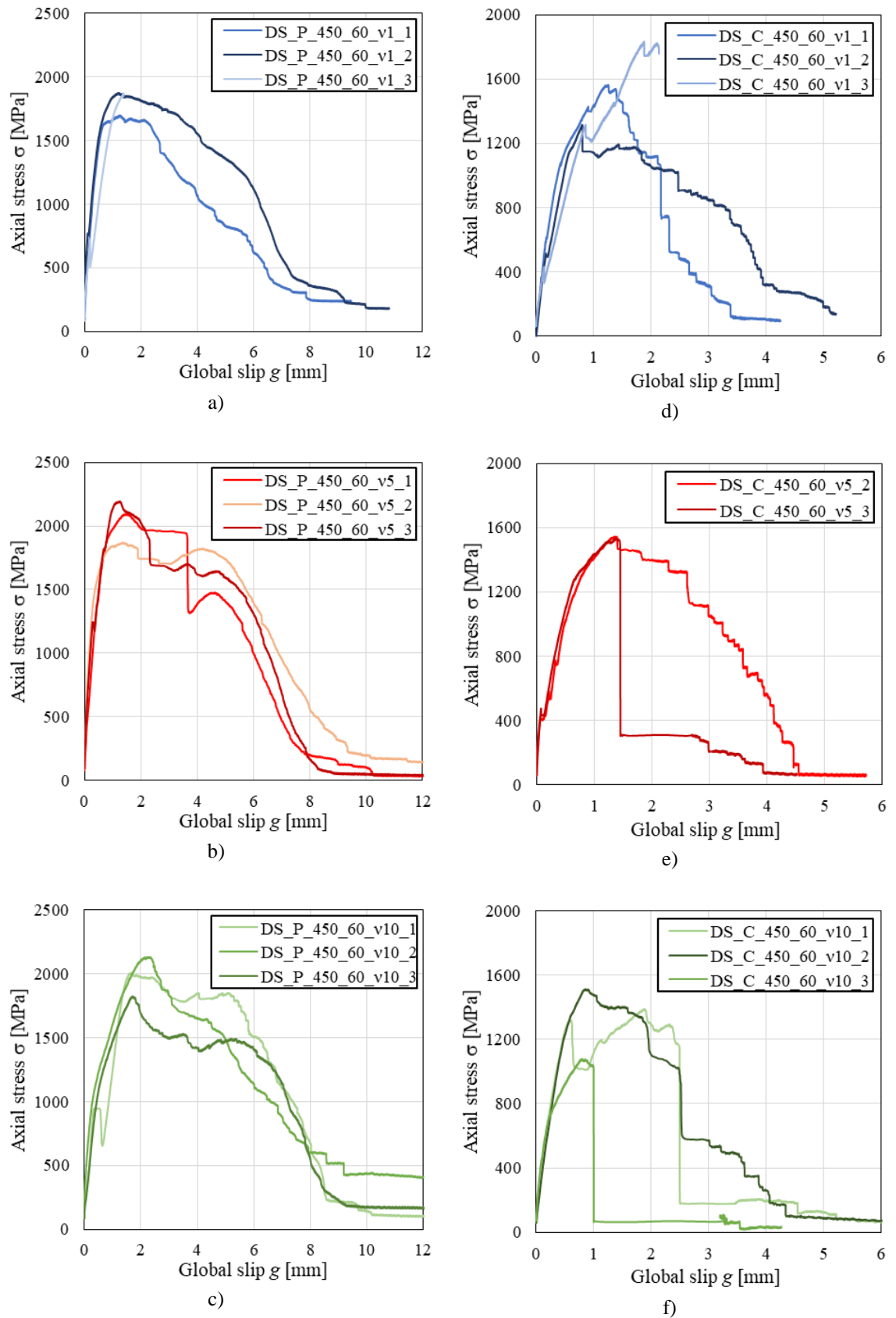
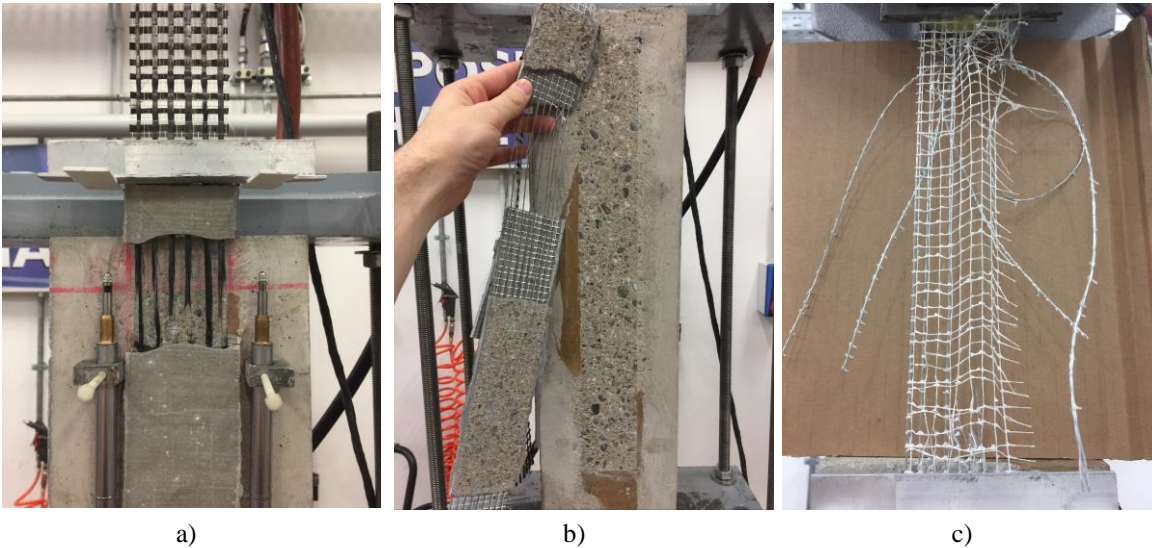


Figure 3.11: Axial stress,  $\sigma$  - global slip,  $g$ , curves for PBO FRCM - a)  $v_s=V1$ ; b)  $v_s=V5$ ; c)  $v_s=V10$ ; and C FRCM - d)  $v_s=V1$ ; e)  $v_s=V5$ ; f)  $v_s=V10$  - specimens.

SRG-strengthened specimens failed according to different failure modes. In the majority of the cases, delamination at the internal-external matrix layer interface was recorded, with splitting of the internal-external matrix layers, often combined with partial or total debonding of the composite strip from the substrate (see Figure 3.12b). All specimens exhibited yielding of steel filaments in the portion of bare textile just outside the composite prism, however, in specimen DS\_S\_450\_60\_v5\_1 this led to the complete rupture of the steel strand, which determined the specimen failure (see Figure 3.12c).



*Figure 3.12: Failure modes of C-FRCM- and SRG-strengthened specimens: a) textile failure; b) internal-external matrix layer interface delamination combined with debonding from substrate; c) strands rupture outside the bonded length.*

Two main stages, an ascending branch and a subsequent horizontal or slightly increasing branch, characterize the typical  $\sigma$ - $g$  response (Figure 3.10b). The ascending branch was associated with the establishment of the stress transfer mechanism and the response was almost linear due to the elastic behaviour of matrix and to its high interlock with steel strands. This stage ended with a sudden stress drop in the  $\sigma$ - $g$  curve, in correspondence with the axial stress value  $\sigma_{cr}$ , which corresponded with a global slip  $g_{cr}$  (see Figure 3.10b). The load drop at the end of the linear branch can be associated with the matrix-fiber interface bond crisis attainment at the loaded-end (corresponding with an average matrix stress of 11.5 MPa, Table 3.3). In some case, the loss of strength corresponding to  $\sigma_{cr}$  was less abrupt, due to a more gradual propagation of the interface failure. In all cases, transversal micro-cracks were visible in the matrix external layer, prior to the attainment of  $\sigma_{cr}$ , however, this affected slightly the linearity of the curve's initial branch, due to a strong interlocking between steel mesh and matrix.

The opening of the interfacial crack determines the shift from the first ascending branch to a second post-linear branch, which is associated with the propagation of the interface crack from the loaded- to the free-end of the specimen. The maximum stress  $\sigma_{MAX}$ , can either be attained at the end of the ascending branch (i.e.  $\sigma_{MAX} = \sigma_{cr}$ ) or in the sub horizontal stage of the response. This stage ended suddenly with the onset of local or partial delamination/debonding, and its amplitude,  $a_{II}$  in Figure 3.10b, depends on the extent of the interfacial crack propagation. The global slip corresponding with failure was indicated with  $g_{II}$  in Figure 3.10b. In no cases free-end readings were recorded, this is due to the strong interlocking between steel strands and matrix, which prevented any telescopic mechanisms and led to the composite loss of effectiveness before the stress transfer zone attained the free-end. Figure 3.13 collects  $\sigma - g$  responses for SRG strengthened specimens.

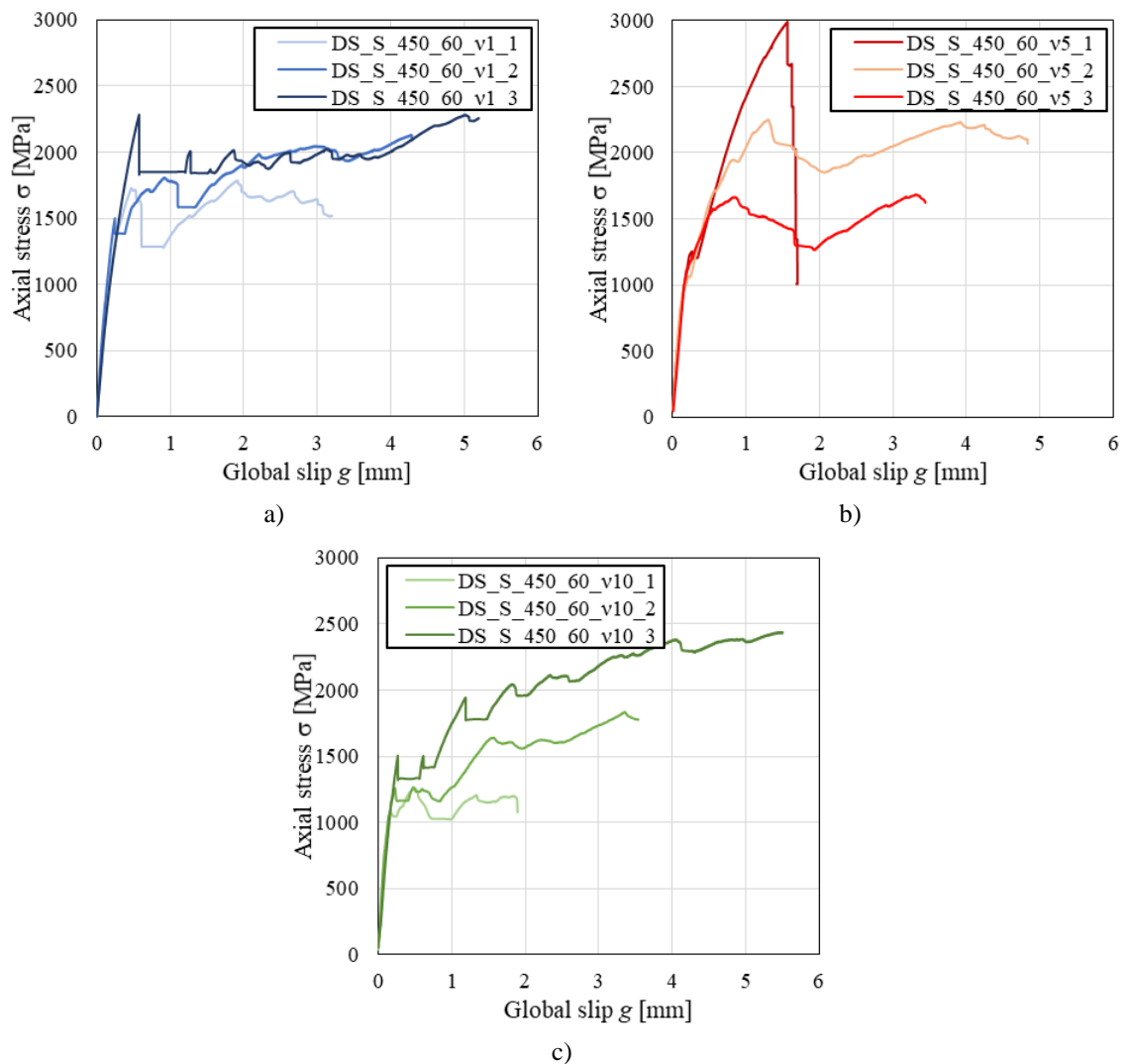


Figure 3.13: Axial stress,  $\sigma$  - global slip,  $g$ , curves of SRG specimens: a)  $v_s=V1$ ; b)  $v_s=V5$ ; c)  $v_s=V10$ .

Key parameters obtained from direct shear testing of FRCM and SRG strengthened specimens are reported in Table 3.2 and Table 3.3, along with average values of nominally equal specimens and corresponding coefficient of variation (CoV)(Figure 3.10). Key parameters for FRCM strengthened specimens include the debonding stress  $\sigma_{deb}$ , corresponding global slip  $g_{deb}$ , peak stress  $\sigma^*$  corresponding global slip  $g^*$  and residual friction  $\sigma_f$  (see Figure 3.10a). Key parameters for SRG strengthened specimens include the stress at the end of the ascending branch  $\sigma_{cr}$ , corresponding global slip  $g_{cr}$ , the maximum stress  $\sigma_{MAX}$ , the amplitude of the post-linear stage,  $a_{II}$  and the global slip at failure,  $g_{II}$  (see Figure 3.10b).

Specimen name	$\sigma_{deb}$ [MPa]	$g_{deb}$ [mm]	$\sigma^*$ [MPa]	$g^*$ [mm]	$\sigma_f$ [MPa]
DS_C_450_60_v1_1	1087	0.43	1563	1.25	108
DS_C_450_60_v1_2	1155	0.59	1314	0.79	134
DS_C_450_60_v1_3	1305	0.84	1832	1.97	-
Average	1182	0.620	1569	1.34	121
CoV [%]	0.094	0.333	0.165	0.443	0.152
DS_C_450_60_v5_1	-	-	-	-	-
DS_C_450_60_v5_2	1278	0.75	1544	1.35	68
DS_C_450_60_v5_3	1234	0.61	1534	1.39	74
Average	1256	0.68	1539	1.37	71
CoV [%]	0.025	0.146	0.005	0.023	0.060
DS_C_450_60_v10_1	1289	0.62	1388	1.88	86
DS_C_450_60_v10_2	1337	0.59	1512	0.85	99
DS_C_450_60_v10_3	987	0.60	1087	0.80	-
Average	1204	0.60	1326	1.18	92.5
CoV [%]	0.158	0.025	0.169	0.518	0.099
DS_P_450_60_v1_1	1642	0.88	1699	1.25	270
DS_P_450_60_v1_2	1710	0.7	1875	1.23	255
DS_P_450_60_v1_3	1780	1.15	1874	1.37	-
Average	1711	0.91	1816	1.28	262
CoV [%]	0.040	0.249	0.056	0.061	0.040
DS_P_450_60_v5_1	1869	0.77	2095	1.46	110
DS_P_450_60_v5_2	1749	0.66	1871	1.36	172
DS_P_450_60_v5_3	1835	0.74	2195	1.25	50
Average	1818	0.72	2053	1.36	111
CoV [%]	0.034	0.079	0.081	0.078	0.551
DS_P_450_60_v10_1	1799	1.33	2005	1.62	165
DS_P_450_60_v10_2	1854	1.39	2132	2.30	420
DS_P_450_60_v10_3	1673	1.36	1826	1.71	172
Average	1775	1.36	1988	1.87	252
CoV [%]	0.052	0.022	0.078	0.197	0.576

Table 3.2: Results of FRCM strengthened specimens.

Specimen name	$\sigma_{cr}$ [MPa]	$g_{cr}$ [mm]	$\sigma_{MAX}$ [MPa]	$a_{II}$ [mm]	$g_{II}$ [mm]
DS_S_450_60_v1_1	1716	0.48	1786	2.72	3.20
DS_S_450_60_v1_2	1498	0.24	2131	4.05	4.29
DS_S_450_60_v1_3	2284	0.57	2284	4.63	5.20
Average	1833	0.43	2067	3.80	4.23
CoV [%]	0.221	0.397	0.123	0.258	0.237
DS_S_450_60_v5_1	1253	0.26	2990	-	-
DS_S_450_60_v5_2	1087	0.26	2250	4.57	4.83
DS_S_450_60_v5_3	1164	0.23	1684	3.21	3.44
Average	1168	0.25	2308	3.89	4.14
CoV [%]	0.071	0.069	0.284	0.248	0.238
DS_S_450_60_v10_1	1069	0.16	1253	1.74	1.9
DS_S_450_60_v10_2	1255	0.22	1834	3.32	3.54
DS_S_450_60_v10_3	1504	0.27	2439	5.24	5.51
Average	1276	0.22	1842	3.43	3.65
CoV [%]	0.171	0.254	0.322	0.511	0.495

Table 3.3: Results of SRG strengthened specimens.

### 3.3.4 Discussion

Three machine stroke rates  $v_s$  were adopted in this experimental study to conduct direct-shear tests on FRCM and SRG strengthened concrete elements. In this section, the rate effect on the debonding stress  $\sigma_{deb}$ , peak stress  $\sigma^*$  and residual friction stress  $\sigma_f$  of FRCM strengthened specimens is analysed. Whereas for SRG strengthened specimens, the stress attained at the end of the ascending stage  $\sigma^*$  and the maximum stress  $\sigma_{MAX}$ , are adopted to evaluate the influence of testing rate on specimen's response. The rate effect on the displacement field (i.e. on the global slip) was also analysed to extend some considerations on the results scatter.

#### 3.3.4.1 Effect of loading rate on FRCM-strengthened specimens

Figure 3.14a ad b show the debonding stress  $\sigma_{deb}$ , peak stress  $\sigma^*$  and residual friction stress  $\sigma_f$  versus rate for tested specimens strengthened with PBO FRCM and carbon FRCM, respectively. A dashed line connecting the average values corresponding to each machine rate value is also reported to show the trend.

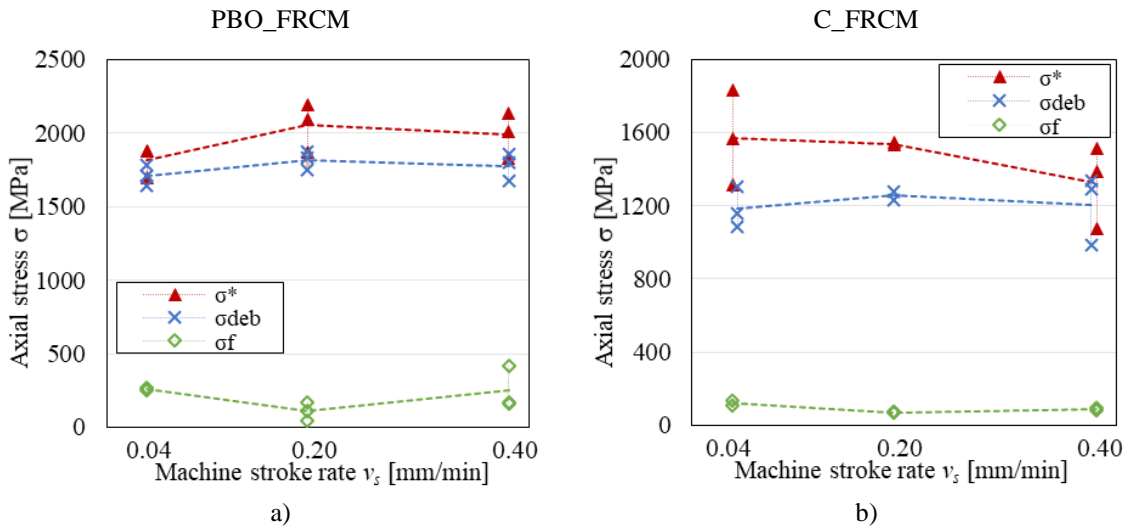


Figure 3.14: Rate effect on the stress field, for specimens strengthened with: a) PBO FRCM; b) Carbon FRCM.

Specimens strengthened with PBO FRCM (see Figure 3.14a) exhibited an average peak stress  $\sigma^*$  increase of roughly 13% as the rate increases from  $v_s=0.04$  to  $v_s=0.20$  mm/min. Whereas the specimen bond capacity remained almost constant with rate varying from  $v_s=0.20$  to  $v_s=0.40$  mm/min. This result is consistent with those presented in [75] on global slip controlled DS tests of PBO FRCM-concrete joints, which showed an increase in the maximum applied load as the global slip rate increased from  $v_g=0.025$  mm/min to  $v_g=0.15-0.25$  mm/min. From Figure 3.14a it is also noticeable that the average debonding stress,  $\sigma_{deb}$ , remained almost constant for the three stroke rates adopted (CoV = 0.030). Whereas a not clear trend in the residual friction stress  $\sigma_f$  versus rate relationship is recognizable from Figure 3.14, due to the high scatter in the results obtained by specimens tested at  $v_s=0.20$  and  $v_s=0.40$  mm/min (CoV = 0.55 and 0.58, respectively). Many factors affect the residual friction stress results variability, such as the matrix impregnation of yarn filaments, the evenness of stress and global slip distribution between the textile bundles, the fiber damaging due to friction throughout the test and presence of normal stress at the matrix-fiber interface (i.e. Mode-I loading) due to out-of-plane movement of the specimen during the test [75].

Carbon FRCM strengthened specimens (Figure 3.14b) showed a decreasing trend in their  $\sigma^*$  -  $v_s$  relationship. Accordingly, the peak stress of C\_FRCM specimens tested under a machine stroke rate of  $v_s=0.04$  mm/min was almost constant with that exhibited by nominally equal specimens subjected to a  $v_s=0.20$  mm/min testing rate, whereas it was 18% higher than that of  $v_s=0.40$  mm/min rate specimens. As well as for PBO FRCM specimens, also Carbon FRCM recorded almost constant values of debonding

stress  $\sigma_{deb}$  with machine stroke rate  $v_s$  increase, whose overall CoV. was equal to 0.031. Due to the premature failure of specimens DS\_C\_300\_60\_v1\_1 and DS\_C\_300\_60\_v10\_3, a proper evaluation of the rate effect on the residual friction stress  $\sigma_f$  cannot be identified. Specimens tested under  $v_s=0.20$  mm/min machine stroke rate showed a relatively reduced scatter in their results (CoV.  $\sigma_{deb}$ ,  $\sigma^*$  and  $\sigma_f$  respectively equal to 0.025, 0.005 and 0.060).

#### 3.3.4.2 Effect of rate on SRG-strengthened specimens

Figure 3.15a shows the trends of peak stress at the end of the ascending stage  $\sigma_{cr}$  and maximum stress  $\sigma_{MAX}$  versus rate, for specimens strengthened with SRG composite. The specimen bond strength  $\sigma_{MAX}$  assumed a maximum average values at the machine stroke rate of  $v_s=0.20$  mm/min. A lower rate ( $v_s=0.04$  mm/min) produced a decrement in  $\sigma_{MAX}$  of 10%, with respect to that of  $v_s=0.20$  mm/min specimens. Whereas a higher rate ( $v_s=0.4$  mm/min) resulted in the least values of bond strength, 20% lower of those exhibited by nominally equal specimens tested at  $v_s=0.2$  mm/min. It should be also reported that a relatively high scatter in the result was registered (see Table 3.3), which can be motivated by uneven distribution of applied pulling force among the steel strands. However, the use of a lower machine stroke rate ( $v_s=0.04$  mm/min) allowed a significant reduction in the results scatter of  $\sigma_{MAX}$ , which was 57% lower than that recorded by  $v_s=0.2$  mm/min rate specimens. This can be attributed to a more effective stress redistribution mechanism among steel strands, promoted by the lower testing rate.

Figure 3.15b depicts the rate effect on the displacement field of direct shear tested specimens, strengthened with SRG. Specimen tested at lower rate values ( $v_s=0.04$  and  $v_s=0.20$ ) exhibited higher amplitudes of the sub-horizontal stage  $a_{II}$  (see Figure 3.10b) which can be associated to a better redistribution of stress mechanism among the steel strands, after matrix cracking. A higher stroke rate value ( $v_s=0.40$  mm/min) led to the lowest average value of  $a_{II}$ , which was roughly 13% lower than both the lower stroke rates. A similar trend was recorded in the  $g_{II}$  versus rate relationship, which showed a gradual reduction of the average global slip value corresponding with failure with the increase of rate. Specimens tested under  $v_s=0.40$  mm/min machine stroke rate showed the highest scatter in the measured result (see Table 3.3) for both  $a_{II}$  and  $g_{II}$ .

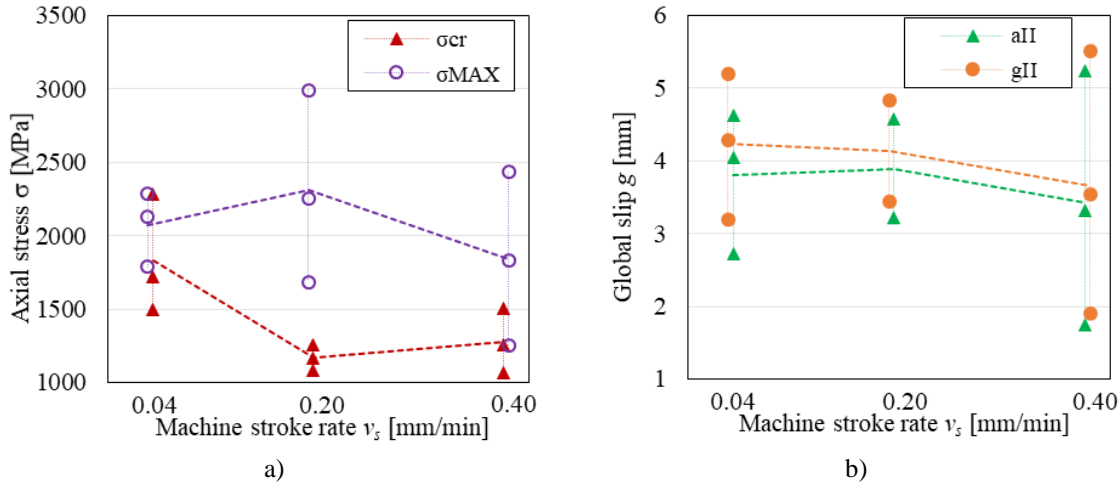


Figure 3.15: Rate effect on the (a) stress and (b) displacement field, for specimens strengthened with SRG

### 3.3.4.3 Remarks on the control type

In direct shear test performed under machine stroke rate control, the testing machine piston applies a monotonic displacement to the loaded end of the specimen (see Figure 3.9b). The elastic strain of the bare textile portion between the clamping device and the loaded end  $l_b$ , determines a variation in the global slip rate with the ongoing of the test. Figure 3.16 shows the experimental variation of global slip rate  $v_g$  with the global slip  $g$  of PBO strengthened specimens tested at constant machine stroke rates  $v_s$ . The horizontal dashed lines identifies the adopted machine stroke rates ( $v_s=0.04$ ,  $v_s=0.20$  and  $v_s=0.40$  mm/min), whereas a grey area (peak strength zone, PSZ) collects the global slip values  $g^*$  at which the peak strength of the analysed specimens was reached (see Table 3.2).

Before the reaching of the response peak (i.e. for  $g < g^*$ , see Table 3.2) and under the hypothesis of rigid support and neglecting the machine head deformation, the drift between the machine stroke rate  $v_s$  and the global slip rate  $v_g$  is mainly accountable to the axial elongation of fiber along the bare portion  $l_b$ , according to Eq. (3.3):

$$v_s = v_g + v_\varepsilon \quad (3.3)$$

with  $v_\varepsilon$  being the axial elongation rate, evaluated as:

$$v_\varepsilon = \frac{\varepsilon l_b}{t} \quad \left[ \frac{m}{sec} \right] \quad (3.4)$$

The elastic strain of fiber  $\varepsilon$  can be evaluated as  $\varepsilon = \sigma / E_f$ , being  $\sigma$  given by Eq.(3.2) and  $E_f$  the elastic modulus of bare textile (i.e. not impregnated with matrix)(see Table 3.1).



In the post peak stage (i.e. for  $g < g^*$ ), the weakening of matrix and the propagation of debonding at the fiber-matrix interface, determines a progressive increase in the global slip rate  $v_g$  concurrently with a reduction of the fiber elongation rate  $v_\varepsilon$  due to the decrease of applied stress  $\sigma$ . This reduces the drift between  $v_s$  and  $v_g$  which eventually equals their values once the debonding mechanism is fully established and  $\sigma = \sigma_f$ .

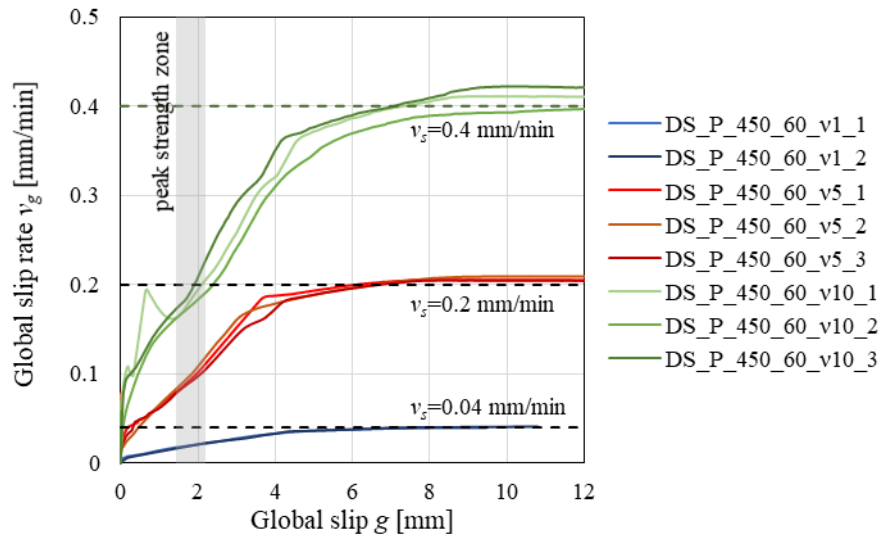


Figure 3.16: comparison between global slip rate and machine stroke rate.

### 3.4 Conclusions and considerations for future guidelines

The present chapter shed light on the relevance of bond in externally bonded FRCM applications. The principal testing methods for the evaluation of FRCM composites bond properties were analysed and discussed, alongside with the corresponding results. Then, an overview on the FRCM strengthening design approach described in the Italian regulation was provided. Finally, an experimental campaign, involving two FRCM and one SRG composite, aimed at investigating the effect of bond test speed rate, was described and discussed. On the basis of the topic analysed, the following conclusions can be drawn:

- Despite of the high tensile properties of FRCM composites, the failure of a strengthened element may occur at a far lower stress level due to a sudden loss of adhesion of the composite strip from the substrate. Debonding may occur at different interface depending on the properties of FRCM constituents, of the substrate and on their compatibility.

- Many set-ups are nowadays available in the scientific literature for the bond characterization of FRCC composites. Bond test set-ups are classified in direct and indirect test set-ups, depending on the structural scheme that transfers the tensile action on the composite. Direct set-ups are widely diffused and easier to realize, however their result may provide a lower bound of the actual bond capacity of an FRCC-substrate joint.
- Debonding may have a dramatic impact on the exploitation of the FRCC tensile properties. When a telescopic failure mode is involved, the maximum stress attained in a bond test may be 50% lower than the ultimate tensile strength of the composite, if a Carbon and a PBO FRCC are considered. Glass and Basalt FRCC may exhibit a higher exploitation of their tensile properties if their debonding mode involves the rupture of fiber layer outside from the composite prism.
- The machine stroke rate has an effect on the results of direct shear bond-test on FRCC and SRG composites. The effect can be quantified differently between the materials tested. Accordingly, specific testing rate can be provided for different materials and applications.
- In displacement (stroke) controlled DS tests, the elastic strain of the bare textile portion, between the loaded-end and the machine clamp, determines a discordance between global-slip and machine-stroke rates. The divergence of the two rates, under certain hypotheses, can be attributed to the bare textile axial elongation rate. The divergence reduces in the ending stage of the test, as a consequence of the decrease of applied stress.



# 4 BOND BEHAVIOUR OF FRCM-MASONRY JOINTS UNDER BENDING CONDITIONS

The European built heritage is largely characterized by the use of unreinforced masonry members, such as masonry structural and infill walls, spandrels and masonry floor-bands, piers, vaults, arches, etc. Because unreinforced masonry is often designed only for vertical loads, its out-of-plane strength is mainly related to the element sectional texture (e.g. presence of diatoni stones, header courses/bricks, tothing with inner filling, etc.) and to the mortar tensile strength. Therefore, unreinforced masonry is particularly vulnerable in the case of seismic events that induce horizontal actions in the structure. Externally bonded fiber-reinforced composites represent an efficient and cost-effective solution to address the out-of-plane vulnerability of unreinforced masonry elements, however their effectiveness is linked with the quality of its bond with the substrate. Studies on the bond behavior of inorganic-matrix composites typically focus on the use of direct shear tests [13,62,64,65], in which the composite is subjected to a pure tangential loading condition (Mode-II loading condition). However, when masonry undergoes out-of-plane displacement (overturning) (Figure 4.1), under the effect of lateral actions, a mixed tangential and normal (Mode I) loading condition is transferred to the composite strengthening, which cannot be captured by traditional direct shear

tests. Indeed, the presence of a non-pure Mode-II loading condition may influence the composite bond behaviour and appropriate test methods need to be adopted to investigate its impact on the strengthened element response.

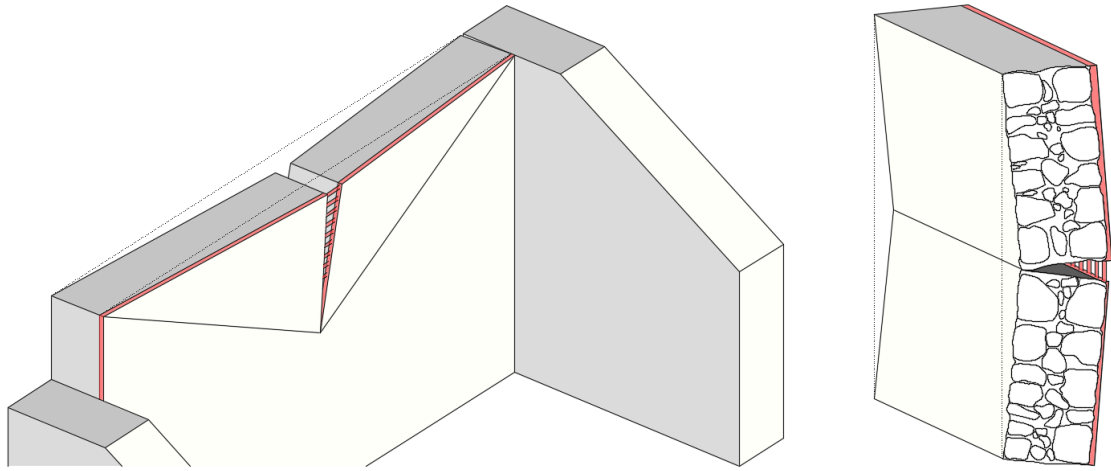


*Figure 4.1: out-of-plane displacement of masonry walls, under the effect of horizontal actions.*

In this section, the debonding process of two different FRCM materials (Carbon FRCM and PBO FRCM) applied to masonry substrate is studied using a modified beam test set-up. The effect of different specimen geometries and different layout of the composite strip is investigated. The results are then compared with those of single-lap direct shear test performed on specimens of the same materials and geometry. Five bond parameters have been compared, namely the debonding axial stress and corresponding global slip, the peak axial stress and corresponding global slip and the residual stress, respectively  $\sigma^*$ ,  $\sigma_{deb}$ ,  $\sigma_f$ ,  $g^*$ ,  $g_{deb}$ . The test modalities, together with the results and analysis are reported and discussed in the following sections.

## 4.1 Material properties

A total of 31 modified beam (MB) tests and 11 single-lap direct shear (DS) tests were performed. Both MB and DS tests were conducted using an electro-mechanic testing machine, equipped with a 50 kN load cell, in displacement control by monotonically increasing the machine stroke at a constant rate of 0.0034 mm/s. Twenty-three specimens (17 MB and 6 DS) were fabricated using a PBO FRCM composite whereas 20 specimens (15 MB and 5 DS) a carbon FRCM composite. Two modified beam test specimen geometries (with a number of bricks in each masonry block equal to 1 or 3, respectively), each with two composite strip layouts (with bare or embedded fibers at

the gap), were considered to study the effect of these particular set-ups on the FRCM composite bond behavior.

Two different FRCM composites were studied in this chapter, one with a PBO fiber textile [80] and one with a carbon fiber textile [81]. Both textiles had bundles (yarns) spaced at 10 mm on center in the longitudinal direction (i.e. aligned with the load direction), whereas the spacing in transversal direction was 17,5 mm and 10 mm on center for the PBO and carbon textile, respectively. The width and thickness of a single yarn  $b_f$  and  $t_f$ , respectively, are reported in Table 4.1 along with the tensile strength  $f_f$ , ultimate strain  $\varepsilon_f$ , and elastic modulus  $E_f$  of the corresponding bare textile obtained by tensile tests [49,54]. The same cement-based matrix was employed for both PBO and carbon FRCM composite. The matrix mean flexural strength  $f_{mt}$  and mean compressive strength  $f_{mu}$  were obtained by testing matrix prisms with dimensions 40×40×160 mm according to EN 1015-11 [38] and are reported in Table 4.1.

The masonry blocks were made using commercially available clay bricks [84] and mortar joints (where present) with nominal thickness of 10 mm and compressive strength lower than 5 MPa [49].

Composite	$b_f$ [mm]	$t_f$ [mm]	$f_f$ [MPa]	$\varepsilon_f$ [-]	$E_f$ [GPa]	$f_{mu}$ [MPa]	$f_{mt}$ [MPa]
PBO FRCM	5	0.092	3014	0.0145	206	25.0	6.1
C FRCM	5	0.084	1944	0.0095	203	25.0	6.1

*Table 4.1: FRCM materials properties.*

## 4.2 Modified beam test set-up

A total of 31 modified beam test specimens were tested using a 4-point bending configuration. In the modified beam test set-up, two masonry blocks were connected by a composite strip on one (bottom) side and by a cylindrical hinge on the opposite (top) side. The specimen was tested using a 4-point bending configuration. The distance between the axes of the two cylindrical supports was 480 mm, whereas the distance between the two cylinders used to apply the load, which were connected to the machine using a spherical joint able to accommodate the specimen irregularities, was 80 mm (see Figure 4.2 and Figure 4.3). Two different specimen types (geometries) were considered in the experimental campaign: i) specimen comprising two masonry blocks (wallets)

including 3 bricks and two mortar joints (Figure 4.2) and ii) specimen comprising two single bricks with no mortar joints (Figure 4.3).

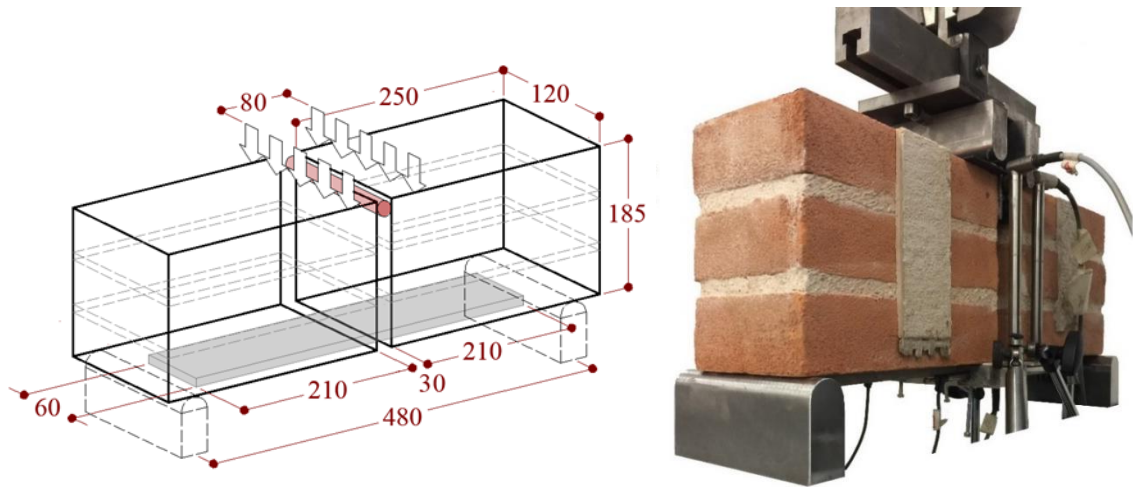


Figure 4.2: Three-brick modified beam test set-ups geometries and dimensions (mm).

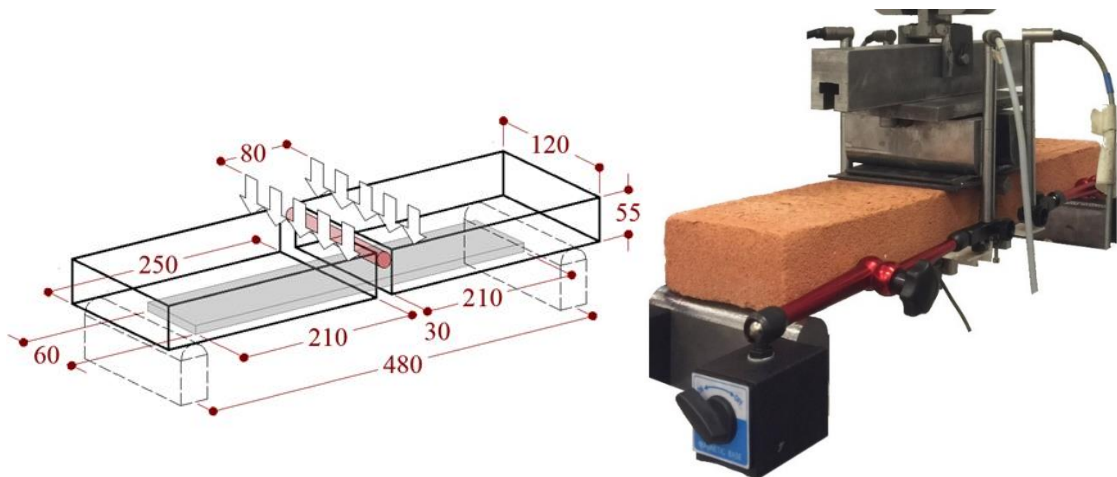


Figure 4.3: One-bricks modified beam test set-ups geometries and dimensions (mm).

Since in both specimen geometries the FRCM strip is bonded to the bottom face of the bricks, the FRCM-substrate interface is the same. However, the different distances between the FRCM strip and the cylindrical hinge axis entail for a different specimen inner level arm, which in turn is responsible for the specimen stiffness. Therefore, the two types of specimen are associated with a different state of stress of the FRCM composite, which can be analyzed to gain information that cannot be obtained with direct-shear tests. Although the application of EB FRCM to the sailor face (i.e. base) of clay brick masonry is in line with some peculiar masonry constructions, such as sailor-bond masonry and Catalan (or thin) vaults, in most of the cases the external leaf of masonry is characterized by the presence of header and stretcher courses, interspersed with head and bed joints (such as the in Stretching bond, Heading bond, Flemish bond,

English bond, Stack bond, etc.). The width of the brick surface and the presence of joints, reportedly affects the bond behaviour of EB FRP composites [70], for which the failure involves a thin layer of substrate [71], and the properties of both brick and mortar (joints) are engaged in the debonding mechanism. In the case of FRCM-masonry applications, the presence of the mortar joints does not affect the composite bond behaviour, provided that failure does not involve the substrate, as generally observed for inorganic-matrix composites [62]. The results obtained by the direct-shear tests confirm that the presence of the mortar joints did not affect the composite load responses, which were similar to those of beam tests and did not show load oscillations typical of the presence of mortar joints with properties different from those of the bricks [71].

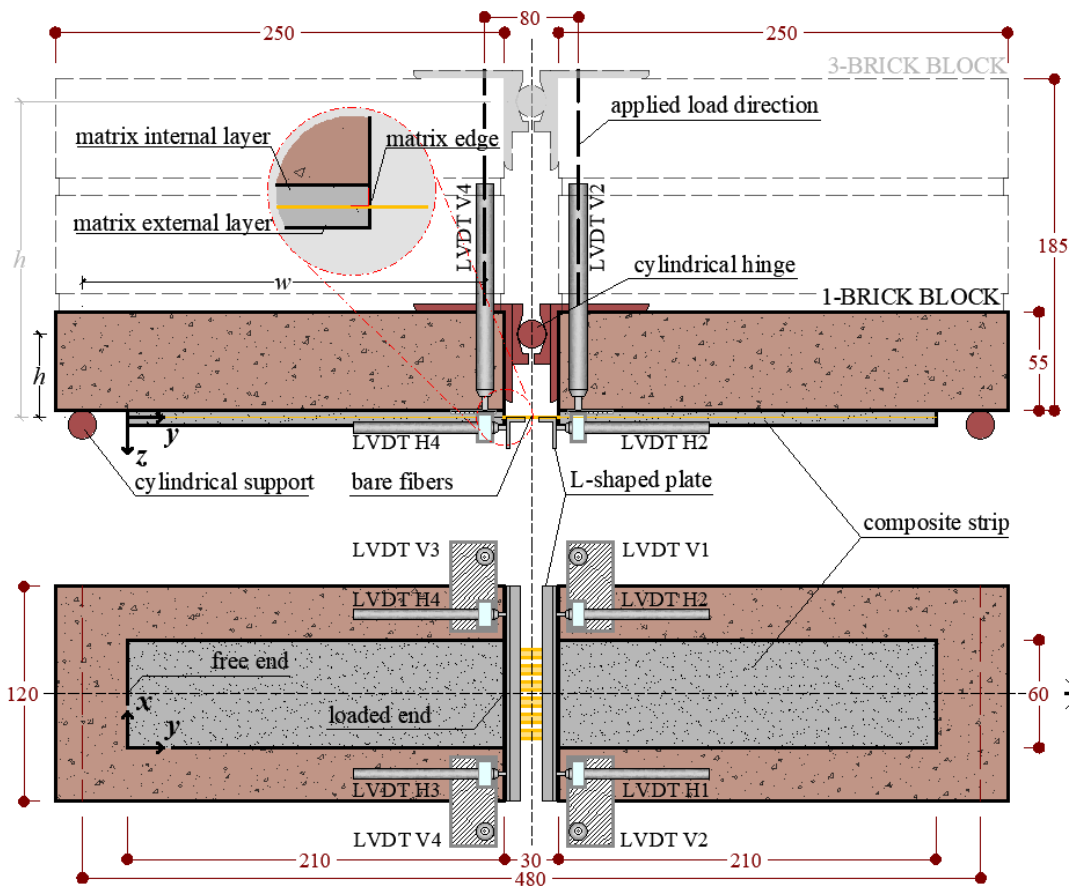


Figure 4.4: Modified beam test set-up with bare fibers at the gap: a) side view and b) bottom view (dimensions in mm).

Due to the presence of the cylindrical hinge, a 30 mm gap was present between the two blocks of the specimen (see Figure 4.2 and Figure 4.3). The composite strips were comprised of two layers of mortar each with a thickness of 4 mm and of one layer of textile. The composite bonded width was 60 mm, which resulted in strips including  $n=6$  yarns in longitudinal direction ( $y$ -direction, see Figure 4.4). The composite bonded



length was 420 mm (210 mm on each block) and started from the brick internal edge, i.e. the brick edge located at the gap between the blocks. It should be noted that in bond tests of FRP-concrete and FRP-masonry joints the bonded length should not be extended up to the edge of the substrate to avoid possible substrate wedge failure [75,85]. However, since bond tests of PBO and carbon FRCM composites showed that failure did not involve the substrate [69,86], the FRCM strip was bonded up to the brick edge to maximize the bonded length. The fibers located at the gap were left bare for some specimens and were embedded within the matrix for others. In the former case, two aluminum L-shaped plates were attached to the bare fibers at the loaded end of the two strips using low-viscosity ethyl cyanoacrylate. Four linear variable displacement transducers (LVDTs), named H1, H2, H3, and H4 in Figure 4.4, were attached to the masonry substrate at the edge of the FRCM strip and reacted off of the L-shaped plates bonded to the bare fibers. The average displacement measured by the two horizontal LVDTs in each block is named global slip (or loaded end slip)  $g$  in this section.

For specimens where the fibers located at the gap were impregnated (embedded), the presence of the matrix did not allow for a direct measurement of the fiber displacement. Therefore, two LVDTs were attached on the sides of the FRCM strip at the loaded end of one block and reacted off of aluminum plates bonded to the opposite block to measure the horizontal relative displacement between the two blocks. Finally, four additional LVDTs, named V1, V2, V3, and V4 in Figure 4.4, were attached to the specimen sides (two LVDTs on each side) and measured the vertical deflection of each block along the applied load directions.

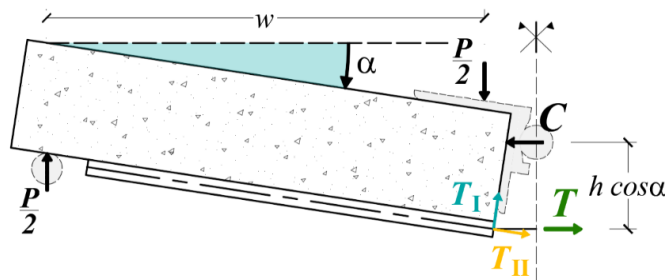


Figure 4.5: Free body diagram of one block of the MB test.

The force at the composite loaded end,  $T$ , was obtained enforcing the equilibrium of the free body diagram of Figure 4.5: where:

$$T = \frac{Pw}{2h \cos \alpha} \quad (4.1)$$

where  $P$  is the force applied to the specimen by the testing machine,  $w$  is the distance between the load application point and the closest support,  $h$  is the distance between the fiber layer and the axis of the hinge and  $\alpha$  is the block rotation angle (Figure 4.5). Eq. (4.1) is based on the assumption that the applied load  $P$  is equally distributed among the two applied point loads. This approximation was justified by the adoption of a spherical joint, which connected the load cylinders to the testing machine, allowing to accommodate eventual differential settlements or rotation of the specimen, and by the reduced distance between the two load cylinders (80 mm, see Figure 4.4). The force at the composite loaded end,  $T_{II}$ , parallel to the fiber direction is:

$$T_{II} = T \cdot \cos \alpha = \frac{Pw}{2h} \quad (4.2)$$

### 4.3 Single-lap direct-shear test set-up

A total of 11 FRCC-masonry joints were tested in direct-shear using a pull-push single-lap configuration (Figure 4.6). They comprised the same composites employed in the modified beam tests (6 specimens included the PBO FRCC and 5 the carbon FRCC). The masonry support was made with the same bricks used in the MB tests and included 5 bricks and 4 mortar joints. A composite strip with the same thickness (8 mm), bonded width (60 mm), and bonded length (210 mm) used in each masonry block of the MB tests was applied to the masonry support. The bonded length started 30 mm apart from the support edge at the loaded end to comply with the indications of the Italian acceptance criteria for FRCC composites [35]. The reinforcing textile was left bare outside the bonded length both at the loaded end and at the free end (Figure 4.6). Two steel plates were epoxy-bonded to the end of the textile left bare at the loaded end to facilitate gripping with the machine. The distance between the composite loaded end and the steel plates was 240 mm. Aluminum L-shaped plates were bonded to the bare fibers just outside the bonded length at the loaded end and at the free end. The average of 2 LVDTs bonded to the masonry support and reacting off of the L-shaped aluminum plate at the loaded end provided the textile global slip  $g$ . Two LVDTs attached to the masonry support and reacting off of the L-shaped aluminum plate at the free end were used to measure the possible textile free end slip. However, the free end slip is not discussed in this section.

It should be noted that in MB tests the composite strip was bonded to the brick base, i.e. without the presence of any mortar joint (see Figure 4.2, Figure 4.3 and Figure 4.4),

whereas in DS tests 4 mortar joints were present along the composite-masonry interface (see Figure 4.6). However, provided that failure occurs within the composite as generally reported for PBO and carbon FRCM composites similar to those tested in this section [69,87], the presence of the mortar joints should not affect the composite bond behavior.

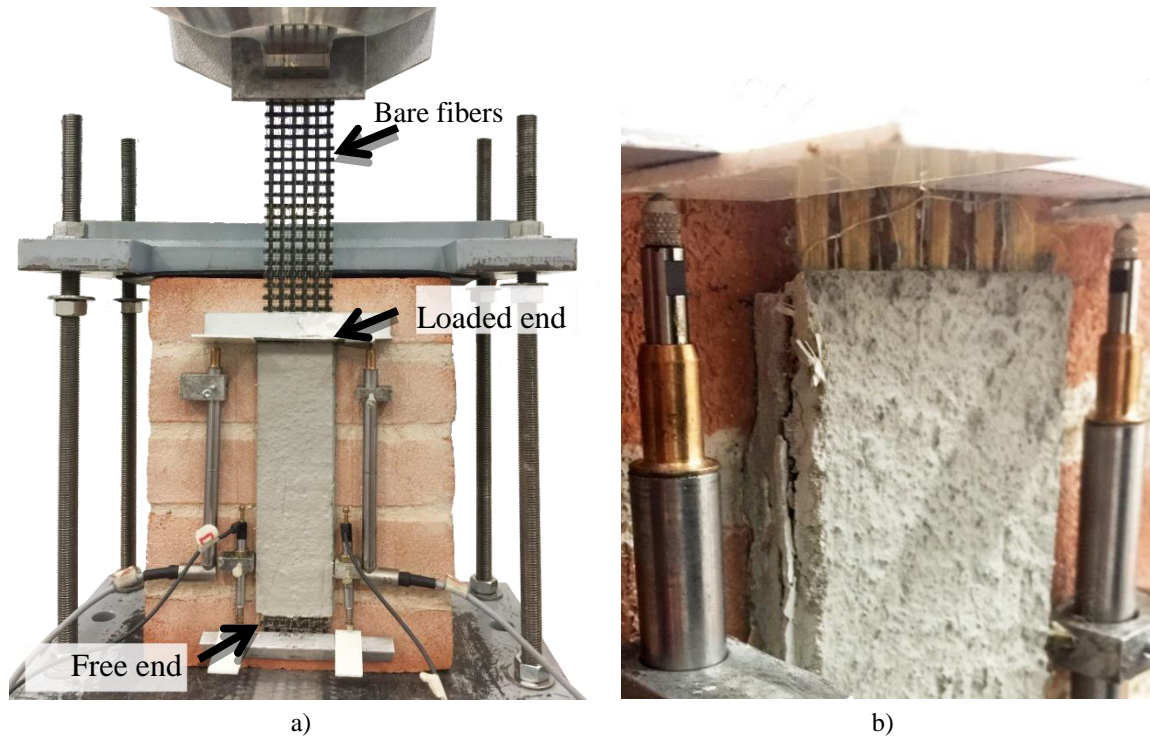


Figure 4.6: a) Photo of the single-lap direct-shear test set-up. b) Detail of the crack at the matrix-fiber interface.

#### 4.4 Test results and discussion

Results for the MB and DS set-ups are reported in Table 4.2. The specimens were named following the notation T\_C\_N\_Y\_X\_B\_n, where T indicates the test set-up (MB=modified beam test, DS=direct shear test), C (if present) =carbon (if omitted indicates specimens with PBO fibers), N=1 or 3 is the number of bricks in each masonry block, Y=bonded length in mm, X=bonded width in mm, B (if present) =bare fibers located at the gap, and n is the specimen number. In Table 4.2, specimens MB\_3\_210\_60\_B\_2, MB\_1\_210\_60\_1, MB\_C\_1\_210\_60\_B\_3, and DS\_210\_60\_2 are not reported because they were interrupted due to machine issues.

In Table 4.2, key values of the fiber axial stress  $\sigma$  and corresponding global slip  $g$  are provided for each specimen. In particular,  $P^*$  is the maximum applied force applied to the specimen,  $\sigma^*$  and  $g^*$  are the axial stress and global slip at the peak load,  $\sigma_A$  and  $g_A$

the axial stress and global slip at the end of the load response linear branch, and  $\sigma_f$  and  $g_f$  are the residual axial stress and the associated global slip. The stress  $\sigma$  is evaluated in the single-lap DS set-up as the ratio between the applied load  $P$  and the cross-sectional area of the fibers  $A=nt^*b^*$ . For the MB set-up, the stress  $\sigma$  is defined according to Eq. (4.2) as the ratio between the force at the composite loaded end parallel to the fiber direction  $T_{II}$  and the cross-sectional area  $A$  of the fibers.

Specimen	Fiber	$w$ [mm]	$h$ [mm]	$P^*$ [kN]	$\sigma^*$ [MPa]	$g^*$ [mm]	$\sigma_A$ [mm]	$g_A$ [mm]	$\sigma_f$ [mm]	$g_f$ [mm]
MB_3_210_60_B_1	PBO	200	175	8.08	1672	1.47	1121	0.62	989	3.17
MB_3_210_60_B_3	PBO	200	175	9.37	1939	2.47	1104	0.45	1198	4.76
MB_3_210_60_B_4	PBO	200	175	7.69	1593	1.77	1199	0.49	1083	3.47
MB_3_210_60_B_5	PBO	200	175	7.75	1604	1.61	1288	0.36	1062	3.60
Average				8.22	1702	1.83	1178	0.48	1083	3.75
CoV [%]				9.51	9.51	24.32	7.16	23.24	7.98	18.60
MB_1_210_60_B_1	PBO	200	45	2.04	1645	1.39	1072	0.17	510	3.98
MB_1_210_60_B_2 <sup>†</sup>	PBO	200	45	2.35	1893	0.98	1415	0.21	-	-
MB_1_210_60_B_3	PBO	200	45	2.45	1971	0.17	1183	0.04	537	3.66
MB_1_210_60_B_4	PBO	200	45	2.46	1983	0.36	1345	0.17	410	3.70
MB_1_210_60_B_5	PBO	200	45	1.87	1503	0.30	1292	0.19	408	3.58
Average				2.23	1799	0.64	1261	0.16	466	3.73
CoV [%]				11.90	11.90	81.97	10.75	42.84	14.44	4.69
MB_1_210_60_2	PBO	200	45	2.81	2261	0.47	705	0.06	551	3.61
MB_1_210_60_3	PBO	200	45	2.31	1860	0.48	787	0.06	488	3.72
MB_1_210_60_4	PBO	200	45	2.57	2070	0.55	947	0.07	688	3.69
MB_1_210_60_6	PBO	200	45	2.71	2181	0.60	546	0.08	549	3.01
MB_1_210_60_7	PBO	200	45	2.54	2042	0.53	396	0.03	496	3.16
Average				2.59	2083	0.53	676	0.06	555	3.44
CoV [%]				7.32	7.32	10.11	31.53	35.42	14.44	9.54
MB_C_3_210_60_B_1	C	200	175	6.52	1351	1.24	1007	0.43	358	2.16
MB_C_3_210_60_B_2	C	200	175	5.56	1152	0.86	571	0.09	510	2.87
MB_C_3_210_60_B_3 <sup>†</sup>	C	200	175	5.79	1199	0.85	860	0.25	-	-
MB_C_3_210_60_B_4	C	200	175	5.30	1096	0.78	772	0.29	493	2.11
MB_C_3_210_60_B_5	C	200	175	4.79	992	0.82	717	0.16	556	2.67
Average				5.59	1158	0.91	785	0.24	479	2.45
CoV [%]				11.45	11.45	20.62	20.67	52.78	17.74	15.34
MB_C_1_210_60_B_1	C	200	45	1.57	1264	0.77	903	0.33	205	2.38
MB_C_1_210_60_B_2	C	200	45	1.54	1242	0.93	1020	0.49	137	2.97
MB_C_1_210_60_B_4	C	200	45	1.52	1221	0.68	1084	0.44	36	2.33
MB_C_1_210_60_B_5 <sup>†</sup>	C	200	45	1.19	954	1.20	857	0.62	-	-
Average				1.45	1170	0.89	966	0.47	126	2.56
CoV [%]				12.40	12.40	25.90	10.79	25.32	67.49	13.95
MB_C_1_210_60_1	C	200	45	1.56	1254	0.59	1047	0.34	55	2.85
MB_C_1_210_60_2	C	200	45	1.75	1408	0.69	816	0.19	202	2.94
MB_C_1_210_60_3	C	200	45	1.76	1413	0.80	1040	0.37	120	2.64
MB_C_1_210_60_4	C	200	45	1.65	1329	1.00	954	0.40	382	2.47
MB_C_1_210_60_5	C	200	45	1.92	1549	0.77	1202	0.20	114	2.67
Average				1.73	1390	0.77	1012	0.30	174	2.71
CoV [%]				7.91	7.91	19.28	13.99	32.77	73.06	6.84

Specimen	Fiber	$w$ [mm]	$h$ [mm]	$P^*$ [kN]	$\sigma^*$ [MPa]	$g^*$ [mm]	$\sigma_A$ [mm]	$g_A$ [mm]	$\sigma_f$ [mm]	$g_f$ [mm]
DS_210_60_1	PBO	-	-	4.77	1729	2.27	1192	0.79	486	7.51
DS_210_60_3	PBO	-	-	5.33	1931	1.85	1036	0.25	448	6.18
DS_210_60_4 <sup>†</sup>	PBO	-	-	4.60	1668	1.68	1133	0.40	-	-
DS_210_60_5	PBO	-	-	5.56	2013	1.38	1011	0.18	340	7.09
DS_210_60_6	PBO	-	-	6.08	2201	1.35	1250	0.47	425	6.57
Average				5.27	1909	1.70	1124	0.42	425	6.84
CoV [%]				11.34	11.34	22.15	9.01	57.22	14.56	8.50
DS_C_210_60_1	C	-	-	3.32	1204	1.05	424	0.18	320	2.00
DS_C_210_60_2	C	-	-	2.85	1032	1.25	646	0.42	239	2.42
DS_C_210_60_3	C	-	-	2.92	1058	1.04	597	0.43	398	2.46
DS_C_210_60_4	C	-	-	1.97	712	1.20	496	0.52	237	2.44
DS_C_210_60_5	C	-	-	2.89	1046	1.24	558	0.31	261	2.41
Average				2.79	1010	1.15	544	0.37	291	2.35
CoV [%]				17.87	17.87	9.02	15.98	34.72	23.60	8.29

<sup>†</sup>Premature failure.

Table 4.2: Experimental test results.

#### 4.4.1 Discussion of the MB tests results

In this section, the MB test results are analyzed and discussed. In particular, the effect of the number of bricks in the masonry blocks, the effect of fiber layouts along the gap, and the behavior of the normal stress component  $\sigma_I$  are studied.

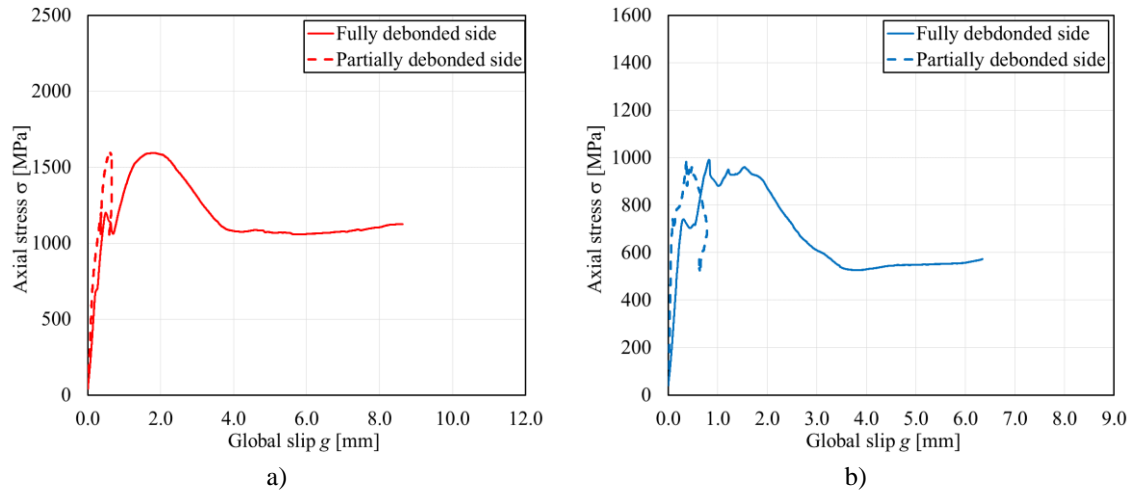


Figure 4.7: Axial stress  $\sigma$  – global slip  $g$  response of specimen a) MB\_3\_210\_60\_B\_4 and b) MB\_C\_3\_210\_60\_B\_5.

##### 4.4.1.1 Representative axial stress $\sigma$ – global slip $g$ response

The axial stress  $\sigma$  – global slip  $g$  response of the MB tests is first presented with reference to 3-brick block specimens with bare fibers along the gap. For these

specimens, failure occurred due to fiber debonding at the matrix-fiber interface, with significant slippage of the fibers with respect to the matrix. The  $\sigma$ - $g$  responses obtained by one representative specimen in series MB\_3\_210\_60\_B and one in series MB\_C\_3\_210\_60\_B are reported in Figure 4.7a and b, respectively.

The stress responses of MB tests with 3-brick blocks showed an initial linear branch, which ended due to the opening of a matrix crack at the matrix-fiber interface at the loaded end of one of the two masonry blocks (Figure 4.8a). During the initial linear stage, the global slips measured at the two loaded ends were symmetric. After the occurrence of the matrix crack, the load response became non-linear and the global slip of the strip attached to one masonry block increased at a higher rate with respect to the global slip of the strip attached to the other masonry block. This un-symmetric response eventually led to complete debonding of the fibers from the matrix on one side of the specimen, named fully debonded side in Figure 4.7, whereas partial fiber debonding occurred on the other side, named partially debonded side in Figure 4.7. Indeed, after the attainment of the peak axial stress  $\sigma^*$ , the increase in the specimen vertical displacement determined the increase of the global slip associated to the fully debonded side, whereas the global slip associated to the partially debonded side remained constant for some specimens or decreased for others due to the recovering of the fiber elastic deformation. When complete fiber debonding occurred, the fiber still provided a residual stress  $\sigma_f$  due to the presence of friction/interlocking at the matrix-fiber interface. Such residual stress  $\sigma_f$  was often previously reported for direct-shear test of PBO FRCM-concrete joints [69,88].

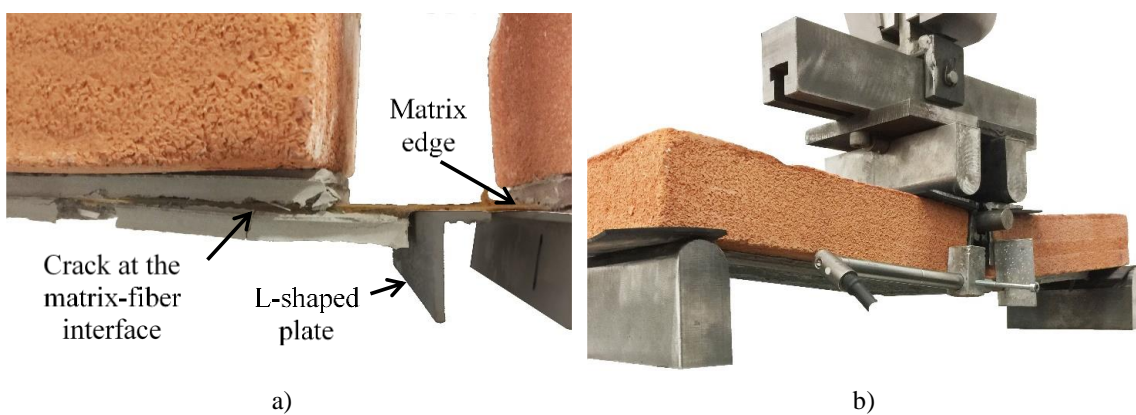


Figure 4.8: a) Opening of the matrix crack at the fiber-matrix interface of specimen MB\_3\_210\_60\_B\_1. b) Specimen MB\_C\_1\_210\_60\_2 at completion of the test.

#### 4.4.1.2 *Effect of the number of bricks in the masonry blocks*

All 1-brick specimens failed due to debonding of the fibers at the matrix-fiber interface, which allowed for attaining a significant midspan deflection at completion of the test (Figure 4.8b). The load (stress) responses of MB tests with PBO fibers and 3- and 1-brick blocks are reported in Figure 4.9a and b, respectively, whereas those corresponding to specimens with carbon fibers and 3- and 1-brick blocks are reported in Figure 4.9c and d, respectively. The load responses obtained were consistent with those of 3-brick specimens, although some differences can be observed. The  $\sigma$ - $g$  curves of specimens in series MB\_1\_210\_60\_B were characterized by a higher slope of the initial linear branch with respect to specimens in series MB\_3\_210\_60\_B. Particularly in the case of PBO fibers, although similar values of  $\sigma^*$  were reported, the use of 1-brick blocks led to global slips  $g^*$  associated with the peak load lower than those obtained using 3-brick blocks. Finally, significantly different values of the residual stress  $\sigma_f$  were obtained, with the highest values provided by 3-brick specimens. The differences observed are due to the effect of the specimen flexibility on the fiber-matrix stress-transfer mechanism. The use of 1- and 3-brick blocks determined a different specimen inner lever arm, i.e. the distance between the hinge axis and the fiber cross-section centroid ( $h$  in Table 4.2). The low inner lever arm of 1-brick specimens entailed for values of curvature and deflection (associated with the specimen flexibility) higher than those of 3-brick specimens for the same cross-section and fiber axial stress. The deflection induced a stress component  $\sigma_I$  normal to the fiber textile plane that tended to push the fiber toward the internal matrix layer (i.e. the matrix layer bonded to the substrate, see Figure 4.4), thus affecting the matrix-fiber bond behavior. Indeed, as in the case of frictional forces proportional to the normal force component, the presence of the normal stress should increase the shear stress at the matrix-fiber interface that in turn reduces the fiber slippage. It should be noted that the increase of the applied stress in a pull-out tests where the applied force is not aligned with the crack surface was previously observed in fiber reinforced materials and is usually referred to as “snubbing effect” [89,90].

Specimens comprising 1-brick blocks, which provided the highest deflection, reported low values of global slip (see Figure 4.9). However, high values of the normal stress component  $\sigma_I$  eventually damaged the fiber, leading to residual shear stress  $\sigma_f$  lower for 1-brick than for 3-brick specimens and, in the case of specimens comprising carbon textiles, to the complete rupture of the fibers ( $\sigma_f$  reduced to quite small values for

specimens in series MB\_C\_1\_210\_60\_B, as shown in Figure 4.9d). Further analyses of the effect of the normal stress component are reported in Section 4.4.1.4.

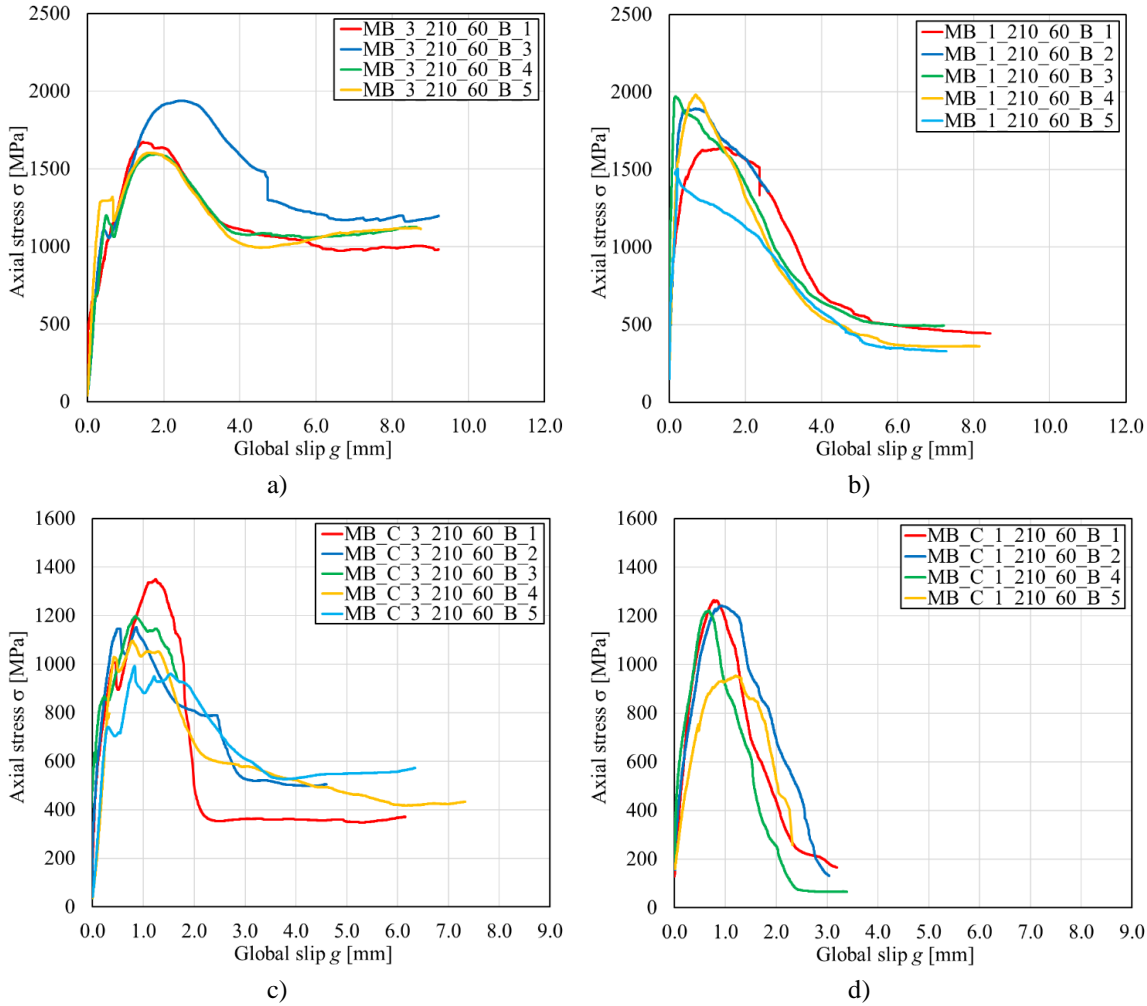


Figure 4.9: Axial stress  $\sigma$  – global slip  $g$  response of specimens in series a) MB\_3\_210\_60\_B, b) MB\_1\_210\_60\_B, c) MB\_C\_3\_210\_60\_B, and d) MB\_C\_1\_210\_60\_B.

#### 4.4.1.3 Effect of the fiber layouts along the gap

Figure 4.10 shows the  $\sigma$ – $g$  curves obtained by 1-brick specimens with PBO and carbon fibers embedded along the gap, where the envelope of load responses obtained by corresponding 1-brick specimens with bare fiber at the gap is also provided for comparison. The difference in the global slip measured in the fully and partially debonded side discussed in Section 4.4.1.1 indicates that the assumption of symmetric composite bond behavior, which is usually assumed for bond tests including symmetric strips, is not always valid. Therefore, in specimens where the fibers located at the gap were embedded within the matrix, symmetric strip behavior was assumed only up to the peak axial stress, whereas slippage on one side only was considered thereafter. Hence,



the global slip  $g$  of specimens in series MB\_1\_210\_60 (Figure 4.10a) and MB\_C\_1\_210\_60 (Figure 4.10b) was defined as half of the average horizontal relative displacement between the two blocks only up to  $\sigma^*$ , whereas it was assumed equal to the entire average relative displacement during the load response softening branch.

The load responses of specimens with fibers fully embedded within the matrix, which failed due to debonding at the matrix-fiber interface, resembled those of specimens with bare fibers at the gap. The global slip considered for fully embedded strips is similar to that directly measured on the bare fibers, which confirms the assumptions of complete debonding of only one side of the specimen. However, the peak stress  $\sigma^*$  provided by specimens in series MB\_210\_60 and MB\_C\_1\_210\_60 were generally higher than those of 1-brick specimens with bare fibers at the gap. This difference was attributed to the presence of the matrix along the gap that protected the fibers limiting the damage induced by the normal stress component discussed in the previous section (see also Section 4.5). For specimens including carbon textiles, the fibers eventually ruptured for high values of global slip  $g$ , which entailed for limited values of residual stress  $\sigma_f$  (Figure 4.10b).

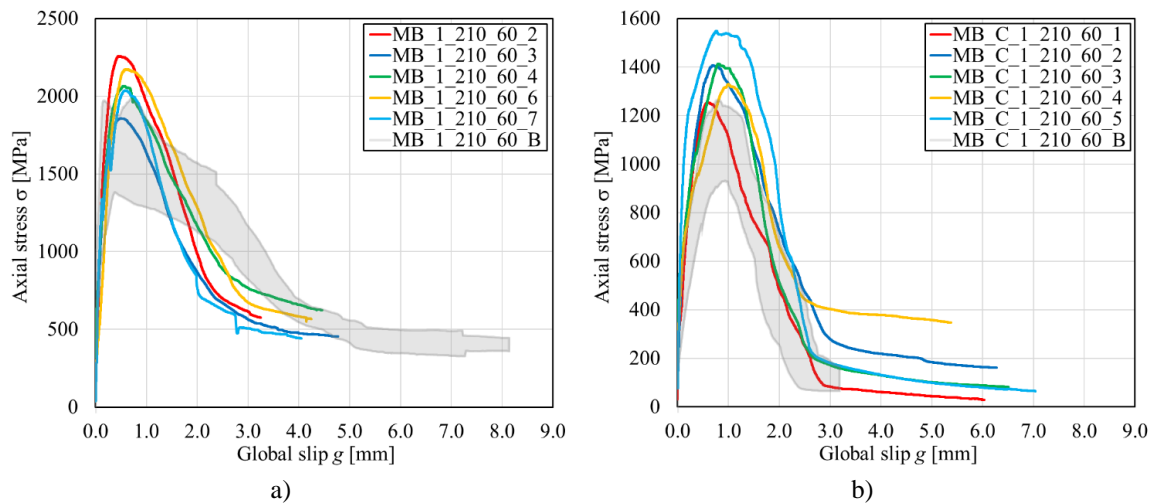


Figure 4.10: Comparison between MB tests with bare and embedded fibers in the gap with a) PBO and b) carbon fibers.

#### 4.4.1.4 Behaviour of the normal stress component $\sigma_l$

As explained in Section 4.4.1.2, different inner lever arms  $h$  entailed for different midspan deflection  $\delta$  of specimens with 3- and 1-brick blocks. The envelope of applied force  $P$  – midspan deflection  $\delta$  curves for MB tests comprising PBO and carbon fibers with 3- and 1-brick blocks are depicted in Figure 4.11a. In Figure 4.11a, the applied force  $P$  was plotted to clearly show that high peak force and lower midspan deflection

were obtained by specimens with high  $h$ . Assuming rigid rotations of the brick blocks, the deflection  $\delta$  can be used to compute the block rotation angle  $\alpha$  (Figure 4.11b):

$$\alpha = \arctan \frac{\delta}{w} \quad (4.3)$$

For specimens including bare fibers, the normal stress component  $\sigma_I$  can be computed as (see Figure 4.11b):

$$\sigma_I = \sigma_0 \sin \alpha = \sigma \tan \alpha \quad (4.4)$$

where  $\sigma_0$  is the stress in the fibers. The axial stress  $\sigma$  and normal stress  $\sigma_I$  computed by Eq. (4.4) for two representative specimens with 3- and 1-brick blocks and PBO fibers are compared in Figure 4.11b. Figure 4.11b shows that  $\sigma_I$  increases non-linearly with the midspan deflection  $\delta$  (see Eq. (4.3)) until the fibers are completely debonded from the embedding matrix. After the axial stress decreased to the residual shear stress value,  $\sigma$  increased in the case of the 3-brick block specimens, whereas it decreased in the case of 1-brick block specimens. This difference could be attributed to fiber damage, which could have increased with the specimen deflection. Nevertheless, according to Eq. (4.4), after the bond contribution to the axial stress was fully exploited, further increase of  $\delta$  resulted in increase of  $\sigma_I$ .

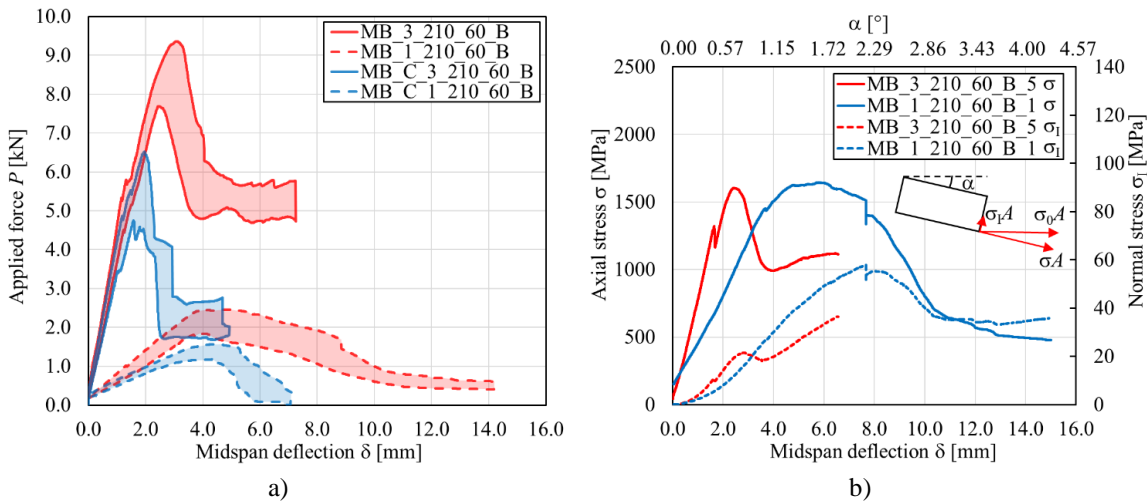


Figure 4.11: a) Envelope of applied force  $P$ – midspan deflection  $\delta$  curves obtained by modified beam tests. b) Comparison between axial stress  $\sigma$  and normal stress  $\sigma_I$  for specimens MB\_3\_210\_60\_B\_5 and MB\_1\_210\_60\_B\_1.

#### 4.4.2 Comparison between MB and DS tests results

The axial stress  $\sigma$  – global slip  $g$  response of PBO and carbon FRCM-masonry joints subjected to single-lap DS tests are reported in Figure 4.12a and b, respectively. In Figure 4.12, the envelope of load responses obtained by 3-brick specimens with bare fiber at the gap with PBO and carbon fibers are also provided for comparison. As in the case of MB tests, debonding of the fibers at the matrix-fiber interface occurred. The load response of DS specimens showed an initial linear behavior that ended due to the opening of a crack at the matrix-fiber interface (Figure 4.6b). After the occurrence of this crack, which induced a slight decrease of the applied stress for most of the specimens, the response became non-linear. When complete debonding of the fibers occurred, the presence of friction/interlocking at the matrix-fiber interface entailed for a residual shear stress  $\sigma_f$  that remained approximately constant with increasing the global slip.

The comparison between MB and DS tests was made considering 3-brick MB specimens because they reported a limited deflection, which entails for a small normal stress component at the matrix-fiber interface. In fact, the deflection observed in 1-brick MB tests specimens determined a high normal stress component, which affected the load responses obtained (see Section 4.4.1.2). In single-lap direct-shear tests, the presence of an inherent eccentricity between the applied load and the support restraint induces a stress normal to the fiber textile plane that tends to separate the textile from the matrix layer bonded to the substrate. Therefore, a non-pure Mode-II loading condition is always present at the matrix-fiber interface in single-lap direct-shear tests [69,91]. However, the presence of the matrix layer covering the fibers was shown to limit this Mode-I loading component, which effect can thus be neglected [92]. Figure 4.12 shows that the matrix-fiber interface normal stress component  $\sigma_I$  did not significantly affect the load response ascending branch, leading to similar values of  $\sigma^*$  for MB and DS tests. However, with increasing global slip, the deflection of MB tests led to an increase of the normal stress component, which in turn determined values of the residual shear stress  $\sigma_f$  higher for MB than for DS test specimens.

The comparison between curves in Figure 4.12 also allowed for confirming that the presence of mortar joints along the FRCM bonded area in DS tests did not influence the FRCM bond behavior, which did not provide variations of the axial stress associated with the presence of substrate portions with different mechanical properties [70].

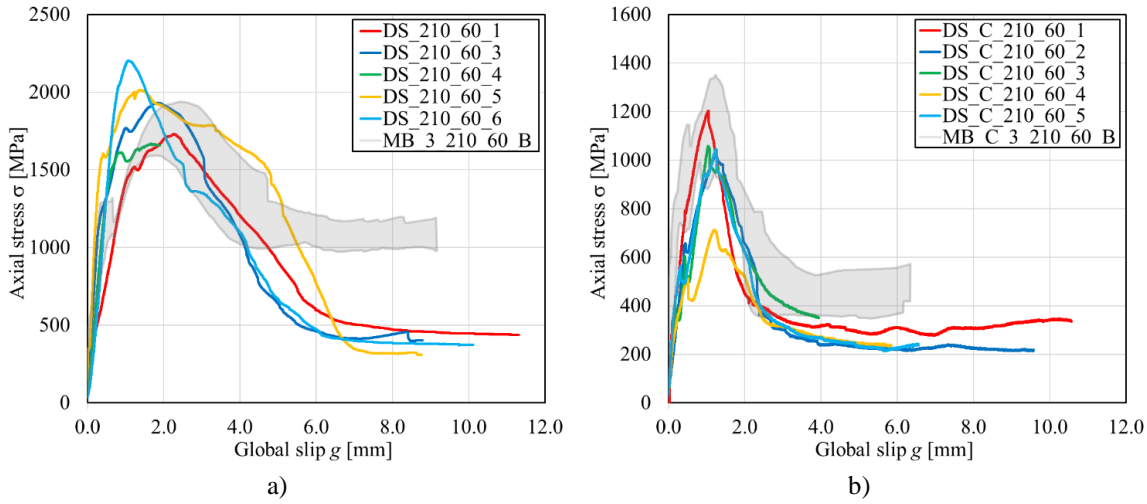


Figure 4.12: Comparison between MB and DS tests with a) PBO fibers and b) carbon fibers.

## 4.5 Analysis of the bond behavior

In this section, key values of axial stress and corresponding global slip obtained by the different tests are analyzed and discussed. Namely, the axial stress at the end of the initial linear branch  $\sigma_A$ , peak axial stress  $\sigma^*$ , residual (friction) axial stress  $\sigma_f$ , and the corresponding global slip  $g_A$ ,  $g^*$ , and  $g_f$ , respectively, were considered. The residual stress  $\sigma_f$  was computed as the average of axial stress values associated with a derivative  $d\sigma/dg$  in the range  $[-200;0]$ , whereas  $g_f$  is the first value that respects the criteria  $-200 \leq d\sigma/dg \leq 0$  (see Chapter 3 and Figure 3.4). The key axial stresses and global slips considered are reported in Table 4.2 for each specimen tested. Furthermore, the average values obtained for each test series are depicted in Figure 4.13a and b for specimens comprising PBO and carbon fibers, respectively.

Considering modified beam tests, the average axial stress associated with the end of the linear branch  $\bar{\sigma}_A$  and average peak axial stress  $\bar{\sigma}^*$  increased with increasing the normal stress component  $\sigma_I$ , i.e. decreasing the number of bricks comprising the masonry blocks (the increase of  $\bar{\sigma}_A$  was 7.04% and 23.07% whereas the increase of  $\bar{\sigma}^*$  was 5.71% and 1.08% for PBO and carbon FRCM, respectively). Only specimens with 1-brick blocks and fully embedded PBO fibers (series MB\_1\_210\_60) provided an average  $\bar{\sigma}_A$  42.59% lower than that obtained with corresponding 3-brick blocks and bare fibers along the gap (series MB\_3\_210\_60\_B). Since  $\sigma_A$  of specimens with fully embedded fibers mainly depends on the matrix ultimate tensile strain, the low average value obtained in series MB\_1\_210\_60 could be attributed to non-perfect curing of the

matrix. However, this circumstance did not affect the average peak axial stress  $\bar{\sigma}^* = 2083$  MPa of specimens MB\_1\_210\_60, which was the highest obtained for specimens with PBO fibers.

The results obtained with 1-brick block specimens showed that embedding the fibers located at the gap improved the specimen capacity, providing an increase of 15.79% and 18.80% for specimens with PBO and carbon fibers, respectively (see Table 4.2 and Figure 4.13). This difference suggested that the presence of the matrix at the gap limited the damage of the fibers eventually caused by the normal stress component  $\sigma_I$  (see Section 4.4.1.4). Indeed, bare fibers located at the gap were pushed toward the edge of the internal matrix layers (see Figure 4.4 and Figure 4.5), whereas in fully embedded strips this edge was not present. The occurrence of fiber damage for high values of the specimen deflection is responsible for the low average residual shear stress  $\bar{\sigma}_f$  provided by specimens with 1-brick blocks with respect to that of specimens with 3-brick blocks (the decrease of  $\bar{\sigma}_f$  was 56.97% and 73.79% for PBO and carbon FRCM, respectively). However,  $\bar{\sigma}_f$  obtained by 1-brick specimens with fully embedded fibers was 19.10% and 38.74% higher than that of corresponding specimens with bare fibers at the gap for PBO and carbon FRCM, respectively, which confirmed that the matrix at the gap limited the fiber damage.

The increase of the axial stress  $\sigma$  induced by  $\sigma_I$  was confirmed by the average stresses  $\bar{\sigma}_A$  and  $\bar{\sigma}^*$  of direct-shear tests, which were lower than those obtained with MB tests comprising 1-brick blocks except in the case of specimens in series BT\_210\_60 that reported a low value of the stress at the end of the linear branch. Furthermore, the average residual shear stress  $\bar{\sigma}_f$  provided by the direct-shear tests, for which an inherent Mode-I loading condition is always present [92], was lower than that obtained with MB tests with 3-brick blocks and similar to that of 1-brick specimens due to the occurrence of fiber damage.

The increase of the average axial stresses  $\bar{\sigma}_A$  and  $\bar{\sigma}^*$  for MB tests with respect to DS tests with PBO fibers was associated with a decrease of the corresponding average global slips  $\bar{g}_A$  and  $\bar{g}^*$ , which was attributed to the presence of  $\sigma_I$  that pushed the fibers against the internal matrix layer contrasting their relative displacement. Even in the case of specimens MB\_1\_210\_60 that reported a  $\bar{\sigma}_A$  39.85% lower than that of

corresponding direct shear tests, the global slip  $\bar{g}^*$  showed a decrease of 68.82% with respect to that of corresponding DS tests.

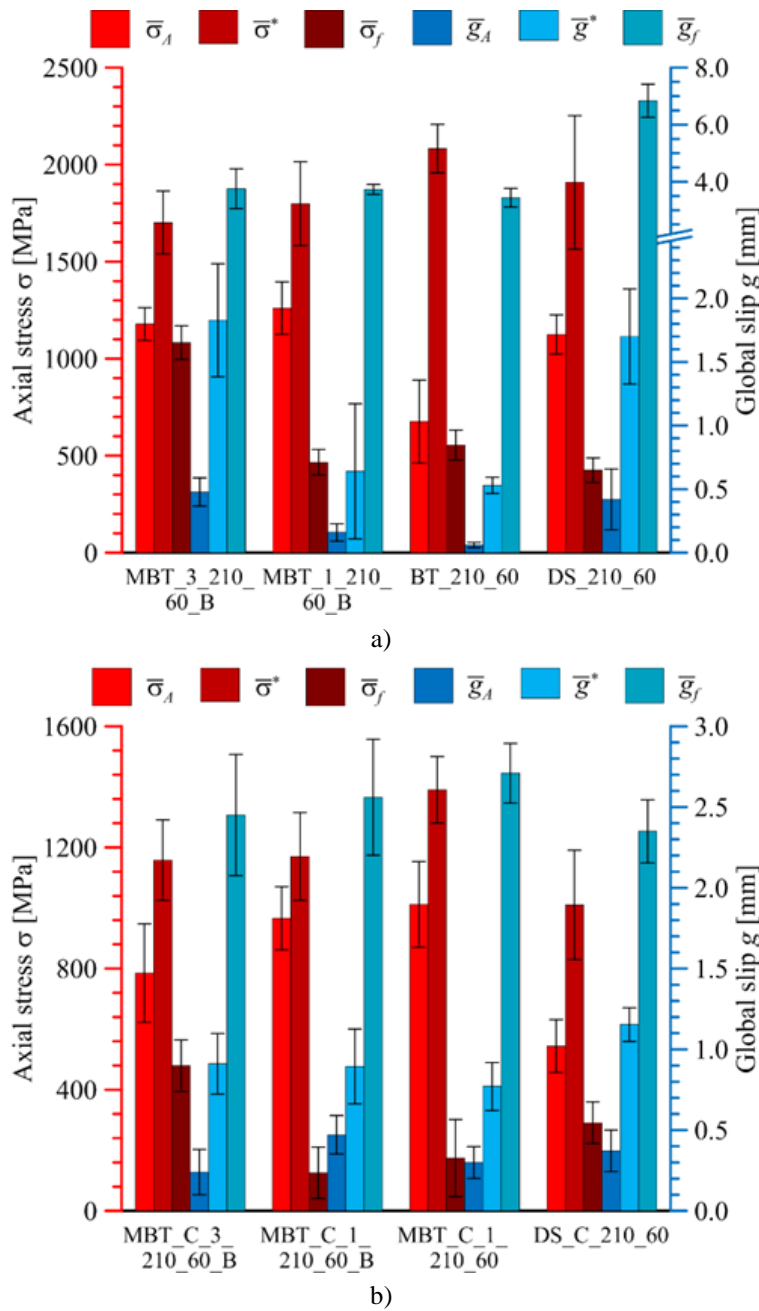


Figure 4.13: Comparison between key average values of axial stress and corresponding global slip for specimens with a) PBO and b) carbon fibers.

The effect of  $\sigma_I$  decreased with the occurrence of fiber damage, which led to values of  $\bar{g}_f$  similar for all MB specimens. In the case of MB specimens with carbon fibers, although the average axial stresses  $\bar{\sigma}_A$  and  $\bar{\sigma}^*$  increased with decreasing the height of the blocks, similar average global slips  $\bar{g}_A$  and  $\bar{g}^*$  were obtained (Figure 4.13b). This

indicated that the effect of  $\sigma_1$  in contrasting the fiber relative displacement is lower for carbon than for PBO fibers, which suggested that the variation of  $g$  is not only a function of  $\sigma_1$  but also of the specific FRCM matrix-fiber bond behavior. Since high fiber damage was reported by carbon FRCM strips,  $\bar{g}_f$  increased with decreasing the block height.

The average residual global slips obtained by MB tests with 3-brick blocks were similar to those of DS tests for both PBO and carbon fibers, except for specimens in series DS\_210\_60 that reported high values of  $\bar{g}_f$  (equal to 6.84 mm, see Table 4.2). This result can be explained by the presence of  $\sigma_1$  that, in the case of PBO textile that showed lower fiber damage than carbon textile, provided a higher contrast during the descending branch of the load response (i.e. for high values of the specimen deflection) than up to the peak stress.

Considering the result obtained and the analysis performed, modified beam test can be considered an effective testing method to evaluate the load-carrying capacity of FRCM-strengthened masonry members for which the composite is subjected to a non-pure Mode-II loading condition, such as vaults and arches. In these cases, the MB test would provide values of fiber stress close to those of the FRCM applied to the strengthened member, whereas DS test was shown to provide a lower bound estimation of the load-carrying capacity [54], involving only parallel action to the composite fiber direction.

## 4.6 Conclusions and considerations for future guidelines

In this chapter, the bond behavior of a PBO and a carbon FRCM composites applied onto a masonry substrate were investigated using different bond tests. Namely, the results of modified beam tests and single-lap direct-shear tests were compared and discussed. Furthermore, the effects of the inner lever arm and of the presence or not of embedded fibers along the gap of modified beam test on the bond behavior observed were investigated. The results obtained allowed for drawing the following main conclusions:

- The load responses of modified beam tests resemble those of corresponding single-lap direct-shear tests. However, the presence of a normal stress component  $\sigma_1$  at the matrix-fiber interface tended to increase the axial stress  $\sigma$  and decrease the global slip  $g$  of MB tests with respect to those of DS tests.

- In MB tests, symmetric behavior can be assumed up to the peak load, whereas debonding of a single strip should be considered during the softening branch. This resulted in un-symmetric behavior after the peak load.
- The analysis of MB tests comprising 3- and 1-brick blocks confirmed that  $\sigma_1$  increase with the specimen deflection. However, the results showed that  $\sigma_1$  eventually caused damage of the fibers leading to a reduction of the residual stress  $\sigma_f$  for specimens that attained a high deflection.
- Specimens with fully embedded fibers generally showed a higher bond capacity and residual shear stress than specimens with bare fibers at the gap. This difference was attributed to the presence of the matrix edges at the FRCM strip loaded ends that increased the fiber damage in specimens with bare fibers along the gap.
- The MB tests represent a valid tool to investigate the effect of the normal stress component at the matrix-fiber interface on the bond behavior of FRCM composites, which may play an important role in the capacity of FRCM strengthened curved members.
- The execution of modified beam test for the evaluation of the bond properties of EB FRCM application requires longer preparation/casting time and higher complexity in the testing procedures, with respect to direct test set-ups (single- and double-lap shear test). A higher number of recording instruments (LVDTs) is needed and the result interpretation may not be immediate. However, it provides a more accurate characterization of the bond behaviour of FRCM application subjected to non-pure Mode-II loading conditions, for which the effect of normal stresses to the composite plane may determine higher capacity or a more severe fiber damaging.





# 5 STUDY OF THE EFFECT OF FLEXURAL DEFLECTION ON THE BOND BEHAVIOUR OF FRCM-CONCRETE JOINTS

In the last few years, fiber-reinforced cementitious matrix composites have been attracting increasing interest as externally bonded reinforcement of existing reinforced concrete structures. The effectiveness of FRCM composites in contributing to the axial [14,15], bending [16,17], and shear [18,19] capacity of RC members, was researched in several studies nowadays available in the scientific literature. However, due to the mentioned poor impregnation capability of inorganic matrix (see Chapter 3), a premature loss of the strengthening contribution may occur due to premature debonding at the matrix-fiber interface and, in some cases, to a textile telescopic failure (Figure 3.2). Accordingly, the FRCM bond capacity represents a fundamental parameter for the estimation of the composite contribution to the strengthened member load-carrying capacity, as recognized by the recently-released Italian guidelines for design and construction of EBR FRCM reinforcements systems for strengthening existing structures [47].

In the literature, different set-ups were adopted to investigate the bond capacity of externally bonded reinforcement of concrete and masonry members, such as single- and double-lap direct shear test, described in Section 3.1.1. In these tests, the interface is

generally assumed to be subjected to a pure fracture mechanics Mode-II loading condition (i.e. only subjected to tangential stresses), although stress components normal to the interface can arise due to the eccentricity between the forces applied to the bonded strips and substrate [68]. The presence of interface normal stress components that tend to open the interface crack, which is thus subjected to a non-pure Mode-II loading condition, was observed at the ends of fiber-reinforced polymer strengthened RC beams and was postulated to be responsible of the plate end debonding failure [67]. However, normal stresses that tend to push the composite toward the interface were observed away from the composite ends in FRP strengthened RC beams. These stresses were assumed to increase the interface bond capacity depending on the member cross-section curvature [93] and were accounted for in the formulation provided by fib bulletin 90 [94] to compute the composite maximum force associated with intermediate-crack induced debonding failure. A beneficial effect of stresses normal to the interface where debonding occurs was also observed in FRP- and FRCM-strengthened curved masonry members with composite strips externally bonded on the member convex face [95,96].

When a unidirectional FRCM strengthening is applied to the intrados (or extrados) of a reinforced concrete beam, subjected to bending, the member cross-section curvature and/or its deflection, determines a misalignment of the tensile force acting on FRCM fibers from the matrix-fiber interface plane, of an angle  $\alpha$ , referred to as deflection angle in Figure 5.1. This, in turn, induces the presence of a load component orthogonal to the FRCM textile plane (i.e. matrix edge reaction force) and may cause a bond behavior different from that observed in direct shear tests. The presence of a stress component orthogonal to the composite plane increases the interface capacity if the sense is toward the support (negative Mode-I component), whereas it may reduce the Mode-II bond capacity if oriented toward the external surface of the composite, i.e. if a positive Mode-I loading condition is present [66]. Experimental direct shear tests were carried out on curved elements, to investigate the effect of interface normal stress components on EB FRP, FRCM, and SRG composites [72,97,98]. These studies showed that interface normal stresses arise along the interface as an effect of the member curvature and confirmed that they can increase the composite bond capacity in the case of convex substrates, whereas they induce premature debonding in the case of concave substrates [73].

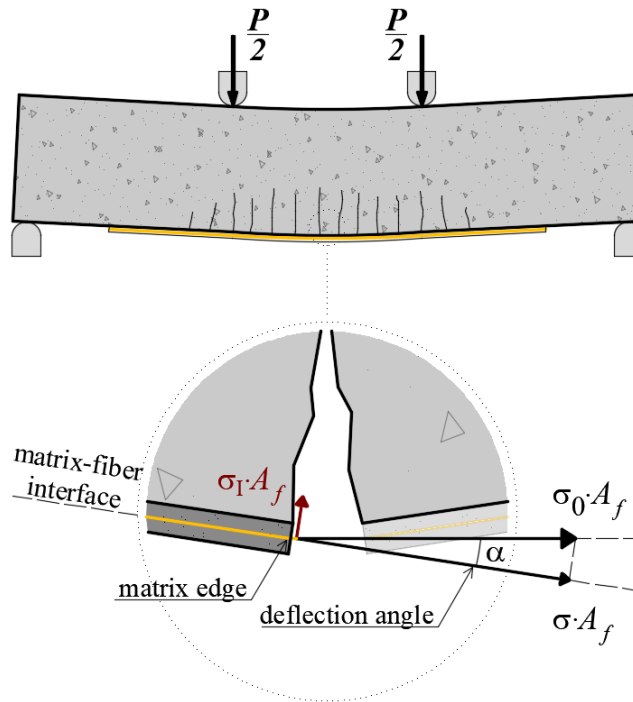


Figure 5.1: Sketch of a FRCM strengthened RC beam undergoing excessive deflection.

To investigate the effect of normal stress component on the FRCM bond behavior, small-scale beam tests can be adopted (see Section 3.1.2). Among them, two principal set-ups have been reported in the literature: 1) in the notched beam test, a single substrate prism is tested in a three-point bending test set-up [99]. The prism is notched similarly to a fracture mechanics test specimen. The FRCM composite strip is then applied to the face of the prism where the notch mouth is located, i.e. perpendicular to the faces of the notch. 2) In the modified beam test, two prisms made of concrete or masonry (depending on the substrate of interest) are connected by a steel element that functions as a cylindrical hinge. The FRCM composite strip is applied to the face of the two prisms opposite to the steel hinge and the assembly is then tested in a three- or four-point bending test set-up. However, quite limited results are available regarding beam tests aimed at studying the FRCM-concrete behavior, whereas more contribution can be found on the behavior of the FRCM-masonry interface due to the significant normal stress component that may arise where cracks in masonry members occur [97,100]. An analogue scenario was experimentally observed by [89,90] throughout the investigations of concrete mixtures enriched with randomly-oriented short steel fibers, whose load bearing capacity increased when, after concrete cracking, fibers were oriented at angles with respect to the pulling action. This was attributed to an additional frictional snubbing force, depending on the orthogonal stress component, and to the bending of the steel fiber at the corner of exit from the matrix.

In this chapter, the effect of normal stress component at the matrix-fiber interface of a polyparaphenylene benzo-bisoxazole (PBO) composite applied onto a concrete substrate is studied. The results of eight single-lap direct shear tests of PBO FRCM-concrete joints and of six modified beam tests with the same PBO FRCM and concrete substrates are presented. The composite bonded length and width were kept constant in the two set-ups. Two different layouts of the composite strips were considered in the modified beam tests to investigate the influence of the matrix at the specimen midspan on the behavior observed. The experimental results described in this chapter help shedding light on the complex bond behavior of FRCM composites when shear and normal stresses are present in the composite-substrate joint.

## 5.1 Materials

A PBO FRCM composite, comprising one layer of an unbalanced textile and two 5 mm thick layers of a cement-based matrix, was used in this study. The textile had longitudinal and transversal bundles spaced at 10 and 17.5 mm on center, respectively [80] (see Figure 3.8a). The equivalent thickness of the textile in longitudinal direction, which was the direction parallel to the composite strip longitudinal axes, was  $t_f=0.046$  mm. The average tensile strength and elastic modulus of the PBO textile in longitudinal direction were obtained in [101] by tensile tests of PBO textile strips with different widths and were equal to 3015 MPa (CoV=6.8%) and 206 GPa (CoV=6.5%), respectively. The cement-based matrix compressive and splitting tensile strength were measured by tests on matrix cylinders with diameter 50 mm and height 100 mm and were equal to 28.4 MPa (CoV=9.2%) and 3.5 MPa (CoV=23.1%), respectively [101].

Two different concrete batches were used for the concrete blocks employed in the modified beam and in the direct shear tests. The blocks employed in all modified beam tests and in the direct shear tests with bonded width  $b_1=60$  mm (see Sections 5.2.1 and 5.2.2) were characterized by compressive tests on six  $150\times 150\times 150$  mm<sup>3</sup> cubes and by splitting tests on five  $100\times 200$  mm<sup>2</sup> cylinders. The average compressive and splitting tensile strengths obtained were 37.9 MPa (CoV=6.02%) and 2.50 MPa (CoV=18.40%), respectively. The blocks employed for the direct shear tests with bonded width  $b_1=50$  mm (see Section 5.2.2) were characterized by compressive tests on seven  $150\times 150\times 150$  mm<sup>3</sup> cubes, which provided an average compressive strength of 29.4 MPa (CoV=5.41%). The corresponding tensile strength was not measured experimentally.

## 5.2 Experimental set-ups

Fourteen tests [8 single-lap direct shear (DS) and 6 modified beam tests (MB)] were performed. The specimen dimensions and test set-ups are shown in Figure 5.2 and are described in the following sections. Both MB and DS tests were performed in displacement control by monotonically increasing the machine stroke at a rate of 0.2 mm/min [35].

### 5.2.1 Modified beam tests

The modified beam (MB) specimens were comprised of two concrete prisms connected by a cylindrical hinge at the top side and by a composite strip along the bottom faces (Figure 5.2a). Two different strip layouts were adopted for these specimens. In the first, named bare-fiber layout, the textile was left bare (i.e. it was not impregnated by the matrix) along 60 mm at the modified beam midspan (Figure 5.2b), which allowed for a direct measure of the bare fiber-substrate relative displacement at the two loaded ends of the specimen (Figure 5.2b). In the second layout, named bond-gap layout, the matrix was not bonded to the substrate along 60 mm at the modified beam midspan (Figure 5.2c). This layout reproduces the composite-substrate bond interruption generally adopted at the loaded end of FRP- and FRCM-concrete direct shear and modified beam tests to prevent the substrate wedge failure [35,102]. For both the bare-fiber and bond-gap layout, the bonded length and width of the strip applied to each concrete prism were  $L=300$  mm and  $b_1=60$  mm (i.e. 6 longitudinal fiber bundles), respectively. A portion of textile was left bare at the strip free ends of specimens with bond-gap layout (Figure 5.2d), to measure the bare fiber-substrate relative displacement at the free ends.

The MB specimens were tested under a 4-point bending configuration. Two cylindrical steel supports were placed at a distance of 900 mm while the load was applied using two steel cylinders placed at a distance of 80 mm from each other and connected to the machine through a spherical hinge. The specimens were equipped with six or eight (depending on the strip layout) linear variable displacement transducers (LVDTs). In bare-fiber specimens, four LVDTs (two on each side of the strip, named LVDT B1, B2, B3, and B4, see Figure 5.2b) were employed to measure the fiber-substrate relative displacement at the two loaded ends. LVDTs B1-B4 were attached to the concrete substrate and reacted off of aluminum L-shaped plates bonded to the bare fibers immediately outside the matrix at the loaded ends. In bond-gap specimens, two LVDTs (one on each side of the strip, named LVDT G1 and G2, see Figure 5.2c) attached to the

concrete block and reacting off of aluminum L-shaped plates attached to the opposite block, were used to measure the relative displacement between blocks. Other four LVDTs (two on each block, one on each side of the composite strip, namely, LVDT G3, G4, G5, and G6, see Figure 5.2d) measured the fiber-substrate relative displacement at the free ends of specimens with bond-gap strip layout. Finally, in all MB specimens, two LVDTs (one on each side of the specimen, named LVDT V1 and V2, see Figure 5.2b and c) were used to measure the vertical deflection at midspan.

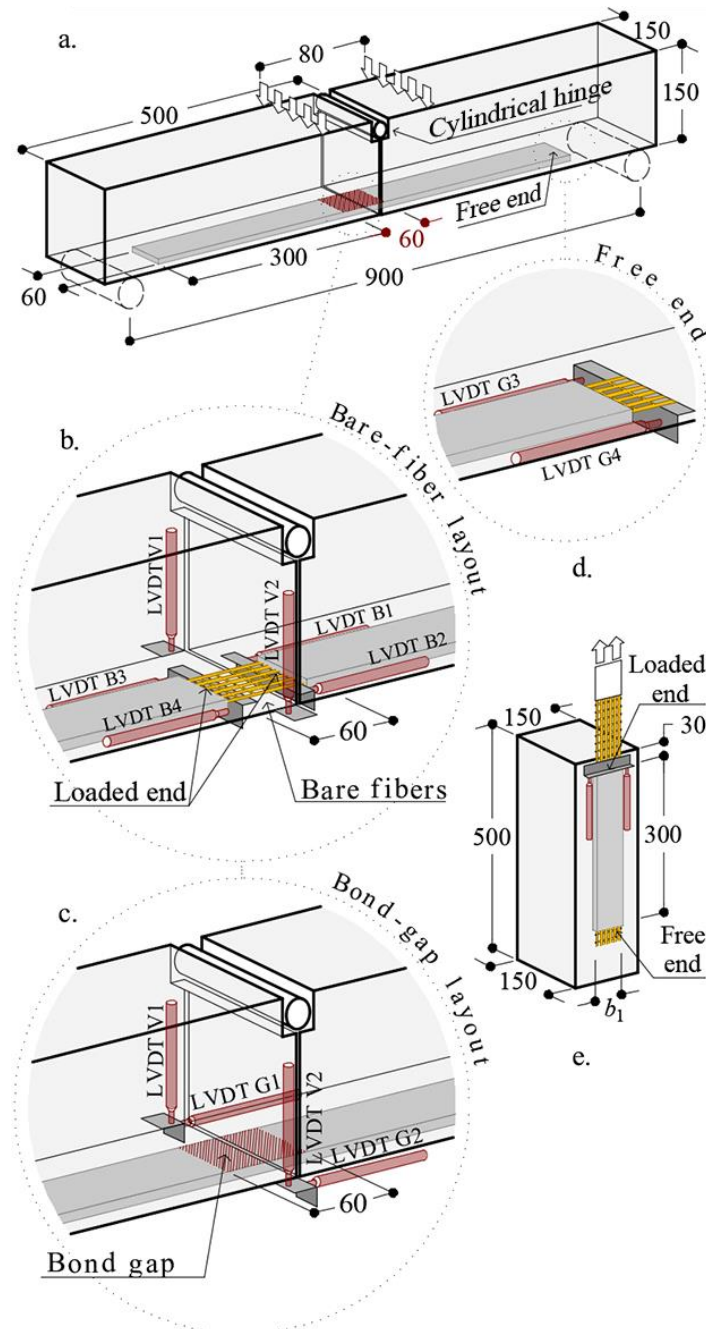


Figure 5.2: a) Modified beam test geometry and set-up: b) bare-fiber, c) bond-gap specimen midspan, and d) detail of the free end. e) Direct shear test geometry and set-up (dimensions in mm).

### 5.2.2 Direct shear test

The DS test specimens were realized by applying the same PBO FRCM used in the MB test to the lateral surface of a concrete prism with  $150 \times 150 \text{ mm}^2$  cross-section and a 500 mm length (Figure 5.2e). The composite bonded length was  $L=300 \text{ mm}$ , whereas two bonded widths, namely  $b_1=50 \text{ mm}$  (including 5 longitudinal fiber bundles) and  $b_1=60 \text{ mm}$  (including 6 longitudinal fiber bundles), were employed. The composite strip loaded end was placed 30 mm far from the concrete block edge, as usually recommended to avoid substrate wedge failure [35,102]. The matrix thickness was in total equal to 10 mm (5 mm for each layer) as in the MB test specimens. The textile was left bare for approximately 300 mm outside the loaded end and was equipped with two epoxy bonded steel plates at the end to facilitate gripping by the testing machine (Figure 5.2e). An L-shaped aluminum plate was glued to the bare textile just outside the composite strip at the loaded end. Two LVDTs were attached to the concrete at the loaded end and reacted off of the L-shaped aluminum plate to measure the fiber-concrete relative displacement.

## 5.3 Test results

Specimens were named following the notation MB\_(or DS)\_X\_Y\_(G or B)\_n, where MB=modified beam test or DS=direct shear test, X and Y are the bonded length and width (in mm), respectively, G (=bond-gap) or B (=bare-fibers) indicates the strip layout for the MB tests, and n is the specimen number. The specimens are listed Table 5.1 in and Table 5.2.

For all specimens, failure occurred due to debonding of the fiber from the embedding matrix, as previously reported for several different FRCM composites comprising one or two layers of textile [50,76,86,103]. In the following sections, the load response and bond behavior of the PBO FRCM observed are discussed for each set-up considered.



Specimen	$w$ [mm]	$h$ [mm]	$l_w$ [mm]	$L^\dagger$ [mm]	$b_1$ [mm]	$\sigma_0^*$ [MPa]	$g^*$ [mm]	$\sigma_{0f}$ [MPa]	$g_f$ [mm]
MB_300_60_B_1						2220	1.47	199	5.59
MB_300_60_B_2	410	150	200	300	60	2124	2.47	481	5.51
MB_300_60_B_3						2135	1.61	430	5.85
Average ( $\bar{\cdot}$ )						2159	1.83	370	6.00
CoV	-	-	-	-	-	0.024	0.243	0.406	0.031
Average curve MB_B_avg ( $\bar{\cdot}$ )						2142	1.32	277	5.55
MB_300_60_G_1						2499	1.89	671	4.59
MB_300_60_G_2	410	150	200	300	60	2514	2.14	283	4.72
MB_300_60_G_3						2617	1.58	434	6.35
Average ( $\bar{\cdot}$ )						2543	1.87	463	5.22
CoV	-	-	-	-	-	0.025	0.149	0.422	0.188
Average curve MB_G_avg ( $\bar{\cdot}$ )						2522	1.89	514	5.94

$^\dagger$ Bonded length of a single block;  $\sigma_0^*$  = peak fiber stress;  $g^*$  = global slip at the peak fiber stress;  $\sigma_{0f}$  = residual fiber stress,  $g_f$  = global slip at the first attainment of the residual fiber stress.

Table 5.1: Modified beam experimental test results.

Specimen	$L$ [mm]	$b_1$ [mm]	$\sigma^*$ [MPa]	$g^*$ [mm]	$\sigma_f$ [MPa]	$g_f$ [mm]
DS_300_60_1			2090	0.95	123	5.98
DS_300_60_2	300	60	1673	2.86	319	6.51
DS_300_60_3			1813	2.15	112	6.20
DS_300_50_1			1938	1.39	239	6.92
DS_300_50_2			2230	0.87	219	7.81
DS_300_50_3	300	50	2224	1.22	231	7.03
DS_300_50_4			2190	1.64	331	6.94
DS_300_50_5			2148	1.15	269	6.92
Average ( $\bar{\cdot}$ )			2038	1.53	230	6.79
CoV	-	-	0.102	0.441	0.350	0.083
Average curve DS_avg ( $\bar{\cdot}$ )			1971	1.15	230	7.15

$\sigma^*$  = peak axial stress;  $g^*$  = global slip at the peak axial stress;  $\sigma_f$  = residual axial stress;  $g_f$  = global slip at the first attainment of the residual axial stress.

Table 5.2: Direct shear experimental test results.

### 5.3.1 Modified beam test - Bare-fiber layout

The load response of specimen MB\_300\_60\_B\_3, which is representative of the load responses obtained with MB tests with bare-fiber layout, is shown in Figure 5.3a. For bare-fiber specimens, the global slip  $g$  is the average of the displacements measured by the two LVDTs reading at the loaded end of the same concrete block (either LVDT B1 and B2 or B3 and B4, see Figure 5.2b), whereas the fiber stress  $\sigma_0$  (see Figure 5.1) was computed according to Eq. (5.1), by enforcing the specimen equilibrium, as shown in Figure 5.4a:

$$\sigma_0 = \frac{T}{A} = \frac{Pw + 2Wl_w}{2h \cos \alpha} \cdot \frac{1}{A} \quad (5.1)$$

where  $T = \sigma_0 A$  is the force in the composite,  $A$  is the fiber cross-sectional area ( $A = t_f b_1$ ),  $\alpha$  is the specimen rotation angle,  $P$  is the load measured by the machine load cell,  $w$  is the distance between one of the two loading points and the closest support,  $W = 258$  N is the self-weight of the prism (assumed concentrated in the prism centroid),  $l_w$  is the horizontal distance between the prism centroid and the closest support, and  $h$  is the vertical distance between the axis of the cylindrical hinge and textile plane (see Table 5.1). Eq. (5.1) assumes that the applied load  $P$  (see Figure 5.4a) is equally distributed among the two applied point loads, which is justified by the adoption of a spherical joint, connecting the load cylinders to the testing machine, and by the reduced distance between the two load cylinders (80 mm, see Figure 5.2a).

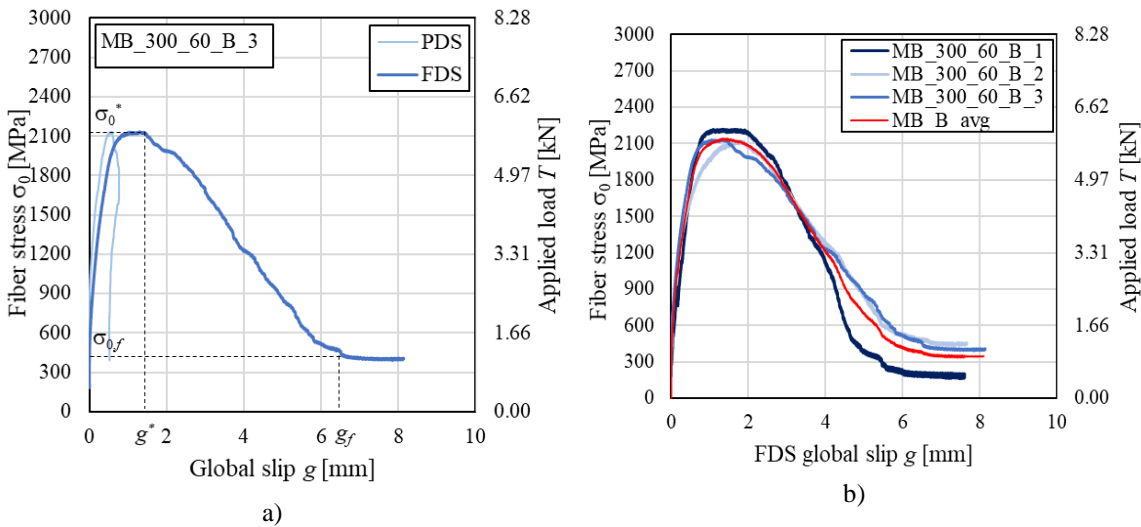


Figure 5.3: Load responses of bare-fiber MB tests: a) specimen MB\_300\_60\_B\_3 ( $g$  measured at the PDS and FDS) and b) specimens MB\_300\_60\_B\_1-3 ( $g$  measured at the FDS).

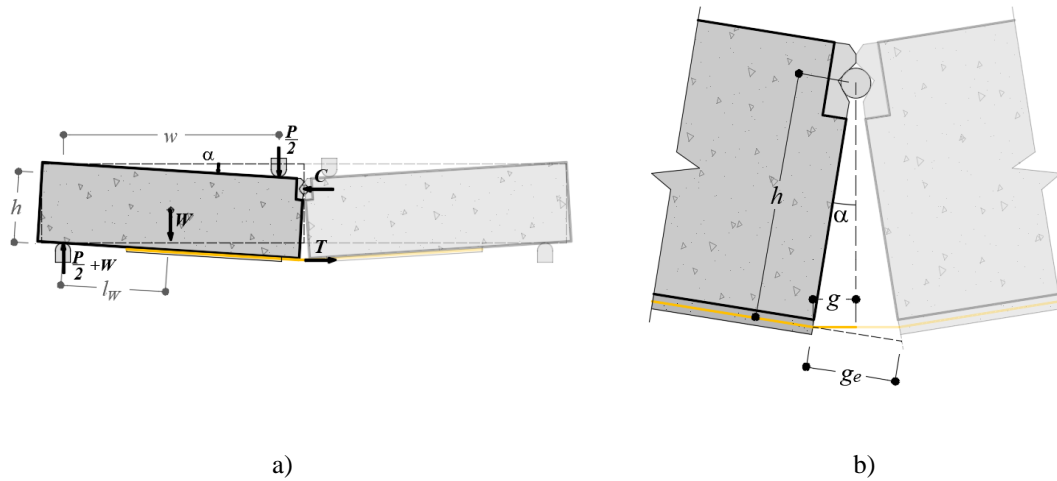


Figure 5.4: a) Free body diagram of the MB test; b) modified beam test: midspan opening displacement  $g_e$ .

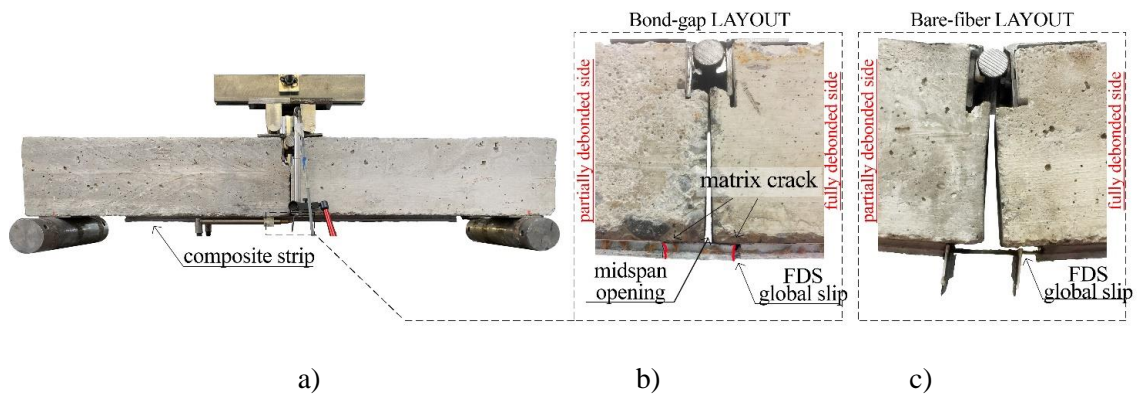


Figure 5.5: MB test: a) side view and detail of the midspan for the b) bond-gap and c) bare-fiber layouts.

In Figure 5.3a, the fiber stress  $\sigma_0$  (or applied load  $T$ ) is plotted versus the global slip measured at the two loaded ends. The side of the specimen associated with each global slip is named fully debonded side (FDS) or partially debonded side (PDS) depending on the behavior observed during the test, as explained in the following.

The load responses in Figure 5.3 showed an initially linear behavior, associated with an almost identical the matrix-fiber slip at the two specimen loaded ends (Figure 5.3a). As the machine stroke was increased, the load response became non-linear due to the presence of micro cracking at the matrix-fiber interface. At the end of the linear branch, the fiber slip at the loaded end associated with the fully debonded side (FDS) started to increase at a higher rate compared to that at the opposite loaded end, which is associated with the partially debonded side (PDS). With increasing machine stroke, the fiber stress attained the peak value  $\sigma_0^*$  (associated to a global slip  $g^*$ ), after which the load (stress)

response showed a softening branch characterized by increasing values of global slip at the FDS, whereas at the PDS  $g$  remained approximately constant or slightly decreased due to the recovery of the fiber elastic deformation (see Figure 5.3a and Figure 5.5c). At the end of the test, the fiber stress attained a constant value, equal to  $\sigma_{0,f}$ , due to the presence of friction at the matrix-fiber interface (see Chapter 3 and Figure 3.4). For specimen MB\_300\_60\_B\_1,  $\sigma_{0,f}$  was lower than that of specimens MB\_300\_60\_B\_2 and 3 (Figure 5.3b). This difference was attributed to the rupture of some fiber filaments, which might have been caused by the stress component normal to the fiber textile plane, as previously observed for modified beam tests comprising masonry blocks.

### 5.3.2 Modified beam test - Bond-gap layout

Figure 5.6a shows the  $\sigma_0 - g_e$  response of a representative MB test with bond-gap layout (specimen MB\_300\_60\_G\_2), where  $g_e$  is the average displacement recorded by LVDT G1 and G2 (see Figure 5.2c and Figure 5.4b) and  $\sigma_0$  is the fiber stress computed by Eq. (5.1). It should be noted that the displacement  $g_e$  is affected by the relative rotation between blocks (Figure 5.4b) and should not be referred to as the global slip  $g$ . The average displacement measured by each couple of LVDTs reading at the free end of each block (either LVDT G3 and G4 or G5 and G6, see Figure 5.2e) was named free end slip  $s_F$ .

The MB tests with bond-gap layout showed an initial linear load response, which was interrupted due to the occurrence of a matrix transversal crack located at one of the two loaded ends (i.e. at the beginning of the bond gap, see Figure 5.5b). This crack occurred at a fiber stress  $\sigma_{0,A}$  of approximately 700 MPa (associated with the displacement  $g_{e,A}$ , see Figure 5.6a), which is equivalent to a matrix stress of  $\sigma_{m,A} = \sigma_{0,A} \times A/A_m = 3.22$  MPa (where  $A_m = 50 \text{ mm}^2$  is the matrix cross-sectional area) that is consistent with the matrix splitting tensile strength measured (3.5 MPa, see Section 5.1). After the occurrence of the first matrix crack, the slope of the load response decreased significantly and, with increasing the machine stroke, a new matrix crack occurred at the loaded end opposite to that where the first matrix crack occurred (Figure 5.5b). These two matrix cracks opened at different rates during the test. After the attainment of the peak fiber stress  $\sigma_0^*$ , which was associated with the displacement  $g_e^*$  (Figure 5.6a), only one of the two matrix cracks [located at the fully debonded side (FDS)], continued to open whereas the width of the other remained approximately constant (PDS). This indicates that, as in the

case of MB test with bare-fiber layout, the composite strip behavior was not perfectly symmetrical during the test and the matrix-fiber slip increased only in one side of the specimen. The LVDTs reading at the free ends confirmed this observation, since free end matrix-fiber slip  $s_F$  was recorded only on the specimen FDS, where the crack whose width increased throughout the entire test was located. The  $\sigma_0 - s_F$  curve of specimen MB\_300\_60\_G\_3 is shown in Figure 5.6a.

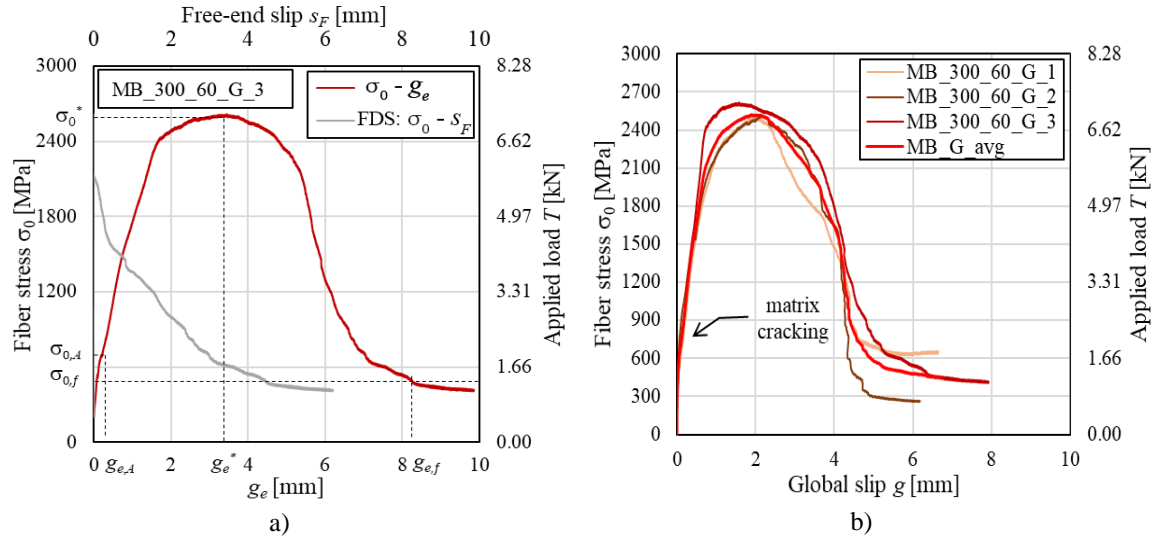


Figure 5.6: Load responses of bond-gap MB tests: a) specimen MB\_300\_60\_G\_2 and b) specimens MB\_300\_60\_G\_1-3 [ $g$  was computed with Eq.(5.2)].

Based on these observations and taking into account the rotation of the concrete blocks (Figure 5.4b), the FDS global slip  $g$  for the MB tests with bond-gap layout was computed as:

$$\begin{aligned}
 g &= \frac{g_e}{2} \left[ \frac{\cos(2\alpha)}{\cos \alpha} \right] & g_e \leq g_{e,A} \\
 g &= \left( \frac{g_e}{2} - \frac{|\sigma_0 - \sigma_{0,A}| l_g}{2E_f} \right) \left[ \frac{\cos(2\alpha)}{\cos \alpha} \right] & g_{e,A} < g_e \leq g_e^* \\
 g &= \left( g_e - \frac{|\sigma_0 - \sigma_{0,A}| l_g}{E_f} \right) \left[ \frac{\cos(2\alpha)}{\cos \alpha} \right] - g^* & g_e > g_e^*
 \end{aligned} \tag{5.2}$$

where  $\sigma_{0,A}$  and  $g_{e,A}$  are the fiber stress at the first matrix crack and the corresponding average displacement measured by LVDTs G1 and G2 (see Figure 5.6a). The first equation in Eq. (5.2) describes the first branch of the  $\sigma_0 - g$  curve, where the matrix is not cracked and the fibers contribution to the composite stress is neglected. The second and third equations in Eq. (5.2) are based on the assumption that the global slip is equal

at the two loaded ends until the attainment of the peak fiber stress  $\sigma_0^*$ , whereas it increases only at one loaded end after  $\sigma_0^*$ . These two latter equations also account for the elastic deformation of the PBO textile along the bond gap length  $l_g=60$  mm (Figure 5.2c), which should not be included in the global slip  $g$ .

Assuming rigid rotation of the concrete blocks, the rotation angle  $\alpha$  can be expressed as:

$$\alpha(g) = \arcsin\left(\frac{g}{h}\right) \quad (5.3)$$

where  $h$  (Figure 5.4b) is the vertical distance between the fiber exit point and the center of rotation of the block. It should be noted that Eq. (5.3) assumes the fiber exit point coincident with the block edge.

The system of non-linear equations comprising Eqs. (5.2) and (5.3) provides, given the LVDT readings  $g_e$ , the global slip  $g$  and the angle  $\alpha$  throughout the entire bond-gap MB test. The fiber stress  $\sigma_0$  – global slip  $g$  curves of specimens MB\_300\_60\_G\_1-3 obtained with Eqs. (5.2) and (5.3) are reported in Figure 5.6b. Figure 5.6b shows that, at completion of the test, the fiber stress plateaued at a constant value  $\sigma_{0,f}$  associated with friction at the matrix-fiber interface.

### 5.3.3 Direct shear test

The load response obtained by DS tests is shown in Figure 5.7a, whereas a photo of specimen DS\_300\_60\_1 is shown in Figure 5.7b. In single-lap direct shear tests, the eccentricity between the force applied to the fiber and the support restraint entails for the presence of a bending moment that induces a Mode-I loading condition at the matrix-fiber interface. Since the presence of the external (i.e. not in contact with the support) matrix layer limits the effect of this Mode-I loading condition, a pure Mode-II loading condition can be postulated at the matrix-fiber interface. Therefore, the axial stress  $\sigma$  of DS tests was simply obtained as the ratio of the force applied by the machine and the cross-sectional area of the fibers  $A$ , whereas the global slip  $g$  was computed as the average of the displacement measured by LVDTs at the loaded end (Figure 5.2e).

Similarly, to modified beam test, the curves showed an initial linear branch until micro-cracking occurred at the matrix-fiber interface and the response became non-linear. After the attainment of the peak axial stress  $\sigma^*$ , a softening behavior was observed, i.e. the applied stress decreased with increasing the global slip  $g$ . At completion of the test,

the applied stress plateaued at a constant value  $\sigma_f$  associated with friction at the matrix-fiber interface (see Chapter 3 and Figure 3.4).

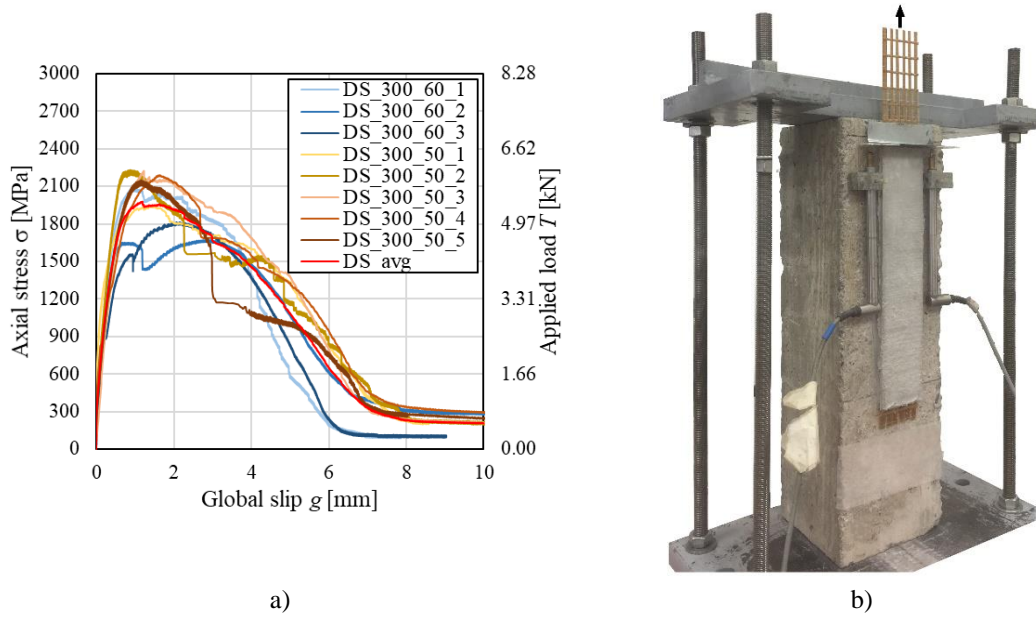


Figure 5.7: a) Load responses of DS tests. b) Direct shear test set-up.

## 5.4 Discussion

Key parameters obtained from MB and DS tests are reported in Table 5.1 in and Table 5.2, respectively, along with average values of nominally equal specimens and corresponding coefficient of variation (CoV). Key parameters include the peak fiber stress  $\sigma_0^*$  (or axial stress  $\sigma^*$  for DS test), corresponding global slip  $g^*$ , residual friction fiber stress  $\sigma_{0,f}$  (or axial stress  $\sigma_f$  for DS test), and the corresponding global slip  $g_f$ . According to Figure 3.4, the residual stresses  $\sigma_{0,f}$  and  $\sigma_f$  were computed as the average applied stress at the end of the test for which the derivative  $d\sigma_0/dg$  or  $d\sigma/dg$  were comprised within the range  $-200$  and  $0$  MPa/mm. The value of  $g_f$  was defined as the first global slip value for which the inequalities  $-200 \leq d\sigma_0/dg \leq 0$  MPa/mm or  $-200 \leq d\sigma/dg \leq 0$  MPa/mm hold.

The envelopes of load responses of nominally equal MB and DS specimens are compared in Figure 5.8a. The results obtained showed that, although the same composite bonded length was considered for MB and DS tests, the average peak fiber stress  $\bar{\sigma}_0^*$  of bond-gap and bare-fiber MB tests ( $\bar{\sigma}_0^* = 2543$  MPa and  $\bar{\sigma}_0^* = 2159$  MPa, respectively) was 24.8% and 5.9% higher than that of DS tests ( $\bar{\sigma}^* = 2038$  MPa). This difference may be attributed to the presence of a fiber stress component,  $\sigma_1$ , normal to the matrix-fiber interface, induced by the specimen deflection in MB tests (Figure 5.4a).

The normal component  $\sigma_1$  (see Figure 5.1) is proportional to the cross-section curvature and tends to enhance the specimen bond capacity generating an additional frictional force at the matrix-fiber interface [90]. The normal component  $\sigma_1$  depends on the variation of the fiber axial direction along the bonded length. Due to the specimen deflection, the fiber pushes against the matrix internal layer (i.e. the matrix layer in contact with the concrete substrate), which deforms determining a variation of the fiber axial direction and, in turn, the presence of a normal stress component. Therefore, the stress component  $\sigma_1$  vary along the bonded length and its evaluation is cumbersome. Assuming rigid rotation of the concrete prisms comprising the MB specimen and neglecting the matrix deformability,  $\sigma_1$  can be assumed as concentrated at the strip loaded end in bare-fiber MB tests and at the bond gap (where matrix crack occurs) in bond-gap MB tests (Figure 5.4a). This simplification allows for studying the global effect of the normal force component on the FRCM-concrete bond behavior, as previously done for FRCM-masonry MB tests (see Chapter 4). It should be noted that the presence of a stress component normal to the fiber longitudinal direction and concentrated at the fiber exit point, i.e. the matrix crack edge, was previously observed in fiber-reinforced concrete and its effect was named snubbing-friction effect[89,90].

$\sigma_1$  can be assumed proportional to the angle of inclination of the fiber with respect to the matrix-fiber interface  $\alpha$  [89,90], which coincides with the angle of rotation of the concrete prisms. Therefore, the snubbing-friction effect is particularly pronounced at the end of the test, when the specimen deflection is maximum. Accordingly, the average residual fiber stress  $\bar{\sigma}_{0,f}$  of bond-gap and bare-fiber MB tests ( $\bar{\sigma}_{0,f}=463$  MPa and  $\bar{\sigma}_{0,f}=370$  MPa, respectively) was 101.3% and 60.9% higher than the corresponding residual axial stress of DS tests ( $\bar{\sigma}_f=230$  MPa).

However, the presence of a normal stress component was also responsible for the rupture of some fiber filaments in MB tests, as revealed by visual inspection of the fibers at the loaded ends and at matrix cracks at the end of the test. This fiber damage, previously observed in carbon and PBO FRCM-masonry bare-fiber MB tests (see Chapter 4), appeared more pronounced in the case of bare-fiber layout than in the case of bond-gap layout. In bare-fiber specimens, the average peak fiber stress  $\bar{\sigma}_0^*=2159$  MPa and residual fiber stress  $\bar{\sigma}_{0,f}=370$  MPa were 15.1% and 20.1%, respectively, lower than those of bond-gap specimens ( $\bar{\sigma}_0^*=2543$  MPa and  $\bar{\sigma}_{0,f}=463$  MPa). This



difference can be attributed to the presence of the matrix along the entire length of the strip in bond-gap specimens, which may have mitigated the fiber damage caused by the matrix-fiber friction at the fiber exit points. Figure 5.8b shows the envelopes of fiber stress  $\sigma_0$  – midspan deflection  $\delta$  curves of bare-fiber and bond-gap MB tests, where  $\delta$  is the average of the two vertical LVDTs V1 and V2 (Figure 5.2b and c). According to Figure 5.8b, bond-gap specimens provided higher maximum midspan deflections than bare-fiber MB tests. This confirms the influence of the normal stress component  $\sigma_1$  on the specimen capacity. Since bare-fiber and bond-gap specimens have the same geometry (except for the absence of matrix along the bond gap in the former specimens), the attainment of a higher midspan deflection in bond-gap specimens was attributed to the low damage to the fiber, which in turn allowed high values of  $\sigma_1$  and  $\sigma_0^*$ . Finally, the result scatter observed in MB and DS tests was similar. The highest scatter was obtained for residual stress values (CoV=0.422 and CoV=0.406 for bond-gap and bare-fiber MB tests, respectively; CoV=0.350 for DS tests), whereas lower scatter was reported for peak stress values (CoV=0.025 and CoV=0.024 for bond-gap and bare-fiber MB tests, respectively; CoV=0.102 for DS tests). This result scatter can be considered small if compared with those reported in the literature for FRCM composite bond tests [13,21,103]. However, they suggest the need of performing a large number of tests to obtain reliable measures of the composite properties.

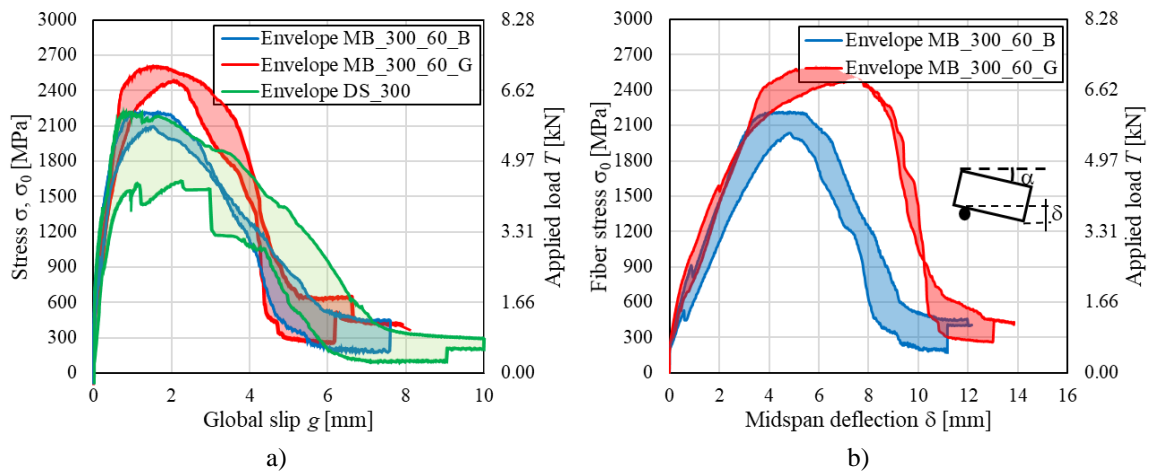


Figure 5.8: Envelopes of a)  $\sigma_0$  - and  $\sigma$  -  $g$  curves of MB and DS tests, respectively, and b)  $\sigma_0$  -  $\delta$  curves of MB tests.

## 5.5 Conclusions and considerations for future guidelines

In this chapter, a direct shear and a modified beam test set-ups were employed to study the bond behavior of a PBO FRCM composite bonded to a concrete substrate. Two different strip layouts, differing for the presence or not of the embedding matrix at the specimen midspan, were investigated in the modified beam tests. The results obtained allowed for drawing the following main conclusions:

- The load response of modified beam tests is consistent with that of direct shear tests. For both set-ups, after an initial linear response, the applied stress became non-linear until reaching the peak stress. The peak stress was followed by a softening branch that ended with constant applied stress due to friction (interlocking) at the matrix-fiber interface.
- Bare-fiber and bond-gap layout exhibited a significant difference in the fatigue lives of corresponding specimens. The former layout allows important simplifications in execution, such as a higher manageability, an easier movement and a direct and independent measurement of global slip at both the loaded-ends. However, the presence of bare fibers across specimen's midspan is poorly representative of a real beam application. The latter specimen layout is closer to a real case application, however, the presence of a continuous strip across the midspan requires a greater care in the casting and setting up procedures, alongside with additional instruments to hold firmly the two blocks to prevent damages to the composite strip.
- The presence of a stress component  $\sigma_1$  orthogonal to the matrix-fiber interface determined an average increase in the MB specimens bond capacity with respect to that of DS test, of approximately 24.8% and 5.9% for bond-gap and bare-fibers specimens, respectively. This was attributed to the snubbing effect of  $\sigma_1$  which tends to enhance the specimen bond capacity, by generating an additional frictional force at the matrix-fiber interface. This effect was shown to be proportional to the cross-section curvature and to the angle of inclination of the fiber with respect to the matrix-fiber interface. Accordingly, the snubbing-friction effect was particularly pronounced at the end of the test, when the specimen deflection was maximum.
- In modified beam tests, the specimen deflection determined the presence of a stress component  $\sigma_1$  normal to the composite plane that tended to push the fibers

against the substrate. The coupling of the stress component  $\sigma_I$  with the shear stress at the matrix-fiber interface, resulted in an average peak stress and friction stress higher than those obtained in direct shear tests. However,  $\sigma_I$  might have been also responsible for local damage of the fiber filaments.

- The modified beam tests clearly showed that the stress component normal to the composite plane have an important effect on the FRCM bond behavior that should be considered for strengthening applications on curved substrates or where significant cross-section curvatures may occur.
- In the face of a longer preparation time demand and a more complex execution, modified beam test provides a more accurate estimation of the bond properties of RC beam externally bonded with FRCM composites subjected to bending, with respect to the commonly employed DS test. Those strengthening applications are influenced by a more pronounced effect of bending moment (and curvature) as an effect of the applied load, which results in the development of normal actions to the composite plane, whose effect cannot be captured by direct test set-ups (such as direct-shear test).

# 6 ANALYTICAL ASSESSMENT OF THE BOND BEHAVIOUR OF FRCM APPLICATIONS USING DS AND MB TESTS.

The analytical study of the bond behaviour of fiber-reinforced composite materials applied to cohesive substrates is fundamental to interpret the composite-substrate stress-transfer mechanism. Differently from what commonly happens in FRP strengthened elements, where failure is due to loss of adhesion at the reinforcement-support interface with removal of a thin layer of substrate (see Figure 3.1c), for FRCM including one layer of textile, failure usually occurs due to debonding of the fiber textile at the matrix-fiber interface with a limited influence of the support mechanical properties (see Chapter 3 and Figure 3.2). In the debonding process of single-layered FRCM composites the tension transfer mechanism, from fibre bundles to embedding matrix, occurs mainly through shear stress exchange at the matrix-fiber interface [104]. The increase of applied load on the composite induces a growth in the interface shear stress, and when it reaches the matrix tensile strength value, a cohesive crack appears in the matrix-fiber interface. The weakening of the matrix under the effect of interfacial stresses is generally referred to as matrix softening and it keeps propagating along the composite length with the increase of textile slippage. The further weakening of the interface, alongside with the propagation of matrix softening, eventually results in local

or complete debonding of the fiber bundles from the embedding matrix, which in turns determines high relative slippage between textile yarns and embedding layer, with residual friction stresses developing at the interface [105].

Several researchers analysed the debonding mechanism of FRCM applications following a fracture mechanic approach and assuming a cohesive material of zero thickness at the textile-matrix interface [69,106–108]. This fictitious material is adopted to introduce a relationship between the applied shear stress  $\tau$  and the corresponding slip  $s$ , along a cohesive surface. This relationship, referred to as cohesive material law or tau-slip ( $\tau$ - $s$ ) law, accounts for both mechanical and geometrical properties of the two materials involved in the cohesive interface and can be determined on the basis of experimental results. Direct shear bond tests can be employed to determine the  $\tau$ - $s$  behaviour of matrix-fiber interface in EB FRCM applications: the relative slip between fiber and matrix is typically measured by means of linear variable displacement transducers (LVDT), the applied load is tracked by the testing machine load cell and the strain field can be recorded using strain gauges applied directly on fibre yarns. However, the presence of the layer of matrix that covers the textile may influence the strain measures for relatively high value of the interface slip, eventually leading to the gauge rupture [104].

Figure 6.1a reports a typical load response of a direct shear test on a PBO FRCM-concrete joint. The axial strain of fiber yarns  $\varepsilon_{xx}(x)$ , was recorded using nine strain gauges placed at different points of the bonded length (i.e. along direction  $x$ , origin at  $x=0$ ). The local strain values experimentally measured, reported in Figure 6.1b, can be fitted using the non-linear equation [105]:

$$\varepsilon_{xx}(x) = \varepsilon_0 + \frac{\alpha + kx}{1 + e^{\frac{x-x_0}{\beta}}} \quad (6.1)$$

with,

$$k = \frac{2\tau_f}{E \cdot t_f} \quad (6.2)$$

where  $\varepsilon_0$ ,  $\alpha$ ,  $\beta$  and  $x_0$  were determined using nonlinear regression analysis of the measured strains, whereas  $\tau_f$  is the friction shear stress associated with the debonded state of the matrix-fiber interface [105].

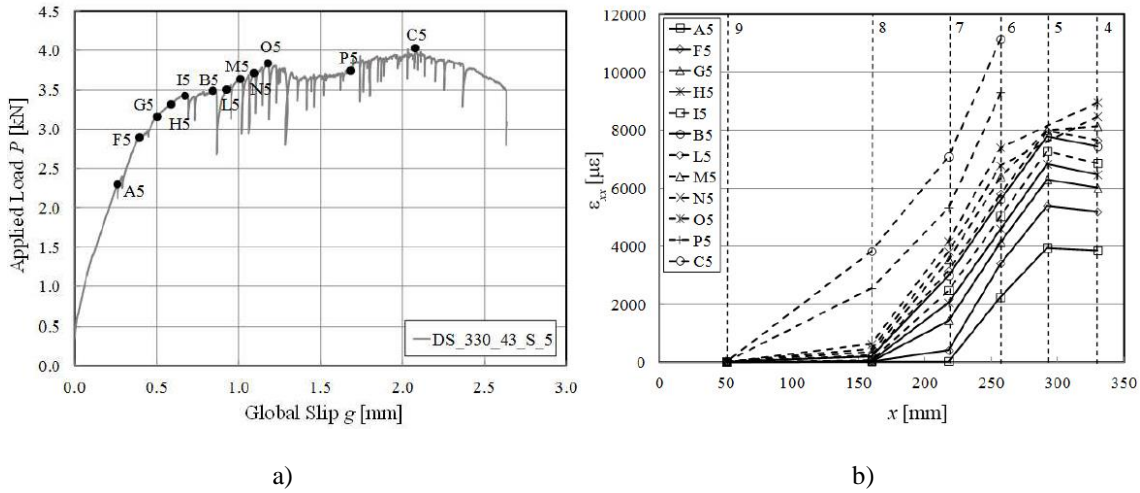


Figure 6.1: direct shear test on PBO-FRCM specimen. a. Applied load  $P$  - global displacement  $g$  curve. b. Interface axial strain  $\epsilon_{yy}$  profiles along the bonded length [105].

A fitting of the  $\epsilon_{xx}(x)$  strain profile with Eq. (6.1) is represented in Figure 6.2a, assuming  $x$  as the applied load direction. The S-shaped strain distribution may be divided into three main parts (Figure 6.2a): Stress Free Zone (SFZ), Stress Transfer Zone (STZ), Fully Debonded Zone (FDZ). In SFZ the axial strain is almost null and the matrix-fiber interface is in its uncracked stage. The STZ is where the stress transfer mechanism mainly takes places. In this zone, the farther part of interface from the loaded end is in its elastic stage whereas the remaining part entered in the softening stage. The length of the STZ, i.e. the minimum distance between the where  $\epsilon_{xx}$  assumes a null value and the point where its derivative reaches a constant value, is referred to as effective bond length,  $l_{eff}$ , or the minimum length needed to fully establish the composite-substrate stress transfer mechanism [105]. In the FDZ, the propagation of the cracking pattern determined the complete debonding at the matrix-fiber interface once  $\epsilon_{deb}$  is reached and strain is linearly increasing due to friction and interlocking phenomena between slipping fiber and matrix.

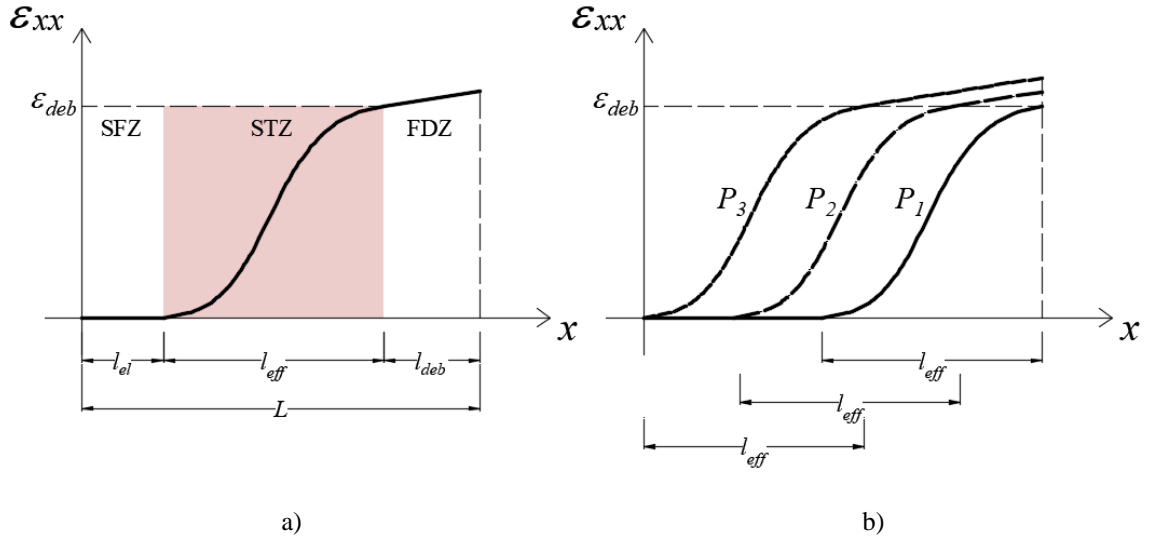


Figure 6.2: a) Fitting curve of  $\epsilon_{xx}$  strain profile along the bonded length  $L$ ;

b) Propagation of the debonding process.

As shown in Figure 6.2b, comparing axial strain profiles corresponding to different applied load values, with  $P_1 < P_2 < P_3$ , a backward translation of the STZ along direction  $x$  can be observed, which corresponds to the propagation of the FDZ along the interface portion closer to the loaded end.

The relative slippage between the fiber and the surrounding matrix, at any point of the bonded length,  $s(x)$ , is the relative displacement between points of the fiber yarn originally in contact before the applied load action and is obtained by integration of the axial strain  $\epsilon_{xx}(x)$ , assuming a pure Mode-II loading condition:

$$s(x) = \int_0^x \epsilon_{xx}(x) dx \quad (6.3)$$

The interfacial shear stress acting along  $x$  direction,  $\tau$ , is obtained by enforcing the equilibrium on an infinitesimal yarn segment of length  $dx$ , as shown in Figure 6.3. The yarn has contact perimeter and elastic modulus respectively equal to  $p$  and  $E$  and is pulled with an applied nominal force  $F$ . The force  $F$ , acting on the single yarn, results from an evenly distributed load  $P$ , acting on the  $n$  yarns included in the composite ( $F=P/n$ ). From the equilibrium along direction  $x$ , one has:

$$(-N + N + dN) = \tau \cdot p \cdot dx \quad (6.4)$$

which results in:

$$\tau(x) = \frac{EA}{p} \cdot \frac{d\epsilon_{xx}(x)}{dx} \quad \text{being } dN = EA \cdot d\epsilon_{xx}(x) \quad (6.5)$$

where  $N$  is the axial force acting on the single fiber bundle cross section area  $A$ .

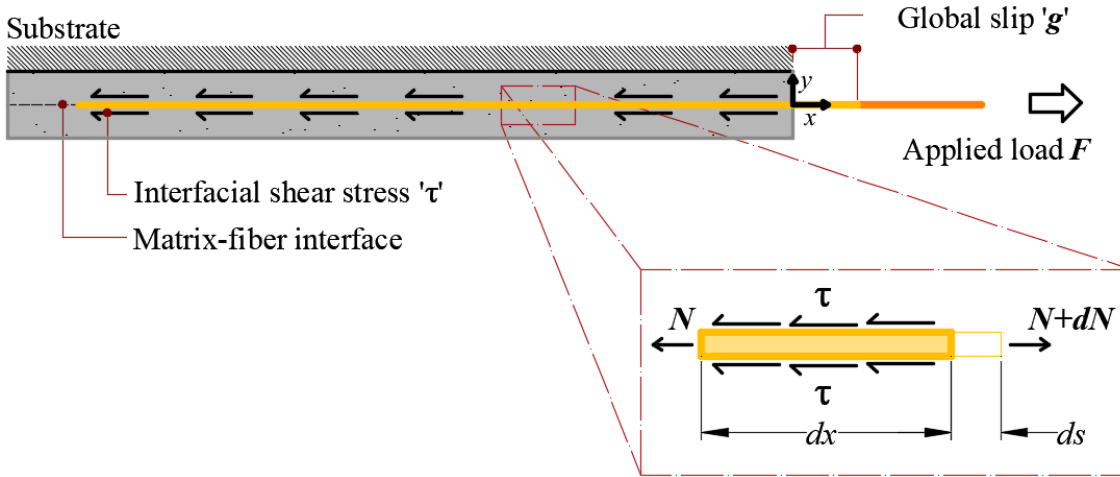


Figure 6.3: Debonding at matrix-fiber interface.

Since the deformation of the matrix layers were reported to be negligible with respect to the fiber-matrix relative displacement [52], named slip  $s$ , the matrix is assumed rigid and the compatibility condition in Eq. (6.6) can be introduced.

$$\varepsilon_{xx}(x) = \frac{ds(x)}{dx} \quad (6.6)$$

Accordingly, Equation (6.5) updates in:

$$\frac{d^2s(x)}{dx^2} - \frac{p}{EA} \tau(s) = 0 \quad (6.7)$$

The axial force  $N(x)$  (the axis are depicted in Figure 6.3) in the bundle is:

$$N(x) = EA \frac{ds}{dx} \quad (6.8)$$

while the bundle slip at the loaded end (i.e.  $x=0$ ), named global slip  $g$ , and the applied force  $F$  at the loaded end are given by  $s(0)$  and  $N(0)$ , respectively. Once a cohesive material law is defined (see Eq.(6.11)), Eq.(6.7) can be solved analytically to obtain the bundle slip  $s(x)$  and the shear stress  $\tau(x)$  along the matrix-fiber interface and to provide the full-range behavior of the FRCM composite.

The  $\tau$ - $s$  relation in FRCM applications is typically non-linear with an ascending and a descending branch followed by an almost horizontal branch (see Figure 6.4). Initially the interface shear stress increases with the slip growth, until reaching a maximum bond stress value,  $\tau_{max}$ , when the slip values  $s_{max}$  is attained. Increasing the relative slippage beyond this value results in the onset of softening in the composite matrix, which in turn



determines a descending branch in the bond-slip law. Once the slip reaches the value  $s_f$ , debonding occurs in the infinitesimal segment of interface, and the corresponding constant value of bond stress,  $\tau_f$ , is due to friction between filaments and between fibres and matrix [105].

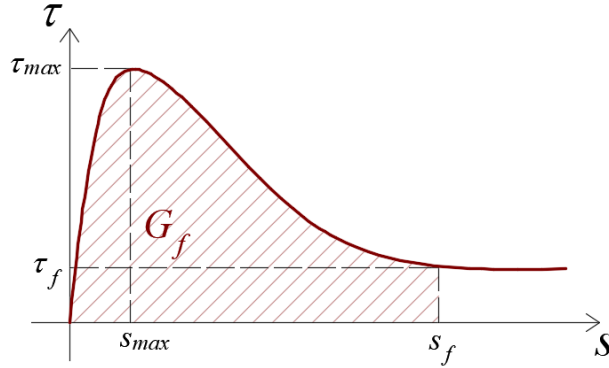


Figure 6.4: Shear stress  $\tau$  - slip  $s$  relation experimentally obtained from specimens equipped with strain gauges.

The area under the bond-slip curve corresponds to the interfacial fracture energy, which is the energy required to create and fully break the elementary unit area of the cohesive crack. In most of the available models in the scientific literature, the composite anchorage strength and the effective bond length are determined as functions of the interfacial fracture energy [105].

$$G_f = \int_0^{s_f} \tau(s) ds \quad (6.9)$$

## 6.1 Rigid-softening simplified model for the CML in FRCM composites

To avoid the need of experimentally measure the fiber strain, indirect methods were proposed to calibrate the CML starting from the load responses of FRCM-substrate joints. In these methods, simplified piece-wise functions with different shapes were adopted for the CML (Figure 6.5). Although piece-wise functions provide a coarser estimation of the FRCM bond behavior than continuous functions, they are particularly attractive because, when simple shapes are adopted (e.g. linear, bilinear, trilinear, etc.), analytical solutions can be obtained [67,109]. Simplified models of CML consist of linearized approximations of the actual bond-slip relations, keeping unaltered the significant parameters of the actual curve, such as  $\tau_{max}$ ,  $\tau_f$ ,  $s_{max}$ ,  $s_f$  and  $G_f$ .

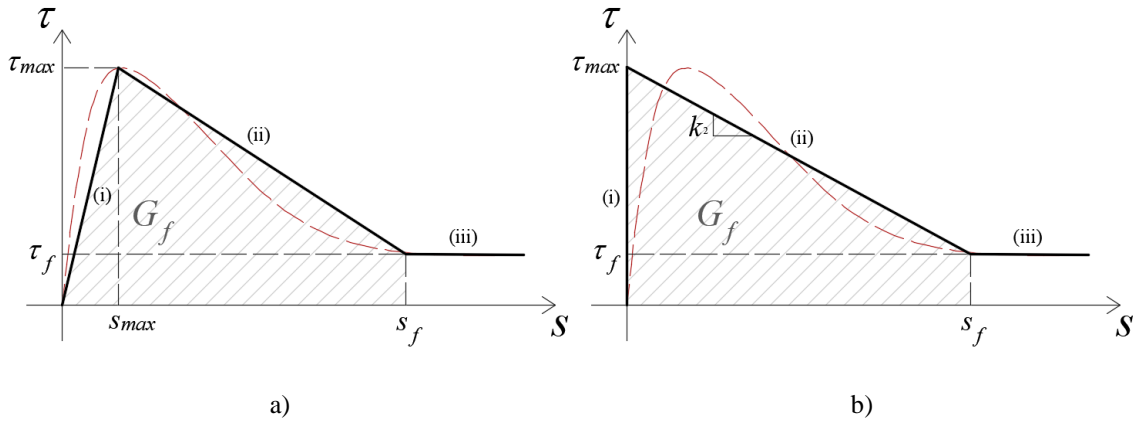


Figure 6.5: Simplified CMLs. a) Tri-linear [105]. b) Rigid-softening

Figure 6.5 reports two simplified CML models. The one proposed in [105](Figure 6.5a) accounted for an initial linear ascending branch representing the uncracked stage of the matrix, that ends when  $\tau = \tau_{max}$ . A descending linear branch follows, responsible for the matrix softening stage, in which the bond stress decreases linearly, due to matrix weakening and cracking, with the slippage increase, until attaining of the limit slip value  $s_f$ . Any further slippage increase beyond this values determined the interface debonding, associate to the horizontal friction branch with  $\tau = \tau_f$ . Eq. (6.10) describes the bond-slip relation for the mentioned simplified model, with  $k_1$  being the slope of the ascending branch and  $-k_2$  the slope of the descending one.

$$\begin{cases} \tau_{zy}(s) = k_1 s & \text{if } 0 \leq s \leq s_{max} \\ \tau_{zy}(s) = -k_2 s + \tau_{max} \left( \frac{k_1 + k_2}{k_1} \right) & \text{if } s_{max} \leq s \leq s_f \\ \tau_{zy}(s) = \tau_f & \text{if } s > s_f \end{cases} \quad (6.10)$$

The analytical solution of the debonding process of FRCM-concrete joints, using the CML showed in Figure 6.5a is presented in [106]. However, for the tri-linear CML adopted, the coexistence of the conditions  $\tau(0)=0$  and  $d\tau/ds \neq \infty$  entail for an non-finite effective bond length. This issue was tackled in [106] and it was showed how this condition does not allow for a simple solution of the analytical problem, unless the assumption of a finite effective length was taken. To overcome this issue, the rigid-softening simplified CML model showed in Figure 6.5b is herein proposed to govern the interface bond-slip behaviour. Accordingly, the interface had infinite stiffness in the initial stage (i.e. until  $\tau = \tau_{max}$ ), whereas a linear softening stage modeled the interface micro cracking and consequent decrease of shear stress with increasing slip. To account for the friction component observed for some FRCM composites, the interface shear

stress did not decrease to zero but remained constant for those interface points that attained the friction shear stress  $\tau_f$  (debonding stage). The interface cohesive material law can be expressed according to Eq. (6.11), where  $-k_2$  is the slope of the linear softening branch.

$$\begin{cases} \tau(s) = \tau_{max} - k_2 s & \text{if } 0 \leq s \leq s_f \\ \tau(s) = \tau_f & \text{if } s > s_f \end{cases} \quad (6.11)$$

The use of the CML proposed in Eq.(6.11) allows for obtaining a closed-form solution of the composite effective bond length, which is a key parameter for the design of FRCM reinforcements.

### 6.1.1 Description of the debonding process

Employing the CML illustrated in Figure 6.5b, the interface shear stress distribution for a bonded length higher than the effective bond length  $l_{eff}$  can be divided in the following stages:

- rigid-softening stage: the interface shear stress is in the softening stage (ii)(see Figure 6.5b) along a length  $l$ , whereas for the remaining bonded length  $L-l$  is in the rigid stage (i) (Figure 6.6).

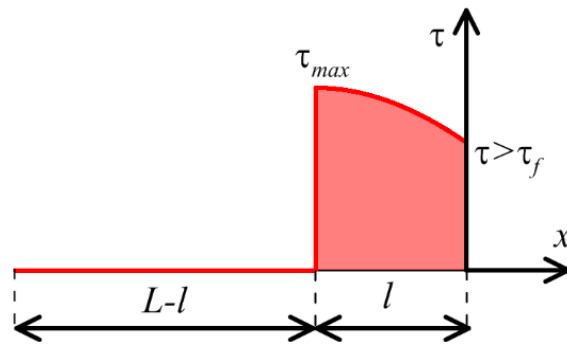


Figure 6.6: Shear stress distribution in the rigid-softening stage ( $L > l_{eff}$ ).

- rigid-softening-debonding stage: when the shear stress at the loaded end is equal to  $\tau_f$ , the bond stress-transfer mechanism is fully established, the length of the softening zone is  $l_{eff}$ , and the rigid-softening stage ends (Figure 6.7a). With increasing global slip, the interface enters in the debonding stage (iii) at the loaded end while the length subjected to the softening stage self-translates toward the free end (i.e.  $x=-L$ ). The interface shear stress distribution in this stage is depicted in Figure 6.7b, where the length of the debonded part is denoted as  $a$ .

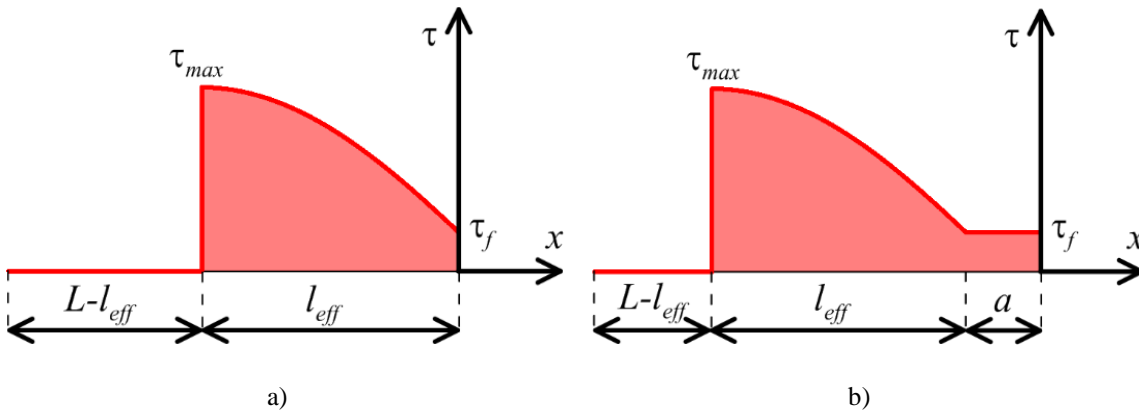


Figure 6.7: Shear stress distribution along the interface a) at the end of the rigid-softening stage and b) during the rigid-softening-debonding stage ( $L > l_{eff}$ ).

- softening-debonding stage: when the interface subjected to the softening stage (ii) reaches the free end, i.e. the shear stress  $\tau(-L) = \tau_{max}$ , the interface enters the softening-debonding stage, the debonded length is equal to  $a = L - l_{eff}$ , and no portion of the interface is in the rigid stage (i) (Figure 6.8a). After this, further increases of the global slip determine the decrease of the interface length subjected to the softening stage (ii) (Figure 6.8b) until the shear stress is equal to the friction stress along the entire bonded length (debonding stage).

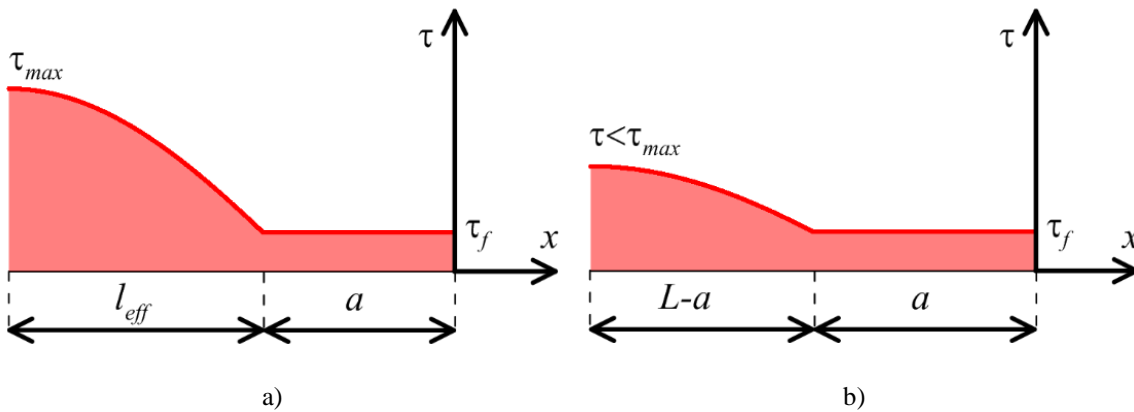


Figure 6.8: Shear stress distribution along the interface a) at the end of the rigid-softening-debonding stage and b) during the softening-debonding stage ( $L > l_{eff}$ ).

When the bonded length is lower than the effective bond length,  $l_{eff}$ , the bond stress-transfer mechanism cannot be fully established and the FRCM debonding interface capacity, i.e. the applied load provided by bond only, cannot be attained [104]. In this case, after a rigid-softening stage (see Figure 6.6) that ends when the shear stress at the free end is equal to  $\tau_{max}$ , the entire interface is subjected to a softening stage where the

shear stress is associated to the descending branch of the bond-slip law, i.e. the softening length  $l$  is equal to the bonded length  $L$  (Figure 6.9a). With increasing global slip, the shear stress at the free end decreases and, when the shear stress at the loaded end attains  $\tau_f$  (Figure 6.9b), the softening stage ends and a softening-debonding stage analogous to that described for  $L > l_{eff}$  (Figure 6.8b) follows.

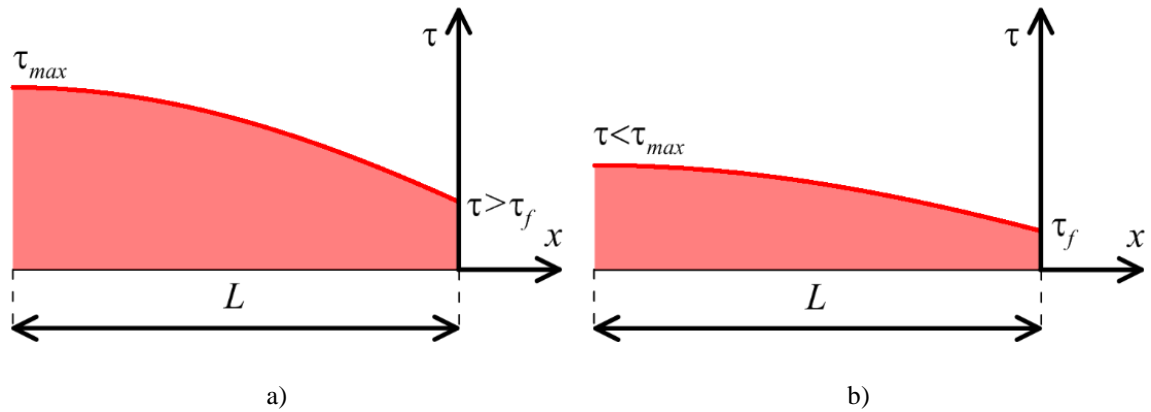


Figure 6.9: Shear stress distribution along the interface a) at the end of the rigid-softening stage and b) during the softening stage ( $L < l_{eff}$ ).

The solution of the bond differential equation in Eq.(6.7) provides the applied load-slip response of each point along the interface. An applied load-global slip curve obtained by solving Eq.(6.7) with the rigid-softening CML proposed and associated to a bonded length higher than the composite effective bond length is reported in Figure 6.10a.

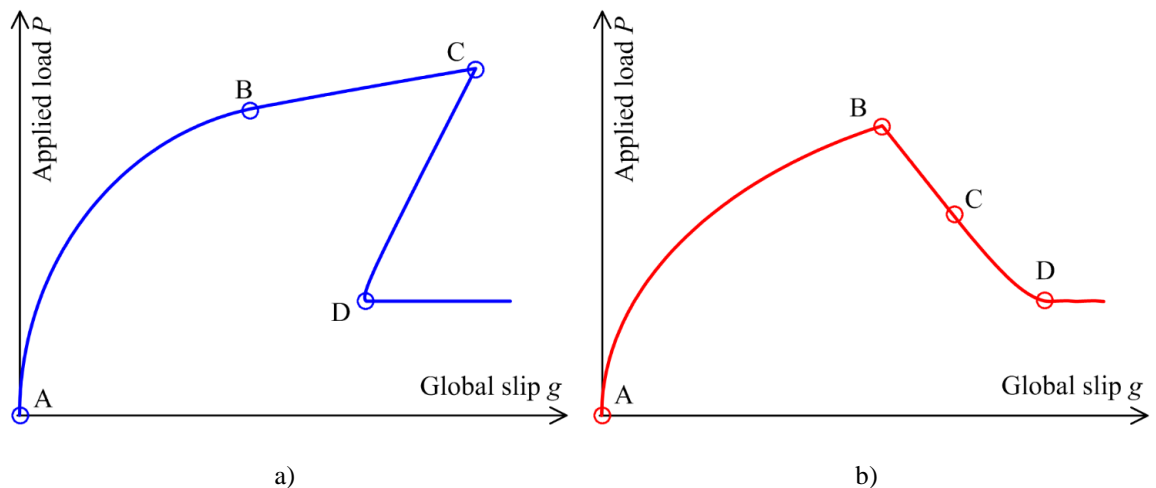


Figure 6.10: Applied load-global slip response for a bonded length a) higher and b) lower than the composite effective bond length,  $l_{eff}$ .

The load response in Figure 6.10a is characterized by the three stages mentioned above for  $L > l_{eff}$ . In the first stage, the applied load-global slip curve is represented by segment

A-B and the interface is in the rigid-softening stage (Figure 6.6). After point B, which coincides with the shear stress distribution depicted in Figure 6.7a, a portion of the interface with length equal to  $a$  enters the debonding stage (iii) while the remaining part is still in the rigid stage (i) (with a length equal to  $L-l_{eff}-a$ ) and in the softening stage (ii) (with a length equal to  $l_{eff}$ ). During the rigid-softening-debonding stage (segment B-C in Figure 6.10a), the bond contribution to the applied load remains constant and the friction contribution increases linearly with increasing the debonded length. When the shear stress at the free end attains  $\tau_{max}$  (end of the rigid-softening-debonding stage, Figure 6.8a), the FRCM provides its maximum capacity (point C in Figure 6.10a). The fact that the peak load is attained when the bonded area associated to the bond stress-transfer mechanism, also referred to as the bond stress-transfer zone (STZ), reaches the free end is a peculiarity of the solution obtained with the rigid-softening CML. For cohesive material laws for which  $\tau(0)=0$  or  $d\tau/ds \neq \infty$ , the applied load may further increase after the STZ attains the free end. However, this increase is limited provided that the friction contribution is small with respect to the bond contribution, as commonly observed in FRCM composites that reported the presence of a friction [52,105].

After point C, with further increase of the debonded length, the shear stress at the free end decreases and the bond contribution to the applied force reduces while the friction contribution still increases (softening-debonding stage). During this stage, the applied load decreases (segment C-D in Figure 6.10a) until the interface is fully debonded and the shear stress is equal to  $\tau_f$  along the entire bonded length (segment following point D in Figure 6.10a). For the load response in Figure 6.10a, the global slip decreases after the FRCM maximum capacity is attained. This phenomenon, referred to as snap-back [110], is caused by the energy released by the unbonded fibers as the applied load decreases and can be observed only for bonded lengths higher than a certain value, as discussed in Section 6.1.2.

An applied load-global slip curve obtained by solving Eq. (6.7) with the rigid-softening CML and associated to a bonded length lower than the composite effective bond length,  $l_{eff}$ , is depicted in Figure 6.10b. As in the case of  $L > l_{eff}$ , the load response is characterized by an initial non-linear behavior associated to the rigid-softening stage (segment A-B in Figure 6.10b). The composite maximum capacity (point C in Figure 6.10b) is attained when the shear stress at the free end is equal to  $\tau_{max}$  (Figure 6.9a). After this point, the interface is in the softening stage (segment B-C in Figure 6.10b)

and further increase of  $g$  determines the decrease of the shear stress and applied load at the loaded end. When  $\tau(0)$  decreases to  $\tau_f$  (point C in Figure 6.10b), debonding occurs at the loaded end and propagates until the entire interface is debonded (point D in Figure 6.10b).

The solution of Eq.(6.7) for bonded lengths higher and lower than  $l_{eff}$  is presented in the following distinguishing between the stages identified above.

#### 6.1.1.1 Rigid-softening stage ( $L \geq l_{eff}$ or $L < l_{eff}$ )

During the rigid-softening stage, which occurs both for  $L \geq l_{eff}$  and  $L < l_{eff}$ , a portion of the interface at the loaded end is in the softening stage (ii) while the remaining part has an infinite stiffness (rigid stage (i)). In the softening stage (ii), the bond-slip relationship is:

$$\tau(s) = \tau_{max} - k_2 s \quad (6.12)$$

Then, Eq.(6.7) becomes:

$$\frac{d^2 s}{dx^2} + \omega^2 s = \frac{p}{EA} \tau_{max} \quad (6.13)$$

where:

$$\omega^2 = \frac{pk_2}{EA} \quad (6.14)$$

The general solution of Eq. (6.13) is:

$$s(x) = C_1 \sin[\omega(x+l)] + C_2 \cos[\omega(x+l)] + \frac{\tau_{max}}{k_2} \quad (6.15)$$

where  $l$  is the interface length along which  $\tau_{max} \geq \tau \geq \tau_f$ , i.e. the softening length. The constants  $C_1$  and  $C_2$  can be found applying the boundary conditions of Eq. (6.16):

$$\begin{cases} s(-l) = 0 \\ N(-l) = 0 \end{cases} \quad (6.16)$$

which provide the following slip distribution along the bonded length:

$$s(x) = \frac{\tau_{max}}{k_2} \{1 - \cos[\omega(x+l)]\} \quad (6.17)$$

The axial force in the yarn can be obtained by Eq. (6.8):

$$N(x) = \frac{P\tau_{max}}{\omega} \sin[\omega(x+l)] \quad (6.18)$$

The applied force  $F$  at the loaded end is equal to  $N(0)$ , therefore:

$$F = \frac{P\tau_{max}}{\omega} \sin(\omega l) \quad (6.19)$$

Eq. (6.19) can be used to compute the length of the softening zone as a function of the applied load  $F$ :

$$l = \frac{1}{\omega} \arcsin\left(\frac{\omega F}{P\tau_{max}}\right) \quad (6.20)$$

while the yarn displacement  $g$  at the loaded end is equal to  $s(0)$  (see Eq. (6.17)):

$$g = \frac{\tau_{max}}{k_2} [1 - \cos(\omega l)] \quad (6.21)$$

Finally, the shear stress distribution along the softening length can be obtained by substituting Eq. (6.17) into Eq. (6.12):

$$\tau(x) = \tau_{max} \cos[\omega(x+l)] \quad (6.22)$$

When the shear stress at the loaded end is equal to  $\tau_f$  and the maximum shear stress along the interface is  $\tau_{max}$  (see Figure 6.7a), the bond stress-transfer mechanism is fully established. The maximum length engaged in the softening behavior, which is equal to the effective bond length  $l_{eff}$  due to the particular shape of the CML adopted, can be computed from Eq. (6.22):

$$l_{eff} = \frac{1}{\omega} \arccos\left(\frac{\tau_f}{\tau_{max}}\right) \quad (6.23)$$

If  $L \geq l_{eff}$ , the force at the loaded end attained at the onset of debonding,  $F_{deb}$  (point B in Figure 6.10a), is (see Eq. (6.19)):

$$F_{deb} = \frac{P\tau_{max}}{\omega} \sin(\omega l_{eff}) \quad (6.24)$$

whereas the corresponding global slip  $g_{deb}$  is (see Eq. (6.21)):

$$g_{deb} = \frac{\tau_{max}}{k_2} [1 - \cos(\omega l_{eff})] = s_f \quad (6.25)$$



If  $L < l_{eff}$ , the bond stress-transfer mechanism cannot be fully established and the peak load  $F^*$  (point B in Figure 6.10b) and corresponding global slip  $g^*$  that can be attained are given by Eqs. (6.26) and (6.27), respectively:

$$F^*(L < l_{eff}) = \frac{P\tau_{max}}{\omega} \sin(\omega L) \quad (6.26)$$

$$g^*(L < l_{eff}) = \frac{\tau_{max}}{k_2} [1 - \cos(\omega L)] \quad (6.27)$$

#### 6.1.1.2 Rigid-softening-debonding stage ( $L > l_{eff}$ )

With further increase of  $g$  after the onset of debonding, the softening length translates toward the free end while the bonded length close to the loaded end is in the debonding stage (iii). If the bonded length is sufficiently long (i.e.  $L > l_{eff}$ ), the interface close to the free end remains in the rigid stage (i) and all the three stages of the bond-slip law are established (see Figure 6.7b). In the debonding stage (iii), the bond-slip law is:

$$\tau(s) = \tau_f \quad (6.28)$$

Then, Eq.(6.7) becomes:

$$\frac{d^2s}{dx^2} = \frac{p}{EA} \tau_f \quad (6.29)$$

The general solution of Eq. (6.29) is:

$$s(x) = \frac{p\tau_f}{2EA} (x+a)^2 + C_3(x+a) + C_4 \quad (6.30)$$

where  $a$  is the length of the debonded interface, which ranges from 0 to  $L-l_{eff}$ . The constants  $C_3$  and  $C_4$  of Eq. (6.30) can be found applying the following boundary conditions:

$$\begin{cases} s(-a) = s_f \\ N(-a) = \frac{p\tau_{max}}{\omega} \sin(\omega l_{eff}) \end{cases} \quad (6.31)$$

With these boundary conditions, the slip along the debonded interface can be obtained:

$$s(x) = \frac{p\tau_f}{2EA} (x+a)^2 + \left[ \frac{p\tau_{max}}{\omega EA} \sin(\omega l_{eff}) \right] (x+a) + s_f \quad (6.32)$$

The axial force in the yarn is obtained by Eq. (6.8):

$$N(x) = p\tau_f(x+a) + \frac{p\tau_{max}}{\omega} \sin(\omega l_{eff}) \quad (6.33)$$

which can be used to compute the force at the loaded end  $F=N(0)$ :

$$F = p\tau_f a + \frac{p\tau_{max}}{\omega} \sin(\omega l_{eff}) \quad (6.34)$$

The slip at the loaded end (i.e. the global slip) can be obtained by Eq. (6.32) for each value of the debonded length  $a$ :

$$g = \frac{p\tau_f}{2EA} a^2 + \left[ \frac{p\tau_{max}}{\omega EA} \sin(\omega l_{eff}) \right] a + s_f \quad (6.35)$$

During the rigid-softening-debonding stage, since the softening contribution to the applied load remains constant while the friction contribution increases linearly with  $a$ , the force at the loaded end increases with a rate  $dF/da=p\tau_f$ . The debonded length  $a$  can be obtained by substituting Eq. (6.23) into Eq. (6.34):

$$a = \frac{F}{p\tau_f} - \frac{1}{\omega} \tan(\omega l_{eff}) \quad (6.36)$$

When the softening length attains the free end, the debonded length is equal to  $a=L-l_{eff}$  and the peak force in the yarn at the loaded end  $F^*$  and the corresponding global slip  $g^*$  can be obtained by Eqs. (6.34) and (6.35), respectively:

$$F^*(L > l_{eff}) = p\tau_f(L-l_{eff}) + \frac{p\tau_{max}}{\omega} \sin(\omega l_{eff}) \quad (6.37)$$

$$g^*(L > l_{eff}) = \frac{p\tau_f}{2EA}(L-l_{eff})^2 + \left[ \frac{p\tau_{max}}{\omega EA} \sin(\omega l_{eff}) \right] (L-l_{eff}) + s_f \quad (6.38)$$

When the bonded length is equal to the effective bond length, the rigid-softening stage is followed directly by the softening-debonding stage.

### 6.1.1.3 Softening-debonding stage ( $L \geq l_{eff}$ or $L < l_{eff}$ )

When the shear stress at the free end attains  $\tau_{max}$ , the interface is subjected only to the softening-debonding stage independently of the bonded length adopted. During this stage, the interface behavior along the softening length is still provided by Eq. (6.13), which general solution is:

$$s(x) = C_1 \sin[\omega(x+l+a)] + C_2 \cos[\omega(x+l+a)] + \frac{\tau_{max}}{k_2} \quad (6.39)$$

The constants  $C_1$  and  $C_2$  can be found applying the following boundary conditions:

$$\begin{cases} s(-a) = s_f \\ N(-l-a) = 0 \end{cases} \quad (6.40)$$

With these boundary conditions, Eq. (6.39) becomes:

$$s(x) = \left( s_f - \frac{\tau_{max}}{k_2} \right) \frac{\cos[\omega(x+l+a)]}{\cos(\omega l)} + \frac{\tau_{max}}{k_2} \quad (6.41)$$

The axial force in the yarn is then (see Eq. (6.8)):

$$N(x) = \frac{p\tau_f}{\omega} \frac{\sin[\omega(x+l+a)]}{\cos(\omega l)} \quad (6.42)$$

The axial force provided by the interface still bonded can be obtained by computing the axial force at the end of the softening stage,  $N(-a)$ :

$$N(-a) = \frac{p\tau_f}{\omega} \tan(\omega l) \quad (6.43)$$

The interface behavior along the debonded length is governed by Eq. (6.29), which provides the general solution of Eq. (6.30). In this case, the constants  $C_3$  and  $C_4$  can be obtained by enforcing the boundary conditions of Eq. (6.44):

$$\begin{cases} s(-a) = s_f \\ N(-a) = \frac{p\tau_f}{\omega} \tan(\omega l) \end{cases} \quad (6.44)$$

The slip  $s(x)$  and axial force in the yarn  $N(x)$  along the debonded length are provided by Eqs. (6.45) and (6.46), respectively:

$$s(x) = \frac{p\tau_f}{2EA} (x+a)^2 + \frac{p\tau_f}{\omega EA} \tan[\omega(L-a)](x+a) + s_f \quad (6.45)$$

$$N(x) = p\tau_f (x+a) + \frac{p\tau_f}{\omega} \tan[\omega(L-a)] \quad (6.46)$$

whereas the applied load  $F$  and corresponding slip  $g$  of the single yarn at the loaded end are given by Eqs. (6.47) and (6.48), respectively:

$$F = p\tau_f a + \frac{p\tau_f}{\omega} \tan[\omega(L-a)] \quad (6.47)$$

$$g = \frac{p\tau_f}{2EA}a^2 + \frac{p\tau_f}{\omega EA} \tan[\omega(L-a)]a + s_f \quad (6.48)$$

When the shear stress at the free end decreases to  $\tau_f$ , the softening-debonding stage ends (point D of Figure 6.10), the debonded length  $a$  is equal to  $L$ , and the applied load  $F_f$  is provided by friction only and remains constant with increasing  $g$  (see Eq. (6.47)):

$$F_f = p\tau_f L \quad (6.49)$$

#### 6.1.1.4 Softening stage ( $L < l_{eff}$ )

For short bonded lengths, the rigid-softening-debonding stage is not present and the rigid-softening stage is followed by a softening stage along the entire interface. During this stage, the governing equation is provided by Eq. (6.13), which can be solved with the boundary conditions of Eq. (6.50):

$$\begin{cases} N(-L) = 0 \\ N(0) = F \end{cases} \quad (6.50)$$

The slip distribution along the interface is then:

$$s(x) = -\frac{F}{\omega EA} \frac{\cos[\omega(x+L)]}{\sin(\omega L)} + \frac{\tau_{max}}{k_2} \quad (6.51)$$

Eq. (6.51) provides the global slip  $g=s(0)$ :

$$g = -\frac{F}{\omega EA \tan(\omega L)} + \frac{\tau_{max}}{k_2} \quad (6.52)$$

The softening stage ends when the  $\tau(0)=\tau_f$  (Figure 6.9b) and is followed by the softening-debonding stage illustrated in Section 6.1.1.3.

#### 6.1.2 Snap-back phenomenon

The occurrence of snap-back phenomena is well known in fracture mechanics and different numerical strategies were proposed to capture this behavior using finite element methods [110]. The snap-back was observed in direct-shear tests of FRP-concrete joints that were performed by controlling the FRP-concrete relative displacement at different locations along the composite strip [111–113]. Although experimental curves showing snap-back are not available in the literature for FRCM-substrate joints or FRCM pull-out tests, this phenomenon was captured by analytical and numerical studies [45,69,114]. The load response snap-back is caused by the elastic

energy release of the unbonded fibers that, when the applied load decreases, recover their elastic deformation causing a decrease of the slip measured at the loaded end (i.e. the global slip). According to the analytical approach proposed in this section and provided a certain shape of the CML, the snap-back occurs only for bonded lengths higher than a certain value, named snap-back length  $l_{sb}$ . The snap-back length  $l_{sb}$  can be identified by studying the derivative of the applied load-global slip response after the peak load is attained. The derivative of the load response descending branch  $dF/dg$  can be evaluated as:

$$\frac{dF}{dg} = \frac{dF}{da} \cdot \left( \frac{dg}{da} \right)^{-1} \quad (6.53)$$

Substituting Eqs. (6.47) and (6.48) into Eq. (6.53) provides the derivative  $dF/dg$  associated with the softening-debonding stage:

$$\frac{dF}{dg} = \frac{EA \tan(\omega l)}{(L-l) \cdot \tan(\omega l) - \frac{1}{\omega}} \quad (6.54)$$

Eq. (6.54) shows that, for any bonded length,  $dF/dg$  tends to 0 when  $a$  tends to  $L$  (point D in Figure 6.10). Therefore, the snap-back occurs only if the derivative of the load response tends to infinite during the post-peak behavior (tract CD in Figure 6.10), before attaining the mentioned null value at the end of the softening-debonding stage (point D in Figure 6.10). This condition is fulfilled if (see Eq. (6.54)):

$$\tan(\omega l) = \frac{1}{\omega(L-l)} \quad (6.55)$$

The solution to the above equality is provided by means of graphic considerations. The intersection of the functions  $f(l)=\tan(\omega l)$  and  $f(l)=1/\omega(L-l)$  is achieved when the vertical asymptote of the first curve stays on the right side of the second curve's asymptote (Figure 6.11). Accordingly, Eq. (6.55) admits solutions only if:

$$L > \frac{\pi}{2\omega} \quad (6.56)$$

Therefore, the softening length  $l_{sb}$  is:

$$l_{sb} = \frac{\pi}{2\omega} \quad (6.57)$$

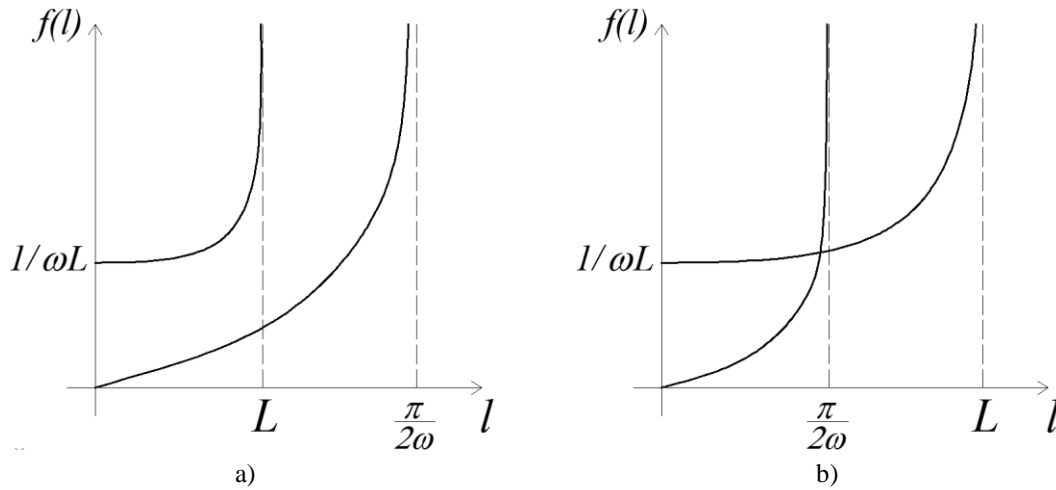


Figure 6.11: Plot of the functions  $f(l)=\tan(\omega l)$  and  $f(l)=1/\omega(L-l)$  in the case: a)  $L < \pi/2\omega$  and b)  $L > \pi/2\omega$ .

In addition to the condition provided by Eq. (6.56), the presence of the snap-back requires that the CML satisfies the inequality in Eq. (6.58):

$$\tan(\omega l_{eff}) \geq \frac{1}{[\omega(L-l_{eff})]} \quad (6.58)$$

It should be noted that, according to Eq. (6.23),  $l_{eff}$  can assume values higher than or equal to 0 and lower than or equal to  $\pi/(2\omega)$ . Therefore, Eq. (6.56) implies that snap-back can occur only for relatively long bonded lengths, i.e. for  $L > l_{eff}$ .

### 6.1.3 Estimation of the cohesive material law parameters

The cohesive material law presented in this chapter is characterized by five parameters, namely  $\tau_{max}$ ,  $k_2$ ,  $\tau_f$ ,  $s_f$ , and the area below the bond slip law  $\Gamma = G_c + \tau_f s_f$  and can be fully defined once three of these five parameters are known. Different strategies can be adopted to estimate the CML starting from experimental load responses. In the following, the debonding load of a single fiber bundle  $F_{deb} = P_{deb}/n$ , peak load  $F^* = P^*/n$ , the associated global slips  $g_{deb}$  and  $g^*$ , respectively, the effective bond length  $l_{eff}$ , and the friction load  $F_f = P_f/n$  obtained from the experimental load responses are employed to estimate four different CMLs, named CML<sub>-j</sub>, where  $j=(1,2,3,4)$  is the CML number. The friction load  $F_f$  is considered between the required parameters for all CML<sub>-j</sub> because it is easily identifiable from the experimental load responses and allows for the direct computation of the friction shear stress  $\tau_f$  rearranging Eq. (6.49):

$$\tau_f = \frac{F_f}{pL} \quad (6.59)$$

CML<sub>j</sub> represent only some of the possible cohesive materials laws that can be estimated from the experimental results. Further CMLs can be obtained by enforcing certain parameters to reproduce specific features of the FRCM-substrate joint or FRCM pull-out test bond behavior.

#### 6.1.3.1 CML\_1 ( $F_{deb}$ , $g_{deb}$ , and $F_f$ known)

CML<sub>1</sub> is estimated employing the debonding load  $F_{deb}$ , corresponding global slip  $g_{deb}$ , and the applied load associated to friction only  $F_f$ . After  $\tau_f$  is defined by Eq. (6.59), the slope  $k_2$  of the softening stage and the maximum shear stress  $\tau_{max}$  can be obtained by solving the system of non-linear equations provided by Eqs. (6.24) and (6.25), where  $\omega$  and  $l_{eff}$  are provided by Eqs. (6.14) and (6.23), respectively.

#### 6.1.3.2 CML\_2 ( $F_{deb}$ , $l_{eff}$ , and $F_f$ known)

If the effective bond length, debonding load, and friction load are known, the CML can be estimated computing  $\tau_f$  from Eq. (6.59) and solving the system of non-linear equations provided by Eqs. (6.23) and (6.24) (where  $\omega$  is provided by Eq. (6.14)) to obtain  $k_2$  and  $\tau_{max}$ .

#### 6.1.3.3 CML\_3 ( $F_{deb}$ , $F^*$ , and $F_f$ known)

CML<sub>3</sub> is defined by enforcing specific values of the applied load, namely the debonding, peak, and friction load. The friction shear stress is provided by Eq. (6.59) whereas the slope  $k_2$  and maximum shear stress  $\tau_{max}$  are obtained by solving the system of non-linear equations consisting of Eqs. (6.24) and (6.37), where  $\omega$  and  $l_{eff}$  are provided by Eqs. (6.14) and (6.23), respectively.

#### 6.1.3.4 CML\_4 ( $F^*$ , $g^*$ , and $F_f$ known)

The peak load, corresponding global slip, and friction force can be easily obtained from the load responses and are employed to estimate CML<sub>4</sub>. As in the previous cases,  $\tau_f$  is provided by Eq. (6.59), while  $k_2$  and  $\tau_{max}$  are obtained by solving the system of non-linear equation consisting of Eqs. (6.37) and (6.38), where  $\omega$  and  $l_{eff}$  are provided by Eqs. (6.14) and (6.23), respectively.

#### 6.1.4 Comparison between analytical provisions and experimental results of pull-out and direct-shear test.

The analytical approach proposed is validated in this section by comparing the experimental load responses of pull-out and direct shear tests, both compatible with pure Mode-II loading condition, with the corresponding analytical provisions. First, procedures and results of a pull-out test campaign recently proposed by D'Antino et al. [59] were presented and discussed. Then, CML\_1-4, estimated enforcing the conditions discussed in Section 6.1.3 on the pull-out experimental result, were employed to solve Eq.(6.7) and provide analytical applied load-global slip curves. Finally, an alternative calibration, referred to as CML\_5, was proposed and calibrated on the results of direct-shear tests presented in Section 5.2.2.

##### 6.1.4.1 Analytical model validation with pull-out test results

D'Antino et al. [59] recently proposed a simple pull-out test set-up to study the bond behavior of FRCC composites that reported failure due to debonding at the matrix-fiber interface. This set-up allows for investigating the effect of the bonded length limiting the presence of fracture mechanics Mode-I loading conditions unavoidable with the classical single-lap shear tests [111]. In this section, the results of 9 pull-out tests of a PBO FRCC composite are presented. The specimens were comprised of a single layer of an unbalanced PBO fiber textile [80] embedded between two 4 mm thick matrix layers (Figure 6.12a). All specimens had matrix-fiber bonded length  $L=330$  mm and included  $n=6$  longitudinal fiber bundles spaced at 10 mm on center, each with a cross-sectional area  $A=0.46$  mm<sup>2</sup>. The matrix-fiber contact perimeter of a single bundle was  $p=10$  mm. The matrix layers had length equal to the matrix-fiber bonded length and width  $b_1=60$  mm, whereas the textile had a length of 600 mm, which resulted in 270 mm of bare longitudinal fibers. Two aluminum plates, 600 mm long, 60 mm wide, and 3 mm thick, were attached on the opposite faces of the composite strip using epoxy resin (Figure 6.12a). The matrix-plate bonded length and width were 330 mm and 60 mm, respectively. The aluminum plates were connected to the testing machine through a spherical joint while the bare textile end was gripped by the machine wedges (Figure 6.12b). Thin steel plates were attached to the bare textile end to improve the machine gripping. Two aluminum L-shaped plates were attached to the bare fiber just outside the composite strip at the loaded end and reacted off of 3 LVDTs attached onto the aluminum plates. One LVDT, named LVDT\_0, was placed at the mid-width of the aluminum plate on one side of the specimen, whereas the remaining 2 LVDTs, named



LVDT\_1 and LVDT\_2 were attached to the aluminum plate on the other side of the specimen. The displacement measured by LVDT\_0 was used to control the test, which was conducted in displacement control at a rate of 0.00084 mm/s. LVDT\_1 and LVDT\_2 were used to have an indirect estimation of the load distribution across the specimen width. The displacement control mode and specific rate adopted were selected to accurately capture the debonding phenomena and compare the results with those of direct-shear tests available in the literature without being affected by the loading rate effect [59,115].

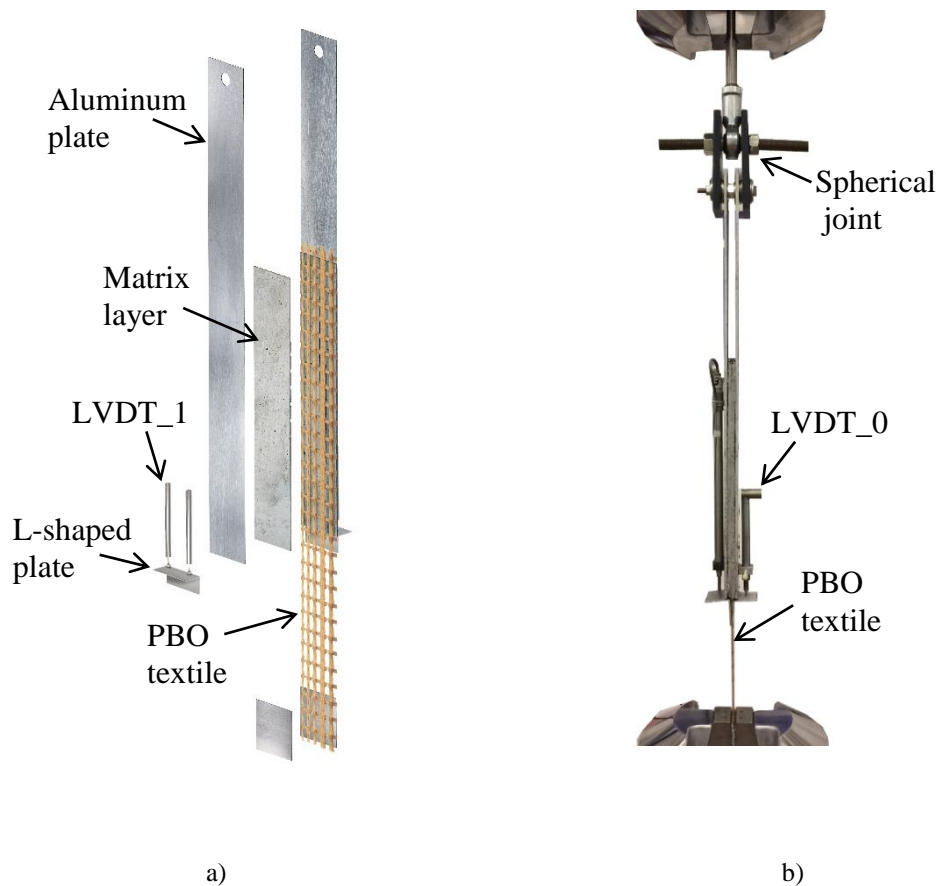


Figure 6.12. a) Exploded view and of the pull-out test set-up and b) photo of specimen *PO\_330\_60\_5*.

Figure 6.13 shows the load responses obtained from 7 specimens, where the global slip  $g$  is the average of the displacements measured by LVDT\_1 and LVDT\_2. Specimens were named following the notation  $PO\_X\_Y\_D\_Z$ , where  $PO$  = pull-out,  $X$  = matrix-fiber and matrix-plate bonded length in mm (equal to 330 mm in all specimens in this section),  $Y$  = matrix-plate bonded width (equal to 60 mm in all specimens in this section),  $D$  (if present) = test conducted until a constant residual applied load was present, and  $Z$  = specimen number. In this section, only those specimens that reported

an even distribution of the applied load across the width according to the criteria proposed in [104] were reported. All specimens reported in Figure 6.12 failed due to debonding of the fibers from the embedding matrix. The experimental  $P$ - $g$  curves are similar to the analytical load responses provided in Figure 6.10a, although the snap-back phenomenon could not be captured because the tests were controlled by monotonically increasing the displacement measured by LVDT\_0. Furthermore, the curves of Figure 6.12 show an initial linear branch that is not modeled by the rigid-softening CML adopted in this section, which does not include an elastic stage with finite stiffness. Specimens PO\_330\_60\_D\_1, 2, and 3 show a residual constant applied load  $P_f$ , which is attributed to the presence of a residual matrix-fiber interface friction.

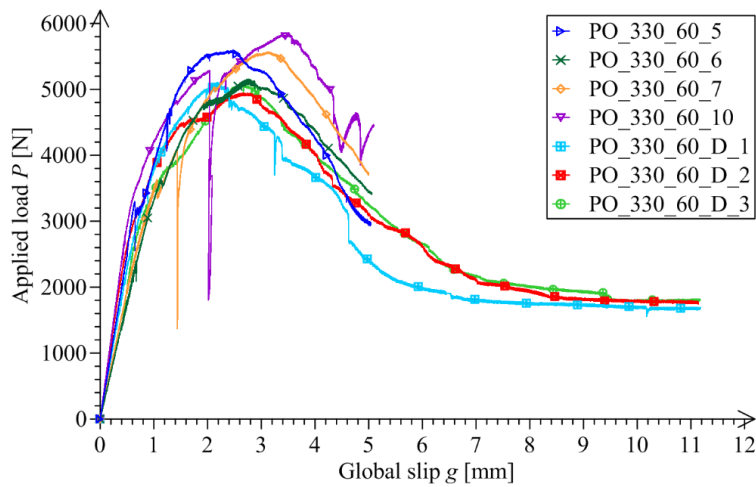


Figure 6.13. Applied load  $P$ -global slip  $g$  response of PBO FRCM composites subjected to pull-out tests.

The average values of the parameters considered to estimate the CMLs, namely  $F_{deb}$ ,  $F^*$ ,  $g_{deb}$ ,  $g^*$ , and  $F_f$ , were obtained from the experimental curves depicted in Figure 6.12 and are reported in Table 6.1, together with the corresponding coefficient of variation (CoV) and with the parameters measured on each curve. In addition to these parameters, the effective bond length value  $l_{eff}=260$  mm, which was reported in the literature for the same PBO FRCM composite subjected to the pull-out tests described in this section [104], was considered in the estimation of the CMLs.

Specimen	$F_{deb}$ [N]	$F^*$ [N]	$F_f$ [N]	$g_{deb}$ [mm]	$g^*$ [mm]
PO_330_60_5	754	931	-	1.24	2.45
PO_330_60_6	791	859	-	1.92	2.77
PO_330_60_7	837	928	-	2.14	3.13
PO_330_60_10	880	972	-	2.04	3.53
PO_330_60_D_1	833	850	280	1.97	2.18
PO_330_60_D_2	758	824	296	1.73	2.69
PO_330_60_D_3	655	848	300	1.46	2.62
Average	787	887	292	1.79	2.77
CoV [%]	9.39%	6.25%	3.75%	18.40%	16.11%

Table 6.1: Parameters obtained from the experimental pull-out load responses.

Following the strategies described in Section 6.1.3, CML\_1-4 were fully defined employing the average parameters reported in Table 6.1 and are shown in Figure 6.14. The shear strength  $\tau_{max}$ , slope of the softening branch  $k_2$ , friction shear stress  $\tau_f$ , slip at the onset of debonding  $s_f$ , fracture energy  $G_f$ , effective bond length  $l_{eff}$ , and snap-back bonded length  $l_{sb}$  computed for each CML\_  $j$  are reported in Table 6.2.

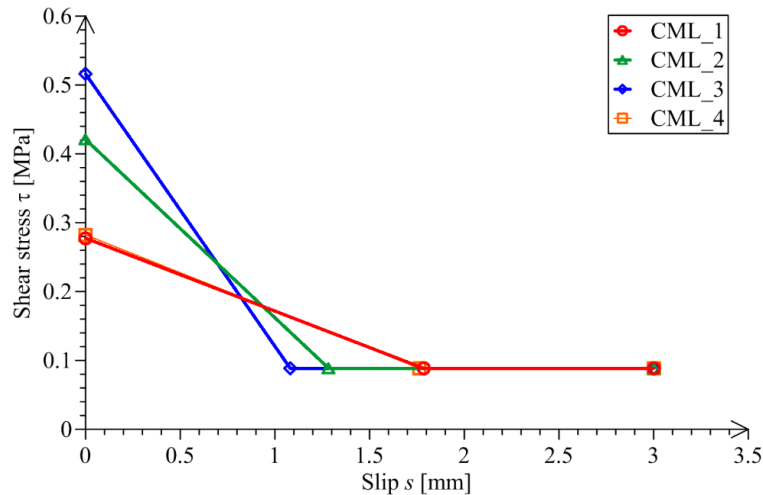


Figure 6.14. Cohesive material laws estimated.

Cohesive material law	$\tau_{max}$ [MPa]	$k_2$ [MPa/mm]	$\tau_f$ [MPa]	$s_f$ [mm]	$G_f$ [N/mm]	$l_{eff}$ [mm]	$l_{sb}$ [mm]
CML_1	0.28	0.11	0.09	1.79	0.169	373	470
CML_2	0.42	0.26	0.09	1.28	0.213	260	301
CML_3	0.52	0.40	0.09	1.08	0.231	216	243
CML_4	0.28	0.11	0.09	1.76	0.171	368	461

Table 6.2: Parameters of the estimated CMLs.

Considering the geometrical and mechanical characteristic of the PBO FRCM subjected to the pull-out tests, Eq.(6.7) was solved with CML\_1-4 and used to compute the analytical applied load  $P$ -global slip  $g$  responses depicted in Figure 6.15. In Figure 6.15,

the envelope of the pull-out curves of Figure 6.13 is also reported for comparison with the analytical provisions.

Figure 6.15 shows that the initial stiffness of experimental and analytical curves is different. Indeed, as previously observed, the use of a rigid-softening cohesive material law does not allow to reproduce the initial linear elastic behavior observed experimentally. However, this branch is usually limited with respect to the non-linear part of the  $P$ - $g$  curves and could be neglected when the study is focused on the FRCM debonding interface capacity rather than on its stiffness.

The main difference between the analytical and experimental load responses is represented by the post-peak behavior. The analytical approach adopted cannot reproduce the softening branch observed in the pull-out tests, which were carried out by monotonically increasing the global slip preventing the occurrence of the snap-back response. However, it should be noted that the shape of the  $P$ - $g$  curve descending branch does not affect the residual load  $P_f$ , which was correctly captured by all CMLs since the friction shear stress  $\tau_f$  was always considered as a calibration parameter.

The strategies employed to obtain CML\_1 and 4 provided approximately the same results, yielding cohesive material laws with an effective bond length higher than the bonded length  $L=330$  mm. Therefore, although the debonding load and peak load were enforced in the estimation of CML\_1 and 4, respectively, the bond stress-transfer mechanism could not be fully established and debonding occurred before  $P_{deb}$  could be attained.

The value of the effective bond length was enforced for the estimation of CML\_2, which provided a load response in good agreement with the experimental measurements. The load response associated with CML\_2 is characterized by the presence of a snap-back, being  $l_{sb}=301$  mm  $<$   $L=330$  mm and the inequality in Eq. (6.58) satisfied in this case. Similarly, CML\_3, which was obtained by enforcing the debonding and peak load along with the friction shear stress, showed a snap-back phenomenon ( $l_{sb}=243$  mm) and well reproduced the experimental behavior. These results indicate that specimens with a bonded length  $L=330$  mm would show the snap-back if the fiber slip would be controlled at different locations along the bonded length [113].

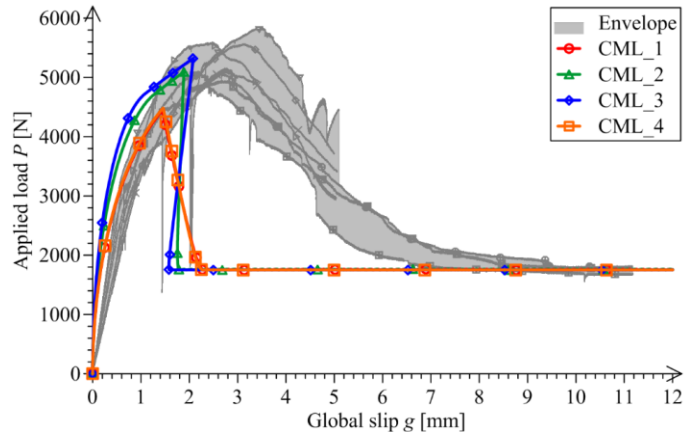


Figure 6.15. Comparison between analytical and experimental load responses.

The results obtained show the importance of considering the effective bond length for the estimation of a CML able to correctly reproduce the experimental load responses. In fact, CMLs that were calibrated without enforcing  $l_{eff}$  showed poor accuracy of the analytical solution with respect to the experimental curves.

#### 6.1.4.2 Alternative model validation with results of direct-shear tests

Alternatively, the five parameters characterizing the rigid-softening CML, namely  $\tau_{max}$ ,  $\tau_f$ ,  $k_2$ ,  $s_f$ , and the area below the curve up to  $s_f$  ( $G_f$  in Figure 6.5b), can be calibrated from the results of DS tests showed in Section 5.2.2 (see Figure 5.7). Different strategies can be adopted to estimate the CML parameters (CML\_1, \_2, \_3 and \_4), comparing key points of the analytical response with corresponding experimental (see Section 6.1.3). In this section, a fifth strategy was adopted, namely CML\_5, which was estimated by enforcing: (i) the residual axial stress  $\bar{\sigma}_f$  at the end of the softening-debonding stage, (ii) the peak axial stress  $\bar{\sigma}^*$ , attained at the end of the rigid-softening-debonding stage, and (iii) the effective bond length  $l_{eff}$ . The residual axial stress  $\bar{\sigma}_f$  and peak axial stress  $\bar{\sigma}^*$  of the average curves, i.e. the load responses obtained by averaging the axial stress  $\sigma$  of nominally equal specimens for a given  $g$ , were considered in the estimation of the CML. Values of  $\bar{\sigma}_f$  and  $\bar{\sigma}^*$  of the average curves of DS tests (DS\_avg) are reported in Table 5.2, whereas values of  $\bar{\sigma}_{0,f}$  and  $\bar{\sigma}_0^*$  of bare-fiber (MB\_B\_avg) and bond-gap (MB\_G\_avg) in Table 5.1.

According to condition (i), the residual axial stress  $\bar{\sigma}_f$  of curve DS\_avg (shown in Figure 6.16) was used to obtain the  $\tau_f$ :

$$\tau_f = \frac{A_f \bar{\sigma}_f}{pL} \quad (6.60)$$

Provided  $\tau_f$ ,  $\tau_{max}$  and  $k_2$  were obtained substituting the peak axial stress  $\bar{\sigma}^*$  of DS\_avg curve in the system of non-linear equations comprising [condition (ii)] the equation providing the stress associated with the end of the rigid-softening-debonding stage (see 6.1.1.2) and [condition (iii)] the equation providing the effective bond length  $l_{eff}$ :

$$\begin{cases} \bar{\sigma}^* = \frac{p\tau_f a}{A_f} + \frac{p\tau_{max}}{\omega A_f} \sin(\omega l_{eff}) & \text{where } \omega^2 = \frac{pk_2}{EA_f} \\ l_{eff} = \frac{1}{\omega} \arccos\left(\frac{\tau_f}{\tau_{max}}\right) \end{cases} \quad (6.61)$$

where  $l_{eff}$  was assumed equal to 260 mm according to data available in the literature for the same PBO FRCM composite considered in this study [101].

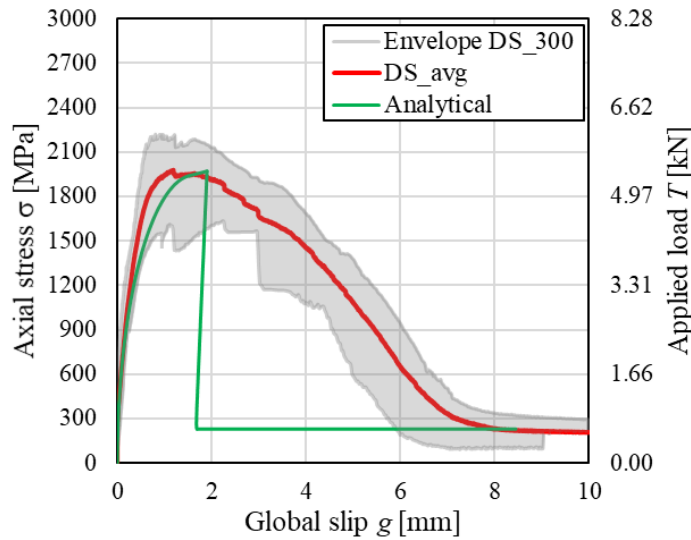


Figure 6.16. Comparison between analytical and experimental  $\sigma$  -  $g$  responses of DS tests.

The solution of Eqs. (6.60) and (6.61) provided  $\tau_{max}=0.517$  MPa,  $\tau_f=0.035$  MPa, and  $k_2=0.32$  MPa/mm, which entails for  $s_f=1.52$  mm. The analytical  $\sigma$  -  $g$  response obtained is compared with the envelope of experimental load responses of DS tests in Figure 6.16. This comparison shows that the CML\_5 calibration strategy adopted was effective, since good agreement between the experimental and analytical load responses was obtained except for the descending branch. For this branch, the analytical solution shows a snap-back whereas an increase of the global slip  $g$  for decreasing values of  $\sigma$  was observed experimentally. This difference is well-known for externally bonded

composites and was ascribed to the test control that did not allow for capturing the snap-back phenomenon [110].

## 6.2 Alternative energetic approach to evaluate the interface capacity

For FRCM bonded composites in which the bond stress-transfer mechanism can be fully established (i.e.  $L \geq l_{eff}$ ), the applied force after the onset of debonding and up to the peak load is provided by Eq. (6.34), which represents the stress-criterion for the matrix-fiber interface capacity. If this stress-criterion is employed to compute the debonding load  $F_{deb}$  and peak load  $F^*$  of a single yarn, the expression of Eqs. (6.24) and (6.37) are obtained, respectively.

The interface stress-transfer mechanism can be studied also adopting an energy approach that distinguishes between the strain, interface surface, and friction energies. According to this approach, the equilibrium of works of the internal and external forces associated with an infinitesimal increase of the debonded length  $da$  is:

$$F \cdot dg = dU_{el} + dU_f + G_c \cdot da \cdot p \quad (6.62)$$

where  $F \cdot dg$  is the work done by the external force  $F$ ,  $U_{el}$  and  $U_f$  are the strain energy and energy dissipated by friction, respectively, and  $G_c$  is the critical energy release rate, which is also referred to as the interface fracture energy. Eq. (6.62) can be conveniently rewritten as:

$$G_c = \frac{1}{p} \left( F \cdot \frac{dg}{da} - \frac{dU_{el}}{da} - \frac{dU_f}{da} \right) \quad (6.63)$$

The first term in Eq. (6.62),  $F \cdot dg/da$ , can be computed considering the global slip  $g$  provided by Eq. (6.35) and the applied force  $F$  provided by Eq. (6.34). The strain energy  $U_{el}$  can be divided in three different contributions:

1.  $U_{el}^1$  = yarn strain energy in the debonded region;
2.  $U_{el}^2$  = yarn strain energy in the bonded region;
3.  $U_{el}^3$  = interface strain energy in the debonded region.

The yarn strain energy  $U_{el}^1$  can be computed considering the linear-elastic behavior of the fibers and the slip along the debonded interface provided by Eq. (6.32):

$$U_{el}^1 = \frac{EA}{2} \int_{-a}^0 \left( \frac{ds}{dx} \right)^2 dx = \frac{p^2}{2EA} \left\{ \tau_f^2 \frac{a^3}{3} + \frac{\tau_f \tau_{max} \sin(\omega l_{eff})}{\omega} a^2 + \left( \frac{\tau_{max} \sin(\omega l_{eff})}{\omega} \right)^2 a \right\}$$

(6.64)

The yarn strain energy  $U_{el}^2$  is computed observing that the force in the yarn at  $x=-a$  is equal to  $F - p\tau_f a$  (see Eqs. (6.33) and (6.34)) and the corresponding slip  $s(-a)=s_f$ :

$$U_{el}^2 = \frac{s_f}{2} \left[ \frac{p\tau_{max} \sin(\omega l_{eff})}{\omega} \right] \quad (6.65)$$

Eq. (6.65) shows that the yarn strain energy in the bonded region does not depend on the debonded length  $a$ . This feature is a peculiarity of the rigid-softening CML adopted that, for  $L \geq l_{eff}$ , entails for a constant softening length after the onset of debonding.

According to the rigid-softening CML, the interface strain energy in the debonded region is always equal to zero.

The energy dissipated by friction  $U_{fr}$  is computed by considering the slip provided by Eq. (6.32):

$$U_{fr} = \int_{-a}^0 p\tau_f s(x) dx = p\tau_f \left\{ \frac{p\tau_f a^3}{6EA} + \frac{p\tau_{max} \sin(\omega l_{eff})}{2\omega EA} a^2 + s_f a \right\} \quad (6.66)$$

The differentiation of the term in Eq. (6.63) provides:

$$\begin{aligned} F \cdot \frac{dg}{da} &= \frac{p^2}{EA} \left\{ \tau_f a + \frac{\tau_{max}}{\omega} \left[ \sin(\omega l_{eff}) \right] \right\}^2 \\ \frac{dU_{el}}{da} &= \frac{p^2}{2EA} \left\{ \tau_f^2 a^2 + \frac{2\tau_f \tau_{max} \sin(\omega l_{eff})}{\omega} a + \left[ \frac{\tau_{max} \sin(\omega l_{eff})}{\omega} \right]^2 \right\} \\ \frac{dU_f}{da} &= \frac{p^2 \tau_f}{EA} \left\{ \frac{\tau_f a^2}{2} + \frac{\tau_{max} \sin(\omega l_{eff})}{\omega} a + \frac{EAs_f}{p} \right\} \end{aligned} \quad (6.67)$$

Substituting Eq. (6.67) into Eq. (6.63), the following expression for the critical energy release rate  $G_c$  is obtained:

$$G_c = \frac{p}{2EA} \left( \frac{\tau_{max} \sin(\omega l_{eff})}{\omega} \right)^2 - s_f \tau_f \quad (6.68)$$



Eq. (6.68) can be rewritten as:

$$G_c = \frac{s_f (\tau_{max} + \tau_f)}{2} - s_f \tau_f \quad (6.69)$$

In Eq. (6.69), the first term is the area under the descending branch of the CML whereas the second term is the energy rate dissipated by friction. The physical meaning of each contribution is illustrated in Figure 6.17.

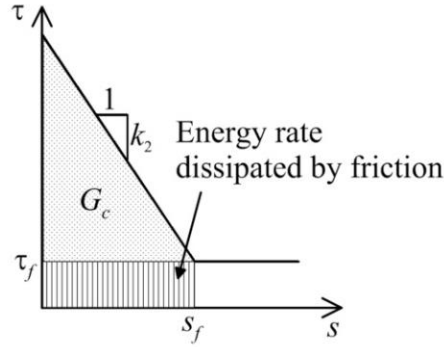


Figure 6.17: Energy rates provided by bond ( $G_c$ ) and friction.

The interface capacity  $F^*$  provided by the stress criterion (see Eqs. (6.34) and (6.37)) can be rewritten as a function of the energy release rate  $G_c$  and the friction shear stress  $\tau_f$  using Eq. (6.69):

$$F^* = p\tau_f (L - l_{eff}) + \left( \frac{p\tau_f}{\omega} + \sqrt{2pEAG_c} \right) \sin(\omega l_{eff}) \quad (6.70)$$

Eq. (6.70) represents the energy criterion for the matrix-fiber interface capacity. It should be noted that in Eq. (6.70) the contribution of bond and friction are decoupled and clearly identified. Besides, Eq. (6.70) can be combined with Eq. (6.37) to obtain the interface shear strength  $\tau_{max}$  as a function of the critical energy release rate:

$$\tau_{max} = \tau_f + \frac{\omega}{p} \sqrt{2pEAG_c} \quad (6.71)$$

### 6.3 Influence of snubbing friction on the bond behaviour of modified beam test on FRCM-concrete joints

The analytical study of the FRCM debonding process is typically approached considering a pure Mode-II condition and assuming a multi-linear bond-slip constitutive relation to model the matrix-fiber interface behavior. However, as discussed in Chapters 4 and 5, when a normal stress component is localized at the fiber exit point ( $\sigma_1$  in Figure 6.18a), such in the case of modified beam test, an additional bond capacity may be exhibited by the specimen, due to a frictional snubbing force, which determines a non-pure Mode-II loading condition. An analogue scenario was experimentally observed by [89,90] in the context of an investigations on concrete mixtures enriched with randomly-oriented short steel fibers, whose load bearing capacity increased when, after concrete cracking, fibers were oriented at angles with respect to the pulling action. This phenomenon may be enhanced by the onset of matrix flattening with fiber compenetration along the debonded length, due to the extension of the snubbing length (see Figure 6.18a). The presence of a stress component orthogonal to the composite plane increases the interface capacity if the sense is toward the support (negative Mode-I component), whereas it reduces the Mode-II bond capacity if it is oriented toward the external surface of the composite, i.e. if a positive Mode-I loading condition is present [66].

Several analytical and numerical models were proposed to reproduce the bond behavior of externally bonded composite subjected either to a pure Mode-II or to a non-pure Mode-II loading condition. A continuous or multi-linear interface shear stress  $\tau$  - slip  $s$  relationship (CML) is typically employed to model the bond behavior under a pure Mode-II condition. Whereas, when orthogonal stresses to the cohesive interface are present, such as in the case of a curved member, externally bonded with a composite plate, a specific distribution of normal stress along the cohesive interface may also be assumed, which is typically considered independent from the tau-slip law (uncoupled models) [68,116–118]. Some authors presented coupled models in which a coupling between tangential and normal CML was defined [71]. The relationship between the normal and tangential CML may be defined by means of coupling parameters or by experimental-based calibration of non-pure Mode-II CML. When interface normal stresses are present, interface normal stress  $\sigma_1$  – crack opening  $w$  relationships are also considered [69].

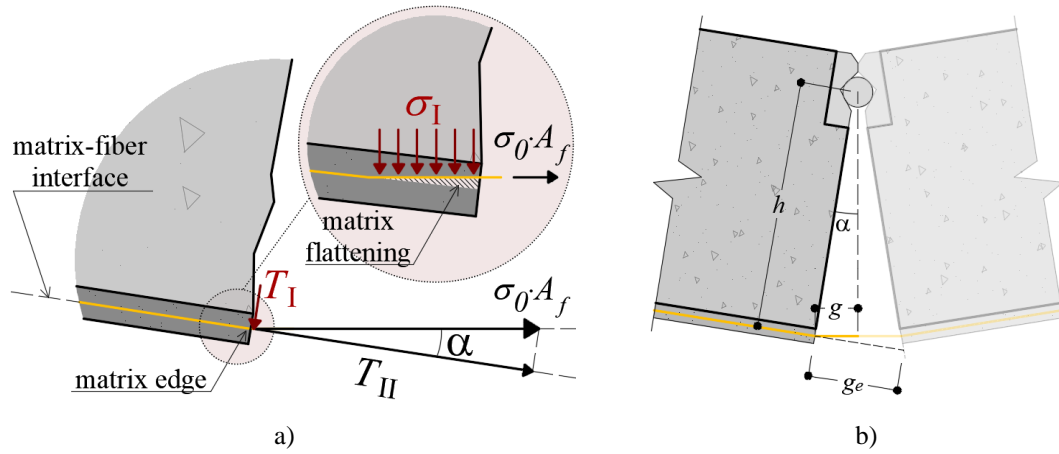


Figure 6.18: a) Fiber pull-out at an angle  $\alpha$ ; b) modified beam test: midspan opening displacement  $g_e$ .

### 6.3.1 Analytical investigation of the debonding process in modified beam test

In the following section, the DS and MB test experimental results presented in Chapter 5, are modeled using an analytical approach which accounts for a combined effect of interfacial shear stresses and a normal stress component  $\sigma_0$ , localized at the fiber exit point (see Figure 6.18a).

Since the presence of a normal component at the matrix-fiber interface affects the composite bond behavior, the relationship between the fiber stress of MB tests (where the normal component is present) and axial stress of DS tests (where the normal component can be neglected), may be described by the function  $\rho(g)$ , which relates the fiber stress  $\sigma_0(g)$  of MB tests ( $\alpha \neq 0$ ) and the axial stress  $\sigma(g)$  of DS tests ( $\alpha = 0$ ) for a given global slip  $g$  (see Figure 6.18a):

$$\rho(g) = \frac{\sigma_0(g)}{\sigma(g)} \quad (6.72)$$

Eq. (6.72) is based on the assumption that the global slip  $g$  is not affected by test set-up, i.e.  $g$  is not influenced by the presence of  $\sigma_I$ . This assumption is supported by the similar average values of global slip at peak stress  $\bar{g}^*$  obtained by the different test set-ups ( $\bar{g}^* = 1.83$  mm, 1.87 mm, and 1.53 mm for bond-gap and bare-fiber MB tests and for DS tests, respectively – see Table 5.1 in and Table 5.2). It must be noted that, despite DS test exhibited 16-18% lower  $\bar{g}^*$  values with respect to MB tests, the assumption can still be considered valid in light of the wide scatter of the experimental results which characterizes FRCM bond test (typically the displacement field ( $g$ ) is

highly scattered than the stress field ( $\sigma$ ) – see Table 5.1 in and Table 5.2) and because, in the lack of a positive Mode-I action, which tends to push fibers against the inner matrix layer (typical of MB test), a lower global slip value in DS tests would scarcely seem justified.

Li et al. (1990) employed Eq. (6.72) to describe the relationship between the maximum force obtained from fiber pull-out test with fiber inclined at an angle  $\alpha \neq 0$  and that of the same fiber with  $\alpha = 0$ . According to the experimental results of pull-out tests on nylon and polypropylene fibers embedded within a concrete matrix (25 mm bonded length), they proposed an exponential shape of  $\rho(\alpha)$  [90]:

$$\rho(\alpha) = e^{(\alpha\mu)} \quad (6.73)$$

where  $\mu$  is the snubbing friction coefficient. Eqs. (6.72) and (6.73) can be related by the expression of the inclination angle  $\alpha$ , given by previously introduced Eq. (5.3) (Section 5.3.3). For the sake of clarity, Eq. (5.3) is reported below:

$$\alpha(g) = \arcsin\left(\frac{g}{h}\right) \quad (5.3)$$

In Eq. (5.3),  $h$  is the vertical distance between the fiber exit point and the center of rotation of the block and  $g$  is the global slip (Figure 6.18b). Therefore, as a first attempt to correlate the bond behavior of DS and MB tests, the increase of bond capacity observed in MB tests with respect to DS tests is attributed to the snubbing-friction effect, which is assumed concentrated at the fiber exit point, and Eq. (6.73) [where  $\alpha$  is obtained by Eq. (5.3)] is considered to describe the behavior of  $\rho(g)$  (see Figure 6.19). Being the bending stiffness of synthetic high-strength fibers employed in FRCM technology typically very low, due to their reduced diameter (usually smaller than 50  $\mu\text{m}$ ), the additional force due to fiber bending is negligible for PBO-FRCM applications [89]. However, for steel fiber reinforced mortars, the increase in bond strength could be higher due to an extra energy required to bent the fiber at the exit point [119]. The coefficient  $\mu$  in Eq. (6.73) is a property of the specific FRCM composite and can be estimated experimentally with pull-out tests of fiber bundles embedded within matrix prisms varying the bonded length and angle of inclination of the pulling force [89]. It should be noted that more complex approaches were adopted to model the bond behavior of FRP and FRCM composites bonded to curved substrates [68,71,116]. However, in these cases the constant curvature of the substrate allowed for a simple solution of the problem, whereas the variation of the bending moment along the axis of

the modified beam would require the use of cumbersome analytical or numerical methods.

Provided the function  $\rho$ , the composite bond behavior observed in MB tests can be described by computing  $\sigma$  from the bond differential equation obtained assuming a pure Mode-II loading condition (see Section 6.3.2) and then computing the fiber stress  $\sigma_0$  accounting for the presence of the snubbing-friction effect substituting Eq. (6.72) into Eq. (6.73) and rearranging it:

$$\sigma_0 = \sigma e^{(\alpha\mu)} \quad (6.74)$$

A plot of  $\sigma$ - $g$  and  $\sigma_0$ - $g$  analytical responses is provided in Figure 6.19, in which the variation of axial and fiber stress with the global slip is compared for a given value of  $\mu$ . The two responses are initially almost coincident, due to the negligible values assumed by  $\alpha$  when the global slip is still limited. With increasing  $g$ , the ratio  $\rho$  grows proportionally, and the gap between  $\sigma$ - and  $\sigma_0$ - $g$  responses becomes more evident. The effect of snubbing friction effect is maximized in the fully-debonded stage (see Table 6.3), where the fiber stress associated with friction increases as a consequence of the widening of the angle  $\alpha$  with increasing  $g$ . This behaviour can be experimentally observed in modified beam test of PBO FRCM-masonry joints [MB\_3\_210\_60\_B\_3, \_4 and \_5 (see Figure 4.9a)], Carbon FRCM-masonry joints [MB\_C\_3\_210\_60\_1 and \_5 (see Figure 4.9c)] and PBO FRCM-concrete joints [MB\_300\_60\_G\_1 (see Figure 5.6)].

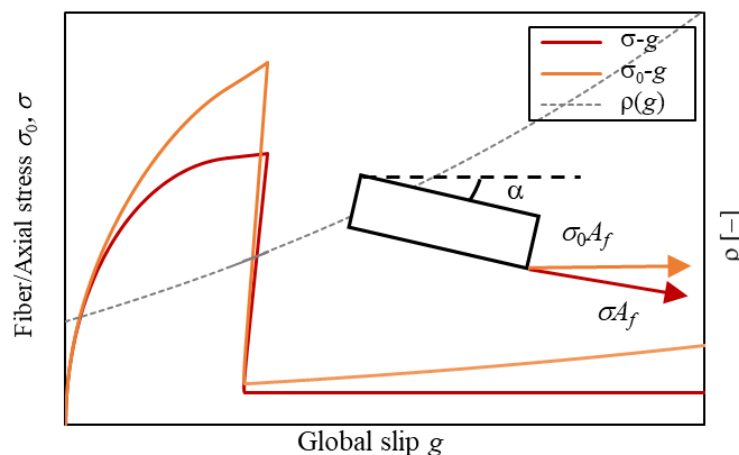


Figure 6.19. Analytical  $\sigma$ - and  $\sigma_0$ - $g$  responses and function  $\rho(g)$  for given  $\mu$ .

### 6.3.2 Analytical solution of the bond differential equation accounting for the snubbing-friction effect

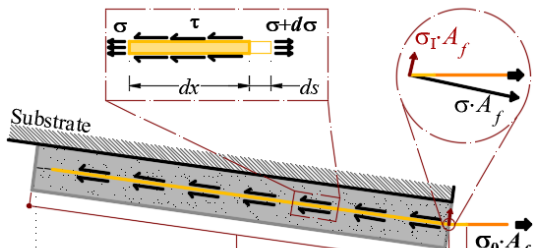
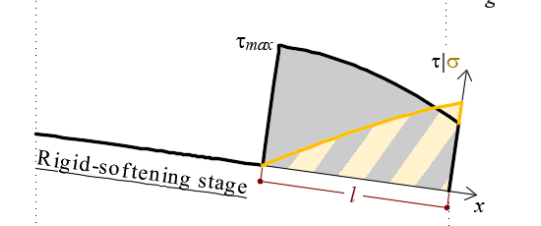
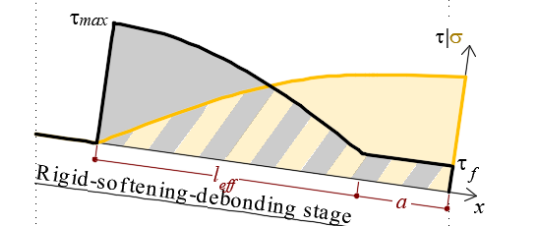
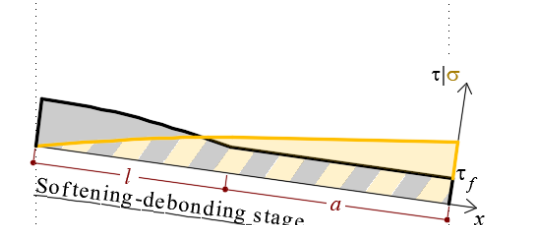
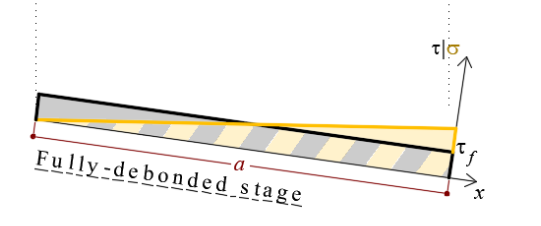
Assuming a localized effect of snubbing-friction phenomenon at the fiber exit point and a pure Mode-II loading condition along the matrix-fiber interface length, governed by the rigid-softening CML proposed in Section 6.1 and in Figure 6.5b, the fiber stress  $\sigma_0$  and corresponding global slip  $g$  can be obtained by substituting the solution of the bond differential equation (Eq.(6.7)) into Eq.(6.74). The full-range behaviour of the cohesive interface, obtained according to the mentioned assumption and procedures is reported in Table 6.3 for each stage.

### 6.3.3 Analytical model of MB tests

The bond behavior of MB tests with bond-gap layout was modeled using Eq. (6.74) with  $\alpha$  measured in degrees [ $^\circ$ ] and defined by Eq. (5.3). The results of MB tests with free-fiber layout were not modeled due to the presence of significant fiber damage, as discussed in Section 5.3.1. It must be noted that, as discussed in Section 3.1.2, in MB tests, the axial stress along the composite strip  $\sigma(x)$  (Table 6.3) is influenced by the variation of bending moment and shear force along the beam. However, under the hypothesis of blocks rigid rotation, the effect of bending stresses on the composite can be neglected. Besides, the presence of tensile stresses in the block, at the interface with composite, which results from the flexural parzialization of the cross section (neutral axis position), may have an influence on the bond behaviour of the specimen. However, this boundary condition is similar to that of pull-pull DS test configuration, for which a clear influence of the substrate tension state on the test response of FRP-concrete joints was not reported in the literature [120].

In Eq. (6.74), the fiber axial stress  $\sigma$  was obtained from the CML calibrated using the DS tests in Section 5.3.3 (where  $\alpha=0$  and the bonded length  $L$  was consistent with that of MB specimens), as showed in section 6.1.4.2, and the global slip  $g$  were obtained from the displacement  $g_e$  (recorded by LVDTs G1 and G2) solving Eqs. (5.2) and (5.3) (see Section 5.3.2). The snubbing friction coefficient  $\mu$  was finally calibrated through a best-fitting analysis. Namely,  $\mu$  was obtained by best fitting the experimental ratio  $\rho$  with the equation obtained substituting Eq. (5.3) into Eq. (6.73):

$$\rho(g) = \frac{\sigma_0(g)}{\sigma(g)} = e^{\left(\mu \arcsin \frac{g}{h}\right)} \quad (6.75)$$

Stage	Fiber stress $\sigma_0$ – Global slip $g$ equations	$\sigma(x)$ and $\tau(x)$ distributions
Initial stage	$\begin{cases} \sigma_0 = 0 \\ g = 0 \end{cases}$	
Rigid-Softening	$\begin{cases} \sigma_0 = \frac{p\tau_{max}}{\omega A_f} \sin(\omega l) e^{(\alpha\mu)} \\ g = \frac{\tau_{max}}{k_2} [1 - \cos(\omega l)] \end{cases}$	
Rigid-Softening-Debonding	$\begin{cases} \sigma_0 = \left[ \frac{p\tau_f a}{A_f} + \frac{p\tau_{max}}{\omega A_f} \sin(\omega l_{eff}) \right] e^{(\alpha\mu)} \\ g = \frac{p\tau_f}{2EA_f} a^2 + \left[ \frac{p\tau_{max}}{\omega EA_f} \sin(\omega l_{eff}) \right] a + s_f \end{cases}$	
Softening-Debonding	$\begin{cases} \sigma_0 = \left\{ \frac{p\tau_f a}{A_f} + \frac{p\tau_f}{\omega A_f} \tan[\omega(L-a)] \right\} e^{(\alpha\mu)} \\ g = \frac{p\tau_f}{2EA_f} a^2 + \frac{p\tau_f}{\omega EA_f} \tan[\omega(L-a)] a + s_f \end{cases}$	
Fully-debonded	$\begin{cases} \sigma_0 = \frac{p\tau_f L}{A_f} e^{(\alpha\mu)} \\ g = \frac{p\tau_f}{2EA_f} L^2 + s_f \end{cases}$	

Note:  $\omega^2 = \frac{pk_2}{EA_f}$ ,  $l_{eff} = \frac{1}{\omega} \arccos\left(\frac{\tau_f}{\tau_{max}}\right)$ .

Table 6.3: Fiber stress  $\sigma_0$  and corresponding global slip  $g$  for each stage of the debonding process.

where  $\sigma_0(g)$  and  $\sigma(g)$  are the fiber stress of bond-gap MB and axial stress of DS tests, respectively, for a given value of  $g$  (and, in turn, of  $\alpha$ ). The average curve  $\sigma_0(g)$  of MB (MB\_G\_avg) and  $\sigma(g)$  of DS (DS\_avg) tests, which are reported in Figure 6.16 and Figure 6.20a, respectively, were considered in Eq. (6.75). The experimental ratio  $\rho$  obtained from the average experimental curves for  $0 < g \leq \bar{g}^*$  is reported in Figure 6.20b, where  $\bar{g}^* = 1.89$  mm is the global slip associated with the peak fiber stress of the MB\_G\_avg curve. The response softening branch ( $g > \bar{g}^*$ ) was not considered to evaluate  $\rho$  because the fiber was increasingly damaged during this phase in MB tests.

Figure 6.20b shows that, after an initial scattered stage ( $g < 0.2$  mm approximatively), the experimental  $\rho$  increases at an approximately constant rate until  $\bar{g}^*$  is attained. The irregularity in the initial trend of  $\rho$  can be attributed to the variability of the load responses at the beginning of the test, which are mainly governed by the portion of bonded length close to the loaded end. Small misalignment of the textile with respect to the applied force direction in DS tests, adjustments of the modified beams, and randomly distributed properties of the matrix-fiber interface may induce scatter of the initial branch of the load responses. With increasing the global slip, the area of matrix-fiber interface engaged in the stress-transfer increases and these differences become less significant. The snubbing friction coefficient  $\mu$  was obtained by best fitting the experimental  $\rho$  curve using Eq. (6.75) considering all data in Figure 6.20a, which provided  $\mu=0.40$  ( $R^2=0.82$ ), and considering only points associated with the increasing rate of  $\rho$ , which provided  $\mu=0.41$  ( $R^2=0.91$ ). The curve described by Eq. (6.75) with  $\mu=0.40$  is shown in Figure 6.20a. Since  $\rho$  obtained by Eq. (6.75) showed an approximately linear behavior, a further best fitting of the experimental  $\rho$  curve was performed considering a linear equation:

$$\rho(g) = 1 + \mu \arcsin\left(\frac{g}{h}\right) \quad (6.76)$$

Eq. (6.76) provided  $\mu=0.45$  ( $R^2=0.82$ ) considering all data in Figure 6.20a and  $\mu=0.46$  ( $R^2=0.94$ ) considering only points associated with the increasing rate of  $\rho$ . The  $\rho$  curve described by Eq. (6.76) with  $\mu=0.45$  is shown in Figure 6.20a.



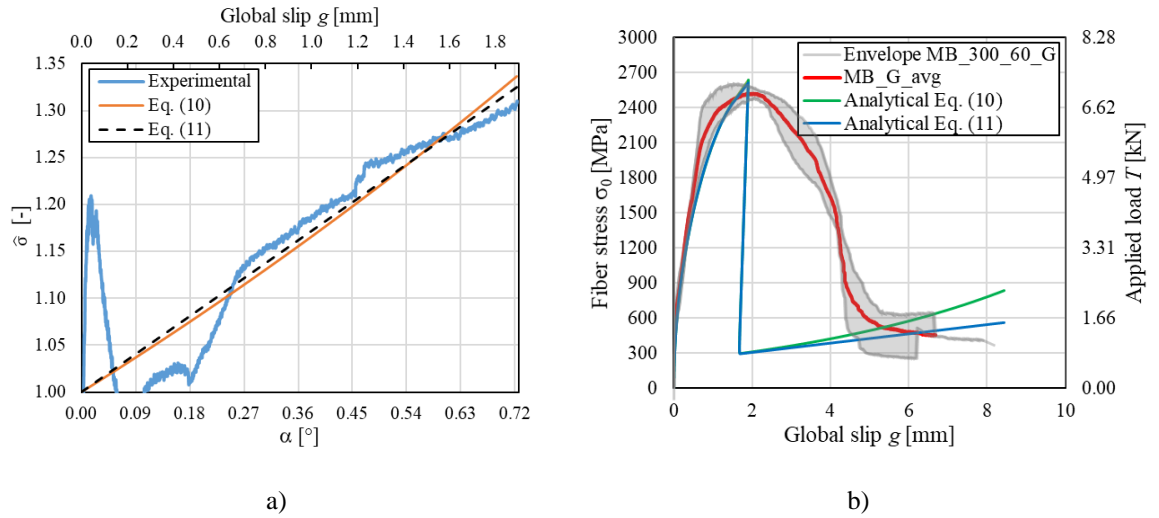


Figure 6.20. a) Experimental and fitted  $\rho$  curves. b) Comparison between analytical and experimental  $\sigma_0 - g$  responses of MB tests.

The analytical  $\sigma_0 - g$  curve obtained by Eq. (6.74), where  $\sigma$  was computed solving the bond differential equation as explained in Section 6.1 and assuming an exponential behavior of  $\rho$  [Eq. (6.75)] with  $\mu = 0.40$ , is compared with the MB\_G\_avg curve and the corresponding envelope in Figure 6.20b. This figure shows also the  $\sigma_0 - g$  curve obtained by Eq. (6.74) assuming a linear behavior of  $\rho$  [Eq. (6.76)] with  $\mu = 0.45$  (note that in this case the solution of the differential equation is the same reported in Table 6.3 substituting the term  $e^{\mu\alpha}$  with  $1 + \mu\alpha$ ). The analytical curves show good agreement with the average load response during the ascending branch. The peak stresses attained by the analytical curves [ $\sigma_0^* = 2638$  MPa for Eq. (6.75) and  $\sigma_0^* = 2614$  MPa for Eq. (6.76)] are only slightly higher than the peak stress attained by the average curve MB\_G\_avg ( $\sigma_0^* = 2522$  MPa). As in the case of the DS tests, the  $\sigma_0 - g$  experimental and analytical descending branches have a different behavior due to the presence of snap-back in the analytical solution (see Section 6.1.2). The final branches of the analytical curves, which are associated with the fully-debonded stage in Table 6.3, show increasing values of the fiber stress associated with friction. This behavior, which is caused by the increase of the angle  $\alpha$  with increasing  $g$ , can be observed for specimen MB\_300\_60\_G\_1 (Figure 5.6), whereas it was not present in the remaining specimens due to the occurrence of fiber damage. The increase of the fiber stress during the fully-debonded stage was observed in MB tests comprising masonry blocks and PBO FRCM strips reported in Chapter 4.

## 6.4 Conclusions and considerations for future guidelines

In this chapter, an analytical solution of the bond differential equation that describes the full-range stress-transfer mechanism at the matrix-fiber interface of FRCM composites was provided. The solution was obtained by adopting a rigid-softening cohesive material law (CML), which considers the possible presence of a residual friction stress component after the complete interface debonding. The results of pull-out and direct-shear tests on a PBO FRCM composite were employed to calibrate five different CMLs and validate the analytical solution. Then, an analytical approach able to account for the presence of stresses normal to the matrix-fiber interface was proposed. This model adopted a snubbing friction coefficient to model the presence of a localized normal stress component to the matrix-fiber interface. The results obtained allowed for drawing the following conclusions:

- The rigid-softening CML allowed for obtaining a closed-form solution of the composite effective bond length, which is a key parameter for the design of FRCM reinforcements.
- The interface fracture energy and energy contributions provided by friction could be identified.
- The minimum bonded length needed to develop a snap-back in the load response, provided a certain shape of the CML, could be obtained.
- The presence of the rigid stage in the CML did not allow for reproducing the initial elastic behavior observed in the experimental pull-out load responses. However, this elastic branch was limited with respect to the ascending non-linear behavior and did not affect the FRCM debonding interface capacity.
- The use of various strategies to estimate the CML provided different results that showed the importance of considering the effective bond length as a parameter for the CML estimation.
- The snubbing friction coefficient can be implemented on this analytical approach to accurately reproduce the load response of bond-gap modified beam tests starting from the CML calibrated on the results of direct shear tests.
- The relationship between the fiber stress of MB tests and axial stress of DS tests can be described by an exponential or a linear function depending on the rotation angle and on the snubbing friction coefficient.



# 7 FATIGUE AND POST-FATIGUE BEHAVIOUR OF FRCM COMPOSITES

A large amount of existing bridges and viaducts in western countries are made of reinforced and pre-stressed concrete. As well known, these structures are subjected to fatigue loads that affect their load-carrying capacity and durability. Moreover, the increasing traffic volume and weight of vehicles induce an increase of the fatigue loads applied to the structure. The combined effect of cyclic (fatigue) loading and steel reinforcement corrosion often results in fatigue crack initiation and propagation within the steel rebar cross-section, eventually resulting in sudden failure of the reinforcement and therefore of the structural element. Fatigue failure of steel rebars in reinforced-concrete elements represents an important cause of deterioration of highways, railroad bridges, and viaducts [121].

Several strengthening techniques have been proposed to extend the service life of bridge structures and prevent traffic obstruction, most of them aiming at reducing the stress level in steel rebar, to prevent the fatigue-crack opening or limit its propagation. Classical strengthening solutions include post-tensioning of external cables or near surface mounted steel bars [122]. The introduction of composite materials in the civil engineering field provided innovative solutions to extend the fatigue life of RC structural members. Externally bonded fiber-reinforced polymers, have proven to be an efficient and cost-effective strengthening solution to extend the fatigue life of RC

members [123,124]. However, FRP composites present some drawbacks, such as the different physico-chemical properties of organic resin and concrete, which is responsible for the poor thermal and vapour compatibility of FRP with concrete, and the poor resistance to relatively high temperatures [125,126]. FRCM composites overcome these issues [127] and proved to be effective solutions for the increase of both the flexural [16,128–130], shear [76,131,132], and axial strength of RC members [133–137], limited work was carried out to investigate the fatigue behaviour of these composites. Failure of FRCM strengthened members is usually caused by debonding of the composite at the matrix-fiber or at the composite-substrate interface [16]. The FRCM-concrete bond behaviour was studied mostly using direct shear test set-ups, where the interface is mainly subjected to shear stress. [64,138,139]. Although bond tests do not exactly reproduce the state of stress of the composite and substrate of a real strengthened member, their result is employed to define the composite effective stress, i.e. the maximum stress that can be applied to the EB composite, by numerous design guidelines (see e.g. [47,76,140]). The available literature regarding the bond behaviour of FRCM composites focused on the quasi-static monotonic response, while quite limited research was done to investigate the effect of fatigue loading on the FRCM-substrate and matrix-fiber bond behaviour [141].

In the present study, first a thorough review of the currently available studies on the fatigue behaviour of RC beams strengthened with FRCM composites is presented, pointing out how different parameters, such as the steel reinforcement ratio, load range, and loading frequency, affect the fatigue life and failure mode of the strengthened member. Then, experimental procedures, results and analysis of an experimental campaign on modified beam specimens with an externally bonded PBO FRCM strip are described to provide an insight on the effect of cyclic (fatigue) load to the FRCM-concrete bond behaviour. The use of a modified beam test set-up allowed for investigating the effect of fiber-matrix interface shear and normal stresses on the specimen fatigue bond behaviour. The results showed that the normal stress component increased the bond capacity in quasi-static monotonic tests (see section 5.4), whereas it induced damage to the fiber that reduced the specimen fatigue life in fatigue tests. These findings indicate that the normal stress component should be accounted for when a cyclic load is applied to the FRCM strengthened member and that further studies are needed to clarify the effect of the fatigue maximum and minimum applied load on the specimen fatigue life.

## 7.1 Fatigue strengthening of RC beam with FRCM composites: state of the art

According to ACI 215 [142], the fatigue limit of plain concrete, which corresponds to 10 million cycles of either compressive, tensile, or flexural loads, is estimated as 55% of its static strength, whereas the stress levels of unembedded steel rebars associated with failure in 2 million cycles are approximately 45-60% of the corresponding yielding stress. Referring to the internal reinforcement, Eurocode 2 [143] requires that steel bars withstand at least 2 million cycles with a stress range higher than or equal to 150 MPa and a recommended maximum fatigue stress of 60% of the bar characteristic yielding strength. Accordingly, if the fatigue stress exceeds this limit, cracks may occur in the reinforcing bar (rebar) and propagate until sudden failure of the element. Rebar crack propagation, which is accelerated by the simultaneous effect of corrosion and applied loads [144,145], results also in a reduction of the member stiffness and local steel concrete debonding. Studies conducted on the performance degradation of RC beams with corroded bars subjected to fatigue loading showed that rebar fatigue cracks are most likely to initiate at the largest corrosion pit location [146]. High levels of corrosion may dramatically reduce the fatigue life of RC beams, which was experimentally 65% lower in the case of 9.03% corrosion loss, compared with that of corresponding non-corroded beam [146].

Four-point bending experimental tests conducted on 2400 mm long RC beam samples showed that the fatigue life of RC beams is characterized by two main stages [147]. In the initial stage, several new concrete cracks formed in the maximum moment region, which determined a significant reduction of the member flexural stiffness. Increasing the number of load cycles, the crack number and flexural stiffness tended to stabilize and the beam entered the second stage, characterized by the steady propagation and widening of the existing cracks toward the compressive zone and by the occurrence of few new cracks. Between the end of the first and the beginning of the second stage, a fatigue crack initiated in the tension steel rebar at location of stress concentration due to bar imperfections (usually at rib root in deformed rebars [121]) and gradually propagated throughout the whole second stage. The beam eventually failed once the propagation of fatigue crack in the rebar caused the bar rupture and consequent compressive concrete crushing.

To increase the fatigue life of RC beams, EB FRCM composites can be employed to reduce the stress level in the steel reinforcement. FRCM composites can provide an

interesting strength contribution being applied at the outermost fibers (top or bottom) of the cross-section, which entails for a large moment arm associated with their tensile force contribution [76,148,149]. Therefore, they can lessen the stress range in the steel rebar, which in turn limits the crack growth rate determining a significant extension of the beam fatigue life. Furthermore, FRCM composites may reduce the beam deflection and limit the cross-section tensile strain [150], determining thinner and more spaced flexural cracks than those of corresponding unstrengthened beams. The presence of multiple fine cracks may improve the RC beam fatigue performance, as experimentally investigated by [151] on engineered cementitious composite (ECC)-strengthened RC beams. The presence of thin cracks would also reduce the rebar exposure to the environment, thus improving the durability of the steel reinforcement [147,150,152].

The following sub-sections provide an overview of the main research studies currently available on the fatigue behaviour of FRCM-strengthened RC beams.

### 7.1.1 Database of existing results

To the author's best knowledge, seven studies investigated the fatigue life of FRCM-strengthened RC beams [2,121,147,150,152–154]. The geometry of specimens considered in the seven studies are reported in Table 7.1 with reference to the parameters depicted in Figure 7.1.

In all tests considered, the specimen was subjected to an initial displacement-controlled quasi-static monotonic ramp that was stopped as the mean fatigue load was reached. Then, the specimen was subjected to a sinusoidal cyclic load. The maximum and minimum values of the cyclic load (which define the amplitude) are termed  $S_{max}$  and  $S_{min}$ , respectively. The cycle amplitude is  $(S_{max} - S_{min})/2$ . In some studies, the beam was subjected to a long-term sustained load and the steel rebar were also artificially corroded prior to the application of the FRCM composite and subsequent fatigue test.

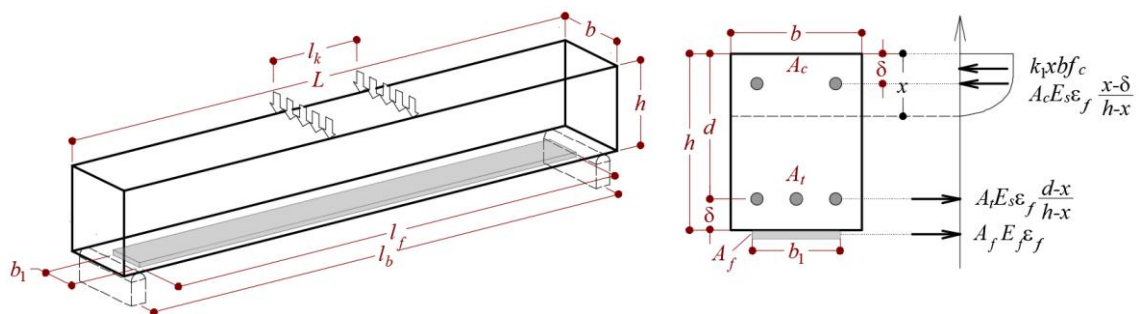


Figure 7.1: Test set-up and cross-section actions under pure bending condition.

Reference	Set-up			RC beam				FRCM		
	$l_b$	$l_k$	$L$	$b$	$h$	$d$	$A_c$	$A_t$	$l_f$	$b_1$
	(mm)	(mm)	(mm)	(mm)	(mm)	(mm)	(mm <sup>2</sup> )	(mm <sup>2</sup> )	(mm)	(mm)
(Jie et al., 2017) [147]	2200	800	2400	120	230	205	101	308	2000	120
(Aljazeera and Myers, 2017) [154]	2032	254	2133	203	305	268	157	236	1880	203
(Elghazy et al., 2018) [2]	2560	800	2800	2345	250	225	101	402	2400	150
(Pino et al., 2017) [121]	1524	0	1829	2972	305	268	142	213	1524	152
(Akbari Hadad et al., 2018) [153]	1524	0	1829	2345	305	268	142	213	1524	152
(Akbari Hadad and Nanni, 2020) [152]	1524	0	1829	2345	305	268	142	213	1524	152
(Su et al., 2020) [150]	1200	400	1500	170	300	262	100	226	1100	170

Table 7.1: Main geometrical characteristics of the experimental tests collected.

Table 7.2 reports the mechanical parameters and results of the specimens considered. For each specimen, the reinforcement ratio  $\beta^f$  [121], which relates the FRCM and steel reinforcement mechanical ratios allowing for expressing the (potential) FRCM strength contribution with respect to the steel reinforcement strength contribution, is reported [152]:

$$\beta^f = \frac{A_f E_f}{h} \cdot \frac{d}{A_t E_s} \quad (7.1)$$

where  $E_s$  and  $E_f$  are the elastic modulus of tension steel, assumed equal to 200 GPa, and the FRCM cracked elastic modulus according to ACI 549.4R-13 (2013) (see Table 2), respectively.  $\beta^f$  and of specimens with steel bars corroded prior to the fatigue test, marked with Y in column ‘‘Corr’’, were computed reducing the bar cross-section of 19% [2]. The FRCM (textile) strain  $\varepsilon_{f,\max}$  associated to  $S_{\max}$  was computed enforcing the cross-section equilibrium according to Eq.(7.2) (see Figure 7.1):

$$\begin{cases} k_1 x b f_c + A_c E_s \varepsilon_{f,\max} \left( \frac{x - \delta}{h - x} \right) - A_t E_s \varepsilon_{f,\max} \left( \frac{d - x}{h - x} \right) - A_f E_f \varepsilon_{f,\max} = 0 \\ k_1 x b f_c (d - k_2 x) + A_c E_s \varepsilon_{f,\max} \left( \frac{x - \delta}{h - x} \right) (d - \delta) + A_f E_f \varepsilon_{f,\max} (h - d) = M_{\max} \end{cases} \quad (7.2)$$

where  $x$  is the neutral axis depth,  $k_1$  and  $k_2$  are coefficients that define the concrete compressive force value and position, respectively [76],  $f_c$  is the concrete compressive strength, and  $M_{\max}$  is the bending moment at beam midspan associated with  $S_{\max}$ . In Eq.(7.2), a parabola-rectangle, elastic-perfectly-plastic, and linear-elastic response were assumed for concrete in compression, longitudinal steel, and FRCM composite, respectively [76]. In Table 7.2,  $P_i/P_u$  indicates the ratio of the long-term sustained load (when applied) to the ultimate load of the corresponding monotonic test, whereas  $\eta$  is



the FRCM strain exploitation ratio, which is the ratio between  $\varepsilon_{f,\max}$  and  $\varepsilon_{f,u}$ , being  $\varepsilon_{f,u}$  the FRCM (textile) strain corresponding to the failure of nominally equal monotonically-tested specimens.  $\varepsilon_{f,u}$  is computed according to Eq.(7.2), assuming  $M_{\max}=M_u$ , being  $M_u$  the bending moment at beam midspan associated with  $P_u$ .  $\eta$  provides a measure of the level at which the composite is working during the cyclic stage, however, for some specimens (indicated with “n.d.” in Table 7.2) the solution of Eq.(7.2) provided excessive values of specimen’s ultimate monotonic strain ( $> 0.05$ ) as a consequence of the compressive failure of concrete at the upper edge of the cross-section, which makes the value assumed by  $\eta$  unreliable. This was attributed to the adoption of the FRCM cracked modulus  $E_f$  for the solution of Eq.(7.2)(in accordance with [127]), which led in those cases to an underestimation of the FRCM contribution.

Finally,  $f$  and  $N$  are the cycle frequency and number of cycles at failure (i.e. fatigue life), respectively, whereas the normalized fatigue life  $\bar{N}$  is the ratio between the fatigue lives of the FRCM strengthened and of the corresponding control specimen. When fatigue failure occurred, i.e. the specimen failed for a number of cycles ( $N$ ) less than 2 million, it was due to steel rebar rupture followed by complete debonding of the FRCM at different interfaces. Three different debonding failure mode (FM) can be identified: I) at the matrix-fiber interface, II) at the composite-substrate interface or III) at the matrix-fiber interface with fiber damage and rupture. It should be noted that local debonding of the FRCM occurred before complete failure of the specimen. The failure modes (FM) observed are reported in Table 7.2, where the symbol “>” indicates that the fatigue test was interrupted after 2 million cycles.

Note: C=carbon, PBO=polyparaphenylene benzo-bisoxazole, G= glass, control=non-strengthened; †Not declared in the publication and assumed equal to that obtained in [24] and[155], respectively.

Ref.	Specimen	FRCM	$E_f$ [GPa]	$A_f$ [mm <sup>2</sup> ]	$\beta^f$ [%]	$\varepsilon_{f,max}$ [-]	$\eta$ [%]	Corr	$P_i/P_u$	$S_{min}/P_u$ [%]	$S_{max}/P_u$ [%]	$f$ [Hz]	$N_F$ [10 <sup>4</sup> ]	$\bar{N}$ [%]	FM
Jie et al. 2017 [147]	H2	control	-	-	-	-	-	Y	0.2	20	70	3	27	1.00	-
	H3	C	80 <sup>†</sup>	9	1.0	-	-	Y	0.2	20	70	3	33.7	1.25	I+III
	H4	C	80 <sup>†</sup>	9	1.0	-	-	Y	0.4	20	70	3	88.4	3.28	I+III
	H5	C	80 <sup>†</sup>	9	1.0	-	-	Y	0.6	20	70	3	60	2.22	I+III
	H6	control	-	-	-	-	-	-	-	20	70	3	31.5	1.00	-
	H7	C	80 <sup>†</sup>	9	1.0	-	-	-	-	20	70	3	41.5	1.32	I+III
	Aljazeera and Myers 2017 [154]	B1-0	control	-	-	-	-	-	-	-	16	32	5	200	1.00
B3-1		PBO	127	11.28	3.3	0.0015	n.d.	-	-	16	32	5	200	1.00	>
B4-1		PBO	127	11.28	3.3	0.0015	n.d.	Y	-	16	32	5	200	1.00	>
B5-1		PBO	127	11.28	3.3	0.0015	n.d.	Y	0.4	16	32	5	200	1.00	>
B6-4		PBO	127	45.12	3.3	0.0024	16.5	-	-	20	40	5	200	1.00	>
B7-4		PBO	127	45.12	3.3	0.0024	9.5	Y	-	20	40	5	200	1.00	>
B8-4		PBO	127	45.12	3.3	0.0024	9.7	Y	0.4	20	40	5	200	1.00	>
Elghazly et al. 2018 [2]	FCU	control	-	-	-	-	-	-	-	21	60	2	39.6	1.00	-
	FCS-2P-I	PBO	121	15	2.5	0.0016	16.4	Y	-	21	60	2	54.5	1.38	II
	FCS-4P-I	PBO	121	30	5.0	0.0018	13.3	Y	-	21	60	2	98.4	2.49	II
	FCS-4P-II	PBO	121	30	5.0	0.0018	13.3	Y	-	21	60	2	149.3	3.77	II
	FCS-3C-II	C	75	70.65	7.3	0.0022	12.4	Y	-	21	60	2	83.4	2.11	II
Pino et al. 2017 [121]	F-CON-0-75a	control	-	-	-	-	-	-	-	13	48	2	91.9	1.00	-
	F-FRCM-3P-90	PBO	128	20.98	5.5	0.0024	8.5	-	-	11	49	2	49.2	0.54	II
	F-FRCM-3P-85	PBO	128	20.98	5.5	0.0022	8.0	-	-	11	46	2	56.2	0.61	II
	F-FRCM-3P-	PBO	128	20.98	5.5	0.0021	7.6	-	-	11	44	2	200	2.18	>
	F-FRCM-3P-	PBO	128	20.98	5.5	0.0020	7.1	-	-	11	44	2	189	2.06	II
	F-FRCM-3P-	PBO	128	20.98	5.5	0.0021	7.6	-	-	11	41	2	200	2.18	>
	F-FRCM-3P-	PBO	128	20.98	5.5	0.0020	7.1	-	-	11	41	2	200	2.18	>
	F-FRCM-1P-75	PBO	128	7	1.8	0.0020	n.d.	-	-	12	50	2	96.2	1.05	I
	F-FRCM-5P-75	PBO	128	34.96	9.2	0.0020	-	-	-	15	46	2	200	2.18	>
Akbari Hadad et al. 2018 [153]	F-CON-75	control	-	-	-	-	-	-	-	14	51	2	82.4	1.00	-
	F-C200-75	C	65	13.38	1.8	0.0022	n.d.	-	-	13	49	2	133.4	1.62	I
	F-C200-70	C	65	13.38	1.8	0.0020	n.d.	-	-	13	45	2	123.1	1.49	I
	F-C200-65	C	65	13.38	1.8	0.0019	n.d.	-	-	13	42	2	200	2.43	>
	F-C200-60	C	65	13.38	1.8	0.0017	n.d.	-	-	13	39	2	200	2.43	>
	F-C600-75	C	64	47.73	6.4	0.0022	7.4	-	-	11	41	2	152.6	1.85	II
	F-C600-70	C	64	47.73	6.4	0.0021	6.9	-	-	11	38	2	195.9	2.38	II
	F-C600-65	C	64	47.73	6.4	0.0019	6.3	-	-	11	35	2	200	2.43	>
(Akbari Hadad and Nanni, 2020) [152]	F-CON-75	control	-	-	-	-	-	-	-	-	51	2	82.4	1.00	-
	F-ARG-85	G	20.3	95.46	4.0	0.0024	18.8	-	-	-	65	2	31.6	0.38	I
	F-ARG-75b	G	20.3	95.46	4.0	0.0021	16.9	-	-	-	59	2	63.5	0.77	I
	F-ARG-70	G	20.3	95.46	4.0	0.0019	15.4	-	-	-	54	2	88.2	1.07	I
	F-ARG-65	G	20.3	95.46	4.0	0.0018	14.3	-	-	-	50	2	200	2.43	>
	F-ARG-60	G	20.3	95.46	4.0	0.0017	13.3	-	-	-	46	2	200	2.43	>
(Su et al., 2020) [150]	F0-I0-0.65	control	-	-	-	-	-	Y	-	13	63	5	17.5	1.00	-
	F0-I20-0.65	control	-	-	-	-	-	Y	-	13	63	5	20.6	-	-
	F2-I0-0.55	C	80 <sup>†</sup>	28.58	5.5	0.0023	10.7	Y	-	11	53	5	130	6.82	I
	F2-I0-0.65	C	80 <sup>†</sup>	28.58	5.5	0.0027	12.8	Y	-	13	63	5	43.7	2.29	III
	F2-I0-0.75	C	80 <sup>†</sup>	28.58	5.5	0.0048	22.6	Y	-	15	73	5	28.5	1.5	III
	F2-I20-0.55	C	80 <sup>†</sup>	28.58	5.5	0.0023	10.7	Y	-	11	53	5	111.3	5.84	III
	F2-I20-0.65	C	80 <sup>†</sup>	28.58	5.5	0.0027	12.8	Y	-	13	63	5	52.8	2.77	III
	F2-I20-0.75	C	80 <sup>†</sup>	28.58	5.5	0.0052	24.7	Y	-	15	73	5	19.4	1.02	III
	F2-I60-0.65	C	80 <sup>†</sup>	28.58	5.5	0.0027	12.8	Y	-	13	63	5	44.7	2.35	III
	F2-I60-0.75	C	80 <sup>†</sup>	28.58	5.5	0.0048	22.6	Y	-	15	73	5	15.1	0.79	III
	F2-I100-0.65	C	80 <sup>†</sup>	28.58	5.5	0.0027	12.8	Y	-	13	63	5	36	1.89	III
	F2-I100-0.75	C	80 <sup>†</sup>	28.58	5.5	0.0048	22.6	Y	-	15	73	5	15.2	0.8	III
	F2-I100-0.85	C	80 <sup>†</sup>	28.58	5.5	0.0104	49.7	Y	-	17	83	5	6.2	0.33	III

Table 7.2: Main mechanical properties of the materials and parameters and results of the experimental tests collected.

### 7.1.2 Discussion of existing results

The fatigue life of the FRCM-strengthened beams analysed was mainly characterized by three stages [2,121,147]. In the first stage, the occurrence of flexural cracks in the RC beam induced a significant decrease of its flexural stiffness and a consequent increase of the midspan deflection. Simultaneously, the formation of transversal cracks (i.e. orthogonal to the longitudinal fiber yarn direction) in the FRCM matrix was observed. For specimens subjected to long-term sustained load before the application of the fatigue load, the number of new cracks that developed in this first stage was inversely proportional to the amount of sustained load applied [147,153].

The second stage, which covers most of the entire fatigue test, was characterized by a progressive and steady propagation of flexural cracks toward the compression zone. In general, during this stage, a primary flexural crack prevails in the maximum moment region or at midspan for specimens subjected to 3-point bending test ( $l_k=0$  in Figure 7.1 and Table 7.1). Elghazy et al. [2] pointed out how the second stage of FRCM-strengthened beams was characterized by a more gradual and steady degradation than what exhibited by unstrengthened beams in the same stage. This effect was attributed to the crack bridging effect of the FRCM composite, which delayed the crack propagation.

During the second stage of FRCM-strengthened beams, fatigue cracks initiated in the steel rebars and steadily propagated with increasing number of cycles, which determined a gradual loss of the specimen flexural stiffness due to the reduction of bar resisting cross-sectional area. During this stage, the widening of FRCM matrix cracks determined local debonding at the matrix-fiber and composite-concrete interface [121]. In sodium chloride corroded beams, a tendency of developing horizontal cracks in the FRCM reinforcement layer was observed, which resulted into the partial detachment of the FRCM strip from concrete, suggesting a detrimental effect of the chemical agent on the matrix-concrete bond capacity [147].

In the third (final) stage, the rebar fatigue crack growth rate rapidly increased and the collapse suddenly occurred due to the rebar rupture. Simultaneously, the large beam deflection induced complete FRCM debonding according to the failure modes described in the previous section (see Table 7.2).

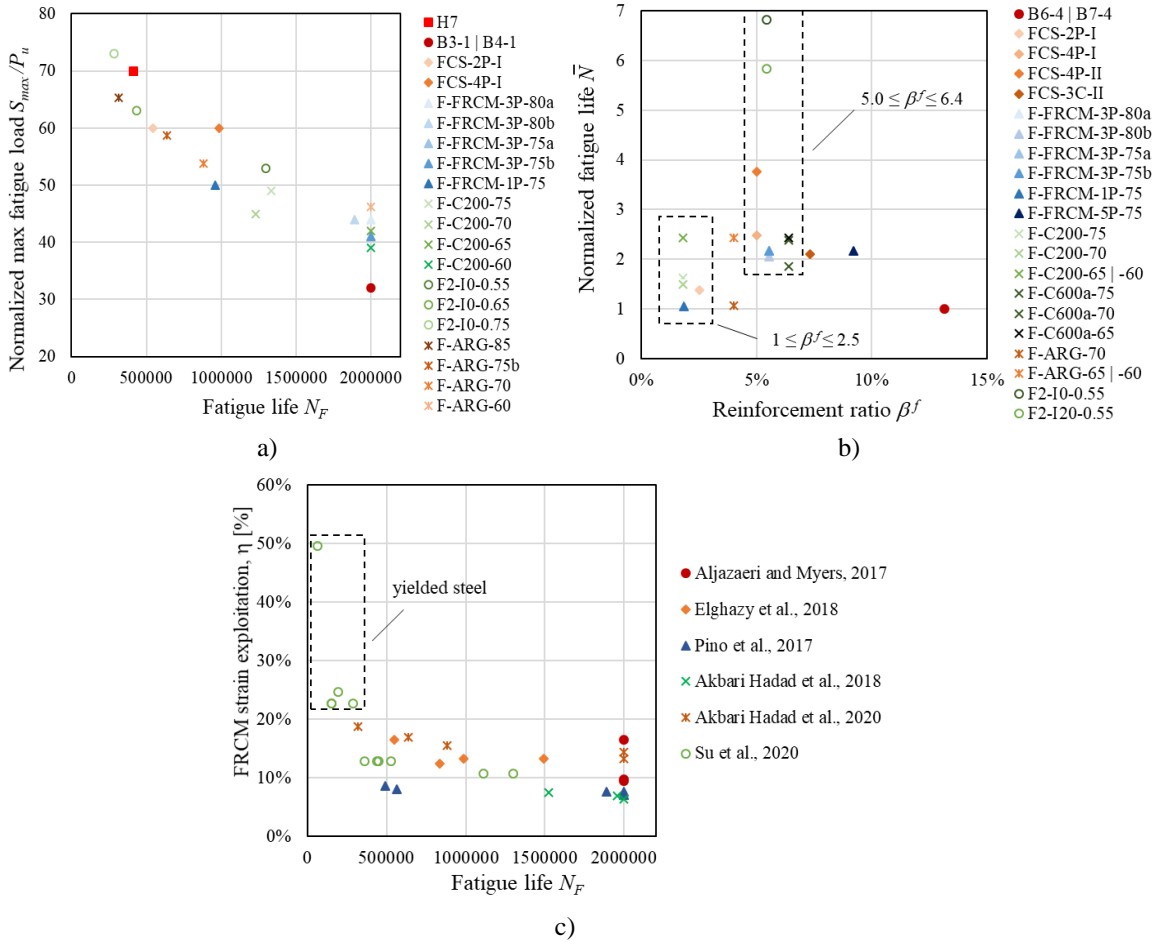


Figure 7.2: State of the art analysis: a) relation between normalized maximum applied fatigue load and fatigue life, b) relation between normalized fatigue life and reinforcement ratio, c) relation between FRCM (fiber) strain exploitation ratio and fatigue life.

Figure 7.2a shows the relationship between the normalized maximum applied fatigue load  $S_{max}/P_u$  and the fatigue life  $N_F$  of specimens characterized by reinforcement ratios  $\beta^f$  between 1% and 5.5% and that were not subjected to long-term sustained load before the fatigue test. The majority of specimens subjected to normalized maximum fatigue load below 45% were able to withstand 2 million cycles, which can be attributed to stress in the steel bars lower than their fatigue limit. With increasing  $S_{max}/P_u$ , an approximately linear reduction of the beam fatigue life was observed (Su et al. 2020), with high  $S_{max}/P_u$  values leading to quite low number of cycles at failure  $N_F$ .

Figure 7.2b shows the relationship between the reinforcement ratio  $\beta^f$  and the normalized fatigue life  $\bar{N}$  of specimens subjected to a maximum fatigue load  $S_{max}$  in the range 35–60% of the corresponding quasi-static monotonic ultimate load  $P_u$ . Specimens showing a premature failure ( $\bar{N} < 1$ , [121,150,152]) were not included in Figure 7.2b. Although the

results reported showed a certain scatter (typically observed in fatigue tests), comparison of  $\bar{N}$  between specimens characterized by low reinforcement ratios ( $1 \leq \beta^f \leq 2.5$ ) with that of moderately reinforced specimens ( $5.0 \leq \beta^f \leq 6.4$ ), suggests a general increase of the normalized fatigue life  $\bar{N}$  with the increase of reinforcement ratio  $\beta^f$ . However, specimens with a reinforcement ratio  $\beta^f > 6.4$  did not show an increase of  $\bar{N}$  with respect to specimens with  $5.0 \leq \beta^f \leq 6.4$  (Figure 7.2b). This result is attributed to the variation of failure modes in FRCM composites with increasing the number of textile layers (i.e. increasing the reinforcement ratio). Indeed, when a high number of textile layers is employed (high values of  $\beta^f$ ), debonding at the composite-substrate interface was observed (failure mode II in Table 7.2), with low increase of capacity with respect to specimens with a smaller number of textile layers [16]. The results analysed suggest a relationship between the reinforcement ratio and the FRCM failure mode. High  $\beta^f$  led to debonding at the composite-concrete interface (failure mode II in Table 7.2), due to the high FRCM stiffness [16,69], whereas low  $\beta^f$  determined matrix-fiber debonding (failure mode I in Table 7.2). However, it should be noted that FRCM complete debonding never occurred before steel rebar fatigue failure.

As pointed out in [2], the capacity of the FRCM composite of reducing the stress in the steel reinforcement is affected by the composite-concrete stress-transfer characteristics, which mainly depend on the matrix-fiber impregnation capability [156,157] and on the matrix compatibility with the substrate [147]. When adequate bond is provided, the effectiveness of FRCM in reducing the tensile stress on rebars under serviceability conditions can be evaluated by solving Eq.(7.2), assuming  $M_{\max} = M_{\text{serv}}$  which corresponds to the acting bending moment due to service loads. The ratio between the tensile stress in the steel reinforcement thus obtained, and that corresponding to the solution of the same equilibrium system under the assumption of  $A_f = 0$  (i.e. lack of FRCM strengthening) for a same  $M_{\text{serv}}$  value, gives a measure of the percentage of stress reduction on steel rebars, provided by the FRCM strengthening. The specimens analyzed in Table 7.2 indicates a rebar tensile stress reduction provided by the FRCM strengthening between 10 and 20%, which varied depending on the composite axial stiffness ( $E_f \times A_f$ ), computed assuming  $M_{\text{serv}}$  as the applied moment inducing a tensile stress in the steel reinforcement equal to 200 MPa. However, it must be noted that the mentioned stress reduction can be lower due to the fact that FRCM strengthenings are usually applied when a significant portion of the service load is already acting on the

structure, and thus, part of the stress is already acting on steel reinforcement at the moment of FRCM application.

The maximum strain  $\varepsilon_{f,max}$  computed (Table 7.2) shows that, independently from the FRCM textile material employed and reinforcement ratio, the majority of the specimens with tensile rebars in the elastic range exhibited a strain approximately equal to 0.2%, whereas only specimens with yielded tensile steel provided high values of  $\varepsilon_{f,max}$ . Figure 7.2c shows the relationship between the FRCM (fiber) strain exploitation ratio  $\eta$  and the fatigue life  $N_F$  of specimens analyzed. Specimens characterized by  $\eta > 20\%$  [150], for which  $S_{max}$  induced yielding in tension rebars, exhibited the shortest fatigue life in reason of the high level of stress transferred to the FRCM layer following steel yielding. For lower  $\eta$  values, an increase in the fatigue life of specimens within the same research work with the decrease of the strain exploitation ratio, was recorded for almost all the studies considered. Specimens included in [154] represented an exception in this analysis, since in all the cases the target number of cycles (2 million) was reached.

## 7.2 Experimental program

Based on the results discussed in the previous section, the effectiveness of FRCM strengthening application appears strongly related to its bond properties. Therefore, the study of the fatigue and post-fatigue behaviour of FRCM composites and of the influence of cyclic load on their bond performances, may provide important information to capture correctly the FRCM contribution to the fatigue life of FRCM-strengthened RC beams. In this section, the results of an experimental campaign on PBO FRCM-concrete joints are presented and discussed. In particular, 17 modified beam tests were performed, 6 subjected to quasi-static monotonic loading (presented in section 5.2.1), 8 subjected to fatigue loading and 3 to post-fatigue. The average ultimate load of the quasi-static monotonic tests was used as a reference to define the parameters of the fatigue load range applied to the specimens subjected to fatigue loading. Specimens were named according to the notation MB\_X\_Y\_B(or G)\_F(or PF)\_n, where MB (=modified beam) indicates the test set-up, X is the bonded length (in mm), Y is the bonded width (in mm), B (=bare-fiber) or G (=bond-gap) indicates the strip layout (see section 5.2.1), F or PF (if present) indicates a fatigue or post-fatigue test, respectively, and n is the specimen number.

### 7.2.1 Specimen geometry and materials

Each specimen (see Figure 7.3) consisted of two concrete prisms that formed a beam as they were joined by a cylindrical hinge (at midspan of the beam) placed near the compression side and by a FRCM strip applied at the bottom (tension) side. The midspan concrete discontinuity in the modified beam simulates the presence and opening of a flexural crack. Employing two separate prisms connected by the cylindrical hinge and by the composite strip, the position of the compression and tensile stress resultants at the midspan cross-section is always known, which allows for eliminating the uncertainties associated with the definition of the stress resultant in the compressed concrete in continuous or notched beam tests [75,76]. This test was originally proposed to study the bond behaviour of steel bars embedded in concrete [158] and was subsequently extended to the study of externally bonded [159] and near surface mounted [160] FRP composites. Recently, it was adopted to study the bond behaviour of FRCM composites applied to concrete and masonry substrates to investigate the effect of interface normal stresses on the specimen capacity [74].

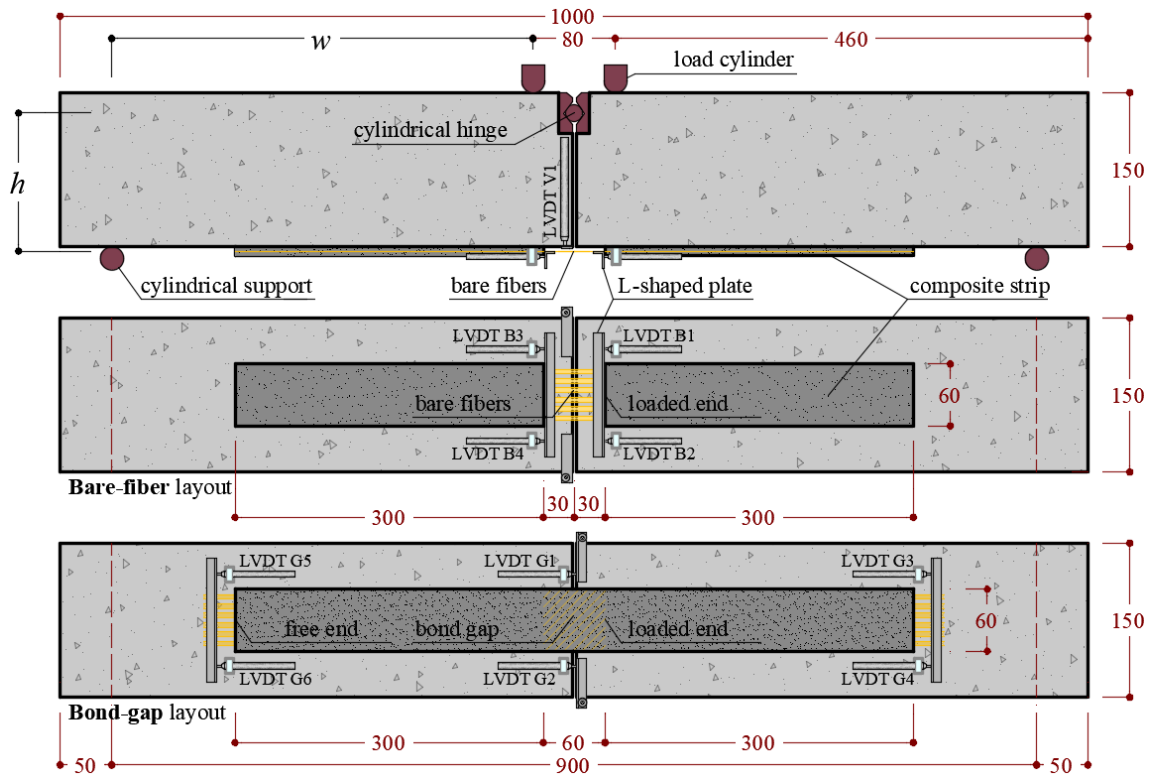


Figure 7.3: Geometry of bare-fiber and bond-gap layout modified beam tests (dimensions in mm).

In this experimental study, the concrete prisms had nominal dimensions equal to 150×150 (cross-section) ×500 (length) mm. The concrete average compressive strength

was measured on six 150 mm side cubes cast from the same batch of concrete used to cast the prisms and was equal to 37.9 MPa (coefficient of variation, CoV, equal to 6.02%). The FRCM composite was comprised of an open-mesh unbalanced PBO textile embedded within two layers of cement-based mortar. The PBO textile had a regular rectangular mesh with a clear space between bundles of 5 mm in the main (longitudinal) directions and 15 mm in the transverse direction [80]. The area of each longitudinal bundle was  $A_f=0.46 \text{ mm}^2$  and each specimen strip included 6 longitudinal yarns, resulting in an overall fiber cross-sectional area  $A=2.76 \text{ mm}^2$ . The composite overall bonded length was 600 mm ( $L=300 \text{ mm}$  on each prism) and width  $b_1$  was 60 mm, respectively. Two FRCM strengthening layouts were adopted, namely Bare-fiber and Bond-gap (see Section 5.3.2). The Bare-fiber layout entails for a 60 mm long bare portion of textile (i.e. the fibers were left bare) close to the specimen's midspan (see Figure 7.3). This discontinuity in the matrix allowed for a direct measurement of the relative slippage between fibers and matrix at the beginning of the bonded region of each prism (termed loaded end in Figure 7.3). The Bond-gap layout consisted of a continuous FRCM strip with a 60 mm non-bonded length across the modified-beam midspan. Adhesive tape was employed to prevent the strip from bonding the substrate along the bond-gap length and this allowed to avoid wedge failure of the specimen, as typically suggested in direct-shear tests.

The bare PBO fiber average tensile strength and elastic modulus, measured by tensile testing of textile strips with different widths, were equal to 3015 MPa (CoV=6.8%) and 206 GPa (CoV=6.5%), respectively [141]. The matrix flexural and splitting strength were 28.5 MPa and 3.5 MPa, respectively [101]. The tensile behaviour of the FRCM composite was previously studied by tensile testing of FRCM coupons using both the clamping-grip and the clevis-grip methods provided by the Italian initial type testing procedure [35] and U.S. acceptance criteria [37] for FRCM composites, respectively. Clamping-grip tests showed a trilinear stress-strain response with failure due to rupture of the embedded fiber textile [24], while clevis-grip tests showed a bilinear behaviour with failure due to debonding at the matrix-fiber interface [24,161]. Further details of these test results can be found in [24,161].

A 4-point bending set-up was used. The beams were placed on two cylindrical supports 900 mm apart, whereas the load was applied by two steel cylinders connected to the machine by a spherical hinge. Six or eight (depending on the strip layout) linear variable displacement transducers (LVDTs) were used to measure the displacement of the fiber



textile with respect to the concrete support and the midspan vertical deflection of the specimen. In bare-fiber specimens, four LVDTs (two on each side of the strip, named LVDT B1, B2, B3, and B4, see Figure 7.3) were employed to measure the fiber-substrate relative displacement at the two loaded ends. LVDTs B1-B4 were attached to the concrete substrate and reacted off of aluminum L-shaped plates bonded to the bare fibers immediately outside the matrix at the loaded ends. In bond-gap specimens, two LVDTs (one on each side of the strip, named LVDT G1 and G2, see Figure 7.3) attached to the concrete block and reacting off of aluminum L-shaped plates attached to the opposite block, were used to measure the relative displacement between blocks. Other four LVDTs (two on each block, one on each side of the composite strip, namely, LVDT G3, G4, G5, and G6, see Figure 7.3) measured the fiber-substrate relative displacement at the free ends of specimens with bond-gap strip layout. Finally, in all MB specimens, two LVDTs (one on each side of the specimen, named LVDT V1 and V2, see Figure 7.3) were used to measure the vertical deflection at midspan.

### 7.2.2 Quasi-static monotonic tests

The results of MB quasi-static monotonic tests were presented in Section 5.3.1 and are adopted in this section to obtain the specimen load carrying capacity, on which the fatigue load range is calibrated. For the sake of clarity, the principal information about the quasi-static test campaign on FRCM-strengthened beam tests is reported in this paragraph.

<i>Specimen</i>	$w$ [mm]	$h$ [mm]	$l_w$ [mm]	$L^\dagger$ [mm]	$b_1$ [mm]	$\sigma_0^*$ [MPa]	$g^*$ [mm]	$\sigma_{0f}$ [mm]	$g_f$ [mm]
MB_300_60_B_1						2220	1.47	199	5.59
MB_300_60_B_2	410	150	200	300	60	2124	2.47	481	5.51
MB_300_60_B_3						2135	1.61	430	5.85
Average						2159	1.83	370	6.00
CoV	-	-	-	-	-	0.024	0.243	0.406	0.031
MB_300_60_G_1						2499	1.89	671	4.59
MB_300_60_G_2	410	150	200	300	60	2514	2.14	283	4.72
MB_300_60_G_3						2617	1.58	434	6.35
Average						2543	1.87	463	5.22
CoV	-	-	-	-	-	0.025	0.149	0.422	0.188

$^\dagger$ Bonded length of a single block;  $\sigma_0^*$  = peak fiber stress;  $g^*$  = global slip at the peak fiber stress;  $\sigma_{0f}$  = residual fiber stress,  $g_f$  = global slip at the first attainment of the residual fiber stress.

*Table 7.3: Modified beam experimental test results.*

Tests were performed by monotonically increasing the vertical displacement (stroke) of the machine head at a constant rate of 0.2 mm/min. The fiber stress  $\sigma_0$  acting at the specimen loaded end, is computed according to Eq. (5.1), whereas the global slip  $g$  was directly measured by LVDTs B1-B2 or B3-B4 (depending on the specimen side where full debonding occurred), in bare-fiber layout specimens, whereas it was extracted from the average reading of LVDTs G1-G2, according to Eq. (5.2), in bond-gap ones. All specimens failed due to debonding of the fiber from the embedding matrix, as observed in single- or double-lap direct shear tests of the same FRCM composite including one or two layers of fiber [139]. The key parameters of all quasi-static monotonic tests are reported in Table 7.3, which is also reported below, for the sake of clarity. Following the procedure proposed in Section 3.1,  $\sigma_{0,f}$  was computed as the average of the applied stress within the range of  $g$  where the first derivative of  $\sigma_0(g)$  with respect to  $g$  was within the range  $[-200,0]$ . All specimens showed an initial linear branch (Figure 5.4b) associated with the elastic behaviour of the matrix-fiber interface. With increasing the machine stroke, micro-cracking at the matrix-fiber interface occurred and the load response became non-linear. In this branch, the global slip at the FDS started increasing at a higher rate with respect to that on the opposite side, named partially debonded side (PDS). As the machine stroke increased, the specimen attained the peak stress  $\sigma_0^*$ . Further increase of the machine stroke after  $\sigma_0^*$  determined a reduction of the applied load with increasing global slip at the FDS; whereas the slip at the loaded end of the PDS remained approximately constant or slightly decreased probably due to the recovery of the elastic deformation of the fibers. The fiber stress eventually plateaued at a value  $\sigma_{0,f}$  associated with the presence of friction at the matrix-fiber interface on the FDS.

### 7.3 Fatigue test

Eight specimens were subjected to fatigue test, 4 strengthened with bare-fiber FRCM strip layout and 4 with bond-gap. A photo of specimen MB\_300\_60\_B\_F\_3 before the beginning of the test is shown in Figure 7.4. The main geometrical properties and the number of cycles at failure  $N_F$  of each specimen are reported in Table 7.4.

Tests were performed by monotonically increasing the vertical displacement (stroke) of the machine head at a constant rate of 0.2 mm/min. The fiber stress  $\sigma_0$  acting at the specimen loaded end, is computed according to Eq. (5.1), whereas the global slip  $g$  was directly measured by LVDTs B1-B2 or B3-B4 (depending on the specimen side where

full debonding occurred), in bare-fiber layout specimens, whereas it was extracted from the average reading of LVDTs G1-G2, according to Eq. (5.2), in bond-gap ones. All specimens failed due to debonding of the fiber from the embedding matrix, as observed in single- or double-lap direct shear tests of the same FRCM composite including one or two layers of fiber [139]. The key parameters of all quasi-static monotonic tests are reported in Table 7.3, which is also reported below, for the sake of clarity. Following the procedure proposed in Section 3.1,  $\sigma_{0,f}$  was computed as the average of the applied stress within the range of  $g$  where the first derivative of  $\sigma_0(g)$  with respect to  $g$  was within the range  $[-200,0]$ .

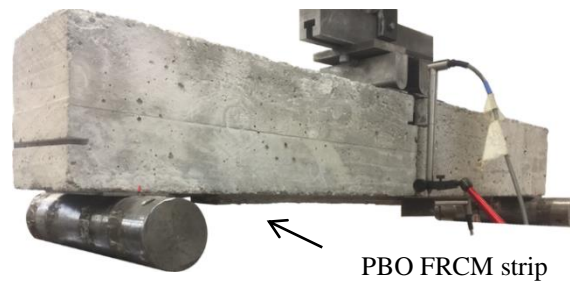


Figure 7.4: Photo of specimen MB\_300\_60\_B\_F\_3 before the beginning of the test.

Specimen	Bonded length <sup>†</sup> [mm]	Bonded width [mm]	Monotonic avg. capacity [ MPa ]	$\sigma_{0,min}$ [MPa]	$\sigma_{0,max}$ [MPa]	$R$ [-]	$N_F$ [10 <sup>6</sup> ]
MB_300_60_B_F_1				558	1015	0.55	0.20
MB_300_60_B_F_2	300	60	2159	550	986	0.56	0.47
MB_300_60_B_F_3				542	1073	0.51	1.22
MB_300_60_B_F_4				537	1065	0.50	0.32
Average				-	-	-	547
CoV	-	-	-	0.016	0.040	0.054	0.830
MB_300_60_G_F_1				673	1212	0.56	0.042
MB_300_60_G_F_2	300	60	2543	669	1231	0.54	0.028
MB_300_60_G_F_3				625	1332	0.47	0.032
MB_300_60_G_F_4				629	1343	0.47	0.01
Average				-	-	-	649
CoV	-	-	-	0.039	0.052	0.092	0.477

<sup>†</sup>Bonded length of each side of the specimen (Figure 7.3).

Table 7.4: Results of fatigue modified beam tests.

The specimens were initially loaded by monotonically increasing the machine stroke at a rate of 0.2 mm/min until the mean fatigue load was attained. Then, a sinusoidal load was applied until  $2 \cdot 10^6$  cycles or specimen failure were reached. The minimum and maximum nominal fiber stress in the fatigue cycles were equal to 25% ( $\sigma_{0,min}=550$  MPa) and 50% ( $\sigma_{0,max}=1050$  MPa) of the average bond capacity of the quasi-static monotonic

tests, respectively. The exact value of  $\sigma_{0,min}$  and  $\sigma_{0,max}$  measured are indicated in Table 7.4. The fatigue load range was determined considering an FRCC-strengthened member for which the composite provides a (relatively) small contribution to the load-carrying capacity under dead loads and is stressed up to half of its quasi-static monotonic load-carrying capacity  $\sigma^*$  under service loads. The fatigue load range determined corresponded to a fiber stress ranging between  $\sigma_{0,min}=550$  MPa and  $\sigma_{0,max}=1050$  MPa, for bare-fiber layout, whereas it ranged between  $\sigma_{0,min}=630$  MPa and  $\sigma_{0,max}=1270$  MPa, for bond-gap layout, in reason of a higher quasi-static capacity. Furthermore, based on load frequencies generally observed in civil engineering structures, which were reported to vary between 1 and 5 Hz [141], a loading frequency equal to 3 Hz was adopted.

### 7.3.1 Bare-fiber layout specimens

The four specimens subjected to fatigue test failed due to matrix-fiber debonding and eventual rupture of the fibers at the strip loaded-ends (failure mode c in Section 7.1.2). Figure 7.5a-d show the load responses of the specimens subjected to fatigue cycles in terms of fiber stress  $\sigma_0$  versus global slip  $g$  on FDS. In particular, Figure 7.5a-d feature the following portion of the response: i) the load response associated with the initial quasi-static monotonic test; ii) representative 10-cycle blocks selected at different number of cycles; and iii) the  $\sigma$ - $g$  response of the 10 cycles preceding failure of the specimen. During the first part of the fatigue test, the behaviour of the FRCC strips attached to the two concrete prisms was symmetrical, as it could be inferred from the readings of LVDTs B1 and B2 and LVDTs B3 and B4 (see Figure 7.5f). As the number of load cycles increased, the global slip measured at one side of the specimen, the FDS, started to increase at a higher rate with respect to that measured on the opposite side (i.e. the PDS) and the specimens entered in the second part of the test (Figure 7.5f). The global slip increase on the FDS could be attributed both to a progressive debonding at the matrix-fiber interface and to damage and eventual rupture of some fiber filaments due to the interlocking action with the embedding matrix [138,141]. Due to the progressive debonding and fiber damage, the stiffness of the specimen decreased, as can be inferred by the decreasing slope of the 10-cycle blocks as the global slip increased. The decrease in stiffness was associated with an increase of area enclosed by each cycle in Figure 7.5a-d. Further analyses are needed to clarify whether the progressive matrix-

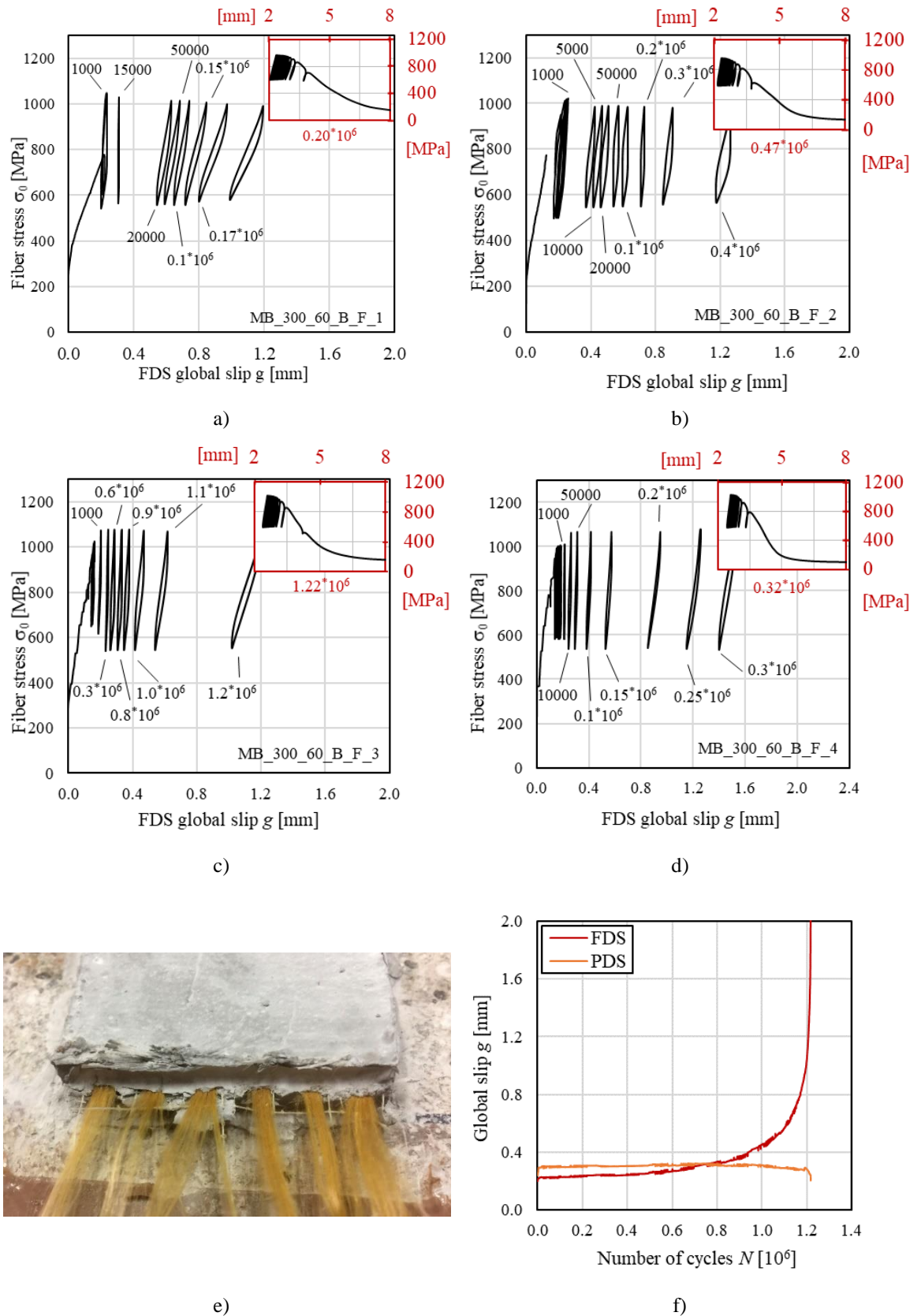


Figure 7.5: Load responses of specimen; a) MB\_300\_60\_B\_F\_1, b) MB\_300\_60\_B\_F\_2, c) MB\_300\_60\_B\_F\_3, and d) MB\_300\_60\_B\_F\_4. e) failure of PBO fibers and f) global slip vs. number of cycles for specimen MB\_300\_60\_B\_F\_3.

fiber debonding or damage and rupture of fiber filaments was mainly responsible for the progressive degradation of the specimen mechanical properties during the fatigue steady stage, will be covered in Section 7.4. With the increase of the number of cycles, the specimens entered a non-steady stage where  $g$  rapidly increased on the FDS until sudden collapse due to complete rupture of all fiber filaments, as shown in Figure 7.5e for specimen MB\_300\_60\_B\_F\_3, occurred. Since the fatigue tests were load-controlled, no residual constant applied stress could be observed at the end of the test. In fact, due to the progressive fiber filaments rupture, the specimens were no longer able to sustain the stress within the fatigue range applied, which determined the complete failure of the fibers.

The global slip  $g$ , computed as the average of the displacements of the two LVDTs on each specimen side (i.e. FDS and PDS), is depicted with respect to the number of cycles  $N$  for specimen MB\_300\_60\_B\_F\_3 in Figure 7.5f. The global slip on the FDS was consistent with the global slip on PDS up to approximately  $0.55 \times 10^6$  cycles, which indicates that the two strips on each side of the specimen behaved symmetrically during the first part of the test. As the number of cycles increased,  $g$  started to increase on the FDS, whereas it remained approximately constant on the PDS. When exceeded  $0.90 \times 10^6$ , the specimen entered the non-steady state, where the crack growth rate on the FDS that can be linked to  $dg/dN$  increased rapidly until failure of the specimen.

Although the same failure mode occurred for all specimens, the number of cycles at failure  $N_F$  was different (see Table 7.4). Figure 7.6a shows the global slip on the FDS versus the number of cycles for all specimens subjected to fatigue, whereas Figure 7.6b shows the same FDS global slip with respect to the normalized number of cycles  $N_n = N/N_F$ . Specimen MB\_300\_60\_B\_F\_1 failed after the lowest number of cycles, i.e.  $N_F = 0.20 \times 10^6$  (Table 7.4). Specimens MB\_300\_60\_B\_F\_2, 3 and 4 failed at  $N_F$  equal to  $0.47 \times 10^6$ ,  $1.22 \times 10^6$  and  $0.32 \times 10^6$ , respectively, which are still limited compared to the target fatigue life of  $2 \times 10^6$  cycles. In general, specimens that experienced high values of FDS global slip at low number of cycles provided a short fatigue life. This might indicate that the specimen degradation occurred progressively and not as a consequence of a sudden damage. In specimen MB\_300\_60\_B\_F\_1, an instantaneous increase of the FDS global slip from 0.3 mm to 0.6 mm was observed at the beginning of the test due to the opening of a matrix crack along the textile plane at the loaded end. This type of crack, which was not observed in other specimens subjected to either fatigue or quasi-static monotonic loading, was attributed to a poor adhesion between the internal, i.e. in

contact with the substrate, and external matrix layer. However, the presence of the crack affected the response of the specimen, which showed a FDS  $g$ - $N$  response during the steady stage with a slope similar to that of specimen MB\_300\_60\_B\_F\_2 and significantly higher than that of specimen MB\_300\_60\_B\_F\_3 (see Figure 7.6a). The steady stage ended at approximately 0.15, 0.45, 0.80 and 0.22 [ $10^6$ ] cycles for specimens MB\_300\_60\_B\_F\_1, \_2, \_3 and \_4, respectively.

The scatter between the results obtained did not allow for identifying a clear effect of the fatigue load on the FRCM-concrete bond behaviour. Comparisons of these results with those of direct shear tests on the same PBO FRCM composite [141] will help understand the effect of the test set-up and FRCM strip layout on the fatigue behaviour of FRCM-concrete joints. Further investigations are needed to clarify the maximum load range that can be applied to the externally bonded FRCM strip to guarantee an adequate fatigue life of the RC strengthened member.

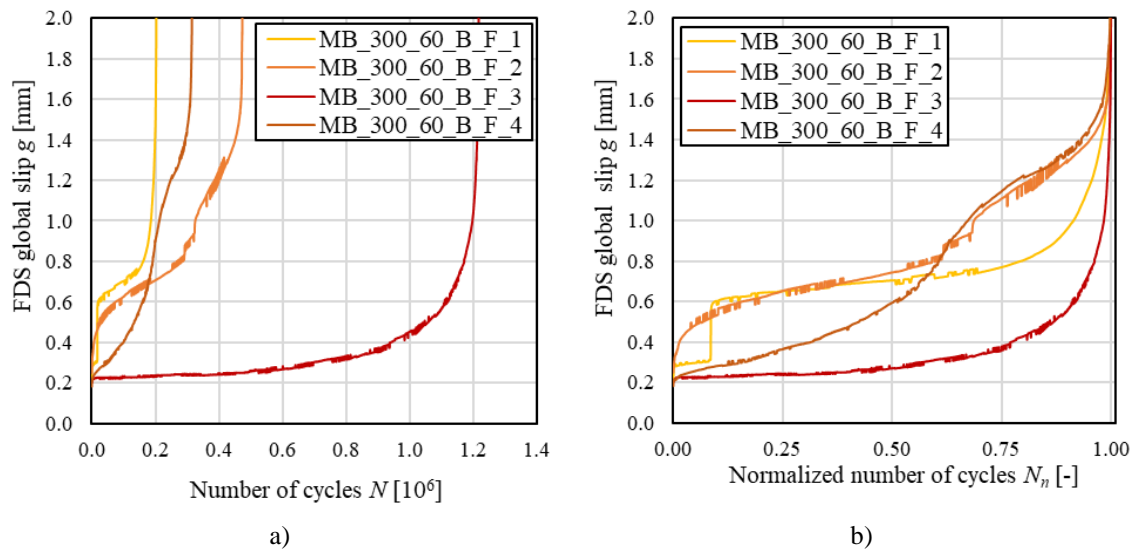


Figure 7.6: FDS global slip vs. a) number of cycles and b) normalized number of cycles for specimen subjected to fatigue test.

### 7.3.2 Bond-gap layout specimens

Specimens with bond-gap layout does not allow for a direct measurement of global slip, due to the presence of matrix along the bond-gap length (60 mm across midspan, see Figure 7.3). For this reason, the load response of specimens with bond-gap layout, subjected to fatigue cycles, is expressed in terms of fiber stress  $\sigma_0$  versus the average

midspan displacement  $g_e$  measured by LVDTs G1 and G2 (see Figure 7.3 and Figure 5.4b).

Figure 7.7a-d shows the  $\sigma_0$ - $g_e$  response for the tested specimens, including (i) the quasi-static monotonic test response (until the reaching of the average fatigue load), (ii) representative 10-cycles blocks corresponding to different stages in the cyclic test, (iii) 10-cycles block preceding the specimen's failure. All the specimens exhibited an initial almost linear branch, associated with the quasi-static monotonic loading ramp. Once, the average fatigue load was attained and fatigue cycles started, all the specimens recorded a significant increase in the midspan displacement  $g_e$ , which is also visible in Figure 7.7e. As the number of cycles increased ( $N=1800$  cycles roughly), specimens entered in a steady stage of the test, where  $g_e$  increased almost linearly with the number of cycles. The steady stage lasted for 36, 16, 25 and  $6 \times 10^3$  cycles for specimens MB\_300\_60\_G\_F\_1, \_2, \_3 and \_4, respectively. Like for bare-fiber layout, also for bond-gap specimens, the midspan displacement increase recorded in this stage could be attributed to a combined action of matrix-fiber debonding and a progressive damaging and rupture of fiber filaments. However, the limited extent of the steady stage recorded by bond-gap specimens, with respect to that of bare-fiber ones, suggests that for the former strip layout, the impact of fiber damaging was higher. This was also confirmed by a faster reduction in the 10-cycles blocks slope and a rapid increase of area enclosed by each cycle (see Figure 7.7a-d). With further increasing the number of cycles beyond the end of the steady stage, specimens entered in a non-steady stage, which lasted for around one quarter of their overall fatigue life (see Figure 7.7f). In this stage, a rapid increase in midspan displacement was recorded, until a sudden failure occurred due to the complete rupture of all the textile filaments along the bond-gap length. In no cases LVDTs G3-G4 and G5-G6 recorded free-end slippage of textile, meaning that debonding never completely established in the specimens, and that the fatigue failure was mainly governed by fiber damaging and rupture.

All the bond-gap layout specimens, tested under cyclic load, failed due to fiber rupture within the bond-gap length, at a number of cycles at failure  $N_F$  in the range  $10 \times 10^3$  -  $42 \times 10^3$  (see Table 7.4). The fatigue life of bond-gap specimens resulted on average 94.5% lower than that of nominally equal specimens with bare-fiber layout (see Table 7.4). This indicates that the presence of embedding matrix along the bond-gap length contributed in enhancing the damaging of fibers throughout the fatigue cycles. Nevertheless, it must be noted that bond-gap specimens were subjected to a higher



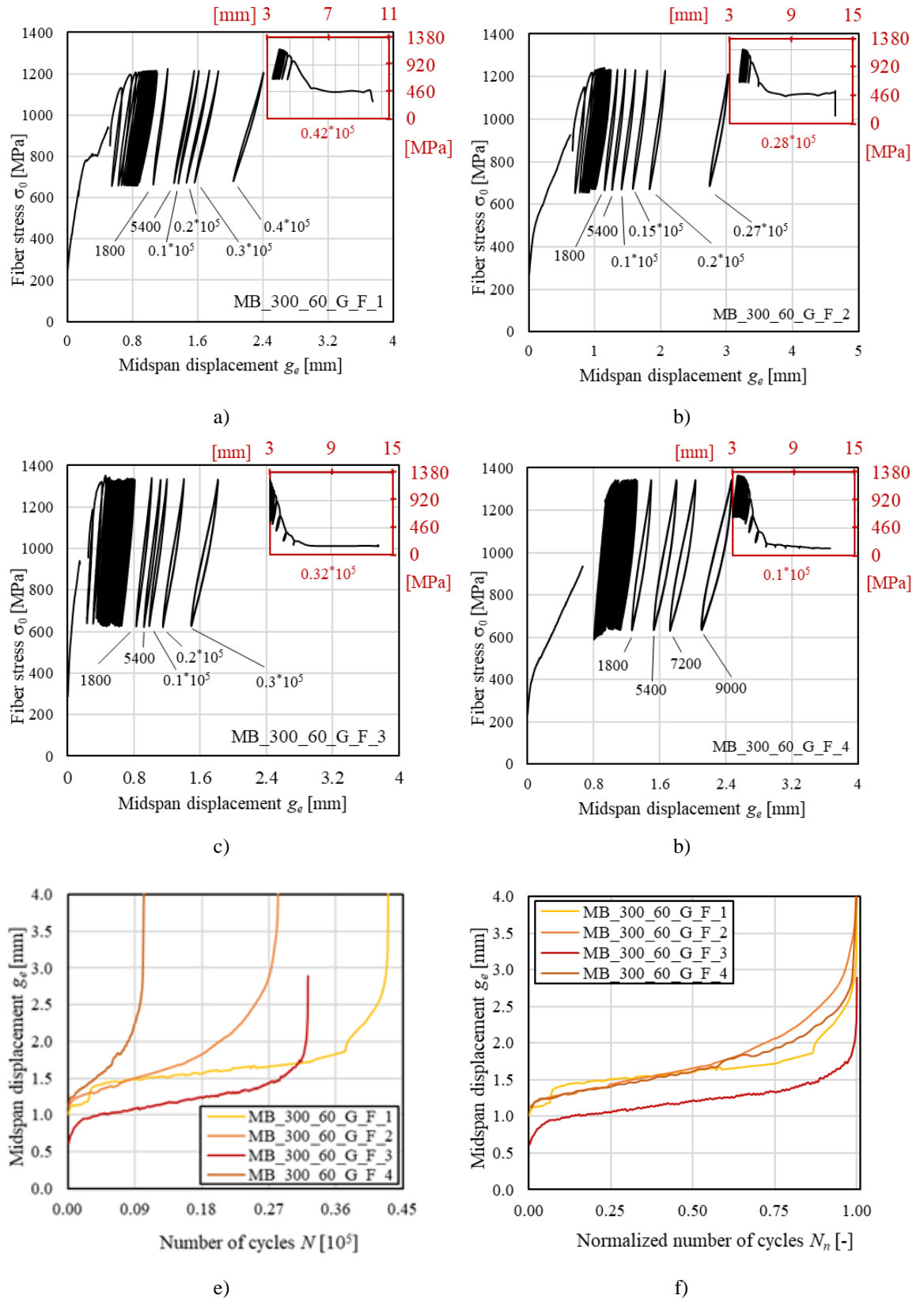


Figure 7.7: Load responses of specimen; a) MB\_300\_60\_G\_F\_1, b) MB\_300\_60\_G\_F\_2, c) MB\_300\_60\_G\_F\_3, and d) MB\_300\_60\_G\_F\_4. Midspan displacement vs. a) number of cycles and b) normalized number of cycles.

fatigue range, with 13% and 17% greater  $\sigma_{0,min}$  and  $\sigma_{0,max}$ , respectively. Indeed, if on the one hand the presence of embedding matrix across midspan, increased the specimen's quasi-static bond capacity (see Section 5.4), it led to a dramatically lower fatigue life, due to the extra damaging that friction and interlocking applied to fibers along that portion of the strip, in the cyclic stage of the test.

The relationship between the midspan displacement  $g_e$  and the normalized number of cycles  $N_n$ , showed in Figure 7.7f, may indicate that, despite of the number of cycles at failure endured by each specimen, their degradation occurred progressively and without any sudden localized rupture, which would have scattered the  $g_e - N_n$  curve.

## 7.4 Post-fatigue test

Specimens tested under fatigue load showed a progressive reduction of the cycles slope and increase in cycle area, which was associated to a decrease in specimen's stiffness. To clarify if whether the progressive matrix-fiber debonding or damage and rupture of fiber filaments was mainly responsible for the progressive degradation of the specimen mechanical properties during the fatigue steady stage, three specimens with a bond-gap strip layout, referred to with MB\_300\_60\_G\_PF\_1, \_2 and \_3, were subjected to a post-fatigue test, with the aim of quantifying the influence of friction on the failure mode of PBO-FRCM composites under high cycles fatigue conditions. The test consisted of three subsequent stages: (i) a displacement-controlled monotonic quasi-static loading ramp, until the average fatigue load was reached, (ii) a 10 or 15 thousand cycles fatigue loading stage (i.e. 33% and 50% of the average fatigue life of bond-gap specimens, see Table 7.4), (iii) a second displacement-controlled monotonic quasi-static stage, until failure of the specimen.

Figure 7.8 reports the fiber stress  $\sigma_0$  – midspan displacement  $g_e$  curves for all the post-fatigue tested specimens. All the specimens failed in the post-fatigue stage due to a telescopic debonding of the embedded fiber at the interface with matrix. The  $\sigma_0 - g_e$  responses showed an almost linear quasi-static monotonic branch, followed by representative 10-cycles blocks extracted each 2500 cycles in the fatigue-load stage. For specimens MB\_300\_60\_G\_PF\_1 and \_2 (see Figure 7.8a and b) a steady growth in the midspan displacement was recorded during the cyclic stage, combined with a progressive reduction of specimen stiffness throughout the cycles, which was denoted by a reduction in the cycles slope and an increase in their area. In the post-fatigue stage,

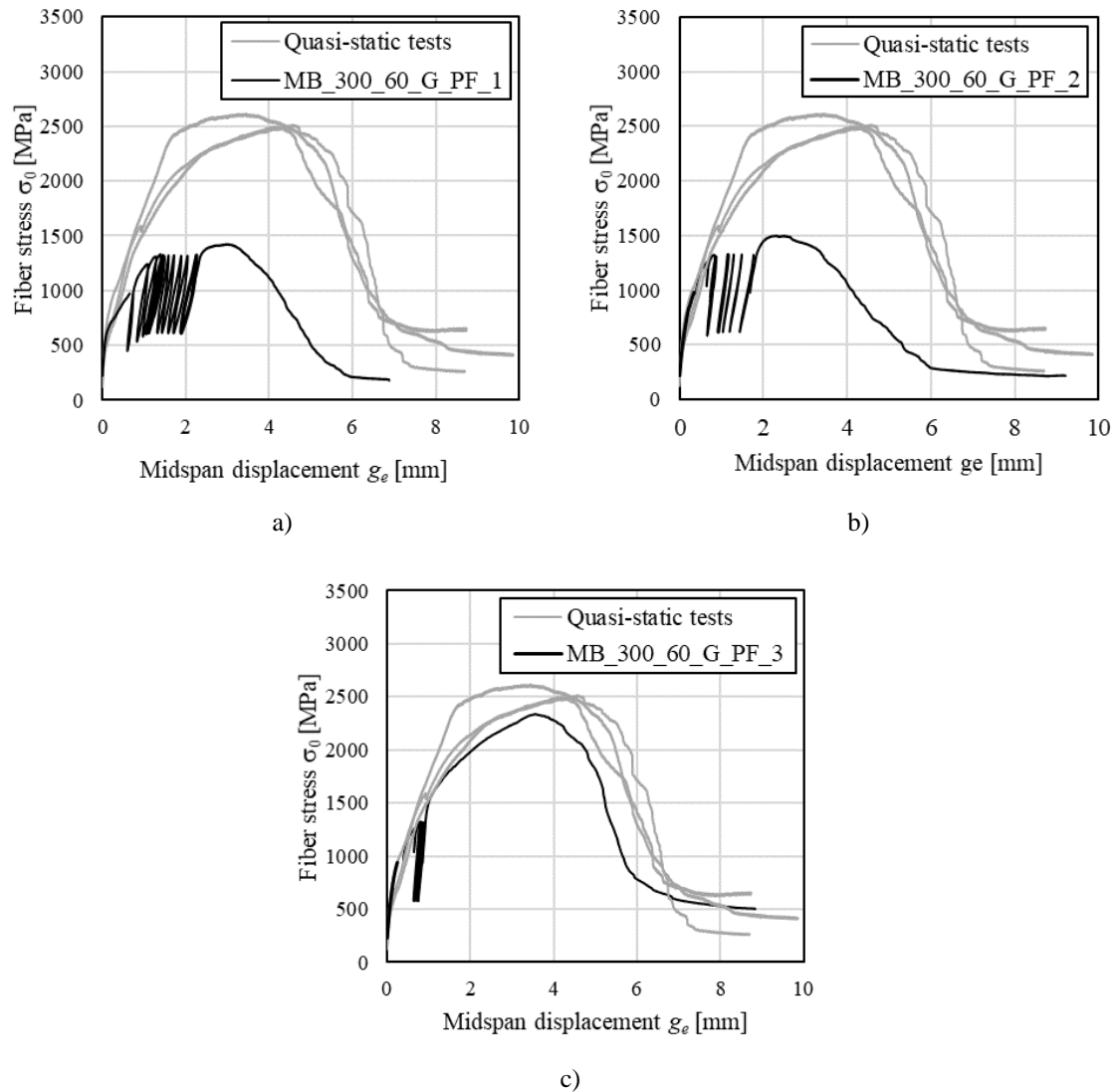


Figure 7.8: Load responses of specimen; a) MB\_300\_60\_G\_PF\_1, b) MB\_300\_60\_G\_PF\_2 and c) MB\_300\_60\_G\_PF\_3.

the response was initially linear, with a slope similar to that of the final cycles block. With increasing the imposed monotonic displacement, the response becomes non-linear, due to the progressive propagation of a cohesive crack at the matrix-fiber interface. The extent of this non-linear ascending branch was inversely proportional to the number of damaged/broken filaments, throughout the cyclic stage. Specimen MB\_300\_60\_G\_PF\_3, which did not undergo a pronounced increase in midspan displacement during the fatigue cycles, exhibited the wider post-fatigue ascending branch, which was similar to that of nominally equal monotonically tested specimens (see Figure 7.8c). The ascending branch of the response ended once the post-fatigue bond capacity  $\sigma_0^*_{PF}$  was reached, in correspondence with a midspan displacement  $g_e^*_{PF}$ . In the post-peak stage the response decreased due to the progressive softening of the

matrix-fiber interface. Eventually the  $\sigma_0-g_e$  curve plateaued at a constant residual friction value  $\sigma_{0,f,PF}$ , representative of the friction and interlocking phenomena between fiber and matrix, following the full debonding of the matrix-fiber interface.

Specimen	$\sigma_{0,min}$ [MPa]	$\sigma_{0,max}$ [MPa]	$R$ [-]	$N_{PF}$ [ $10^3$ ]	$\sigma_{0}^*_{PF}$ [MPa]	$g_e^*_{PF}$ [mm]	$\sigma_{0,f,PF}$ [MPa]
MB_300_60_G_PF_1	611	1326	0.46	10	1425	2.98	205
MB_300_60_G_PF_2	616	1325	0.46	10	1499	2.50	258
Average	613	1325	0.46	-	1462	2.74	231
CoV	0.006	0.001	-	-	0.036	0.124	0.162
MB_300_60_G_PF_3	583	1316	0.44	15	2338	3.56	590

Table 7.5: Results of post-fatigue tested modified beam specimens – BOND GAP layout.

Table 7.5 includes the test results for all post-fatigue tested specimens, where  $\sigma_{0,min}$  and  $\sigma_{0,max}$  indicates the minimum and maximum fiber stress in the oscillatory stage,  $N_{PF}$  is the number of load cycles of stage (ii),  $\sigma_{0}^*_{PF}$  and  $g_e^*_{PF}$  are the maximum fiber stress attained in the post-fatigue stage and the corresponding midspan opening, whereas  $\sigma_{0,f,PF}$  is the residual stress attained at the end of the post-fatigue stage. Specimens MB\_300\_60\_G\_PF\_1 and \_2 (see Figure 7.8a and b) exhibited a post-fatigue capacity  $\sigma_{0}^*_{PF}$ , respectively 44% and 41% lower than the average quasi-static bond capacity of nominally equal specimens ( $\bar{\sigma}_0^* = 2543$  MPa, see Table 7.4). This significant reduction in the post-fatigue bond capacity of the specimen, is attributed to the rupture of part of the filaments in the textile layer, throughout the 10 thousand cycles. The same trend is recorded in the post-fatigue residual friction capacity  $\sigma_{0,f,PF}$ , which resulted 57% and 44% lower than the average quasi-static residual capacity  $\bar{\sigma}_{0,f} = 463$  MPa (see Table 7.4), for specimen MB\_300\_60\_G\_PF\_1 and \_2, respectively. The rupture of a number of fiber filaments may justify this reduction, indeed, with a lower amount of fibers exchanging friction and interlocking with matrix along the debonded portion of the strip, the corresponding residual friction stress reduces. This is also confirmed by analytical considerations, if Eq. (6.49) is considered. Eq. (6.49) defines the applied load  $F_f = p\tau_f L$  which is borne by the composite strip when its fiber-matrix interface is fully debonded. A reduction in the friction exchange perimeter  $p$ , due to a premature rupture of filaments, may justify a reduction in the residual applied load  $F_f$ .

Specimen MB\_300\_60\_G\_PF\_3 (see Figure 7.8c), despite of a more extended fatigue stage (15 thousands cycles, 50% higher than that of specimens MB\_300\_60\_G\_PF\_1

and \_2, see Table 7.5), exhibited the highest post-fatigue bond capacity,  $\sigma_{0}^*_{PF} = 2338$  MPa, which was only 8% lower than the average capacity of corresponding quasi-static monotonic tests ( $\bar{\sigma}_0^* = 2543$  MPa, see Table 7.4). Similarly, also the post-fatigue residual capacity  $\sigma_{0,f,PF} = 590$  MPa, resulted higher than the corresponding quasi-static one ( $\bar{\sigma}_{0,f} = 463$  MPa, see Table 7.3). This behaviour can be attributed to a more homogenous distribution of tensile stresses among the textile yarns, which in turn resulted in a less aggressive impact of load cycles on the specimen post-fatigue performance. This was also confirmed by the even midspan deflection registered at the two specimen's sides throughout the cyclic stage (equal readings of LVDT V1 and V2, Figure 7.3), as shown in Figure 7.9a. A not regular midspan deflection in the specimen, due to differential blocks rotation, may generate stress concentrations in the textile which in turn determines localized damages in the reinforcing layer. Figure 7.9b shows that irregularity in the beam deflection may have an influence on the specimen's cyclic-stage behaviour, determining a higher residual midspan displacement throughout the cycles.

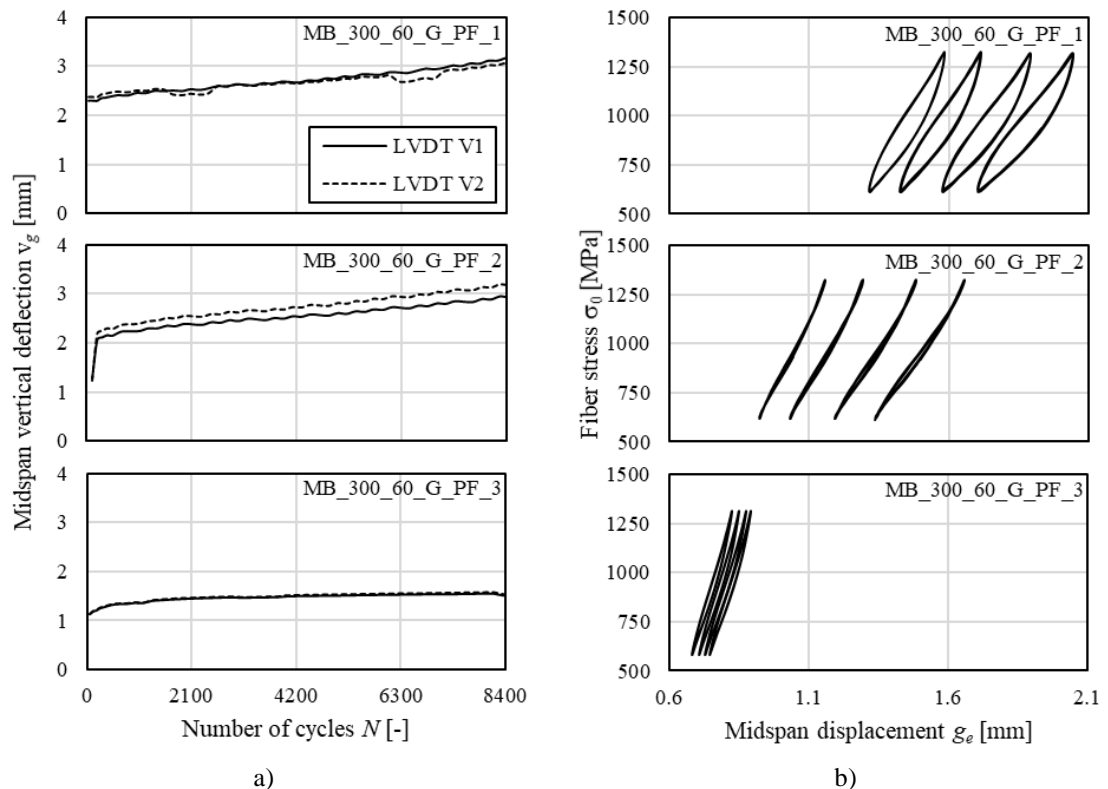


Figure 7.9: Cyclic stage of specimens MB\_300\_60\_G\_PF\_1-3, a) Midspan vertical deflection  $v_g$ , number of cycles  $N$  curves ; b) Representative 10-cycles block selected at  $N=1000, 3800, 5600$  and  $8300$ .

## 7.5 Conclusions and considerations for future guidelines.

In this chapter, an overview of the effect of high-cycles fatigue on the bond between FRCCM composites and RC beams, collected from the literature, was presented. Furthermore, the results of an experimental campaign to study the fatigue and post-fatigue response of modified beam test specimens, comprising PBO FRCCM strips and concrete prisms, were discussed. Based on the literature review and results herein presented, the following conclusions can be drawn:

- The fiber reinforcement ratio  $\beta^f$  has an important role in the fatigue life of FRCCM-strengthened RC beams due to its influence on the composite (debonding) failure mode. As a consequence, high reinforcement ratios did not provide significant increase in the specimen fatigue life due to the attainment of the composite bond capacity.
- The fatigue modified beam tests failed due to rupture of the fiber filaments with a number of cycles at failure between  $0.20 \times 10^6$  cycles and  $1.22 \times 10^6$  cycles, for bare-fiber layout specimens, and between  $0.01 \times 10^6$  cycles and  $0.042 \times 10^6$  cycles, for specimens with bond-gap layout. The failure mode did not allow to verify whether the progressive matrix-fiber debonding or damage of the fiber was mainly responsible for the progressive degradation of the specimen stiffness.
- Bond-gap layout showed higher sensitivity to friction between fiber and matrix throughout the load cycles, due to the presence of embedding matrix along the whole beam intrados, which resulted in a more severe damaging of textile that was not captured in bare-fiber specimens. Accordingly, bond-gap layout is not recommended for FRCCM samples involving textile with high sensitivity to friction damaging.
- Fatigue test on bond-gap layout specimens showed a fatigue life 94.5% lower than that of bare-fiber specimens. This difference was attributed to a more pronounced effect of damaging and rupture for fiber filaments, executed by the presence of embedding matrix along the bond-gap length.
- Bond-gap layout specimens, tested after 10 or 15 thousand fatigue cycles exhibited a lower bond and residual capacity than that of corresponding quasi-static test. This can be attributed to the rupture of a part of the composite

strengthening fibers, throughout the cyclic stage. Only in one case, the fatigue loading has not affected the residual capacity of the specimen, and this was attributed to a more homogeneous distribution of stress along the textile layer.

The results obtained are valid only for the PBO FRCM composite studied. The mode of failure observed, i.e. debonding at the matrix-fiber interface, showed the importance of the matrix-fiber bond properties and indicate that new experimental tests are needed if the fiber or matrix are varied.

## 8 GENERAL CONCLUSIONS AND FUTURE WORKS

The thesis work embraced some aspects of great importance for the complete assessment of the mechanism of adhesion to the support of inorganic matrix composites. In particular, the analysis focused on the effect of out-of-plane bending and fatigue on the bond behaviour of externally bonded FRCC composites, applied to reinforced concrete and masonry substrates. On that purpose, an in-depth review of the available concerning literature was carried out. The lit-review outcomes allowed arranging a many-sided experimental campaign, aimed at investigating how and in which measure, bending and fatigue may influence the bond performances of FRCC applications. The campaign involved both direct-shear and modified-beam test, on different FRCC materials, including PBO, carbon and steel (SRG). The results of experimental conducted on FRCC strengthened masonry and concrete substrates subjected to bending, showed that the application's bond capacity could be enhanced by the effect of a stress component normal to the matrix-fiber interface, attributed to the effect of substrate out-of-plane rotation.

The experimental campaign was supported by predictive analytical models, based on a fracture mechanics approach and calibrated on experimental results. The models proposed adopted a bi-linear rigid-softening cohesive material law, which allowed obtaining a simplified closed-form solution of the bond differential equation. Furthermore, to predict this extra bond capacity exhibited by modified beam test of



FRCM strengthened specimens, a snubbing-friction coefficient may be included, calibrated on the specific fiber-matrix pairing.

The experimental results of FRCM strengthened concrete specimens subjected to fatigue, proved the effectiveness of those materials to withstand a considerable number of load cycles. This makes those materials eligible for the strengthening of bridges, viaducts and aqueducts, which, due to their intended use, are constantly subjected to oscillatory load over their entire service life. From the review of the concerning scientific literature, two main parameters appeared to affect the effectiveness of FRCM applications subjected to fatigue, namely the reinforcement ratio and the fatigue load amplitude. An important aspect emerged from the comparison between experimental results and corresponding analytical prevision, is the effect of fiber damaging and deterioration on the effectiveness of FRCM application. This aspect may assume a crucial relevance under specific circumstances, such as the presence of sharp corner at the fiber exit point of strengthened substrates subjected to out-of-plane rotation, or in the case of deflected RC beam subjected to cyclic action. Fabric deterioration dramatically reduced both the bond capacity and the fatigue life of quasi-static and fatigue tested MB test, respectively. The effect could be more evident if a brittle fiber textile was employed, such as carbon or glass.

The experimental procedures described and the corresponding results, alongside with the predictive analytical models, represents a valid database for the development of future works on those topics. Due to the poor capability of inorganic matrix to penetrate and impregnate the fiber layer, result of experimental test conducted on FRCM specimens are affected by high scatter, especially if compared to that of FRPs. This will require a wider number of test to validate hypothesis ad theses presented in this study.

## 9 REFERENCES

- [1] Milano L, Mannella A, Morisi C, Martinelli A. Schede illustrative dei principali meccanismi di collasso locali negli edifici esistenti in muratura e dei relativi modelli cinematici di analisi. Allegato Alle Linee Guida per La Riparazione e Il Rafforzamento Di Elementi Strutturali, Tamponature e Partizioni (2008)(Accessed: 21 February 2012) 2008.
- [2] Elghazy M, El Refai A, Ebead U, Nanni A. Fatigue and Monotonic Behaviors of Corrosion-Damaged Reinforced Concrete Beams Strengthened with FRCM Composites. *J Compos Constr* 2018;22:04018040. [https://doi.org/10.1061/\(ASCE\)CC.1943-5614.0000875](https://doi.org/10.1061/(ASCE)CC.1943-5614.0000875).
- [3] De Lorenzis L, Teng JG. Near-surface mounted FRP reinforcement: An emerging technique for strengthening structures. *Composites Part B: Engineering* 2007;38:119–43. <https://doi.org/10.1016/j.compositesb.2006.08.003>.
- [4] Huang L, Yan B, Yan L, Xu Q, Tan H, Kasal B. Reinforced concrete beams strengthened with externally bonded natural flax FRP plates. *Composites Part B: Engineering* 2016;91:569–78. <https://doi.org/10.1016/j.compositesb.2016.02.014>.
- [5] Peled A. Confinement of Damaged and Nondamaged Structural Concrete with FRP and TRC Sleeves. *Journal of Composites for Construction* 2007;11:514–22. [https://doi.org/10.1061/\(ASCE\)1090-0268\(2007\)11:5\(514\)](https://doi.org/10.1061/(ASCE)1090-0268(2007)11:5(514)).
- [6] Pellegrino C, Modena C. An experimentally based analytical model for the shear capacity of FRP-strengthened reinforced concrete beams. *Mech Compos Mater* 2008;44:231–44. <https://doi.org/10.1007/s11029-008-9016-y>.
- [7] Pellegrino C, Modena C. Fiber-Reinforced Polymer Shear Strengthening of Reinforced Concrete Beams: Experimental Study and Analytical Modeling. *SJ* 2006;103:720–8. <https://doi.org/10.14359/16924>.
- [8] Teng JG, Chen JF, Smith ST, Lam L. Behaviour and strength of FRP-strengthened RC structures: A state-of-the-art review. *Proceedings of the Institution of Civil Engineers: Structures and Buildings* 2003;156:51–62. <https://doi.org/10.1680/stbu.2003.156.1.51>.

- [9] Triantafillou TC, Antonopoulos CP. Design of concrete flexural members strengthened in shear with FRP. *Journal of Composites for Construction* 2000;4:198–205. [https://doi.org/10.1061/\(ASCE\)1090-0268\(2000\)4:4\(198\)](https://doi.org/10.1061/(ASCE)1090-0268(2000)4:4(198)).
- [10] National Research Council. Guide for the design and construction of externally bonded FRP systems for strengthening existing structures. CNR-DT 200/R1. Rome, Italy: CNR; 2013.
- [11] Wang X, Ghiassi B, Oliveira DV, Lam CC. Modelling the nonlinear behaviour of masonry walls strengthened with textile reinforced mortars. *Eng Struct* 2017;134:11–24. <https://doi.org/10.1016/j.engstruct.2016.12.029>.
- [12] Al-Salloum YA, Almusallam TH, Elsanadedy HM, Iqbal RA. Effect of elevated temperature environments on the residual axial capacity of RC columns strengthened with different techniques. *Constr Build Mater* 2016;115:345–61. <https://doi.org/10.1016/j.conbuildmat.2016.04.041>.
- [13] De Felice G, D’Antino T, De Santis S, Meriggi P, Roscini F. Lessons Learned on the Tensile and Bond Behavior of Fabric Reinforced Cementitious Matrix (FRCM) Composites. *Front Built Environ* 2020;6. <https://doi.org/10.3389/fbuil.2020.00005>.
- [14] Donnini J, Spagnuolo S, Corinaldesi V. A comparison between the use of FRP, FRCM and HPM for concrete confinement. *Compos Part B* 2019;160:586–94. <https://doi.org/10.1016/j.compositesb.2018.12.111>.
- [15] Faleschini F, Zanini MA, Hofer L, Toska K, De Domenico D, Pellegrino C. Confinement of reinforced concrete columns with glass fiber reinforced cementitious matrix jackets. *Eng Struct* 2020;218:110847. <https://doi.org/10.1016/j.engstruct.2020.110847>.
- [16] D’Ambrisi A, Focacci F. Flexural Strengthening of RC Beams with Cement-Based Composites. *J Compos Constr* 2011;15:707–20. [https://doi.org/10.1061/\(ASCE\)CC.1943-5614.0000218](https://doi.org/10.1061/(ASCE)CC.1943-5614.0000218).
- [17] Babaeidarabad S, Loreto G, Nanni A. Flexural Strengthening of RC Beams with an Externally Bonded Fabric-Reinforced Cementitious Matrix. *J Compos Constr* 2014;18:04014009. [https://doi.org/10.1061/\(ASCE\)CC.1943-5614.0000473](https://doi.org/10.1061/(ASCE)CC.1943-5614.0000473).
- [18] Younis A, Ebead U, Shrestha KC. Different FRCM systems for shear-strengthening of reinforced concrete beams. *Constr Build Mater* 2017;153:514–26. <https://doi.org/10.1016/j.conbuildmat.2017.07.132>.
- [19] Ombres L, Verre S. Shear performance of FRCM strengthened RC beams. ACI SP-324, vol. 2017- March, Gianmarco de Felice, Lesley H. Sneed, Antonio Nanni; 2018.
- [20] Prota A, Marcari G, Fabbrocino G, Manfredi G, Aldea C. Experimental In-Plane Behavior of Tuff Masonry Strengthened with Cementitious Matrix–Grid Composites. *J Compos Constr* 2006;10:223–33. [https://doi.org/10.1061/\(ASCE\)1090-0268\(2006\)10:3\(223\)](https://doi.org/10.1061/(ASCE)1090-0268(2006)10:3(223)).
- [21] D’Antino T, Carozzi FG, Colombi P, Poggi C. Out-of-plane maximum resisting bending moment of masonry walls strengthened with FRCM composites. *Compos Struct* 2018;202:881–96. <https://doi.org/10.1016/j.compstruct.2018.04.054>.

- [22] Valluzzi MR, da Porto F, Garbin E, Panizza M. Out-of-plane behaviour of infill masonry panels strengthened with composite materials. *Mater Struct* 2014;47:2131–45. <https://doi.org/10.1617/s11527-014-0384-6>.
- [23] Alecci V, Focacci F, Rovero L, Stipo G, De Stefano M. Intrados strengthening of brick masonry arches with different FRCM composites: Experimental and analytical investigations. *Composite Structures* 2017;176:898–909. <https://doi.org/10.1016/j.compstruct.2017.06.023>.
- [24] Arboleda D, Carozzi FG, Nanni A, Poggi C. Testing procedures for the uniaxial tensile characterization of fabric-reinforced cementitious matrix composites. *J Compos Constr* 2016;20. [https://doi.org/10.1061/\(ASCE\)CC.1943-5614.0000626](https://doi.org/10.1061/(ASCE)CC.1943-5614.0000626).
- [25] Ruregold. Technical datasheet of MX-PBO CALCESTRUZZO 2019.
- [26] Ruregold. Technical datasheet of MX-C 50 CALCESTRUZZO 2019.
- [27] Ruregold. Technical datasheet of MX-PBO MURATURA 2019.
- [28] Ruregold. Technical datasheet of MX-C 25 MURATURA 2019.
- [29] Phoenix SL, Taylor HM. The Asymptotic Strength Distribution of a General Fiber Bundle. *Advances in Applied Probability* 1973;5:200–16. <https://doi.org/10.2307/1426033>.
- [30] Wolstenhooime LC, Smith RL, Bader MG. Statistical Inference About Stress Concentrations in Fibre-Matrix Composites. In: Bunsell AR, Lamicq P, Massiah A, editors. *Developments in the Science and Technology of Composite Materials: ECCM3 Third European Conference on Composite Materials 20.23 March 1989 Bordeaux-France*, Dordrecht: Springer Netherlands; 1989, p. 411–7. [https://doi.org/10.1007/978-94-009-1123-9\\_56](https://doi.org/10.1007/978-94-009-1123-9_56).
- [31] Contamine R, Si Larbi A, Hamelin P. Contribution to direct tensile testing of textile reinforced concrete (TRC) composites. *Mater Sci And Eng A* 2011;528:8589–98. <https://doi.org/10.1016/j.msea.2011.08.009>.
- [32] D’Antino T, Papanicolaou C. Comparison between different tensile test set-ups for the mechanical characterization of inorganic-matrix composites. *Constr Build Mater* 2018;171:140–51. <https://doi.org/10.1016/j.conbuildmat.2018.03.041>.
- [33] Donnini J, Chiappini G, Lancioni G, Corinaldesi V. Tensile behaviour of glass FRCM systems with fabrics’ overlap: Experimental results and numerical modeling. *Comp Struct* 2019;212:398–411. <https://doi.org/10.1016/j.compstruct.2019.01.053>.
- [34] Hartig J, Jesse F, Schicktanz K, Häußler-Combe U. Influence of experimental setups on the apparent uniaxial tensile load-bearing capacity of Textile Reinforced Concrete specimens. *Mater Struct* 2012;45:433–46. <https://doi.org/10.1617/s11527-011-9775-0>.
- [35] CSLPP - Servizio Tecnico Centrale. *Linee guida per la identificazione, la qualificazione ed il controllo di accettazione di compositi fibrorinforzati a matrice inorganica (FRCM) da utilizzarsi per il consolidamento strutturale di costruzioni esistenti*. Rome, Italy: 2019.
- [36] Carozzi FG, Poggi C. Mechanical properties and debonding strength of Fabric Reinforced Cementitious Matrix (FRCM) systems for masonry strengthening. *Compos Part B* 2015;70:215–30. <https://doi.org/10.1016/j.compositesb.2014.10.056>.

- [37] International Code Council Evaluation Service (ICC-ES). *Masonry and Concrete Strengthening Using Fabric-reinforced Cementitious Matrix (FRCM) and Steel Reinforced Grout (SRG) Composite Systems*. AC434. Whittier, CA: 2018.
- [38] European Committee for Standardization. *Methods of test for mortar for masonry. Determination of flexural and compressive strength of hardened mortar*. EN 1015-11:1999. Brussels, Belgium: CEN; 1999.
- [39] D’Antino T, Calabrese AS, Poggi C, Colombi P, Fava G, Bocciarelli M. *Strengthening of Different Types of Slabs with Composite-Reinforced Mortars (CRM)*. *Buildings for Educations* 2020. [https://doi.org/10.1007/978-3-030-33687-5\\_26](https://doi.org/10.1007/978-3-030-33687-5_26).
- [40] European Committee for Standardization. *Steel for the reinforcement and prestressing of concrete - Test methods. Part 2: welded fabric and lattice girders*. EN ISO 15630-2:2019. Brussels, Belgium: CEN; 2019.
- [41] Carabba L, Santandrea M, Carloni C, Manzi S, Bignozzi MC. *Steel fiber reinforced geopolymer matrix (S-FRGM) composites applied to reinforced concrete structures for strengthening applications: A preliminary study*. *Compos Part B* 2017;128:83–90. <https://doi.org/10.1016/j.compositesb.2017.07.007>.
- [42] De Santis S, de Felice G. *Steel reinforced grout systems for the strengthening of masonry structures*. *Composite Structures* 2015;134:533–48. <https://doi.org/10.1016/j.compstruct.2015.08.094>.
- [43] Porto F da, Stievanin E, Gabin E, Valluzzi MR. *SRG Application for Structural Strengthening of RC Beams*. *SP* 2012;286:1–14. <https://doi.org/10.14359/51683908>.
- [44] Borri A, Castori G, Corradi M, Speranzini E. *Shear behavior of unreinforced and reinforced masonry panels subjected to in situ diagonal compression tests*. *Constr Build Mater* 2011;25:4403–14. <https://doi.org/10.1016/j.conbuildmat.2011.01.009>.
- [45] Bertolesi E, Milani G, Carozzi FG, Poggi C. *Ancient masonry arches and vaults strengthened with TRM, SRG and FRP composites: Numerical analyses*. *Compos Struct* 2018;187:385–402. <https://doi.org/10.1016/j.compstruct.2017.12.021>.
- [46] Borri A, Casadei P, Castori G, Hammond J. *Strengthening of Brick Masonry Arches with Externally Bonded Steel Reinforced Composites*. *Journal of Composites for Construction* 2009;13:468–75. [https://doi.org/10.1061/\(ASCE\)CC.1943-5614.0000030](https://doi.org/10.1061/(ASCE)CC.1943-5614.0000030).
- [47] National Research Council. *Guide for the design and construction of externally bonded fibre reinforced inorganic matrix systems for strengthening existing structures*. CNR-DT 215/2018. Rome, Italy: CNR; 2018.
- [48] Nerilli F, Marfia S, Sacco E. *Micromechanical modeling of the constitutive response of FRCM composites*. *Construction and Building Materials* 2020;236:117539. <https://doi.org/10.1016/j.conbuildmat.2019.117539>.
- [49] Carozzi FG, Bellini A, D’Antino T, de Felice G, Focacci F, Hojdys Ł, et al. *Experimental investigation of tensile and bond properties of Carbon-FRCM composites for strengthening masonry elements*. *Comp Part B* 2017;128:100–19. <https://doi.org/10.1016/j.compositesb.2017.06.018>.

- [50] Donnini J, Corinaldesi V. Mechanical characterization of different FRCM systems for structural reinforcement. *Constr Build Mater* 2017;145:565–75. <https://doi.org/10.1016/j.conbuildmat.2017.04.051>.
- [51] Bencardino F, Condello A, Ashour AF. Single-lap shear bond tests on Steel Reinforced Geopolymeric Matrix-concrete joints. *Compos Part B* 2017;110:62–71. <https://doi.org/10.1016/j.compositesb.2016.11.005>.
- [52] Focacci F, D’Antino T, Carloni C, Sneed LH, Pellegrino C. An indirect method to calibrate the interfacial cohesive material law for FRCM-concrete joints. *Materials & Design* 2017;128:206–17. <https://doi.org/10.1016/j.matdes.2017.04.038>.
- [53] Banholzer B. Bond Behaviour of a Multi-Filament Yarn Embedded in a Cementitious Matrix. RETH Aachen University, 2004.
- [54] Sneed LH, D’Antino T, Carloni C, Pellegrino C. A comparison of the bond behavior of PBO-FRCM composites determined by double-lap and single-lap shear tests. *Cement Concr Compos* 2015;64:37–48. <https://doi.org/10.1016/j.cemconcomp.2015.07.007>.
- [55] Alecci V, Focacci F, Rovero L, Stipo G, De Stefano M. Extrados strengthening of brick masonry arches with PBO–FRCM composites: Experimental and analytical investigations. *Compos Struct* 2016;149:184–96. <https://doi.org/10.1016/j.compstruct.2016.04.030>.
- [56] Bizindavyi L, Neale KW. Transfer Lengths and Bond Strengths for Composites Bonded to Concrete. *Journal of Composites for Construction* 1999;3:153–60. [https://doi.org/10.1061/\(ASCE\)1090-0268\(1999\)3:4\(153\)](https://doi.org/10.1061/(ASCE)1090-0268(1999)3:4(153)).
- [57] Chajes MJ, Finch WW, Jr. TFJ, Thomson TA, Jr. Bond and Force Transfer of Composite-Material Plates Bonded to Concrete. *SJ* 1996;93:209–17. <https://doi.org/10.14359/1491>.
- [58] Täljsten B. Defining anchor lengths of steel and CFRP plates bonded to concrete. *Int J Adhesion and Adhesives* 1997;17:319–27. [https://doi.org/10.1016/S0143-7496\(97\)00018-3](https://doi.org/10.1016/S0143-7496(97)00018-3).
- [59] D’Antino T, Carozzi FG, Colombi P, Poggi C. A new pull-out test to study the bond behavior of fiber reinforced cementitious composites. *Key Engineering Materials* 2017;747 KEM:258–65. <https://doi.org/10.4028/www.scientific.net/KEM.747.258>.
- [60] Ombres L, Iorfida A, Verre S. FRCM/SRG - Masonry Joints: Experimental Investigation and Numerical Modelling. *Key Eng Mater* 2019. <https://doi.org/10.4028/www.scientific.net/KEM.817.3>.
- [61] Carloni C. Analyzing bond characteristics between composites and quasi-brittle substrates in the repair of bridges and other concrete structures. In: Kim YJ, editor. *Advanced Composites in Bridge Construction and Repair*. Chapter 3, Woodhead Publishing; 2014, p. 61–93. <https://doi.org/10.1533/9780857097019.1.61>.
- [62] D’Ambrisi A, Feo L, Focacci F. Experimental analysis on bond between PBO-FRCM strengthening materials and concrete. *Compos Part B* 2013;44:524–32. <https://doi.org/10.1016/j.compositesb.2012.03.011>.

- [63] Ombres L. Analysis of the bond between Fabric Reinforced Cementitious Mortar (FRCM) strengthening systems and concrete. *Comp Part B* 2015;69:418–26. <https://doi.org/10.1016/j.compositesb.2014.10.027>.
- [64] Raoof SM, Koutas LN, Bournas DA. Bond between textile-reinforced mortar (TRM) and concrete substrates: Experimental investigation. *Comp Part B* 2016;98:350–61. <https://doi.org/10.1016/j.compositesb.2016.05.041>.
- [65] Younis A, Ebead U. Bond characteristics of different FRCM systems. *Construction and Building Materials* 2018;175:610–20. <https://doi.org/10.1016/j.conbuildmat.2018.04.216>.
- [66] De Lorenzis L, Zavarise G. Modeling of mixed-mode debonding in the peel test applied to superficial reinforcements. *Int J Solids and Fract* 2008;45:5419–36. <https://doi.org/10.1016/j.ijsolstr.2008.05.024>.
- [67] Achintha M, Burgoyne CJ. Fracture mechanics of plate debonding: Validation against experiment. *Constr Build Mater* 2011;25:2961–71. <https://doi.org/10.1016/j.conbuildmat.2010.11.103>.
- [68] De Lorenzis L, Zavarise G. Interfacial stress analysis and prediction of debonding for a thin plate bonded to a curved substrate. *International Journal of Non-Linear Mechanics* 2009;44:358–70. <https://doi.org/10.1016/j.ijnonlinmec.2009.01.002>.
- [69] Carloni C, D’Antino T, Sneed LH, Pellegrino C. Three-Dimensional Numerical Modeling of Single-Lap Direct Shear Tests of FRCM-Concrete Joints Using a Cohesive Damaged Contact Approach. *J Compos Constr* 2018;22:04017048. [https://doi.org/10.1061/\(ASCE\)CC.1943-5614.0000827](https://doi.org/10.1061/(ASCE)CC.1943-5614.0000827).
- [70] Carloni C, Focacci F. FRP-masonry interfacial debonding: An energy balance approach to determine the influence of the mortar joints. *European Journal of Mechanics, A/Solids* 2016;55:122–33. <https://doi.org/10.1016/j.euromechsol.2015.08.003>.
- [71] Malena M. Closed-form solution to the debonding of mortar based composites on curved substrates. *Composites Part B: Engineering* 2018;139:249–58. <https://doi.org/10.1016/j.compositesb.2017.11.044>.
- [72] Basilio I, Fedele R, Lourenço PB, Milani G. Assessment of curved FRP-reinforced masonry prisms: Experiments and modeling. *Construction and Building Materials* 2014;51:492–505. <https://doi.org/10.1016/j.conbuildmat.2013.11.011>.
- [73] Malena M, de Felice G. Debonding of composites on a curved masonry substrate: Experimental results and analytical formulation. *Compos Struct* 2014;112:194–206. <https://doi.org/10.1016/j.compstruct.2014.02.004>.
- [74] Falope FO, Lanzoni L, Tarantino AM. Modified hinged beam test on steel fabric reinforced cementitious matrix (SFRCM). *Comp Part B* 2018;146:232–43. <https://doi.org/10.1016/j.compositesb.2018.03.019>.
- [75] Carloni C, Santandrea M, Imohamed IAO. Determination of the interfacial properties of SRP strips bonded to concrete and comparison between single-lap and notched beam tests. *Eng Fract Mech* 2017;186:80–104. <https://doi.org/10.1016/j.engfracmech.2017.09.020>.
- [76] D’Antino T, Focacci F, Carloni C, Sneed LH. Relationship between the effective strain of FRCM-strengthened RC beams and the debonding strain of direct shear

- tests. *Engineering Structures* 2020. <https://doi.org/10.1016/j.engstruct.2020.110631>.
- [77] International Code Council Evaluation Service (ICC-ES). Acceptance criteria for masonry and concrete strengthening using fabric-reinforced cementitious matrix (FRCM) and steel reinforced grout (SRG) composite systems. AC434. Whittier, CA: 2018.
- [78] Shen D, Shi X, Ji Y, Yin F. Strain rate effect on bond stress–slip relationship between basalt fiber-reinforced polymer sheet and concrete: *Journal of Reinforced Plastics and Composites* 2015. <https://doi.org/10.1177/0731684415574539>.
- [79] Yuan C, Chen W, Pham TM, Hao H, Cui J, Shi Y. Strain rate effect on interfacial bond behaviour between BFRP sheets and steel fibre reinforced concrete. *Composites Part B: Engineering* 2019;174:107032. <https://doi.org/10.1016/j.compositesb.2019.107032>.
- [80] Ruregold S.r.L. Technical datasheet of PBO-Mesh Gold 70/18 2019.
- [81] Ruregold S.r.L. Technical datasheet of C-Mesh Gold 84/84 2019.
- [82] Kerakoll. Technical datasheet of GeoSteel G600 2020.
- [83] Kerakoll. Technical datasheet of GeoLite 2019.
- [84] Terreal San Marco. Technical datasheet 2017. <https://sanmarco.it/scheda-prodotto.php?id-categoria=2&id-prodotto=36> (accessed August 15, 2019).
- [85] Pan J, Leung CK. Effect of Concrete Composition on FRP/Concrete Bond Capacity. *J Compos Constr* 2007;11:611–8. [https://doi.org/10.1061/\(ASCE\)1090-0268\(2007\)11:6\(611\)](https://doi.org/10.1061/(ASCE)1090-0268(2007)11:6(611)).
- [86] Ombres L, Mancuso N, Mazzuca S, Verre S. Bond between Carbon Fabric-Reinforced Cementitious Matrix and Masonry Substrate. *J Mater Civil Eng* 2019;31:04018356. [https://doi.org/10.1061/\(ASCE\)MT.1943-5533.0002561](https://doi.org/10.1061/(ASCE)MT.1943-5533.0002561).
- [87] D’Ambrisi A, Focacci F, Luciano R, Alecci V, De Stefano M. Carbon-FRCM materials for structural upgrade of masonry arch road bridges. *Comp Part B* 2015;75:355–66. <https://doi.org/10.1016/j.compositesb.2015.01.024>.
- [88] Askouni PD, Papanicolaou CG. Experimental investigation of bond between glass textile reinforced mortar overlays and masonry: the effect of bond length. *Mater Struct* 2017;50:164. <https://doi.org/10.1617/s11527-017-1033-7>.
- [89] Fu S-Y, Lauke B. The fibre pull-out energy of misaligned short fibre composites. *J Mater Sci* 1997;32:1985–93. <https://doi.org/10.1023/A:1018593931951>.
- [90] Li VC, Wang Y, Backer S. Effect of inclining angle, bundling and surface treatment on synthetic fibre pull-out from a cement matrix. *Composites* 1990;21:132–40. [https://doi.org/10.1016/0010-4361\(90\)90005-H](https://doi.org/10.1016/0010-4361(90)90005-H).
- [91] Carrara P, Ferretti D, Freddi F. Debonding behavior of ancient masonry elements strengthened with CFRP sheets. *Comp Part B* 2013;45:800–10. <https://doi.org/10.1016/j.compositesb.2012.04.029>.
- [92] D’Antino T, Sneed LH, Carloni C, Pellegrino C. Effect of the inherent eccentricity in single-lap direct-shear tests of PBO FRCM-concrete joints. *Comp Struct* 2016;142:117–29. <https://doi.org/10.1016/j.compstruct.2016.01.076>.



- [93] Finckh W, Zilch K. Influence of the Curvature on the Bond Force Transfer of EBR. *SP* 2011;275:1–20. <https://doi.org/10.14359/51682432>.
- [94] Federation Internationale du Beton. fib Bulletin 90. Externally applied FRP reinforcement for concrete structures. fib. The International Federation for Structural Concrete; 2019. <https://doi.org/10.35789/fib.BULL.0090>.
- [95] Alecci V, Focacci F, Rovero L, Stipo G, De Stefano M. Extradados strengthening of brick masonry arches with PBO–FRCM composites: Experimental and analytical investigations. *Compos Struct* 2016;149:184–96. <https://doi.org/10.1016/j.compstruct.2016.04.030>.
- [96] Pantò B, Cannizzaro F, Caddemi S, Calì I, Chácará C, Lourenço PB. Nonlinear Modelling of Curved Masonry Structures after Seismic Retrofit through FRP Reinforcing. *Buildings* 2017;7:79. <https://doi.org/10.3390/buildings7030079>.
- [97] De Santis S. Bond behaviour of Steel Reinforced Grout for the extradados strengthening of masonry vaults. *Construction and Building Materials* 2017;150:367–82. <https://doi.org/10.1016/j.conbuildmat.2017.06.010>.
- [98] Rotunno T, Fagone M, Bertolesi E, Grande E, Milani G. Curved masonry pillars reinforced with anchored CFRP sheets: An experimental analysis. *Composites Part B: Engineering* 2019;174:107008. <https://doi.org/10.1016/j.compositesb.2019.107008>.
- [99] ASTM International. Standard Test Method for Evaluation of Performance for FRP Composite Bonded to Concrete Substrate using Beam Test. ASTM D7958/D7958M - 17. ASTM International; n.d. [https://doi.org/10.1520/D7958\\_D7958M-17](https://doi.org/10.1520/D7958_D7958M-17).
- [100] Alecci V, Misseri G, Rovero L, Stipo G, De Stefano M, Feo L, et al. Experimental investigation on masonry arches strengthened with PBO-FRCM composite. *Comp Part B* 2016;100:228–39. <https://doi.org/10.1016/j.compositesb.2016.05.063>.
- [101] D’Antino T, Carloni C, Sneed LH, Pellegrino C. Matrix–fiber bond behavior in PBO FRCM composites: A fracture mechanics approach. *Eng Fract Mech* 2014;117:94–111. <https://doi.org/10.1016/j.engfracmech.2014.01.011>.
- [102] ASTM International. Standard Test Method for Evaluation of Performance for FRP Composite Bonded to Concrete Substrate using Beam Test. ASTM D7958/D7958M - 17. ASTM International; n.d. [https://doi.org/10.1520/D7958\\_D7958M-17](https://doi.org/10.1520/D7958_D7958M-17).
- [103] Koutas LN, Tetta Z, Bournas DA, Triantafillou TC. Strengthening of Concrete Structures with Textile Reinforced Mortars: State-of-the-Art Review. *J Compos Constr* 2019;23:03118001. [https://doi.org/10.1061/\(ASCE\)CC.1943-5614.0000882](https://doi.org/10.1061/(ASCE)CC.1943-5614.0000882).
- [104] Carloni C, D’Antino T, Sneed LH, Pellegrino C. Role of the Matrix Layers in the Stress-Transfer Mechanism of FRCM Composites Bonded to a Concrete Substrate. *J Eng Mech* 2015;141:04014165. [https://doi.org/10.1061/\(ASCE\)EM.1943-7889.0000883](https://doi.org/10.1061/(ASCE)EM.1943-7889.0000883).
- [105] D’Antino T, Colombi P, Carloni C, Sneed LH. Estimation of a matrix-fiber interface cohesive material law in FRCM-concrete joints. *Composite Structures* 2018;193:103–12. <https://doi.org/10.1016/j.compstruct.2018.03.005>.

- [106] Colombi P, D'Antino T. Analytical assessment of the stress-transfer mechanism in FRCM composites. *Comp Struct* 2019;220:961–70. <https://doi.org/10.1016/j.compstruct.2019.03.074>.
- [107] Zhang SS, Teng JG, Yu T. Bond–slip model for CFRP strips near-surface mounted to concrete. *Eng Struct* 2013;56:945–53. <https://doi.org/10.1016/j.engstruct.2013.05.032>.
- [108] Zou X, Sneed LH, D'Antino T. Full-range behavior of fiber reinforced cementitious matrix (FRCM)-concrete joints using a trilinear bond-slip relationship. *Composite Structures* 2020;239. <https://doi.org/10.1016/j.compstruct.2020.112024>.
- [109] Triantafillou TC. Fracture mechanics approaches to concrete strengthening using FRP materials. *Proceedings Framcos-3 1996*.
- [110] Carrara P, Ferretti D, Freddi F, Rosati G. Shear tests of carbon fiber plates bonded to concrete with control of snap-back. *Eng Fract Mech* 2011;78:2663–78. <https://doi.org/10.1016/j.engfracmech.2011.07.003>.
- [111] Barbieri G, Biolzi L, Bocciarelli M, Cattaneo S. Size and shape effect in the pull-out of FRP reinforcement from concrete. *Composite Structures* 2016;143:395–417. <https://doi.org/10.1016/j.compstruct.2016.01.097>.
- [112] Carrara P, Ferretti D. A finite-difference model with mixed interface laws for shear tests of FRP plates bonded to concrete. *Composites Part B: Engineering* 2013;54:329–42. <https://doi.org/10.1016/j.compositesb.2013.05.030>.
- [113] Colombi P, Fava G, Poggi C. End debonding of CFRP wraps and strips for the strengthening of concrete structures. *Composite Structures* 2014;111:510–21. <https://doi.org/10.1016/j.compstruct.2014.01.029>.
- [114] Milani G, Grande E. Simple bisection procedure in quickly convergent explicit ODE solver to numerically analyze FRCM strengthening systems. *Composites Part B: Engineering* 2020;199. <https://doi.org/10.1016/j.compositesb.2020.108322>.
- [115] Carloni C, Verre S, Sneed LH, Ombres L. Loading rate effect on the debonding phenomenon in fiber reinforced cementitious matrix-concrete joints. *Composites Part B: Engineering* 2017;108:301–14. <https://doi.org/10.1016/j.compositesb.2016.09.087>.
- [116] Biscaia HC, Chastre C, Silva MAG. Analytical model with uncoupled adhesion laws for the bond failure prediction of curved FRP-concrete joints subjected to temperature. *Theoretical and Applied Fracture Mechanics* 2017;89:63–78. <https://doi.org/10.1016/j.tafmec.2017.01.008>.
- [117] Kafkalidis MS, Thouless MD. The effects of geometry and material properties on the fracture of single lap-shear joints. *International Journal of Solids and Structures* 2002;39:4367–83. [https://doi.org/10.1016/S0020-7683\(02\)00344-X](https://doi.org/10.1016/S0020-7683(02)00344-X).
- [118] Li S, Thouless MD, Waas AM, Schroeder JA, Zavattieri PD. Mixed-mode cohesive-zone models for fracture of an adhesively bonded polymer–matrix composite. *Engineering Fracture Mechanics* 2006;73:64–78. <https://doi.org/10.1016/j.engfracmech.2005.07.004>.
- [119] Bentur A, Mindess S, Mindess S. *Fibre Reinforced Cementitious Composites*. CRC Press; 2006. <https://doi.org/10.1201/9781482267747>.

- [120] Mazzotti C, Bilotta A, Carloni C, Ceroni F, D'Antino T, Nigro E, et al. Bond between EBR FRP and concrete, 2015, p. 39–96. [https://doi.org/10.1007/978-94-017-7336-2\\_3](https://doi.org/10.1007/978-94-017-7336-2_3).
- [121] Pino V, Akbari Hadad H, De Caso y Basalo F, Nanni A, Ali Ebead U, El Refai A. Performance of FRCM-Strengthened RC Beams Subject to Fatigue. *J Bridge Eng* 2017;22:04017079. [https://doi.org/10.1061/\(ASCE\)BE.1943-5592.0001107](https://doi.org/10.1061/(ASCE)BE.1943-5592.0001107).
- [122] Herbrand M, Adam V, Classen M, Kueres D, Hegger J. Strengthening of Existing Bridge Structures for Shear and Bending with Carbon Textile-Reinforced Mortar. *Materials* 2017;10:1099. <https://doi.org/10.3390/ma10091099>.
- [123] Carloni C, Subramaniam K, Savoia M, Mazzotti C. Experimental determination of FRP–concrete cohesive interface properties under fatigue loading. *Compos Struct* 2012;94:1288–96. <https://doi.org/10.1016/j.compstruct.2011.10.026>.
- [124] Ekenel M, Myers JJ. Fatigue Performance of CFRP Strengthened RC Beams under Environmental Conditioning and Sustained Load. *J Compos Constr* 2009;13:93–102. [https://doi.org/10.1061/\(ASCE\)1090-0268\(2009\)13:2\(93\)](https://doi.org/10.1061/(ASCE)1090-0268(2009)13:2(93)).
- [125] Del Prete I, Bilotta A, Nigro E. Performances at high temperature of RC bridge decks strengthened with EBR-FRP. *Compos Part B Eng* 2015;68:27–37. <https://doi.org/10.1016/j.compositesb.2014.08.011>.
- [126] Ombres L, Iorfida A, Mazzuca S, Verre S. Bond analysis of thermally conditioned FRCM-masonry joints. *Measurement: Journal of the International Measurement Confederation* 2018;125:509–15. <https://doi.org/10.1016/j.measurement.2018.05.021>.
- [127] American Concrete Institute. Guide to design and construction of externally bonded Fabric-Reinforced Cementitious Matrix (FRCM) systems for repair and strengthening concrete and masonry structures. ACI 549.4R-13. Farmington Hills, 48331 MI: ACI; 2013.
- [128] Escrig C, Gil L, Bernat-Maso E. Experimental comparison of reinforced concrete beams strengthened against bending with different types of cementitious-matrix composite materials. *Constr Build Mater* 2017;137:317–29. <https://doi.org/10.1016/j.conbuildmat.2017.01.106>.
- [129] Ombres L, Verre S. Flexural Strengthening of RC Beams with Steel-Reinforced Grout: Experimental and Numerical Investigation. *J Compos Constr* 2019;23:04019035. [https://doi.org/10.1061/\(ASCE\)CC.1943-5614.0000960](https://doi.org/10.1061/(ASCE)CC.1943-5614.0000960).
- [130] Park J, Park S-K, Hong S. Experimental study of flexural behavior of reinforced concrete beam strengthened with prestressed textile-reinforced mortar. *Materials* 2020;13. <https://doi.org/10.3390/ma13051137>.
- [131] Blanksvärd T, Täljsten B, Carolin A. Shear strengthening of concrete structures with the use of mineral-based composites. *J Compos Constr* 2009;13:25–34. [https://doi.org/10.1061/\(ASCE\)1090-0268\(2009\)13:1\(25\)](https://doi.org/10.1061/(ASCE)1090-0268(2009)13:1(25)).
- [132] Tetta ZC, Koutas LN, Bournas DA. Textile-reinforced mortar (TRM) versus fiber-reinforced polymers (FRP) in shear strengthening of concrete beams. *Compos Part B Eng* 2015;77:338–48. <https://doi.org/10.1016/j.compositesb.2015.03.055>.
- [133] Trapko T. Stress–strain model for FRCM confined concrete elements. *Compos Part B Eng* 2013;45:1351–9. <https://doi.org/10.1016/j.compositesb.2012.07.001>.

- [134] Di Ludovico M, Prota A, Manfredi G. Structural upgrade using basalt fibers for concrete confinement. *J Compos Constr* 2010;14:541–52. [https://doi.org/10.1061/\(ASCE\)CC.1943-5614.0000114](https://doi.org/10.1061/(ASCE)CC.1943-5614.0000114).
- [135] Cascardi A, Longo F, Micelli F, Aiello MA. Compressive strength of confined column with Fiber Reinforced Mortar (FRM): New design-oriented-models. *Constr Build Mater* 2017;156:387–401. <https://doi.org/10.1016/j.conbuildmat.2017.09.004>.
- [136] Cascardi A, Aiello MA, Triantafillou T. Analysis-oriented model for concrete and masonry confined with fiber reinforced mortar. *Mater Struct* 2017;50:202. <https://doi.org/10.1617/s11527-017-1072-0>.
- [137] Trapko T, Musiał M. Effect of PBO–FRCM Reinforcement on Stiffness of Eccentrically Compressed Reinforced Concrete Columns. *Materials* 2020;13. <https://doi.org/10.3390/ma13051221>.
- [138] Bilotta A, Lignola GP. Effects of Defects On Bond Behavior Of Fiber Reinforced Cementitious Matrix Materials. *Materials* 2020;13. <https://doi.org/10.3390/ma13010164>.
- [139] D’Ambrisi A, Feo L, Focacci F. Bond-slip relations for PBO-FRCM materials externally bonded to concrete. *Compos Part B Eng* 2012;43:2938–49. <https://doi.org/10.1016/j.compositesb.2012.06.002>.
- [140] American Concrete Institute. Guide to design and construction of externally bonded FRP systems for strengthening concrete structures. ACI 440.2R-17. Farmington Hills, 48331 MI: ACI; 2017.
- [141] D’Antino T, Carloni C, Sneed LH, Pellegrino C. Fatigue and post-fatigue behavior of PBO FRCM-concrete joints. *Int J Fatigue* 2015;81:91–104. <https://doi.org/10.1016/j.ijfatigue.2015.06.008>.
- [142] American Concrete Institute. 215R-92. Considerations for Design of Concrete Structures Subjected to Fatigue Loading 1997.
- [143] European Committee for Standardization. Eurocode 2: Design of concrete structures - Part 1-1: General rules and rules for buildings. Brussels, Belgium: CEN; 2004.
- [144] Moore HFB, Kommers JBB. *The Fatigue of Metals*. FRANKLIN CLASSICS TRADE PR; 1927.
- [145] Yi W, Kunnath S, Sun X, Shi C, Tang F. Fatigue Behavior of Reinforced Concrete Beams with Corroded Steel Reinforcement. *ACI Struct J* 2010;107.
- [146] Ma Y, Wang G, Su X, Wang L, Zhang J. Experimental and modelling of the flexural performance degradation of corroded RC beams under fatigue load. *Construction and Building Materials* 2018;191:994–1003. <https://doi.org/10.1016/j.conbuildmat.2018.10.031>.
- [147] Jie S, Shi-ping Y, Fei W, YangYang. Experimental study on the fatigue behaviour of RC beams strengthened with TRC after sustained load corrosion. *Constr Build Mater* 2017;131:713–20. <https://doi.org/10.1016/j.conbuildmat.2016.11.030>.
- [148] Curbach M, Ortlepp R, Triantafillou TC. TRC for rehabilitation. *Textile Reinforced Concrete: State of the Art Report, RILEM TC 201-TRC*, Paris, France: Brameshuber W; 2006, p. 221–36.

- [149] Wiberg A. Strengthening of concrete beams using cementitious carbon fibre composites. PhD Thesis. Royal Institute of Technology, 2003.
- [150] Su M-N, Wei L-L, Liang H-S, Zhu J-H, Ueda T, Xing F. Fatigue behaviour and design of corroded reinforced concrete beams intervened by ICCP-SS. *Composite Structures* 2020. <https://doi.org/10.1016/j.compstruct.2020.113295>.
- [151] Leung CKY, Cheung YN, Zhang J. Fatigue enhancement of concrete beam with ECC layer. *Cement and Concrete Research* 2007;37:743–50. <https://doi.org/10.1016/j.cemconres.2007.01.015>.
- [152] Akbari Hadad H, Nanni A. Fatigue Behavior of FRCM-Strengthened RC Beams. *Journal of Composites for Construction* 2020;24. [https://doi.org/10.1061/\(ASCE\)CC.1943-5614.0001084](https://doi.org/10.1061/(ASCE)CC.1943-5614.0001084).
- [153] Akbari Hadad H, Nanni A, Ebead UA, El Refai A. Static and Fatigue Performance of FRCM-Strengthened Concrete Beams. *J Compos Constr* 2018;22:04018033. [https://doi.org/10.1061/\(ASCE\)CC.1943-5614.0000868](https://doi.org/10.1061/(ASCE)CC.1943-5614.0000868).
- [154] Aljazaeri ZR, Myers JJ. Fatigue and Flexural Behavior of Reinforced-Concrete Beams Strengthened with Fiber-Reinforced Cementitious Matrix. *J Compos Constr* 2017;21:04016075. [https://doi.org/10.1061/\(ASCE\)CC.1943-5614.0000726](https://doi.org/10.1061/(ASCE)CC.1943-5614.0000726).
- [155] Jabr A, El-Ragaby A, Ghrib F. Effect of the Fiber Type and Axial Stiffness of FRCM on the Flexural Strengthening of RC Beams. *Fibers* 2017;5:2. <https://doi.org/10.3390/fib5010002>.
- [156] D'Antino T, Poggi C. Stress redistribution in glass fibers of G-FRCM composites. *Key Eng Mater* 2019. <https://doi.org/10.4028/www.scientific.net/KEM.817.520>.
- [157] Signorini C, Nobili A, Sola A, Messori M. Designing epoxy viscosity for optimal mechanical performance of coated Glass Textile Reinforced Mortar (GTRM) composites. *Constr Build Mater* 2020;233:117325. <https://doi.org/10.1016/j.conbuildmat.2019.117325>.
- [158] Rilem TC 9-RC. Bond test for reinforcement steel. 1. Beam test. RILEM Technical Recommendations for the testing and use of construction materials., CRC Press; 1994.
- [159] De Lorenzis L, Miller B, Nanni A. Bond of FRP laminates to concrete. *ACI Mater J* 2001;98.
- [160] Kotynia R. Bond between FRP and concrete in reinforced concrete beams strengthened with near surface mounted and externally bonded reinforcement. *Constr Build Mater* 2012;32:41–54. <https://doi.org/10.1016/j.conbuildmat.2010.11.104>.
- [161] Focacci F, D'antino T, Carloni C. Analytical modelling of the tensile response of PBO-FRCM composites. *Lecture Notes in Mechanical Engineering* 2020:527–36. [https://doi.org/10.1007/978-3-030-41057-5\\_43](https://doi.org/10.1007/978-3-030-41057-5_43).

## Published works by the author

- [i] Calabrese, A.S., Colombi, P., D'Antino, T. A bending test set-up for the investigation of the bond properties of FRMC strengthenings applied to masonry substrates. *Key Engineering Materials*, 2019. <https://doi.org/10.4028/www.scientific.net/KEM.817.149>
- [ii] Calabrese, A.S., Colombi, P., D'Antino, T. Analytical solution of the bond behavior of FRMC composites using a rigid-softening cohesive material law. *Composites Part B: Engineering*, 2019. <https://doi.org/10.1016/j.compositesb.2019.107051>
- [iii] D'Antino, T., Calabrese, A.S., Poggi, C., Colombi, P., Fava, G., Bocciarelli, M. Strengthening of different types of slabs with composite-reinforced mortars (CRM). *Springer - Research for Development*, 2020. [https://doi.org/10.1007/978-3-030-33687-5\\_26](https://doi.org/10.1007/978-3-030-33687-5_26)
- [iv] Calabrese, A.S., D'Antino, T., Poggi, C., Colombi, P., Fava, G., Pisani, M.A. Application of externally bonded inorganic-matrix composites to existing masonry structures. *Springer - Research for Development*, 2020. [https://doi.org/10.1007/978-3-030-33687-5\\_25](https://doi.org/10.1007/978-3-030-33687-5_25)
- [v] Calabrese, A.S., D'Antino, T., Colombi, P., Poggi, C. Study of the bond behavior of FRMC-masonry joints using a modified beam test. *Lecture Notes in Mechanical Engineering*, 2020. [https://doi.org/10.1007/978-3-030-41057-5\\_38](https://doi.org/10.1007/978-3-030-41057-5_38)
- [vi] Calabrese, A.S., D'Antino, T., Colombi, P., Carloni, C., Poggi, C. Fatigue behavior of PBO FRMC composite applied to concrete substrate. *Materials*, 2020. <https://doi.org/10.3390/ma13102368>
- [vii] D'Antino, T., Calabrese, A.S., Poggi, C. Experimental procedures for the mechanical characterization of composite reinforced mortar (CRM) systems for retrofitting of masonry structures. *Materials and Structures/Materiaux et Constructions*, 2020. <https://doi.org/10.1617/s11527-020-01529-1>
- [viii] Calabrese, A.S., D'Antino, T., Colombi, P., Poggi, C. Study of the influence of interface normal stresses on the bond behavior of FRMC composites using direct shear and modified beam tests. *Construction and Building Materials*, 2020. <https://doi.org/10.1016/j.conbuildmat.2020.120029>
- [ix] Calabrese, A.S., D'Antino, T., Colombi, P. Experimental and analytical investigation of PBO FRMC-concrete bond behaviour using direct and indirect shear test set-ups. *Submitted to Composite Structures*, 2021.
- [x] Calabrese, A.S., D'Antino, T., Colombi, P., Poggi, C., Carloni, C. Influence of the test set-up on the bond behavior of FRMC composites. *In press on ACI SP*, 2021.
- [xi] Calabrese, A.S., D'Antino, T., Colombi, P., Carloni, C., Poggi, C. Fatigue behavior of FRMC strengthened RC beams: state of the art and future developments. *Submitted to CICE 2021*
- [xii] D'Antino, T., Calabrese, A.S., Colombi, P., Poggi, C. Numerical study of the effective lap-splice length of FRMC composites. *Submitted to CICE 2021*

